

**From Small Molecules to Polymers: Linear and Nonlinear Optical Properties of
Organic Conjugated Systems for Solar Applications**

by

Bradley Austin Keller

A dissertation submitted in partial fulfillment
of the requirements for the degree of
Doctor of Philosophy
(Macromolecular Science and Engineering)
in the University of Michigan
2018

Doctoral Committee:

Professor Theodore G. Goodson III, Chair
Professor Jinsang Kim
Associate Professor Dominika Zgid
Assistant Professor Paul M. Zimmerman

Bradley Austin Keller

kellerab@umich.edu

ORCID: 0000-0001-7198-5124

© Bradley Austin Keller 2018

DEDICATION

This dissertation is dedicated to all of those that have helped me along the way.

TABLE OF CONTENTS

DEDICATION.....	ii
LIST OF FIGURES	vi
LIST OF TABLES.....	xv
LIST OF APPENDICES.....	xvii
ABSTRACT.....	xviii
Chapter 1 Introduction and Background.....	1
1.1 Energy Sources of the World Background	1
1.2 Solar Energy Harvesting Principles	7
1.3 Silicon Solar Cells	13
1.4 Non-Silicon Inorganic Solar Cells.....	17
1.5 Organic Solar Cell Properties	18
1.6 Organic Solar Cells Advantages and Disadvantages.....	21
1.7 Organic Solar Cell Architecture.....	24
1.8 Different Types of Organic Light Harvesting Materials for Solar Cells ..25	
1.8.1 Organic Dye Solar Cells	25
1.8.2 Macromolecules: Homopolymers.....	26
1.8.3 Conjugated Donor-Acceptor Polymers.....	29
1.8.4 Donor Subunits in Donor-Acceptor Polymers.....	32
1.8.5 Acceptor Subunits in Donor-Acceptor Polymers	34
1.8.6 Acceptor Materials for Organic Solar Cells	35
1.9 Dissertation Outline	37
Chapter 2 Experimental Theory and Techniques.....	54
2.1 Overview	54
2.2 Steady-State Spectroscopy.....	54
2.3 Time-resolved fluorescence upconversion	59
2.4 Two-photon Absorption Spectroscopy	62
2.5 Transient absorption spectroscopy.....	65
2.6 Computational methods	69

Chapter 3 Ultrafast Spectroscopic Study of Donor-Acceptor Benzodithiophene Light Harvesting Organic Conjugated Polymers.....	74
3.1 Abstract.....	74
3.2 Introduction.....	75
3.3 Experimental.....	78
3.3.1 Steady State UV-Vis and Emission Measurements	78
3.3.2 Fluorescence Lifetime Measurements	78
3.3.3 Two-Photon Absorption Measurements	79
3.4 Results.....	80
3.4.1 Synthesis	80
3.5 Molecular Weight Determination	82
3.6 Linear Absorption	83
3.7 Fluorescence Spectra	85
3.8 Two-Photon Absorption Measurements	87
3.9 Fluorescence Upconversion Dynamics.....	88
3.10 Discussion.....	93
3.11 Conclusions.....	96
Chapter 4 The Role of Donor Conjugation Length on the Optical Properties of Donor-Acceptor Light Harvesting Conjugated Polymers: An Investigation of Thiophene Additions to s-Indacene Donors with Diketopyrrolopyrrole, Isoindigo, and Thienothiophene Acceptors	101
4.1 Abstract.....	101
4.2 Introduction.....	102
4.3 Experimental.....	108
4.3.1 Steady State UV-Vis and Emission Measurements	108
4.3.2 Two-Photon Absorption (TPA) Experiments	109
4.3.3 Fluorescence Upconversion Experiments	110
4.3.4 Transient Absorption Experiments	110
4.4 Molecular Structures and Molecular Properties	111
4.5 Steady State.....	113
4.5.1 Absorption.....	113
4.5.2 Fluorescence	116
4.6 Quantum-Mechanical Calculations.....	120
4.6.1 Basis Set and Level of Theory	120
4.6.2 Computation.....	121
4.6.3 Molecular Orbital Energies of Monomers	121
4.7 Polymerization Effects on Molecular Orbital and Electronic Structure Calculations	124
4.7.1 Polymerization Effect on Bandgap	124

4.7.2 Polymerization Effects on Electronic Structure Calculations ..	125
4.7.3 Polymer Electronic Structure Absorption Calculations	126
4.8 Two-photon absorption	138
4.9 Time Resolved Fluorescence	140
4.10 Ultrafast Transient Absorption	143
4.11 Nanosecond Transient Absorption.....	151
4.12 Conclusion	154
Chapter 5 Nanosecond Two-Photon Excitation Fluorescence Design of Experiment and Preliminary Data	163
5.1 Introduction.....	163
5.2 Experimental	163
5.3 Preliminary Data	183
5.4 Conclusion	187
Chapter 6 Nanosecond Transient Absorption Experiment and Preliminary Data	188
6.1 Introduction.....	188
6.2 Experimental	188
6.3 Preliminary Data	200
6.4 Conclusion	202
Chapter 7 Overall Summary and Future Direction	203
7.1 Overall Summary	203
7.2 Future Directions	206
Appendices.....	209

LIST OF FIGURES

Figure 1.1.1 World energy consumption by energy source	2
Figure 1.1.2 Energy Consumption 1991-2016.....	2
Figure 1.1.3. Normalized Spectral at AM 1.5.....	5
Figure 1.1.4. Major advances of Photovoltaics	6
Figure 1.2.1. Solar harvesting schematic: 1 absorption, 2 exciton formation and diffusion, 3 charge dissociation, 4 charge carrier diffusion, and 5 charge collection.	8
Figure 1.2.2. Solar cell diagram.....	9
Figure 1.2.3. Fill Factor	12
Figure 1.2.4. Solar Cell Efficiency	13
Figure 1.3.1. Electronic energy level diagram of metals, semiconductors, and insulators.....	14
Figure 1.3.2. Silicon Solar Cell	16
Figure 1.4.1 CdTe Typical Solar Cell	17
Figure 1.5.1. Electronic state diagram of organic solar cell	20
Figure 1.5.2. Electronic state diagram of photon absorption of electron from HOMO to LUMO in Organic System	21
Figure 1.7.1. Organic solar cell architecture.....	25
Figure 1.8.1.1. Typical dye sensitized solar cell	26
Figure 1.8.2.1. Energy level modulation via increasing polymerization	28
Figure 1.8.3.1. Energy level modulation in donor-acceptor polymer	30
Figure 2.2.1. Agilent 8453 UV-Vis spectrophotometer schematic	57

Figure 2.2.2. Fluoromax-2 schematic	59
Figure 2.3.1. Fluorescence upconversion setup	61
Figure 2.4.1. Ultrafast TPEF Setup	65
Figure 2.5.1. Pump-probe concept used in transient absorption spectroscopy. A is excited state absorption, B is a bleach state, and C is stimulated emission.	66
Figure 2.5.2. Ultrafast transient absorption setup.	69
Figure 3.4.1. Investigated polymers. For PTB7, R ₁ =2-ethylhexyl. For the other polymers, R ₁ =2-ethylhexyl, and R ₂ =4-octylphenyl.	80
Figure 3.6.1. Absorption spectra of PBTCT, PBT8PT, PBTT17T, PBTFDO, and PTB7. The absorption spectra are normalized	85
Figure 3.7.1. Emission(PBTCT, PBT8PT, PBTT17T: Excitation wavelength: 400nm. PBTFDO: Excitation wavelength: 450nm. PTB7: Excitation wavelength: 517 nm). Emission intensities are normalized.	87
Figure 3.9.1. Fluorescence Upconversion of PBTCT(top left) at 400nm excitation and 600nm emission., PBT8PT(top right) at 400nm excitation and 650nm emission., PBTT17T(bottom left) at 400nm excitation and 650nm emission., and PBTFDO(bottom right) at 400nm excitation and 700nm emission.	90
Figure 3.9.2. Fluorescence Upconversion of PTB7 at 400nm excitation and 700nm emission.	91
Figure 3.9.3. Anisotropic measurements. PBTCT (top left). PBT8PT (top right). PBTT17T (bottom left). PBTFDO (bottom right)	93
Figure 4.4.1. Polymer Structures (blue portion is the donor and red portion is the acceptor).	113
Figure 4.5.1.1. Normalized steady state absorption of more conjugated donor polymer series P1-P3(left) and less conjugated polymer series P4-P6(right).	116
Figure 4.5.2.1. Normalized steady state fluorescence of P1-P3(Left) and P4-P6(Right) at 430 nm excitation for donor excitation (solid line) and >600 nm excitation for acceptor excitation(dashed line).	119
Figure 4.6.3.1. Molecular orbital energy diagram of monomers of polymers P1-P6 using B3LYP functional.	122
Figure 4.6.3.2. Molecular orbital energy diagram of monomers of polymers P1-P6 using wB97x-D functional.	123

Figure 4.7.1.1. Bandgap of monomer, dimer, trimer, and tetramer of P1-P6 using wB97x-D functional.	124
Figure 4.7.2.1. Electronic geometries for donor-acceptor monomers.	126
Figure 4.7.3.1. The electronic structure calculations for the trimers for P1-P6.....	128
Figure 4.7.3.2. Electronic structure for the ground state (left) and excited state (right) that contribute to the low energy S_0 to S_1 transition for P1 (a.) and P4 (b.). The red arrows represent the qualitative magnitudes of the electron density change.....	130
Figure 4.7.3.3. Electronic structure for the ground state (left) and excited state (right) that contribute to the high energy transition for P1 (a.) and P4 (b.). The red arrows represent the qualitative magnitudes of the electron density change.	132
Figure 4.7.3.4. Electronic structure for the ground state (left) and excited state (right) that contribute to the low energy S_0 to S_1 transition for P2 (a.) and P5 (b.). The red arrows represent the qualitative magnitudes of the electron density change.....	133
Figure 4.7.3.5. Electronic structure for the ground state (left) and excited state (right) that contribute to the high energy S_0 to S_{22} transition for P2 (a.) and P5 (b.). The red arrows represent the qualitative magnitudes of the electron density change.....	135
Figure 4.7.3.6. Electronic structure for the ground state (left) and excited state (right) that contribute to the low energy S_0 to S_1 transition for P3 (a.) and P6 (b.). The red arrows represent the qualitative magnitudes of the electron density change.....	136
Figure 4.7.3.7. Electronic structure for the ground state (left) and excited state (right) that contribute to the high energy S_0 to S_9 transition for P3 (a.) and P6 (b.). The red arrows represent the qualitative magnitudes of the electron density change.....	137
Figure 4.8.1. Logarithmic plot of the quadratic dependence(counts per second vs power) for standards styryl 9m, zn-tetra-tert-butyl-pc, and the investigated polymers. 1300 nm excitation was used for P1, P2, P4, P5, and styryl 9m. 1250 nm excitation was used for P3 and P6(not shown), and zn-tetra-tert-butyl-pc. All have a slope ~ 2 and $R^2 > 0.99$	140
Figure 4.9.1. Fluorescence upconversion of P1 (top left),P4 (top right), P3 (bottom left), and P6 (bottom right) at 400 nm excitation and 680 nm emission.	143
Figure 4.10.1. Transient absorption spectra and kinetic fits of P1 (a.) and P4 (b.).	145
Figure 4.10.2. Energy level diagrams of transient absorption processes for P1 (left) and P4 (right).	146
Figure 4.10.3. Transient absorption spectra and kinetic fits of P2 (a.) and P5 (b.).	147
Figure 4.10.4. Energy level diagrams of transient absorption processes for P2 (left) and P5 (right).	148

Figure 4.10.5. Transient absorption spectra and kinetic fits of P3 (a.) and P6 (b.).	150
Figure 4.10.6. Energy level diagrams of transient absorption processes for P3 (left) and P6 (right).	151
Figure 4.11.1. Ultrafast transient absorption spectra (top) for P1 (left) and P4 (right). Nanosecond transient absorption spectra (bottom) for P1 (left) and P4 (right).	152
Figure 4.11.2. Ultrafast transient absorption spectra (top) for P2 (left) and P5 (right). Nanosecond transient absorption spectra (bottom) for P2 (left) and P5 (right).	153
Figure 4.11.3. Ultrafast transient absorption spectra (top) for P3 (left) and P6 (right). Nanosecond transient absorption spectra (bottom) for P3 (left) and P6 (right).	154
Figure 5.2.1. Quanta-Ray Laser System	167
Figure 5.2.2. Schematic setup of OPO VersaScan	170
Figure 5.2.3. Desktop location for ScanMaster SHG	171
Figure 5.2.4. Location of the calibration wizard.	172
Figure 5.2.5. Base calibration selection	172
Figure 5.2.6. Crystal configuration selection window	173
Figure 5.2.7. Calibration wizard window	174
Figure 5.2.8. Nanosecond TPA Setup	177
Figure 5.2.9. SRS 250 gated integrator	178
Figure 5.2.10. Block diagram of initialization of custom data collection program	179
Figure 5.2.11. Block diagram data collection for first for loop	180
Figure 5.2.12. Block diagram for sequence that creates a user interface for scan breaks	180
Figure 5.2.13. Block diagram for sequence that plots and saves the data to a file	181
Figure 5.2.14. User interface for the TPEF collection program.	181
Figure 5.2.15. User parameters inputted before turning on SRS 250	182
Figure 5.3. Two-photon absorption results from 750 nm to 1100 nm for Rhodamine B	186
Figure 5.3.2. Two-photon absorption results from 850 nm for Acridine Orange	186
Figure 6.1. Nanosecond transient absorption setup	189

Figure 6.2. LP980 setup	190
Figure 6.3. Kinetic Absorption Setup window.	191
Figure 6.4. Oscilloscope tab	192
Figure 6.5. Measurement tab	193
Figure 6.6. Background tab	193
Figure 6.7. Wavelength selection window.....	195
Figure 6.8. Data slicing window	195
Figure 6.9. Kinetic absorption setup for RuBPY	196
Figure 6.10. Laser mode window	197
Figure 6.11. Prism compartment for adjusting laser alignment to the sample	198
Figure 6.12. Sample compartment with iris	198
Figure 6.13. Lamp housing chamber	198
Figure 6.14. Configuration for Lamp alignment.....	199
Figure 6.15. Mirror screws for adjustments.....	200
Figure 6.16. Nanosecond transient absorption of Ru(BPY) ₃	224
Figure 6.6. Background tab	201
Figure A.3.1. Jablonski diagram for the states of intramolecular singlet fission, 1ET, and 2ET with chemical structures of QOT2/AQ	211
Figure A.3.2. Optimized structure of QOT2/AQ before ET (top panel; QOT2 TT/AQ), after 1ET (middle panel; QOT2+ TD/AQ-), and after 2ET (bottom panel; QOT22+ DD/AQ2-) described by CDFT. Color scheme: hydrogen atom, white; carbon atom, cyan; nitrogen atom, blue; oxygen atom, red; sulfur atom, yellow	212
Figure A.3.3. Absorption spectra predicted by XMS-CASPT2 and Spin-Flip RAS for (top) QOT2 21Ag state, and (middle and bottom) its oxidized forms, QOT2+ 12Bg and QOT22+ 11Bu states	214
Figure A.3.4. Transmission profile of pure acetonitrile (Blank, black line), QOT2 (yellow square), and QOT2/AQ (blue circle) for the probe light of 880 nm as the function of the pump power at 440 nm	215

Figure A.3.5. Transient absorption spectrum of QOT2/AQ at selected decaying time as the function of probe wavelength. The characteristic bands of QOT2 (GSB and ESA I) are marked with yellow arrows, and newly arising features (ESA II, III, and IV) are indicated with blue arrows.....	216
Figure AS1: (A) QOT2 chromophore. (B) Model of QOT2 with the β,β' substituents removed	220
Figure AS2: UV-Vis absorption of QOT2, AQ, and QOT2/AQ in AN.	224
Figure AS3: Fluorescence emission of QOT2, AQ, and QOT2/AQ in AN. The spectrum of AQ is enlarged in the inset	225
Figure AS4: Relative energy levels of QOT2, AQ, and their relevant ET products	225
Figure AS5: Position of localized positive (negative) charge on the isolated QOT2 (AQ) molecule	226
Figure AS6: Position of localized charges on the ground state QOT2/AQ complex	227
Figure AS7: CDFT Becke population analysis of QOT2/AQ after 2ET	228
Figure AS8: Distortion of carbonyl group from planarity in AQ as the result of maximizing Coulomb interaction.....	228
Figure AS9: Time-resolved fluorescence anisotropy measurement of QOT2 and QOT2/AQ	229
Figure AS10: Transient absorption spectrum of QOT2 at selected decaying time as the function of probe wavelength. The characteristic bands of QOT2 (GSB and ESA I) are marked with yellow arrows.....	230
Figure AS11: Yield of two-electron transfer and charge carrier extraction as the function of yield of one-electron transfer	236
Figure B.4.1. Normalized absorption and emission spectra of C1 in solvents of different polarity	250
Figure B.4.2. Normalized absorption and emission spectra of C2 in solvents of different polarity	251
Figure B.4.3. Normalized absorption and emission spectra of C1 and C2 in DCM and EtOH	252
Figure B.5.1. Frontier molecular orbitals of C1 and C2 at the optimized S_0 geometry (H means here HOMO and L means LUMO).....	257

Figure B.5.2. Frontier molecular orbitals of C1 and C2 at the optimized S_1 geometry (LSOMO is the lowest singly occupied molecular orbital; HSOMO is the highest singly occupied molecular orbital)	258
Figure B.5.3. Difference of electron density between states for the $S_0 \rightarrow S_1$ and $S_1 \rightarrow S_0$ transitions of compounds C1 and C2 in DCM (in the figures the colours violet and cyan correspond to an increase and a decrease in electron density, respectively)	259
Figure B.6.1. Pump–probe absorption of C1 in CHCl_3 ($\lambda_{\text{exc}}=400$ nm): A) contour plot of the experimental data, B) time resolved absorption spectra recorded at different delays after the laser pulse. Insets: decay kinetics recorded at meaningful wavelengths together with the corresponding fitting traces and C) Species Associated Spectra (SAS) of the decay components obtained by Target Analysis	265
Figure B.6.2. Pump–probe absorption of C1 in MeOH ($\lambda_{\text{exc}}=400$ nm): A) contour plot of the experimental data, B) time resolved absorption spectra recorded at different delays after the laser pulse. Insets: decay kinetics recorded at meaningful wavelengths together with the corresponding fitting traces and C) Species Associated Spectra (SAS) of the decay components obtained by Target Analysis	265
Figure B.6.3. Pump–probe absorption of C2 in CHCl_3 ($\lambda_{\text{exc}}=400$ nm): A) contour plot of the experimental data, B) time resolved absorption spectra recorded at different delays after the laser pulse. Insets: decay kinetics recorded at meaningful wavelengths together with the corresponding fitting traces and C) Species Associated Spectra (SAS) of the decay components obtained by Target Analysis	266
Figure B.6.4. Pump–probe absorption of C2 in MeOH ($\lambda_{\text{exc}}=400$ nm): A) contour plot of the experimental data, B) time resolved absorption spectra recorded at different delays after the laser pulse. Insets: decay kinetics recorded at meaningful wavelengths together with the corresponding fitting traces and C) Species Associated Spectra (SAS) of the decay components obtained by Target Analysis	266
Figure B.6.5. Fluorescence up–conversion kinetics ($\lambda_{\text{exc}}=400$ nm) of C1 and C2 in MeOH and EtOH (dots) together with the best fittings (full lines) obtained by use of poly–exponential functions (see Table 4)	267
Figure B.7.1. Logarithmic plot of the quadratic dependence (counts vs. power) for: Styryl 9M in EtOH (black line), C1 in DCM (blue line) and C2 in DCM (red line)	268
Figure BS1. Normalized absorption spectra of concentrated and diluted solution of C1 in DCM and 2-PrOH	275
Figure BS2. Normalized absorption spectra of concentrated and diluted solution of C2 in DCM and MeOH.....	276
Figure BS3. Pump–probe absorption of C1 in DCM ($\lambda_{\text{exc}}=400$ nm): A) contour plot of the experimental data, B) time resolved absorption spectra recorded at different delays after the laser pulse. Insets: decay kinetics recorded at meaningful wavelengths together with the corresponding fitting traces and C) Species Associated Spectra (SAS) of the decay components obtained by Target Analysis	278

Figure BS4. Pump–probe absorption of C1 in EtOH ($\lambda_{exc}=400$ nm): A) contour plot of the experimental data, B) time resolved absorption spectra recorded at different delays after the laser pulse. Insets: decay kinetics recorded at meaningful wavelengths together with the corresponding fitting traces and C) Species Associated Spectra (SAS) of the decay components obtained by Target Analysis	278
Figure BS5. Pump–probe absorption of C2 in DCM ($\lambda_{exc}=400$ nm): A) contour plot of the experimental data, B) time resolved absorption spectra recorded at different delays after the laser pulse. Insets: decay kinetics recorded at meaningful wavelengths together with the corresponding fitting traces and C) Species Associated Spectra (SAS) of the decay components obtained by Target Analysis	279
Figure BS6. Pump–probe absorption of C2 in EtOH ($\lambda_{exc}=400$ nm): A) contour plot of the experimental data, B) time resolved absorption spectra recorded at different delays after the laser pulse. Insets: decay kinetics recorded at meaningful wavelengths together with the corresponding fitting traces and C) Species Associated Spectra (SAS) of the decay components obtained by Target Analysis	279
Figure C.3.1. NMR spectra of fused and non-fused compounds.....	294
Figure C.3.1.2. (a) Absorption spectra of ladder molecules; (b) CV of ladder molecules in CHCl ₃	295
Figure C.3.2. (a) Emission spectra of ladder molecules; (b) Fluorescence decay dynamic of ladder molecules at ~ 600 nm emission	296
Figure C.3.3. (a) Two photon emission spectra of ladder molecules; (b) Power dependence of the two-photon-excited emission of ladder molecules at ~ 720 nm	297
Figure CS1. TGA curves (left) of all compounds: heating rate: 10 oC /min. from 70 oC to 550 oC under nitrogen atmosphere. Thermogravimetric analysis (TGA) reveals that both non-fused ring and fused ring molecules are thermally stable up to 400 °C. DSC measurements (right) were also performed on a DSC 2920 instrument. Samples (~5 mg) were annealed by heating to 300 oC at 20 oC/min, cooled to 0 oC at 20 oC/min, and then analyzed while being heated to 300 oC at 20 oC/min. No obvious melting peak was shown in the temperature window.....	311
Figure CS2. Variable temperature 1H NMR spectra of 3r showing the split of proton a result from hindered rotation of the asymmetry ethylhexyl groups.....	311
Figure CS3. COSY (up) and NOESY (down) spectra of 3r in 353 K in C ₂ D ₂ Cl ₄	312
Figure CS4. NOESY spectra of C3r (up) and C5r (down) in 353 K in C ₂ D ₂ Cl ₄	313
Figure CS5. Optimized geometry of ladder type molecules. To facilitate the calculation, the heptylhexyl chains in PDI were replaced with a methyl group, while the ethylhexyl groups in heteroacenes were replaced by isobutyl to avoid missing the steric hindrance effect.....	189
Figure CS6. HOMO and LUMO molecular orbital distribution and the energy levels of ladder type molecules. Isovalue was 0.02 for printing both HOMO and LUMO orbitals	314

Figure CS7. CV of ladder type molecules in CHCl_3	314
Figure CS8. (a) Absorption spectra of thienoacenes and PDI unit; (b) Fluorescence spectra of thienoacenes and PDI unit; (c) Absorption spectra of non-fused ring compounds; (d) Molecular structures of thienoacenes and PDI unit	314
Figure CS9. Energy rising component of the C3r at 600 emission wavelength	315
Figure CS10. Power dependence of the two-photon-excited emission of all molecules at ~440-460 nm	315

LIST OF TABLES

Table 3.5.1. Molecular weight and steady state properties of studied polymers	82
Table 3.8.1. TPA properties of studied polymers	87
Table 3.9.1. Fluorescence lifetime of polymer samples	91
Table 3.10.1. Anisotropy and Power Conversion Efficiency.	95
Table 4.4.1. Molecular Properties	112
Table 4.5.1.1. Steady state absorption properties(Molar absorptivities: $\epsilon/10^4 \text{ L mol}^{-1} \text{ cm}^{-1}$)	116
Table 4.5.2.1. Steady state fluorescence properties	120
Table 4.6.3.1. HOMO, LUMO and Bandgap energies for monomers of polymers P1-P6 using B3LYP functional	122
Table 4.6.3.2. HOMO, LUMO and Bandgap energies for monomers of polymers P1-P6 using wB97x-D functional.	124
Table 4.7.1.1. Bandgap of monomer, dimer, trimer, and tetramer of polymers P1-P6 using wB97x-D functional in eV	125
Table 4.8.1. TPA cross-section	140
Table 4.9.1. Fluorescence decay dynamics	142
Table 4.10.1. Transient absorption kinetic fits at selected wavelengths for P1 and P4.....	145
Table 4.10.2. Transient absorption kinetic fits at selected wavelengths for P2 and P5.....	148
Table 4.10.3. Transient absorption kinetic fits at selected wavelengths for P3 and P6.....	150
Table A.3.1. Assignment of Characteristic Bands Present in the Transient Absorption Spectra Depending on One- or Two-Electron Transfer	217
Table AS1. Characterization of diabatic states of the QOT2/AQ complex investigated in this study using charge and spin	221
Table AS2 Coulomb interaction between four point charges in QOT2/AQ complex.....	227

Table AS3 Population of QOT2 TT, and ionized QOT2 TT	229
Table AS4 Lifetime excited singlet state of QOT2 and QOT2/AQ using time-resolved fluorescence anisotropy	230
Table AS5 Assignment of ESA II, III, and IV with the position of peak and oscillator strength	237
Table B.4.1. Spectral properties and fluorescence quantum yields of C1 and C2 in several solvents of different polarity $f(\epsilon, n_2) = [(\epsilon - 1)/(2\epsilon + 1)] - [(n_2 - 1)/(2n_2 + 1)]$	251
Table B.5.1. Dipole moments of the ground state (S ₀), the Frank–Condon first excited singlet state (S _{1,FC}) and the relaxed first excited singlet state (S _{1,opt}) of compounds C1 and C2 in DCM obtained by the B3LYP/6–31G(d) model followed by QTAIM: total modulus (μ_{Tot}) and Cartesian components (μ_x , μ_y and μ_z).....	254
Table B.6.1. Spectral and kinetic properties of the transients of C1 and C2 in solvents of different polarity (obtained by femtosecond transient absorption measurements upon excitation at 400 nm).	264
Table B.6.2. Decay components of C1 and C2 obtained by the decay kinetics of the up–conversion fluorescence recorded at 688 nm ($\lambda_{exc} = 400$ nm)	267
Table B.7.1. TPA cross sections determined for C1 and C2 in DCM by exciting at 1300 nm together with that of the reference compound (Styryl 9M) in EtOH. The parameters used for the calculations by equation 2 are also reported 125 Table 4.7.1.1. Bandgap of monomer, dimer, trimer, and tetramer of polymers P1-P6 using wB97x-D functional in eV	269
Table B.7.2. Wavelengths (λ), cross sections (δ) and polarization ratios (R) computed for the lowest excited singlet states of C1 and C2 in DCM (PCM) by B3LYP/6–31G(d) (Dalton2016.1).....	271
Table BS1. Full Width at Half Maximum (FWHM) of the absorption and emission bands of C1 and C2 in different solvents	276
Table BS2. Transition energy, nature and oscillator strength of the lowest excited singlet states of C1 in DCM calculated by TD-DFT B3LYP/6-31G(d), together with the experimental absorption and emission maxima (λ_{exp}) in the same solvent.....	277
Table BS3 Two photon transition tensor (a.u.; 1 a.u.= 1.896788×10^{-50} cm ⁴ s photon ⁻¹) of C1 and C2 in DCM (PCM) computed by B3LYP/6-31G* (Dalton2016.1).....	280
Table C.3.1 Energy levels and photophysical properties.....	294

LIST OF APPENDICES

A. Enacting Two-Electron Transfer from a Single-Photon-Excited Chromophores.....	209
A.1 Abstract	209
A.2 Introduction	210
A.3 Results and Discussion.....	211
A.4 Conclusions	217
B. Two-Photon Absorption Enhancement Parallels Intramolecular Charge Transfer Efficiency in Quadrapolar Versus Dipolar Cationic Chromophores	239
B.1 Abstract	239
B.2 Introduction	240
B.3 Experimental	243
B.4 Results and Discussion.....	247
B.5 Quantum-Mechanical Calculations	252
B.6 Femtosecond Transient Absorption and Fluorescence Up-Conversion	259
B.7 Two Photon Excited Fluorescence Measurements	268
B.8 Conclusions	273
C. Two Photon Absorption Study of Low-Bandgap, Fully Conjugated Perylene Diimide Thienoacene Perylene Diimide Ladder-Type Molecules	289
C.1 Abstract	289
C.2 Introduction	290
C.3 Results and Discussion.....	291
C.4 Conclusions	298
C.5 Experimental Section	299

ABSTRACT

The world is seeing rapid population growth and with this growth, energy demands have soared. Traditionally, fossil fuels have been used to meet these demands, but extraction of fossil fuels is detrimental to the environment, burning of fossil fuels contributes significantly to adding pollutants to the environment, and have directly resulted in climate change. This has spurred the public and scientists to search for energy sources that are more environmentally friendly and are renewable. The sun is the largest energy source in the solar system. If materials and devices can be designed to collect even a fraction of the sun's energy, humanity's energy needs will be met many times over. One of the most promising light harvesting materials is organic light harvesting materials because of their ease of processing, lightweight, high absorption capabilities, and flexibility.

In this thesis, the optical properties of conjugated organic light harvesting materials were investigated. In order to improve the efficiency of these devices, the fundamental optical properties need to be understood. In the first study, the optical properties of light harvesting donor-acceptor polymers with the same donor monomer with different strength acceptors were investigated. Stronger acceptor donor-acceptor polymers had enhanced charge transfer characteristics, lower quantum yields, and shorter fluorescence lifetimes compared to weaker acceptor polymers. In the second study, the effect of donor conjugation length on the optical properties of donor-acceptor light harvesting polymers was investigated with ultrafast spectroscopic techniques. Polymers with longer donor conjugation lengths had higher extinction coefficients, higher charge transfer characteristics, and transient absorption experiments revealed additional species in the excited state. Computational studies related the electronic structures to the optical properties of the investigated polymers. Two new

experiments were designed and installed for unprecedented wavelength selection and unprecedented long timescale investigations. An overview of a new nanosecond system that I have installed and two-photon absorption experiment that I have designed is presented. The experimental procedure and design is described. Preliminary results are presented demonstrating the success of this new system and experimental design. A new nanosecond transient experiment was installed. The experimental procedure for the nanosecond transient experiment is described. Preliminary results are presented demonstrating the successful implementation and operation of this new system.

Chapter 1

Introduction and Background

1.1 Energy Sources of the World Background

The current world population is approximately 7.5 billion with an annual growth rate of over 1 percent, with projections of 10 billion people by the year 2056.¹ Such rapid population growth has put significant stress on natural resources, water security, environment, and energy security.²⁻⁵ In particular, energy security has presented significant challenges for the future of humanity, with energy demand increasing by approximately 1% in 2016 with projections of energy consumption increasing 28% by 2040 as seen in **Figure 1.1.1.**⁶⁻⁷ The predominant energy source for the global consumption are fossil fuels, such as coal, oil, and natural gas, which supply over 80% of energy demand as seen in **Figure 1.1.2.**⁸ But using fossil fuels as humanity's major energy source has significant obstacles. Fossil fuels were formed by the gradual decomposition of flora and fauna over millions of years at high pressures and temperatures, thus they are non-replenishable for current energy demands and impractical as long term energy sources since it is non-renewable over human timescales.⁹ The extraction of fossil fuels involve significant damage to the local environment.¹⁰ And one of the biggest issues for fossil fuels is that they are major source of harmful emissions.¹¹ The combustion of fossils results in the significant release of sulfur dioxides which are responsible for environmental destruction due to acid rain, and nitrous oxides and carbon oxides which are responsible for devastating climate change.¹² These significant drawbacks have led to intense investigation into new energy sources, technologies, materials, methods, and policies. In particular, there has been

significant attention given to alternative energy sources such as nuclear and renewable energy sources such as geothermal, hydroelectric, wind, and solar.

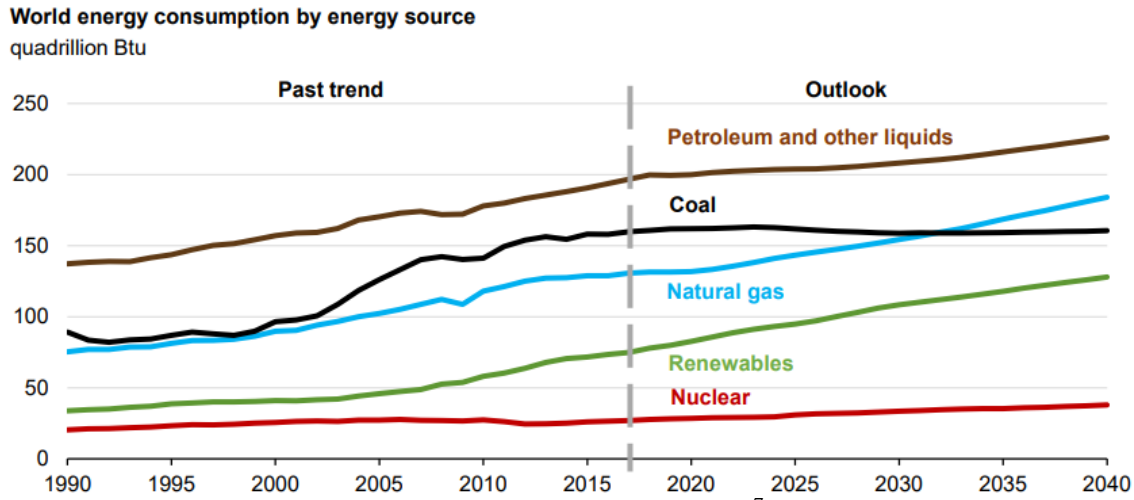


Figure 1.1.1 World energy consumption by energy source⁷

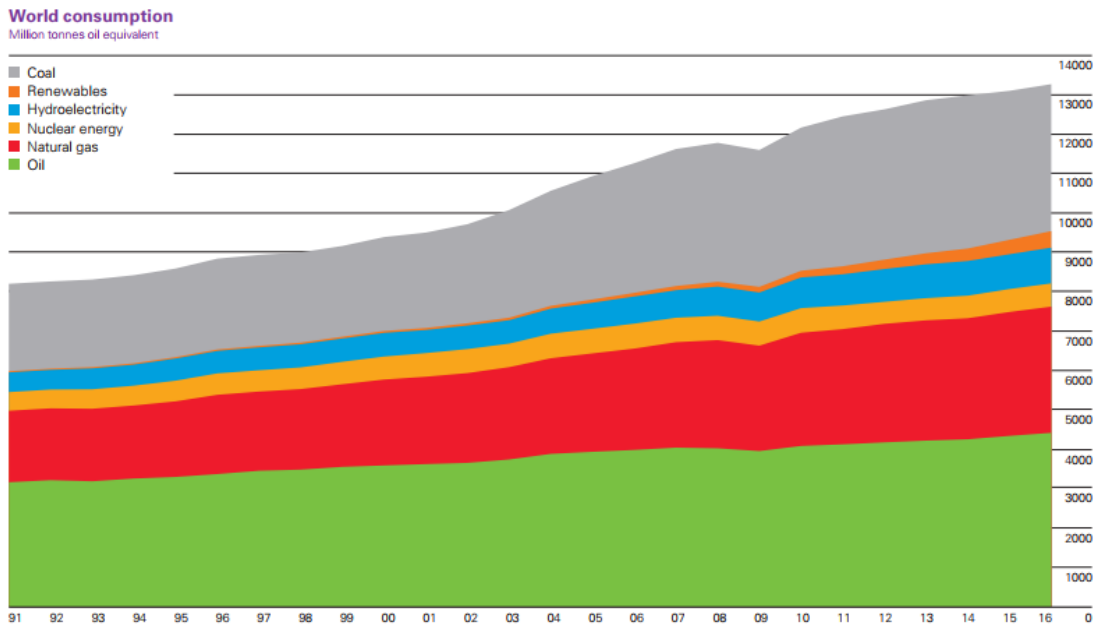


Figure 1.1.2 Energy Consumption 1991-2016⁶

Nuclear power is a controversial alternative energy source but has seen production capacity growth.⁶ Nuclear power uses the heat generated by nuclear fission of radioactive nuclei to heat up water that is then used to generate steam to turn turbines. Nuclear power has come a long way from generation I, prototype proof, of concept reactors from the 1950's to 1960's.¹³

Indeed, there have been significant improvement of the generation II reactors that are currently in use today. These improved generation II reactors are more efficient and safer than earlier models of the same generation, such as those involved in the Chernobyl and Three Mile Island accidents.¹⁴ The most advanced systems in use today are the Generation III reactors, which have significant improvements in efficiency, improved fuel technologies, and safety systems that use passive systems to improve safety.¹⁵ There are also plans for generation IV reactors that will reduce the lifetime of spent fuel, increase energy yield, and increase safety.¹⁶⁻¹⁷ The newer designs and new technologies have made nuclear significantly safer compared to the earlier generations. There are no emissions associated with nuclear power generation. There is an extremely high energy production to weight ratio.¹⁸ Nuclear power can steadily supply power and output can be tailored to meet high load needs, which is in stark contrast to many renewable energy sources that experience variability.¹⁹ But there are still significant drawbacks presented by nuclear power. Even some of the most sophisticated nuclear power plants in operation have failed catastrophically.²⁰ The energy source is non-renewable and uses rare earth metals.²¹ Nuclear plants also need to be built in regions that minimize exposure to natural disasters. The waste generated needs complex storage facilities that can store the waste for millennia. And perhaps the biggest obstacle for nuclear power generation is public and social opposition, which is even harder to quantify.

Hydroelectric power generation is another renewable energy resource that has shown great promise; with approximately 3% growth in production capacity.⁶ Hydroelectric power generation uses either the flow of water or gravitational potential energy of water to drive turbines in order to generate electricity. Hydroelectric power can directly convert the flow of the water source into electricity, but this method is limited by the seasonal water flow.²²

Hydroelectric power can use manmade storage dams, which negates seasonal flow changes, but is limited by the volume of water stored, and by the height that is responsible for gravitational potential energy difference between the source and outflow.²³ Since none of these hydroelectric power generation systems consume fuel, there are no emissions which is a significant advantage over fossil fuels. Unfortunately, all hydroelectric power generation is limited to areas with large flowing water sources. It also disrupts wildlife and can significantly affect downstream ecosystems.²⁴

Wind energy has seen the largest increase in production capacity and has represented the largest increase in renewable use.⁶ Wind power generation uses the wind to drive large rotating blades that drive turbines for electricity generation. Wind has the advantage of being able to be installed in remote areas due to the fact that it does not rely upon large facilities for fuel storage or power generation. It has the advantage over other alternative energy sources because it does not need additional resources in order to generate power, such as water sources that are needed for geothermal and nuclear, and hydroelectric. Since wind is powered by local air currents, there is no need for external fuels which results in no emissions. However, wind power is variable because it relies on the variability of the wind which makes it a poor choice for primary energy source.²⁵ It has to be used in areas with stable wind patterns and cannot be used in areas that experience high winds because of the structural risks.²⁶ There are also concerns how turbines affect wildlife.²⁷ The two biggest problems with wind power, even if the wind conditions are ideal, are energy storage and transmission.²⁸ Since wind is intermittent, energy that is not used during demand must be stored, which makes this renewable energy reliant on storage technologies.²⁹

One of the most promising energy sources is the Sun. The Sun is the most powerful energy source in our entire solar system. It produces 3.828×10^{26} J of energy every second, to put that into perspective, the Sun releases more energy in one second than 1 million times the annual global energy consumption.³⁰ Of course, all of that energy does not reach the earth, 4.5×10^{24} J of energy reaches the earth per year in the form of electromagnetic radiation, as seen in **Figure 1.1.3**, which is 100 times the annual global energy consumption.⁷ The Sun is the largest energy source that is available to humanity, yet, it is one of the most neglected energy sources in terms of power generation because of a significant knowledge gap that existed for harvesting that energy.

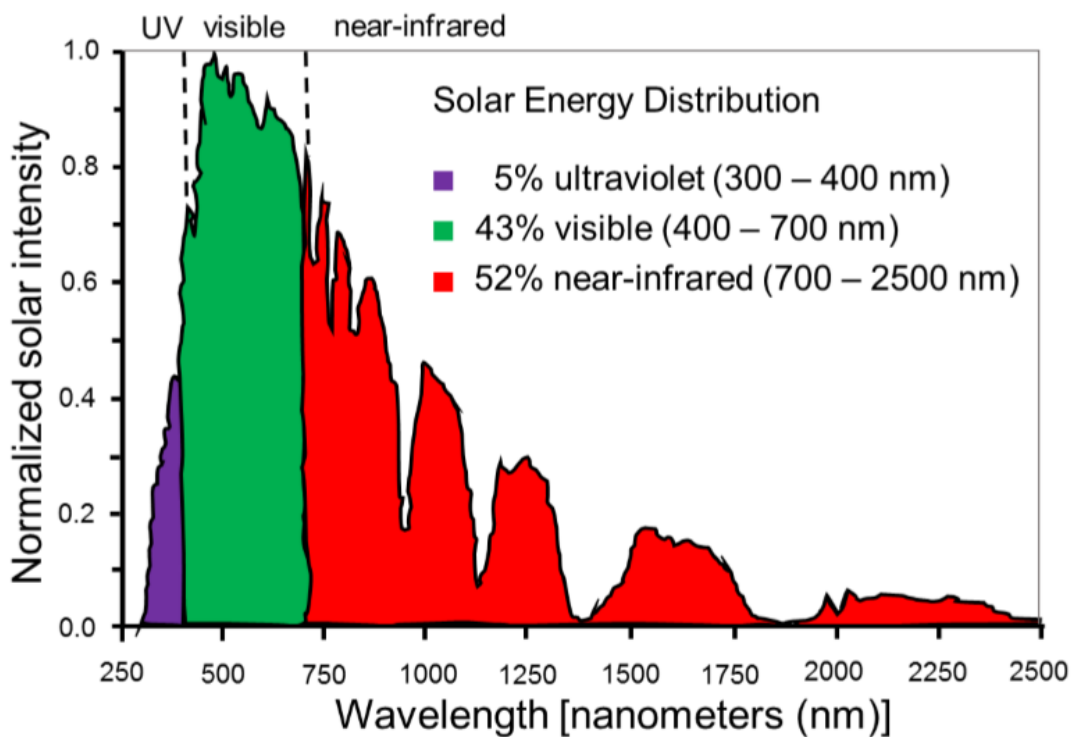


Figure 1.1.3. Normalized Spectral at AM 1.5³¹

Harvesting solar photons and converting these into usable electrical energy is no easy task. It was not until the 1800s that the photovoltaic effect was even observed³². And in the late 1800s, the photoelectric effect was scientifically investigated.³³ Then it was not until 1905 that

the photoelectric effect was described by quantum mechanics by Albert Einstein.³⁴ Then in 1954, more 60 years before this dissertation was written, the first practical silicon solar cell was constructed by Bell Labs with 6% conversion efficiency.³⁵ From this point forward, solar energy harvesting became a reality for humanity as seen in **Figure 1.1.4**.

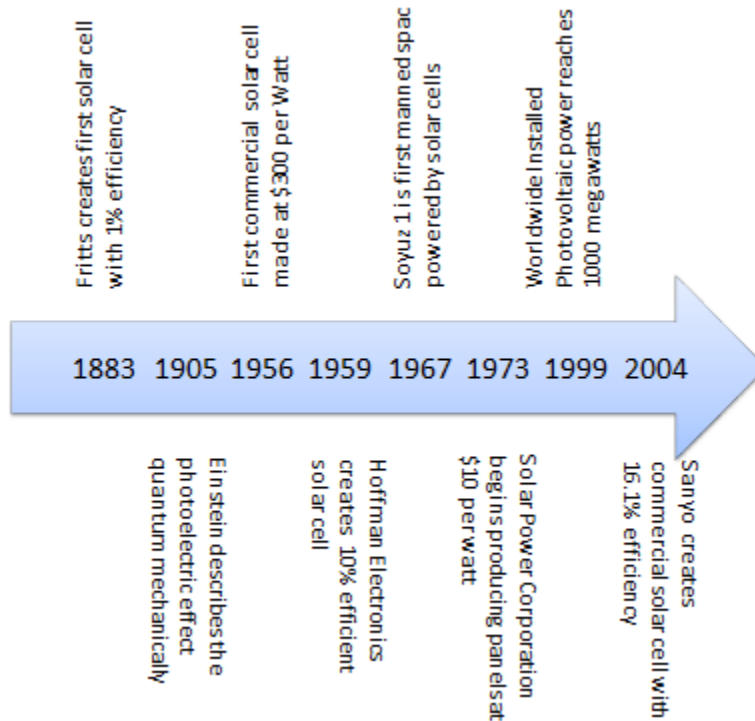


Figure 1.1.4. Major advances of Photovoltaics^{7, 36-38}

Initially, commercialization was very limited because of the high cost of manufacturing of the silicon and because of the expensive materials used in the fabrication of the solar cell, and because the low cost of fossil fuels.³⁸ Early implementation began in specialized applications where other energy sources could not be used, such as satellites and space applications. But with rapid advances in materials engineering, fabrication techniques, and technology; commercialization and mass implementation became a reality.³⁸ We now can harvest the energy from the Sun. Solar energy harvesting can produce energy without generating harmful emissions that contribute to climate change. Solar cells can be placed in remote areas, on buildings, on

roads, on cars; it can be used anywhere there is sunlight. There are no moving parts, which are traditionally failure points that increase costs due to down time and due to manufacturing costs. But there are drawbacks for solar energy harvesting. Solar cells must be placed in areas that get adequate sunlight, for regions that are frequently cloudy or experience significant periods without sunlight, this technology will not be viable. Even for regions that get adequate sunlight, the sun is not in a fixed place in the sky.

1.2 Solar Energy Harvesting Principles

Currently the most common form of solar energy harvesting uses semiconducting materials that converts light into usable electricity by utilizing the photoelectric effect, which is called photovoltaics. The first step of solar energy harvesting involves the absorption of light. The solar harvesting material must have strong absorption in the visible portion of the electromagnetic and preferably be able to absorb photons in the high solar flux region of the solar spectrum. The second step is the formation of charge carriers. Once the energy has been absorbed, an electron hole pair is formed. The third step is the dissociation of the charges. If the negative electron attraction to the positive hole is too strong, they will recombine and no electricity can be generated. The fourth step is the diffusion of the charge carriers. The charges need to be able to diffuse through absorbing material. If there are inhomogeneities in the material or if the distance is too great for the charge to migrate, the hole or electron will become trapped or recombine and no usable electricity will be generated. The fifth and final step is the collection of the charge carriers with the holes diffusing to the anode and the electrons diffusing to the cathode. The biggest obstacle for the last step is ensuring that carriers are not lost at the interface between the absorbing active material and the cathode and anode. The schematic of this process can be seen in **Figure 1.2.1**.

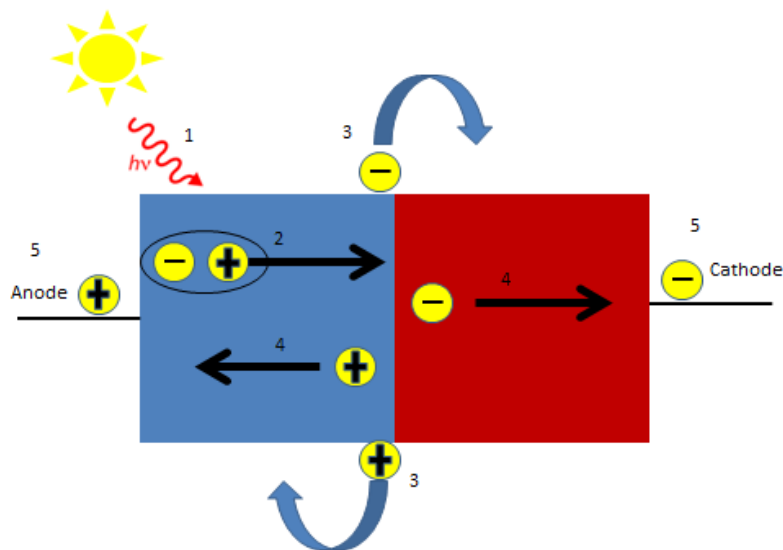


Figure 1.2.1. Solar harvesting schematic: 1 absorption, 2 exciton formation and diffusion, 3 charge dissociation, 4 charge carrier diffusion, and 5 charge collection.

The typical solar cell consists of antireflection coating, transparent cathode, active absorbing material, and finally an anode. The antireflection coating is extremely important in order to ensure that photons are not lost at the surface air boundary.³⁹ The cathode must be transparent in order to allow the photons to reach the absorbing material and must have good electron conductivity in order to collect electrons from the active material.⁴⁰ The active material must have strong absorption in the visible region of the electromagnetic spectrum, have good carrier transport properties, stable to illumination over long time periods, easily obtained source materials, and be easily fabricated.⁴¹⁻⁴⁵ And the anode must have good hole collection properties and must interface well with the active material.⁴⁶ All of these properties must be taken into account for all types of solar cells, regardless if they are constructed of organic materials, inorganic materials, or hybrid materials. A typical solar cell can be seen in **Figure 1.2.2.**

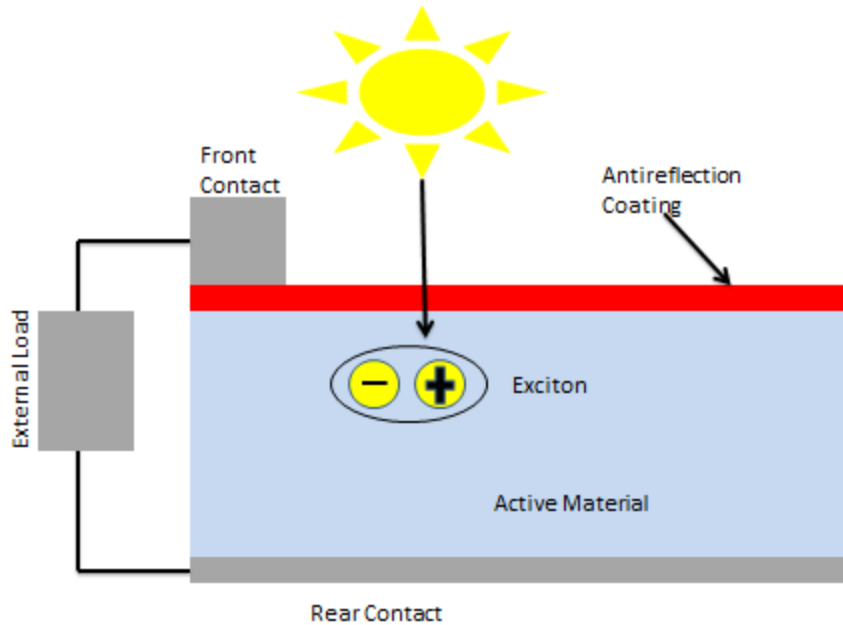


Figure 1.2.2. Solar cell diagram

A few parameters are used in order to characterize the efficiency of different types of solar cells. Quantum efficiency (QE) is a key parameter that measures the conversion of the incident photons into current. The quantum efficiency can be broken down into two parts: external quantum efficiency (EQE) and internal quantum efficiency (IQE). The external quantum efficiency is the ratio of the number charge carriers collected by the solar cell to the number of incident photons on the solar cell. Some of the photons that are incident upon the solar cell are not collected because of reflection losses and transmission losses. The generated charge carriers can also recombine which results in no charge carrier collection. External quantum efficiency is a good measure of these losses. Thus, the external quantum efficiency depends on the absorption properties of the active material and on the ability to separate the charge carriers in order for them to travel to their respective terminals. The internal quantum efficiency is the ratio of number of charge carriers collected by the solar cell to the number of

absorbed photons. Thus the internal quantum efficiency is a good measure of the carrier transport properties of the material. Since not all of the incident photons are absorbed, the external quantum efficiency is typically less than the internal quantum efficiency.

Device efficiency is often characterized by considering the open-circuit voltage. The open-circuit voltage is the maximum voltage that can be obtained from the solar cell and occurs when there is no net current through the device. The open-circuit voltage is defined in **Equation 1.2.1**, where T is temperature in Kelvin, n is an ideality factor which accounts for recombination mechanisms, k is Boltzmann's constant in C/K, q is the absolute value of the charge in Coulombs, I_0 is the dark saturation current which is the maximum current that can be generated without being illuminated, and I_L is the photogenerated current. Thus the open-circuit voltage is determined by the thermal voltage, nkT/q , the maximum current that can be generated, I_0 , and the observed current generated by illumination, I_L .

$$V_{OC} = \frac{nkT}{q} \ln \left(\frac{I_L}{I_0} + 1 \right) \quad \text{Equation 1.2.1.}$$

Another parameter that is used for solar cell efficiency characterization of solar cells is the short-circuit current (J_{SC}). The short-circuit current is the current that is generated by the generation and collection of the light-generated carriers and occurs when the voltage across the cell is zero. The short-circuit current is equivalent to the I_L with moderate loss mechanisms. Thus, the short-circuit current is the maximum current that can be obtained from the device. The short-circuit current depends on a few factors. Since the short-circuit current is dependent on generating the charge carriers, the short-circuit current is limited by the absorption properties of the material. Photons that are reflected, are converted to heat, are not absorbed, or do not go towards charge carriers are wasted. The short-circuit current is also limited by the diffusion

characteristics of the charge carriers and their ability to be collected thus they will be limited by the mobility of the carriers and their recombination rates.

The short-circuit current is the maximum current that can be generated from the solar cell, but it occurs at 0 voltage so no useable power is available. Likewise, the open-circuit voltage is the maximum voltage that can be obtained from the solar cell, but it occurs at 0 current, so again, no useable power is available. Thus, the maximum theoretical power at simultaneous maximum voltage and maximum current is not obtainable, but it is helpful to consider the maximum power that can be generated compared to realizable power. This is represented by the fill factor (FF) parameter which compares the maximum power of the solar cell to the product of the short-circuit current and the open-circuit voltage. Determining the FF can be accomplished by integrating the area with the boundary created by voltage (V_{mp}) that creates the maximum power and the current that creates the maximum power (I_{mp}), and dividing that area by the area created by the product of the open-circuit voltage and short-circuit current which is seen in **Figure 1.2.3**.

The FF is reduced by two main factors: series resistance and shunt resistance. In series resistance the voltage difference between the voltage of the active material and the voltage of the terminal becomes smaller for the same current, which then reduces the overall power of the solar cell by reducing the fill factor. Series resistance is due to the movement of the current through the active material of the solar cell, the resistance between the active material and the terminal contacts, and intrinsic resistance of the terminals. Since the series resistance is dependent on the movement of the current through the active material, the series resistance is higher at high illuminations. Shunt resistance is caused by alternative pathways for light-generated current to travel which is often due to defects due to manufacturing or due to material defects. This lowers

the overall current of the solar cell which results in a lower FF and lower power. Shunt resistance has a higher impact at lower illumination because shunt resistance is dependent on the light-generated current.

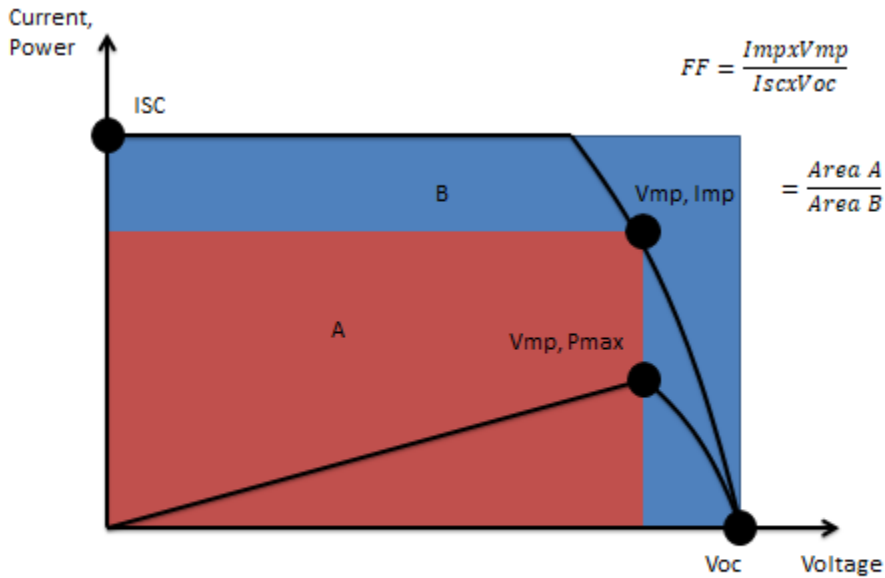


Figure 1.2.3. Fill Factor

The most important metric used to describe the device efficiency is the power conversion efficiency (PCE). The power conversion efficiency is the percentage of the incident photon energy that is converted into electrical energy. Ideally the power conversion efficiency would be 100%, the power output would be the same as the input power, but with all energy sources today, ideality has not been obtained. For photovoltaics, PCE is limited by losses due to the material deficiencies, morphology deficiencies, and device deficiencies. Thus, although ideality may not be feasible currently, or may never be possible, there is still room for improvement for better power conversion efficiencies.⁴⁷ In order to compare the many various types of solar cells, the power conversion efficiency is generally performed at standard conditions at a temperature of

25°C, irradiance of 1000 W/m² and an air mass 1.5 (AM 1.5) spectrum. The PCE can be related to the fill factor, open-circuit voltage, and short-circuit current as seen in **Figure 1.2.4**.

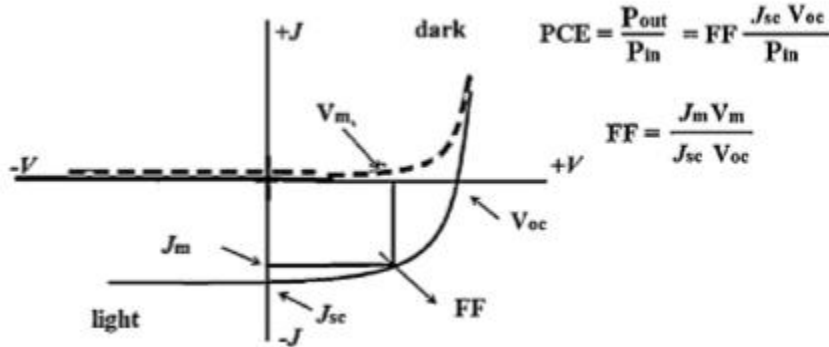


Figure 1.2.4. Solar Cell Efficiency⁴⁸

1.3 Silicon Solar Cells

Silicon is one of the most abundant elements on earth, making up 25% of the Earth's crust. Silicon is non-toxic which makes it an ideal material to work with and be used in manufacturing. Silicon is mildly conductive in its pure state but a marked increase in its conductivity can be accomplished by doping.⁴⁹ Silicon has four valence electrons that are fixed to the silicon atom, but when a Group III element with its 3 valence electrons is introduced to the silicon, called doping, conductivity is increased in the crystal because there is now a vacant orbital that can hold an electron. This type of doping is called p-type doping because there is a deficiency of electrons in the lattice, causing there to be a positive site called a hole. In p-type silicon, the hole is the major charge carrier in conduction with electrons being the minority carrier. Silicon can also be doped with Group V elements which have 5 valence electrons, which introduces an excess of electrons in the lattice. This type of doping is called n-type doping because of the excess electrons that are part of the crystal lattice. In n-type silicon, the electron is the major charge carrier responsible for conduction with holes being the minority carrier. Both types of doping add an excess of a charge carrier that increases the conductivity of the

silicon. This doping creates a valence band and conduction band that has a small energy gap that is smaller than an insulator but does not overlap like metals, seen in **Figure 1.3.1**. Silicon also has good absorption in the visible spectrum, making it a good candidate for use in the active layer of solar cells. Silicon solar cells are also stable under long periods of illumination.

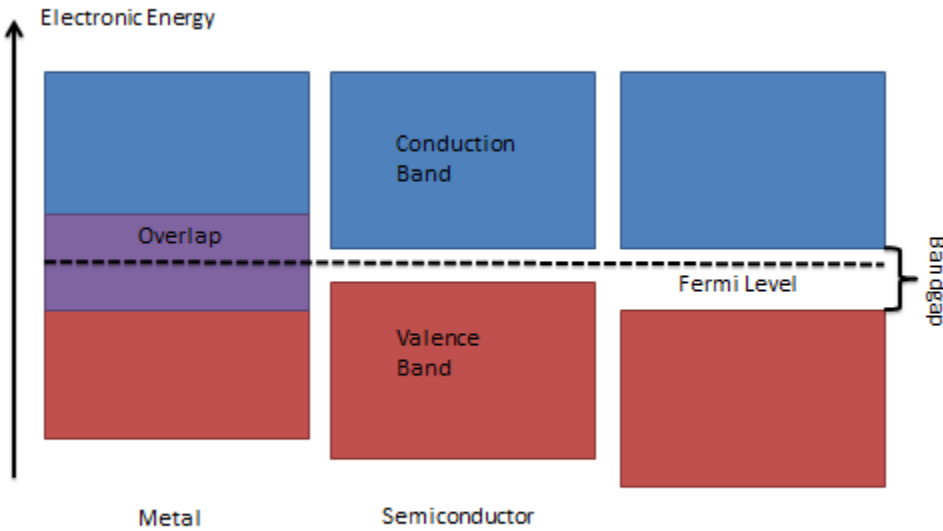


Figure 1.3.1. Electronic energy level diagram of metals, semiconductors, and insulators

The typical active layer of a silicon solar cell consists of a p-n junction. The p-n junction is composed of a grown negatively doped (n-doped) crystalline silicon layer and a grown positively doped (p-doped) silicon layer that are combined to form a p-n junction. The electrons in the n-type silicon migrate to the holes in the p-type silicon and recombine, while forming positive holes where the electrons have left. The holes in the p-type silicon also diffuse to the n-type silicon and recombine, leaving behind electrons that form a negative region. This causes a positive region in the n-type silicon and a negative region in the p-type silicon, which creates an electric field that eventually provides an opposing force that stops diffusion of the holes and

electrons, creating a depleted zone. A photon with enough energy can be absorbed by the silicon, which will dissociate an electron from a hole. Since there is an electric field in the depletion zone, the electrons will travel to the n-type layer and the holes will travel to the p type layer. If the n-type layer is connected to the p-type layer by a wire, the electrons will travel from the n-type layer to the p-type layer by crossing the depletion zone, then go through the wire back to the n-type layer, creating electricity flow. The typical active layer of a silicon solar cell can be seen in **Figure 1.3.2**.

The first silicon solar cell was a crystalline melt-grown pn-junction developed by Ohl, but had a power conversion efficiency of less than one percent.⁵¹ A big breakthrough occurred in the 1950s when Bell Labs created its first p-type silicon that had an efficiency around 4%.⁵² The first commercially viable solar cell was a crystalline silicon solar cell that was constructed by Bell Labs with a 6% conversion efficiency in 1954.⁵² This achievement began the explosion in photovoltaic research. By the 1980s, silicon solar cells had achieved efficiencies of around 20%.⁵³ Currently, the highest efficiency achieved for silicon solar cells is 26%, which is near the maximum theoretical efficiency of 29%.⁵⁴

Although, crystalline silicon solar cells have high efficiencies, they are reaching their theoretical maximum efficiency. Crystalline silicon solar cells must be made from extremely pure silica, because small impurities in the material will drastically reduce the efficiency.⁵⁵ They must be grown which is a time intensive and expensive process.⁵⁶ Crystalline silicon is also brittle, which limits the applications it can be used in. Because crystalline silicon is an indirect band gap semiconductor, the minimum energy of the conduction band and the maximum energy in the valence band do not occur at the same crystal momentum, which means the excitation of an electron from the valence band to the conduction band requires a photon with energy higher

than the band gap or a photon with energy equal to the band gap with additional energy supplied by a phonon. Thus, the transition is less probable, so a thicker material is needed in order to ensure absorption which increases the cost of the solar cell compared to thin cell technologies.⁵⁷

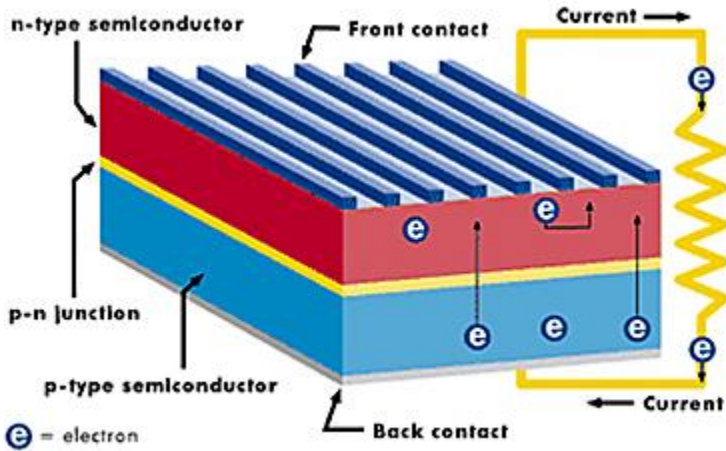


Figure 1.3.2. Silicon Solar Cell⁵⁰

The limitations of crystalline silicon have led to the investigation of amorphous silicon for use as an active material. Amorphous silicon does not exhibit long range order that is seen in crystalline silicon, instead it forms a continuous random network which leads to unique properties such as a pronounced flexibility.⁵⁸ Amorphous silicon solar cells have distinct advantages over crystalline silicon. One clear advantage of amorphous silicon is its flexibility which has potential use in more diverse applications such as flexible solar cells or where lightweight solar cells are needed suited.⁵⁹ Amorphous silicon solar cells can be made into lightweight thin films that can be rolled onto surfaces such as plastics, metals, or glasses, or be used as a solar absorbing coating.⁶⁰ Amorphous silicon solar cells have exhibited efficiencies that are almost 14%, although this is much lower than efficiencies achieved by crystalline silicon solar cells.⁶¹ Amorphous silicon also has slower deposition rates which leads to more expensive manufacturing costs.⁶²

1.4 Non-Silicon Inorganic Solar Cells

Crystalline silicon is the leading material used for the active material of solar cells, but it has significant limitations, which has led to investigation in other inorganic active materials. One promising non-silicon inorganic solar cell material is Cadmium telluride (CdTe). CdTe is a direct band gap semiconductor, which can be made into thin films.⁶³ CdTe has a band gap of ~1.5 eV which is ideal for absorbing photons in the high solar flux region of the solar spectrum.⁶⁴ CdTe has also shown efficiencies of around 20%.⁶⁵ The CdTe solar cell has a similar construction as the crystalline silicon solar cell, p-n junction of a p-layer of CdTe and an n-layer of CdS sandwiched between a two conducting layers, seen in **Figure 1.4.1**, but has the added benefit of being thinner and flexible which can help with cost effectiveness. CdTe could be as cost effective as crystalline silicon, but it has two significant draw backs. Cadmium is a toxic heavy metal which makes mining and manufacturing dangerous.⁶⁶ Tellurium is a rare and mildly toxic metalloid which also makes manufacturing and mining dangerous.⁶⁷ This also makes CdTe solar cell disposal problematic.

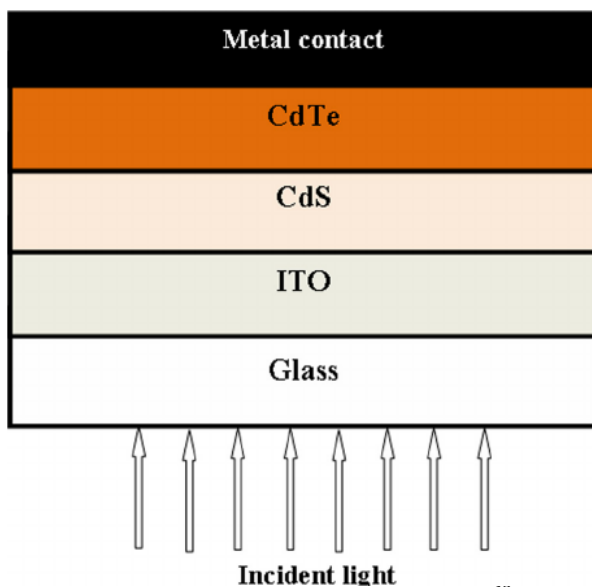


Figure 1.4.1 CdTe Typical Solar Cell⁶⁸

Another promising active material is copper indium gallium selenide (CIGS). Similar to CdTe, CIGS can be used in thin film technologies allowing them to be used in flexible applications. CIGS has high absorption in the visible spectrum, with absorptivities of up to $10^5/\text{cm}$ and a band gap that is tunable from 1.0 eV to 1.7 eV.⁶⁹ CIGS solar cells have also shown efficiencies of greater than 20%.⁷⁰ Although CIGS solar cells shown promise, they have yet to reach wide scale adoption.

Gallium arsenide (GaAs) is another solar active material that has seen a lot of research interest. GaAs has a low temperature coefficient, which allows it to operate at higher temperatures than crystalline silicon with lower efficiency losses.⁷¹ It has a small band gap and few crystalline defects, which results in less leakage current.⁷²⁻⁷⁴ Like CIGS and CdTe, it is flexible and lightweight which makes it ideal for thin film applications.⁷⁵ The biggest advantage of GaAs is that it has the highest efficiency, with of efficiencies greater than 25%.⁷⁶ The greatest disadvantage of GaAs is that is made with arsenic which is toxic to humans and it is an environmental hazard.⁷⁷ Gallium is rare which also limits its availability to byproducts of other mineral extraction industries.⁷⁸

1.5 Organic Solar Cell Properties

Organic solar cells use conductive small organic molecules or organic polymers for light absorption and charge transport for electricity production from absorbing solar photons.⁷⁹⁻⁸¹ In general the solar organic materials are composed of large extended conjugated systems, where a system of p orbitals overlap resulting in a delocalization of electrons across the molecule leading to the conductive nature of solar organic materials.^{82,83} But the use of organic materials for solar harvesting is a relatively surprising light harvesting material for photovoltaics. Traditionally, organic materials have been viewed as insulators and have been implemented as insulators for

conductors and semiconductors. In fact, the photoconductivity of organic materials was not observed until the early 1900s when Pochettino and Volmer observed the photoconductivity of anthracene, an organic molecule consisting of three fused benzene rings.⁸⁴ The first organic solar cell was developed by Kallmann and Pope in 1959, but only had a power conversion efficiency below 0.1%.⁸⁵ The next breakthrough in organic solar cells did not even occur almost 30 years later, when in 1986, Tang used a p-type copper phthalocyanine and n-type bisbenzimidazo[2,1-a:2',1'-a']anthra[2,1,9-def:6,5,10-d'e'f']diisoquinoline-10,21-dione bilayer cell to reach an efficiency of ~1%, which still paled in comparison to silicon solar cell efficiencies that were developed 30 years earlier.⁸⁶ The biggest breakthrough occurred in the 1990s when bulk heterojunctions (BHJ) were introduced, where power conversion efficiencies of ~3% were obtained.⁸⁷ Since that breakthrough, efficiencies of over 10% have been achieved.⁸⁸

Organic solar cells operate under similar principles as inorganic solar cell. A solar photon is absorbed, charge carriers are formed with an electron hole pair, the electron and hole dissociate from each other, the charge carriers diffuse, and then they are collected at the anode and cathode, , seen in **Figure 1.5.1**.⁸⁹ But unlike inorganic solar semiconductor materials, instead of forming a conduction and valence band by introducing impurities to cause conductivity, conductivity is accomplished via molecular orbital delocalization for organic solar harvesting materials. Atoms have electrons in atomic orbitals, which are regions that surround the nucleus of the atom where there are high probabilities of encountering the atoms electrons. Electrons in the outermost orbitals that are unpaired are responsible for bonding between atoms and overlap forming the bond. In molecules, the atomic orbitals can hybridize forming molecular orbitals, where the electrons are shared within the molecule and resulting in lower

energy orbitals. The molecular orbitals form σ bonds where the electrons are considered localized between two atoms, and π bonds that are delocalized across the molecule. In the molecular orbital system, the molecular orbitals that have the highest probability of finding the electron are the highest occupied molecular orbitals (HOMO) and the orbitals with the lowest probability of finding the electron are the lowest occupied molecular orbitals (LUMO). The HOMO is the equivalent of the valence band of inorganic light harvesting materials and the LUMO is the equivalent of the conduction band of inorganic light harvesting materials.⁹⁰ The energy difference between the HOMO and the LUMO is the band gap and the absorption of an electron that matches the band gap will promote an electron from the HOMO to the LUMO, similar to the promotion of an electron in the valence band to the conduction band in inorganic systems.⁹¹

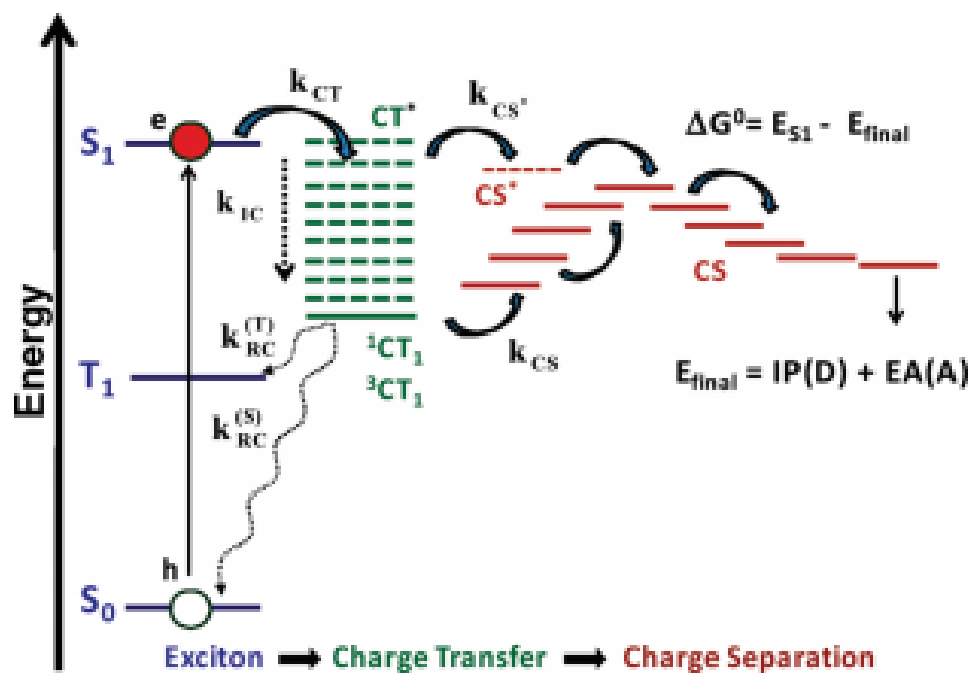


Figure 1.5.1. Electronic state diagram of organic solar cell⁸⁹

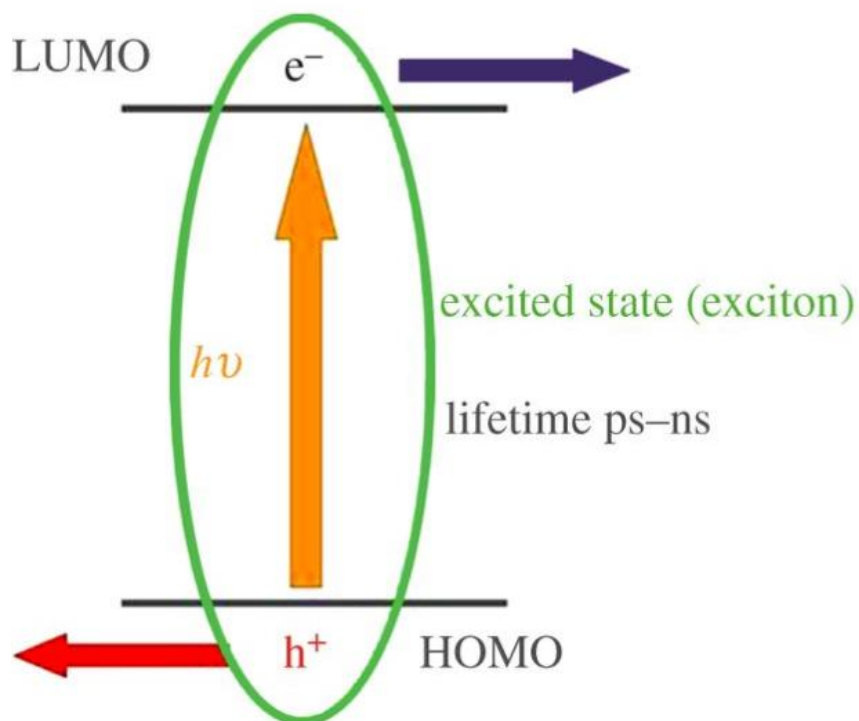


Figure 1.5.2. Electronic state diagram of photon absorption of electron from HOMO to LUMO in Organic System⁹¹

1.6 Organic Solar Cells Advantages and Disadvantages

Inorganic solar active materials have shown great promise but they have significant limitations and drawbacks, which has spurred interest in organic light harvesting materials. The precursors to the organic solar harvesting materials are quite abundant, similar to their organic counterparts but do not require the high level of purity that is needed for their inorganic counterparts. Organic active materials have much higher absorption coefficients compared to their inorganic counterparts.⁹² Processing of organic materials is much easier compared to their inorganic counterparts. They are readily soluble in solvents which allow them to be dissolved and then solution processed by roll to roll processing, printed, or spin coating into a film to be used for fabricating organic solar cells, which drastically reduces the manufacturing costs compared to inorganic solar active materials.⁹³⁻⁹⁷ Because they have high absorption, are

flexible, and are readily solution processed, the active materials can be made into thin films, which are less than 100 nm compared to their inorganic counterparts which are on the order of 1 μm to 100 μm , which drastically decreases the material needed to form the active layer and reduces the weight and cost.⁹⁸⁻¹⁰² The morphology can be easily be modified with additives, annealing, or mechanical processing which can control orientation, long range ordering, crystallinity, optical properties, and electrical properties.¹⁰³⁻¹⁰⁷ One of the great benefits of organic active materials is that the small molecules or polymers that make up the active layer can be easily made by well-defined synthetic pathways. The synthesis of small molecules and polymers is greener than inorganic solar cell fabrication because it does not involve toxic heavy metals, although the use of organic solvents still proves to be problematic for a completely green process.¹⁰⁸ One of the greatest advantages of organic active solar materials is their ease of tunability of their optical and electrical properties.¹⁰⁹ Slight modifications of molecular structures can lead to pronounced changes in their optical and electrical properties. The organic materials electrical and optical properties can be modified by augmenting the aromaticity, stiffness, planarity, electron donating strength, electron withdrawing strength, and steric hindrance.¹¹⁰⁻¹¹⁶ The absorption properties of organic materials, which are much higher than inorganic active solar materials, can be enhanced or modified. The absorption extinction coefficient can be enhanced; the peak absorption wavelength can be modified; the band gap can be easily tuned; and the spectral range can be modified.¹¹⁷⁻¹¹⁸ The electronic properties can be modified by augmenting electron mobilities, hole mobilities, and exciton diffusion properties.¹¹⁹⁻

120

Although, organic solar cell materials do still have significant barriers to overcome in order to overtake their inorganic counterparts. Organic solar cells require rare transition metals

for catalytic synthesis of the active organic materials. Rare transition metal catalysts are expensive, owing to their low abundance of rare transition metals, are not stable under mild conditions, and are limited by their catalytic lifetime before being poisoned, thus greater improvements are needed in order to decrease the costs of synthesis of organic solar harvesting materials.¹²¹⁻¹²⁴ The longevity of the organic active layer is another concern for the successful implementation of organic solar cell technologies. The organic active layer can be easily oxidized by oxygen if the organic active layer has a high reducing potential.¹²⁵ The organic active layer is also susceptible to UV damage and must be adequately protected.¹²⁶ As discussed earlier, although there is no net carbon emission from energy production, making it greener than other forms of energy production methods, the extensive use of organic solvents is a workplace hazard and environmental hazard.

Organic light harvesting materials also have significant optical and electrical limitations. Although organic light harvesting materials have very good absorption properties, they have poorer electrical properties than inorganic light harvesting materials. The dissociation of electron from the hole in organic light harvesting materials requires a much higher energy than their inorganic counterparts.¹²⁷ Organic light harvesting materials are relatively disordered compared to their well-ordered and crystalline inorganic counterparts, which results in slower charge mobilities with increases charge recombination and lower power conversion efficiencies.¹²⁸ The biggest obstacle to organic light harvesting materials is they have much lower power conversion efficiencies than their inorganic counterparts, with the maximum efficiencies that are half the efficiencies obtained by their inorganic counterparts.¹²⁹ In order for organic light harvesting materials to be competitive with inorganic light harvesting materials, their power conversion efficiencies must be improved. Thus it is imperative to investigate the

fundamental properties, such as structure optical property relationships of organic light harvesting materials in order to improve the power efficiencies of organic light harvesting materials.

1.7 Organic Solar Cell Architecture

Unlike in inorganic solar materials, charge carriers in organic systems have much shorter life times.¹³⁰⁻¹³¹ This has led to an evolution of architectures of organic solar cells. If a thin film of the organic active material was used in a single layer between the anode and cathode, the hole and electron would be drawn to their respective electrodes, but the attraction between the hole and electron is still high and there is a high probability of hole and electron recombining.¹³² This led to the investigation of bilayer structures similar to inorganic solar cell architectures, where there is an electron deficient organic layer and an electron rich organic layer. This motif has the benefit of having a stronger driving force to separate the hole and the electron in the exciton.¹³³ But similar to the single layer, recombination probability is also high. The diffusion length of an exciton in organic materials is ~10 nm, whereas the thickness of the each layer in the bilayer is ~100 nm.¹³⁴ Thus the majority of excitons are prevented from reaching the bilayer interface, which severely limits the number of charge carriers that can be generated. To overcome the intrinsically shorter lifetimes of the charge carriers of organic light harvesting materials, the bulk heterojunction organic photovoltaic has been implemented in order to increase charge carrier generation and subsequently increase power conversion efficiency.¹³⁵ In a bulk heterojunction, the electron deficient organic material is mixed with the electron rich organic material which allows for interpenetrating networks of the electron deficient organic material with the electron rich organic material. This creates smaller domains which allow for greater surface area for the exciton to move to the interface for electron hole separation with subsequently greater charge

carrier generation which results in higher power conversion efficiency.¹³⁶ Because there is a better chance for charge carrier generation, this design is the most common design used when constructing organic solar cells. Representations of each type of architecture can be seen in

Figure 1.7.1.

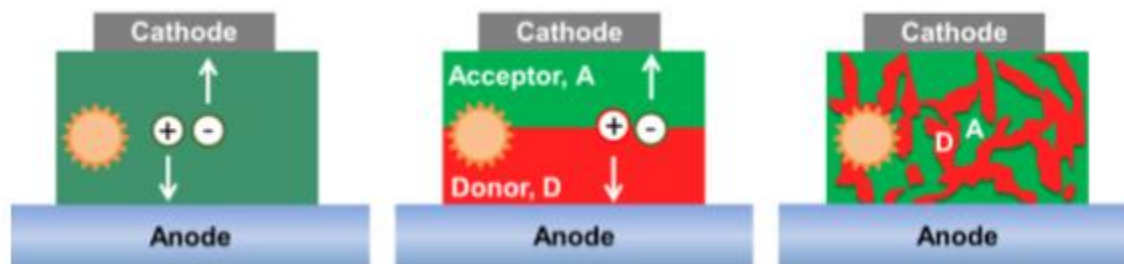


Figure 1.7.1. Organic solar cell architecture¹³⁷

1.8 Different Types of Organic Light Harvesting Materials for Solar Cells

1.8.1 Organic Dye Solar Cells

Dye-sensitized solar cells (DSSC) are an organic-inorganic hybrid thin film solar cell technology. In the 1960s, experiments showed illuminating organic dyes could lead to photoconductivity when near oxide electrodes.¹³⁸ In the early 1990s, Gratzel et al were able to demonstrate low-cost and high efficiency solar DSSCs.¹³⁹ This led to a boom in research into DSSCs. In a DSSC solar cell, a layer of highly porous titanium dioxide (TiO_2) nanoparticle is impregnated with light absorbing organic dyes. The nanoparticles are then immersed in an electrolyte solution and sandwiched between two electrodes. Photons excite the organic dyes, and electrons flow from the organic dyes into the TiO_2 nanoparticles. The electrons then flow to an electrode where the electricity is generated to power a load. The electron then travels to counter electrode. Then the electron is shuttled back to the organic dye by the liquid redox electrolyte which regenerates the dye. This schematic can be seen in **Figure 1.8.1.1**. This type of solar cell has shown great promise, with efficiencies near 10%.¹⁴⁰ Although there have been rapid advancements in DSSC technologies, there are significant drawbacks. Similar to other

organic solar cell materials, DSSC is susceptible to UV damage and oxidation. The use of rare metals such as platinum and ruthenium increases the cost of DSSCs, and so far alternatives have not been found to reduce that cost.¹⁴¹ The biggest drawback of DSSCs are the use of liquid electrolytes.¹⁴² Great care must be taken to ensure that liquid electrolyte is adequately contained, any physical damage to the containment will result in the loss of the electrolyte and complete loss solar conversion. The electrolyte also uses organic solvents which can pose workplace hazards and environmental hazards. Since it is liquid, it must survive a wide array of weather conditions from freezing temperatures in cold climates to high temperatures that can cause evaporation of the liquid electrolyte in order for DSSCs to be a practical replacement for conventional solar cells. Indeed, much research has been dedicated to replacing liquid electrolytes with solid state electrolytes, with high efficiencies of 15% being achieved.¹⁴³ But even the solid state electrolytes have suffered high degradation during its operational lifetime.

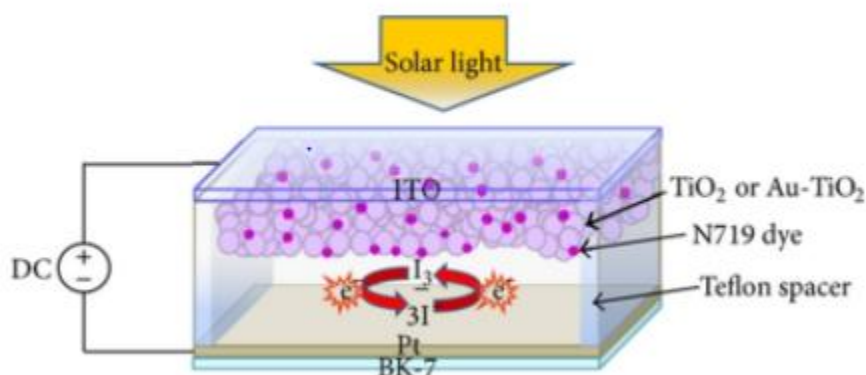


Figure 1.8.1.1. Typical dye sensitized solar cell¹⁴⁴

1.8.2 Macromolecules: Homopolymers

The evolution of humans has seen evolution in technologies that humans have used; from the Stone Age, to the Bronze Age, and to the Iron Age. Currently, we are in the “Polymer Age”. Polymers are large molecules, macromolecules, that are made up of repeating molecular

subunits. Polymers are used extensively in our daily life, from cell phones, to clothes, to construction materials, to lights, to furniture, to transportation, to photovoltaic materials, and even people are composed of biopolymers. Polymers can be insulating or semiconducting. Polymers are flexible, lightweight, chemical resistant, exhibit high strength, and are easily modified.¹⁴⁵⁻¹⁴⁷

A special type of polymer can be used as light harvesting material for solar cells. Conjugated polymers composed of the same repeat unit, homopolymers, can be used as the light harvesting material in solar cells and serve as the donor of electron density. As discussed earlier, the formation of a molecule is due to the hybridization of atomic orbitals forming molecular orbitals. These orbitals form LUMO and HOMO energy levels for the molecular system. Similar to how functional groups can modify the energy levels, polymerization leads to modulation of LUMO and HOMO energy levels, eventually leading to conduction and valence band-like energy levels as seen in **Figure 1.8.2.1**. This allows for the polymer to take on a semiconductor-like behavior and become photoconductive, thus being able to act as the light harvesting material in organic solar cells. The electron rich homopolymer can serve as the photon absorbing material and electron donor, and it can be mixed with an electron deficient acceptor material in order to promote charge separation to increase power conversion efficiency of the organic solar cell.

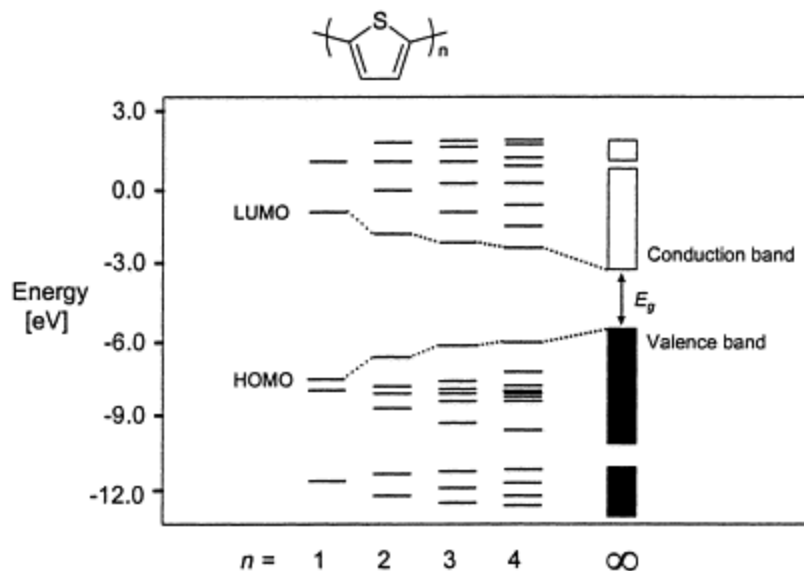


Figure 1.8.2.1. Energy level modulation via increasing polymerization¹⁴⁸

One of the most studied light harvesting homopolymers is poly(3-hexylthiophene) (P3HT). P3HT is considered the model light harvesting homopolymer and is one of the most used homopolymers in organic solar cells.¹⁴⁹ It has a broad absorption spectrum, ranging from 350 nm to 650 nm, allowing the polymer to absorb the high and low energy photons of solar radiation.¹⁵⁰ P3HT has high charge carrier mobilities which is one of the disadvantages that organic solar harvesting materials often face.¹⁵¹ It is relatively easy to synthesize and the regioregularity can be easily controlled. Regioregularity is important for the absorption and charge carrier mobilities. More regioregular structures lead to more planar structures which enhances conjugation along the polymer backbone which promotes better absorption and better charge carrier mobilities.¹⁵² Although, higher crystallinity can lead to aggregation of P3HT and phase separation from the acceptor material resulting in lower power conversion efficiencies. Higher molecular weight polymers have shown to have better hole mobilities.¹⁵³ Unfortunately, P3HT has a high band gap of ~1.9 eV which limits its ability to absorb photons in the near-infrared region and infrared region.¹⁵⁴ It also has a high HOMO level, -5.19 eV, which makes it susceptible to oxidation and limits the open circuit voltage.¹⁵⁵

Due to limitations of P3HT, much research has focused on trying to find homopolymers that exhibit low band gaps, high short circuit currents, and open-circuit voltages. Homopolymers that contain benzodithiophene (BDT) have shown great promise. Benzodithiophene unit is a promising donor material because its fused structure prevents intramolecular rotation which maximizes the π overlap between monomer units.¹⁵⁶ The planar structure promotes π stacking in devices which improves charge transport through intermolecular hopping.¹⁵⁷ The planarity of the BDT unit is important for lowering the band gap and improving the absorption range, as well as enhancing the molar absorptivity. One particular BDT homopolymer, poly(4,8-bis(5-(2-ethylhexyl)thiophen-2-yl)benzo[1,2-b:4,5-b']dithiophene) (PBDTT), has shown great optical and electrical properties. PBDTT has a power conversion efficiency of 6.12%, high open circuit voltage of 0.93 and short circuit current of 11.95 mA cm^{-2} .¹⁵⁸ These remarkable values have also been achieved without solvent additives or thermal annealing, which would reduce the cost of commercial manufacturing. It also reduces the complexity of fabrication because it removes the step of removing high-boiling point additives. The stability of solar cell is also improved since residual solvent will not cause phase separation of the donor and acceptor, and the solar cells uniformity from batch to batch can be achieved. Unfortunately, PBDTT has poor absorption in the near-infrared and infrared region which limits the efficiency of these types of solar cells.

1.8.3 Conjugated Donor-Acceptor Polymers

The most promising organic solar active materials are conjugated donor-acceptor polymers. The donor-acceptor material serves as the photon absorbing material and donates electrons to an electron deficient acceptor material in polymer organic solar cells. Donor-acceptor polymers benefit from energy modulation due to polymerization which is also seen in

homopolymers, but they have distinct advantages that are only offered by the donor-acceptor motif. A donor-acceptor polymer is composed of electron rich donor monomer covalently linked to an electron deficient monomer in an alternating motif. This motif results in a hybridization of the energy levels of the donor monomer and the acceptor monomer, with the HOMO of the new polymer closely resembling the HOMO of the donor monomer and the LUMO closely resembling the LUMO of the acceptor monomer as seen in **Figure 1.8.3.1**.¹⁵⁹ This results in decreasing the band gap which broadens the absorption which lowers the short-circuit current of the organic polymer solar cell. The energy level of the LUMO of the donor-acceptor polymer can be modulated in order to ensure that there is an adequate mismatch between the LUMO of the acceptor material in order to overcome the exciton binding energy, which is typically in the range of 0.1 to 0.5 eV.¹⁶⁰ The alternating donor acceptor motif introduces an electropotential gradient which increases charge separation and increases charge mobilities.¹⁶¹ The energy level of HOMO can be modulated to optimize the energy difference between the HOMO of the polymer with the LUMO energy of the acceptor to maximize the open-circuit voltage.¹⁶²

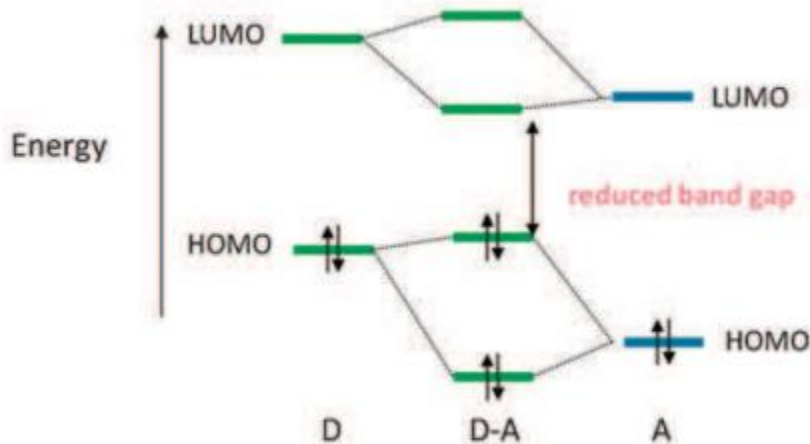


Figure 1.8.3.1. Energy level modulation in donor-acceptor polymer¹⁵⁹

The electron-donating and electron-accepting properties of the monomers can be easily tuned. The donating strength of the donor can be modified by introducing different strength donating functional groups or electron-withdrawing strength of the acceptor can be modified by introducing different strengths of electron-withdrawing functional groups. This allows for the optical band gap to be precisely tuned and for the absorption range to be broadened. It can promote higher charge separation, higher charge mobilities, more energy transfer, and can decrease undesirable photovoltaic pathways.¹⁶³⁻¹⁶⁴ But great care must be taken in order to enhance desirable properties and not introduce undesirable properties. If the electron-donating strength is too high, the donor can be easily be oxidized which can destroy the light-harvesting ability of the donor-acceptor polymer.¹⁶⁵ If the electron-withdrawing strength is too high, the electron can be trapped resulting in low conductivities resulting in poor solar cell performance.¹⁶⁶

The addition of functional groups can also be used to modify other polymeric properties of the donor-acceptor polymer. Large bulky side groups can be added in order to relieve steric hindrance between monomer subunits which allows more a more planar backbone to promote better charge mobilities.¹⁶⁷ Side-chains can also introduce steric hindrance between monomer subunits which causes backbone twisting which can disrupt π - π interaction along the backbone which affects the electrical and optical properties.¹⁶⁸ It can also disrupt intermolecular stacking between polymer chains, but the twisting can lead to better phase-mixing between the donor polymer and organic acceptor.¹⁶⁹ Side-chains can also improve the stability of polymer organic solar cells.¹⁷⁰ One of the most important functions of side-chains is to improve solubility of the donor-acceptor polymer in solvents. Without solubility side-chains, these macromolecules are insoluble in solvents or marginally soluble. This makes industrial roll to roll processing, ink-jet

processing, spinning coating, or any other wet processing impossible. This would increase manufacturing costs and could make cost-effective organic alternatives impossible.

Besides modifying the polymer periphery, the polymer backbone can be easily modified to modulate the optical and electrical properties. Heavy atoms can be introduced in the polymer backbone in order to produce high molecular weights, strong absorption, narrow band gaps, and high charge-carrier mobilities.¹⁷¹ Heteroatoms can replace carbon atoms within the polymer backbones which can modulate the photophysical properties, conformational, and molecular packing properties of donor-acceptor conjugated polymers.¹⁷²⁻¹⁷³ The conjugation of each subunit in the donor-acceptor polymer can affect the effective conjugation length, the number of repeat units that form the optical unit of the donor-acceptor polymer.¹⁷⁴ The conjugation of the donor and acceptor subunits can also affect the interaction between the donor-acceptor interface along the polymer backbone. The oscillator strength, the quantity that describes the probability of an absorption or emission of photons, can be modified by fusing the subunits in the polymer backbone or introducing aromatic subunits to increase the stiffness of the polymer backbone.¹⁰

1.8.4 Donor Subunits in Donor-Acceptor Polymers

The optical and electrical properties of donor-acceptor polymers are the sum of its individual parts, the donor and acceptor subunits. The donor should have low HOMO energy level, be electron rich, be strong enough to donate an electron to the acceptor but not too strong to where the donor is easily oxidized by its environment.¹⁷⁵ The donor subunit should also have high hole mobilities in order to ensure efficient electron and hole separation.¹⁷⁶

One of the most popular donor subunits is 3,4-ethylenedioxythiophene (EDOT). EDOT has good redox potential, good stability, and good conductive properties.¹⁷⁷ The alkylenedioxy bridge across the 3- and 4- positions on the thiophene subunit increases the electron density to

the aromatic ring from the donating properties of the oxygens. This reduces the oxidation potential of both the donor monomer and the polymer as a whole. This results in the stabilization of the charge transfer state. Donor-acceptor polymers containing EDOT donor subunits have shown band gaps from 1.91 eV to 1.13 eV, high short circuit currents of up to 15 mA cm^{-2} , open circuit voltage of up to 0.91 V, and power efficiencies of up to 2.5%.¹⁷⁸ Although, EDOT donor monomers have shown promise for incorporation in donor-acceptor polymers, power conversion efficiencies of 2.5% are on the lower end of efficiencies for donor-acceptor polymers.

Another promising donor monomer is fluorene. Fluorene is a polycyclic aromatic monomer, where two benzenes are fused via a cyclopentane. It traditionally used for its photoluminescence properties because of ease of tunability of its fluorescence wavelength and high quantum yields, but incorporation of fluorene in donor-acceptor polymers has also been successful due to the ease of tuning the absorption properties and electronic energy levels.¹⁷⁹ This has allowed the absorption spectrum of the donor-acceptor polymer to be adjusted to coincide with the maximum photon flux region of the solar spectrum.¹⁸⁰ Also, the stiffness of the fluorene monomer increases the oscillator strength which increases the absorption properties of the donor-acceptor polymer. Indeed, donor-acceptor polymer incorporating fluorene donors have shown efficiencies of 6.2% with a high fill factor of 0.70.¹⁸¹

Benzodithiophene (BDT) monomers have also shown great promise as donors in donor-acceptor polymers. BDT based monomers have a large planar conjugated structure and introduces little steric hindrance when incorporated in donor-acceptor polymers.¹⁸² The large planar conjugated structure maximizes the π -orbital overlap by restricting intramolecular rotation in the polymer backbone. The BDT unit makes the polymer backbone more rigid which broadens the absorption spectrum of the donor-acceptor polymer. The more planar and rigid

backbone can lead to better stacking between adjacent polymers in the organic solar cell, promoting intermolecular charge transfer.^{157, 183} Donor-acceptor polymers that have incorporated BDT donor units have reached high power conversion efficiencies of over 10%.¹⁸⁴

1.8.5 Acceptor Subunits in Donor-Acceptor Polymers

As important as the donor subunit is, the acceptor subunit is as important if not more important in the donor-acceptor polymer. The acceptor monomer must have strong electron-withdrawing characteristics in order to promote charge transfer and charge separation. Although, too strong of an acceptor can lead to the electron being trapped which lowers charge mobility which limits device performance. Since the LUMO of the polymer is best represented by the LUMO of the acceptor, the LUMO of the acceptor must be matched appropriately with the acceptor material in order to ensure efficient electron transfer to the acceptor material.¹⁸⁵

One of the most promising acceptors is the diketopyrrolopyrole (DPP) monomer. DPP is a strong electron accepting fused bicyclic monomer. It has a fused planar structure that improves conjugation along the polymer backbone and the planar structure can promote intermolecular π - π stacking in solar devices.¹⁸⁶ The lactam groups on the rings are strong electron-withdrawing groups that facilitate large intramolecular charge transfer.¹⁸⁷ DPP also exhibits excellent photochemical, mechanical and thermal stability which is important for the stability of DPP-based donor-acceptor polymers.¹⁸⁸ Polymers that have incorporated DPP acceptors have shown power conversion efficiencies of over 10%.¹⁸⁹

Isoindigo (II) acceptor monomers have also drawn attention for incorporation into donor-acceptor polymers. II is an isomer of indigo; it is composed of two pyrrolidine rings connected by a double bond with two fused benzene rings on the periphery of each pyrrolidine ring. The II acceptor is relatively planar which provides excellent electronic communication of the phenyl

and the ketopyrrole carbonyl π -electrons.¹⁹⁰ Similar to DPP, the ketopyrrole is responsible for the strong electron-withdrawing effects of the acceptor unit. Isoindigo based donor-acceptor based polymers show weak fluorescence which is ideal for high efficiency light harvesting donor-acceptor polymers. Isoindigo acceptors have also shown great photostability. Isoindigo based donor-acceptor polymers have exhibited power conversion efficiencies of over 6%.¹⁹¹

One of the most studied and maybe highest potential acceptor monomers have been thiophene based acceptors. Thiophene based acceptors can be easily modified. The conjugation length can be readily increased by fusing other conjugated aromatic rings. Other thiophene rings can be attached in a variety of different ways from fusing rings together to covalently linking thiophenes by single bonds. The electron-withdrawing properties are easily modulated by attaching electron-withdrawing functional groups to the thiophene acceptor. One of the early best performing donor-acceptor polymers, PTB7, used a thiophene acceptor.¹⁹² Polymers using thiophene acceptors have shown power conversion efficiencies of over 10%.¹⁹³

1.8.6 Acceptor Materials for Organic Solar Cells

In organic solar cell, solar energy to electrical power conversion is accomplished by photo-induced electron transfer process between an organic electron donating material and an electron-accepting material. A lot of focus has been on the photon absorbing materials that are responsible for donating an electron that is used in the electricity generation, but the organic electron accepting material is equally important. The acceptor material accepts the excited electron from the LUMO of donor, so the LUMO of the acceptor must be low-lying in order to successfully dissociate the electron from the exciton on the donor material. The acceptor material can also be photoexcited in order to generate an exciton that can migrate to the donor-acceptor interface of the organic solar cell. The hole can migrate to the donor material and the

electron can migrate from the acceptor material to the electrode to generate electricity. Thus the acceptor must be strong enough to dissociate the electron from the organic donor material as well as have high electron mobilities to allow the electron to reach the electrode.¹⁹⁴

By far the most popular organic accepting materials are fullerene based acceptors. Since their introduction in organic bulk heterojunctions in the 1990s, they have continued to one of the most popular acceptor materials.⁸⁷ Fullerenes have low-lying LUMO level, in the range of -3.5 eV to -4.5 eV, which provides excellent electron-accepting properties.¹⁹⁵⁻¹⁹⁶ Fullerenes have fast charge transfer rates and low charge separation energy barriers.¹⁹⁷ Recently, photo-physical investigation and theoretical calculation showed evidences on the unique fast charge transfer rate.¹⁹⁸ Fullerenes have been utilized as the organic acceptor in many of the highest performing organic solar cells, but it has significant drawbacks. Fullerene based acceptors are expensive materials to synthesize due to their complexity and 3-dimensional structure, which has attracted interest in investigated cheaper synthetic methods.¹⁹⁹ Fullerene based acceptors also have poor absorption properties in the visible spectrum, which means one half of the donor-acceptor active material is not involved in absorbing photons to be used in electricity generation.²⁰⁰

The drawbacks of fullerene based acceptor materials have led to intense research into alternative organic electron accepting materials. Non-fullerene acceptors can have tunable absorption properties, tunable electron mobility, solubility can be modified to enhance phase mixing between the donor and acceptor material, the morphology can easily be modified, and they have lower production costs.²⁰¹⁻²⁰⁴ One such non-fullerene acceptor material is naphthalene diimide (NDI) oligomers with donor-acceptor motifs. NDI based acceptors have tunable optical band gaps and they can be tuned from 2.1 eV to 1.4 eV.²⁰⁵ This is a marked improvement in absorption properties compared to fullerene based acceptors. The planarity and extended π -

conjugation lends itself to π - π stacking which can promote intermolecular photoinduced charge transfer from the donor material to the acceptor material. Open-circuit voltages of up to 0.81 V and short-circuit currents of up to 18.18 mA cm⁻² with power conversion efficiencies of up to 8% have been achieved.²⁰⁶

One of the most promising non-fullerene acceptors are perylene diimide (PDI) acceptors. PDI is similar to NDI, with the naphthalene subunit replaced by a perylene subunit. The large relatively planar structure can promote π - π stacking with donor material which can promote intermolecular charge transfer from between the donor material to the acceptor material. It can also promote crystallinity to improve charge mobilities. PDI acceptors show broad and strong absorption in the region of 300–700 nm with a maximum extinction coefficient of 3.21×10^4 L mol⁻¹ cm⁻¹ at 349 nm.²⁰⁷ Highly efficient solar cells have produced power conversion efficiencies of almost 8%.²⁰⁸

1.9 Dissertation Outline

So far in this dissertation, energy generation technologies have briefly been introduced, photoharvesting material technologies have been discussed, the various organic solar harvesting materials have been discussed, and device architectures discussed. There have been extensive improvements in the understanding of synthetic methods to develop organic photovoltaic materials. There have been extensive investigations of device fabrication. But there still is much to learn about the optoelectronic properties of these light harvesting materials.

In the rest of this thesis, steady-state spectroscopy, ultrafast time-resolved fluorescence spectroscopy, ultrafast two-photon absorption spectroscopy, nanosecond two-photon absorption spectroscopy, ultrafast transient absorption spectroscopy, and nanosecond transient absorption spectroscopy; as well as quantum mechanical calculations were used to investigate the optical

and electric properties of organic light harvesting materials. With the hopes of giving insight into the property structural relationships of organic light harvesting materials, so that new and improved organic light harvesting materials can be developed. Steady-state spectroscopy gives insight into the steady-state absorption and steady-state fluorescence properties. Two-photon absorption spectroscopy gives insight into the two-photon absorption cross-section which is proportional to the transition dipole moment which is proportional to the charge transfer character of the organic light harvesting materials. The ultrafast time-resolved fluorescence spectroscopy gives insight into the fluorescence dynamics of exciton decay and energy transfer. The nanosecond time-resolved fluorescence spectroscopy gives insight in to long timescale fluorescence decay processes. The ultrafast transient absorption spectroscopy can give insight into the excited state dynamics. The nanosecond transient absorption spectroscopy can give insight in the long-lived excited state dynamics. The quantum mechanical calculations can give insight into the molecular structures responsible for the experimental results.

In chapter 2, the experimental techniques used to investigate the organic light harvesting will be discussed. The theory of each technique will be discussed as well as the practical aspects will be discussed.

In chapter 3, the optical and electronic properties of light harvesting donor-acceptor polymer with various electron-withdrawing strengths was investigated. The influence of the electron-withdrawing strength on the optical properties of the donor-acceptor polymers was investigated. The exciton lifetime was investigated in respect to acceptor strength.

In chapter 4, the optical and electronic properties of light harvesting donor-acceptor polymers with various donor conjugation lengths were investigated. The effect of donor conjugation length on optical properties was investigated. Quantum mechanical calculations

were used to offer further insight into the electronic structures responsible for the optical properties.

In chapter 5, a new nanosecond laser experiment for two-photon excitation fluorescence was designed. The design of experiment is described and the description for operation is provided. A new SRS 250 gated integrator was incorporated for data collection. A new program was coded to handle the data collection and to save the data for manipulation.

In chapter 6, a new nanosecond transient absorption experiment was installed and aligned. The design of the experiment is described and the description for operation is provided. A new LP980 system was installed for data collection and electronic control of the probe source.

In chapter 7, a summary is provided with the future directions for organic light-harvesting materials.

References

- (1) United Nations, Department of Economic and Social Affairs, Population Division. <https://esa.un.org/unpd/wpp/Graphs/Probabilistic/POP/TOT>.
- (2) Speidel, J. J.; Weiss, D. C.; Ethelston, S. A.; Gilbert, S. M. Population Policies, Programmes and the Environment. *Phil. Trans. R. Soc. B.* **2009**, *364*, 3049-3065.
- (3) Vorosmarty, C. J.; McIntyre, P. B.; Gessner, M. O.; Dudgeon, D.; Prusevich A.; Green, P.; Glidden, S.; Bunn, S. E.; Sullivan, C. A.; Liermann C. R.; Davies P. M. Global Threats to Human Water Security and River Biodiversity. *Nature.* **2009**, *467*, 555-561.
- (4) Karp, A.; Richter, G. M. Meeting the Challenge of Food and Energy Security. *J. Exp. Bot.* **2011**, *62*, 3263-3271.
- (5) Jacobson, M. Z. Review of Solutions to Global Warming, Air Pollution, and Energy Security. *Energy Environ. Sci.* **2009**, *2*, 148-173.
- (6) BP Statistical Review of World Energy June 2017. <https://www.bp.com/content/dam/bp/en/corporate/pdf/energy-economics/statistical-review-2017/bp-statistical-review-of-world-energy-2017-full-report.pdf>.
- (7) U.S. Energy Information Administration. International Energy Outlook. https://www.eia.gov/pressroom/presentations/mead_91417.pdf.
- (8) World Energy Council. World Energy Resources 2016. https://www.worldenergy.org/wp-content/uploads/2016/10/World-Energy-Resources_SummaryReport_2016.10.03.pdf.

- (9) Pimentel, D.; Patzek, T. Green Plants, Fossil Fuels, and Now Biofuels. *BioScience*. **2006**, *56*, 875.
- (10) Butt, N.; Beyer, H. L.; Bennett, J.R.; Biggs, D.; Maggini, R.; 1 Mills, M.; Renwick, A.R.; Seabrook, L. M.; Possingham, H. P. Biodiversity Risks from Fossil Fuel Extraction. *Science*. **2013**, *342*, 425-426.
- (11) Hook, M.; Tang, X. Depletion of Fossil Fuels and Anthropogenic Climate Change-A Review. *Energy Policy*. **2013**, *52*, 797-809.
- (12) Likens, G. E.; Bormann, H. F. Acid Rain: A Serious Regional Environmental Problem. *Science*. **1974**, *184*, 1176-1179.
- (13) Piro, I.; Duffey, R. Nuclear Power as a Basis for Future Electricity Generation. *J. Nuclear Rad. Sci.* **2015**, *1*, 1-19.
- (14) Goldberg, S. M.; Rosner, R. Nuclear Reactors: Generation to Generation. *Am. Acad. Arts. Sci.* **2011**, 1-25.
- (15) Dragunov, A.; Saltanov, E.; Piro, I.; Kirillov, P.; Duffey, R. Power Cycles of Generation III and III+ Nuclear Power Plants. *J. Nuclear Rad. Sci.* **2015**, *1*, 1-10.
- (16) Moir, R. W.; Teller, E. Thorium-Fueled Underground Power Plant Based on Molten Salt Technology. *Nucl. Tech.* **2005**, *151*, 334-340.
- (17) Abu-Khader, M. M. Recent Advances in Nuclear Power: A Review. *P. Nucl. Energy*. **2009**, *51*, 225-235.
- (18) Hippel, F. The Uncertain Future of Nuclear Energy. *International Panel on Fissile Materials*. **2010**, 1-108. <http://fissilematerials.org/library/rr09.pdf>
- (19) Khajavi, M. N.; Menhaj, M. B.; Suratgar, A. A. A Neural Network Controller for Load Following Operation of Nuclear Reactors. *Annals Nucl. Energy*. **2002**, *29*, 751-760.
- (20) Chino, M.; Nakayama, H.; Nagai, H.; Terada, H.; Katata, G.; Yamazawa, H. Preliminary Estimation of Release Amounts of ^{131}I and ^{137}Cs Accidentally Discharged from the Fukushima Daiichi Nuclear Power Plant into the Atmosphere. *J. Nucl. Sci. Technol.* **2012**, *48*, 1129-1134.
- (21) Hileman, B. Nuclear Waste Disposal. *Environ. Sci. Technol.* **1982**, *16*, 271A-275A.
- (22) Paish, O. Small Hydro Power: Technology and Current Status. *Renew. Sus. Energy Reviews*. **2002**, *6*, 537-556.
- (23) Anagnostopoulos, J. S.; Papantonis, D. E. Pumping Station Design for a Pumped-Storage Wind-Hydro Power Plant. *Energy Conv. Mang.* **2007**, *48*, 3009-3017.
- (24) Bilotta, G. S.; Burnside, N. G.; Gray, J. C.; Orr, H. G. The Effects of Run-of-River Hydroelectric Power Schemes on Fish Community Composition in Temperate Streams and Rivers. *PLoS One*. **2016**, *11*, 1-15.
- (25) Paatero, J. V.; Lund, P. D. Effect of Energy Storage on Variations in Wind Power. *Wind Energ.* **2005**, *8*, 421-441.
- (26) Rose, S.; Jaramillo, P.; Small, M. J.; Grosmann, I.; Apt, J. Quantifying the Hurricane Risk to Offshore Wind Turbines. *Proc. Natl. Acad. Sci.* **2012**, *109*, 3247-3252.

- (27) Kunz, T. H.; Arnett, E. B.; Erickson, W. P.; Hoar, A. R.; Johnson, G. D.; Larkin, R. P.; Strickland, D. M.; Thresher, R. W.; Tuttle, M. D. Ecological Impacts of Wind Energy Development on Bats: Questions, Research Needs, and Hypotheses. *Front. Ecol. Environ.* **2007**, *5*, 315-324.
- (28) Richardson, D. R.; McNearney, G. M. Wind Energy Systems. *Proc. IEEE.* **1993**, *81*, 378-389.
- (29) Abbey, C.; Joos, G.; Supercapacitor Energy Storage for Wind Energy Applications. *IEEE Trans. Indust. App.* **2007**, *43*, 769-776.
- (30) Zhu, X. G.; Long, S. P.; Ort, D. R. What is the Maximum Efficiency with which Photosynthesis can Convert Solar Energy into Biomass?. *Curr. Op. Biotech.* **2008**, *19*, 153-159.
- (31) ASTM International. Standard Test Method for Electrical Performance of Photovoltaic Cells Using Reference Cells Under Simulated Sunlight.
- (32) Becquerel, A. E. Recherches sur les effets de la radiation chimique de la lumiere solaire au moyen des courants electriques. *Comptes Rendus de L'Academie des Sciences.* **1839**, *9*, 145-149.
- (33) Adams, W. G.; Day, R. E. The Action of Light on Selenium. *Proc. R. Soc. London, Ser. A.* **1877**, *A25*, 113-117.
- (34) Einstein, A. Concerning an Heuristic Point of View Toward the Emission and Transformation of Light. *Annalen der Physik.* **1905**, *17*, 132-148.
- (35) Chapin, D.; Fuller, C.; Pearson, G. A new silicon p-n junction photocell for converting solar radiation into electrical power. *J Appl Phys.* **1954**, *25*, 676-677.
- (36) Fritts, C. On the Fritts Selenium Cell and Batteries. *Van Nostrands Eng. Mag.* **1885**, *32*, 388-395.
- (37) U.S. Department of Energy. Energy Efficiency and Renewable Energy. The History of Solar. https://www1.eere.energy.gov/solar/pdfs/solar_timeline.pdf
- (38) Green, M. A. Silicon Photovoltaic Modules: A Brief History of the First 50 Years. *Prog. Photovolt: Res. Appl.* **2005**, *13*, 447-455.
- (39) Ha, D.; Fang, Z.; Hu, L.; Munday, J. N. Paper-Based Anti-Reflection Coatings for Photovoltaics. *Adv. Energy Mater.* **2014**, *4*, 1-5.
- (40) Jung, G. H.; Hong, K.; Dong, W. J.; Kim, S.; Lee, J-L. BCP/Ag/MoO₃ Transparent Cathodes for Organic Photovoltaics. *Adv. Energy Mater.* **2011**, *7*, 1023-1028.
- (41) Tang, Z.; Tress, W.; Inganas, O. Light Trapping in Thin Film Organic Solar Cells. *Mater. Today.* **2014**, *17*, 389-396.
- (42) Gao, J.; Jeong, S.; Lin, F.; Erslev, P. T.; Semonin, O. E.; Luther, J. M.; Beard, M. C. Improvements in Carrier Transport Properties by Mild Thermal of PBS Quantum Dot Solar Cells. *Appl. Phys. Lett.* **2013**, *102*, 1-5.
- (43) Yang, S.; Fu, W.; Zhang, Z.; Chen, H.; Li, C-Z. Recent Advances in Perovskite Solar Cells: Efficiency, Stability, and Lead-Free Perovskite. *J. Mater. Chem. A.* **2017**, *5*, 11462-11482.

- (44) Kalapathy, U.; Proctor, A.; Shultz, J. A Simple Method for Production of Pure Silica from Rice Hull Ash. *Biores. Tech.* **2000**, *73*, 257-262.
- (45) Saga, T. Advances in Crystalline Silicon Solar Cell Technology for Industrial Mass Production. *NPG Asia Mater.* **2010**, *2*, 96-102.
- (46) Yin, Z.; Wei, J.; Zheng, Q. Interfacial Materials for Organic Solar Cells: Recent Advances and Perspectives. *Adv. Sci.* **2016**, *3*, 1-37.
- (47) Forrest, S. R. The Limits to Organic Photovoltaic Cell Efficiency. *MRS Bull.* **2005**, *30*, 28-32.
- (48) Xu, T.; Yu, L. How to Design Low Bandgap Polymers for Highly Efficient Organic Solar Cells. *Mater. Today.* **2014**, *17*, 11-15.
- (49) Pearson, G. L.; Bardeen, J. Electrical Properties of Pure Silicon and Silicon Alloys Containing Boron and Phosphorus. *Phys. Rev.* **1949**, *75*, 865-883.
- (50) Osueke, C. O.; Onyekachi, E. M.; Nwabueze, I. O. Combating Problems with Solar Power: A Cost Effective Improvement on the Conversion Efficiency of Solar Panels. *Inter. J. Sci. & Eng. Res.* **2011**, *2*, 1-9.
- (51) Ohl, R. S. Light-Sensitive Electric Device. *U.S. Patent.* **1914**, *2*, 402, 602.
- (52) Chapin, D. M.; Fuller, C. S., and Pearson, G. L. A New Silicon P-N Junction Photocell for Converting Solar Radiation into Electrical Power. *J. Appl. Phys.* 1954, *25*, 676-677.
- (53) Blakers, A. W.; Green, M. A. 20% Efficiency Silicon Solar Cells. *Appl. Phys. Lett.* **1986**, *48*, 215-217.
- (54) Yoshikawa, K.; Kawasaki, H.; Yoshida, W.; Irie, T.; Konishi, K.; Nakano, K.; Uto, T.; Adachi, D.; Kanematsu, M.; Uzu, H.; Yamamoto, K. Silicon heterojunction solar cell with interdigitated back contacts for a photoconversion efficiency over 26%. *Nature Energy* **2017**, *2*, 1-8.
- (55) Davis, J. R.; Rohatgi, A.; Hopkins, R. H.; Blais, P. D.; Rai-Choudhury, P.; McCormick, J. R.; MollenKopF, H. C. Impurities in Silicon Solar Cells. *IEEE Trans. Elec. Dev.* **1980**, *27*, 677-687.
- (56) Fujiwara, K.; Pan, W.; Usami, N.; Sawada, K.; Tokairin, M.; Nose, Y.; Nomura, A.; Shishido, T.; Nakajima, K. Growth of Structure-Controlled Polycrystalline Silicon Ingots for Solar Cells by Casting. *Acta Mater.* **2006**, *54*, 3191-3197.
- (57) Guo, Y.; Wang, Q.; Kawazoe, Y.; Jena, P. A New Silicon Phase with Direct Band Gap and Novel Optoelectronic Properties. *Sci. Rep.* **2015**, *5*, 1-7.
- (58) Sokolov, A. P.; Shebanin, A. P., Golikova, O. A.; Mezdrogina, M. M. Structural Order in Amorphous Silicon and Its Alloys: Raman Spectra and Optical Gap. *J. Non-Cryst. Solids.* **2017**, *471*, 490-495.
- (59) Schubert, M. B.; Werner, J. H. Flexible Solar Cells for Clothing. *Mater. Today.* **2006**, *9*, 42-50.
- (60) Rech, B.; Wagner, H. Potential of Amorphous Silicon for Solar Cells. *Appl. Phys. A.* **1999**, *69*, 155-167.

- (61) Sai, H.; Matsui, T.; Koida, T.; Matsubara, K.; Kondo, M.; Sugiyama, S.; Katayama, H.; Takeuchi, Y.; Yoshida, I. Triple-Junction Thin-Film Silicon Solar Cell Fabricated on Periodically Textured Substrate with a Stabilized Efficiency of 13.6%. *Appl. Phys. Lett.* **2015**, *106*, 1-4.
- (62) Meillaud, F.; Cocard, M.; Bugnon, M.; Despeisse, M.; Hanni, S.; Haug, F.-J.; Persoz, J.; Schuttauf, J.-W.; Stuckelberger, M.; Ballif, C. Recent Advances and Remaining Challenges in Thin-Film Silicon Photovoltaic Technology. *Mater. Today.* **2015**, *18*, 378-384.
- (63) Lalitha, S.; Karazhanov, S. Z.; Ravindran, P.; Senthilarasu, S.; Sathyamoorthy, R.; Janabergenov, J. Electronic Structure, Structural and Optical Properties of Thermally Evaporated CdTe Thin Films. *Phys. B: Condens. Matter.* **2007**, *387*, 227-238.
- (64) Fonthal, G.; Tirado-Mejia, L.; Marin-Hurtado, J. I.; Ariza-Calderon, H.; Mendoza-Alvarez, J. G. Temperature Dependence of the Band Gap Energy of Crystalline CdTe. *J. Phys. Chem. Solids.* **2000**, *61*, 579-583.
- (65) Gloeckler, M.; Sankin, I.; Zhao, Z. CdTe Solar Cells at the Threshold to 20% Efficiency. *IEEE J. Photovolt.* **2013**, *3*, 1389-1393.
- (66) Godt, J.; Scheidig, F.; Grosse-Siestrup, C.; Esche, V.; Brandenburg, P.; Reich, A.; Groneberg, D. A. The Toxicity of Cadmium and Resulting Hazards for Human Health. *J. Occ. Med. Toxicol.* **2006**, *1*, 1-6.
- (67) Vij, P.; Hardej, D. Evaluation of Tellurium Toxicity in Transformed and Non-Transformed Human Colon Cells. *Environ. Toxicol. Pharmacol.* **2012**, *34*, 768-782.
- (68) Mohamed, H. A. Dependence of Efficiency of Thin-Film CdS/CdTe Solar Cell on Optical and Recombination Losses. *J. Appl. Phys.* **2013**, *113*, 1-6.
- (69) Ramanujam, J.; Singh, U. P. Copper Indium Gallium Selenide Based Solar Cells- A Review. *Energy Environ. Sci.* **2017**, *10*, 1306-1319.
- (70) Jackson, P.; Hariskos, D.; Wuerz, R.; Kiowski, O.; Bauer, A.; Friedlmeier, T.; Powalla, M. Properties of Cu(In,Ga)Se₂ Solar Cells with New Record Efficiencies up to 21.7%. *Phys. Status Solidi RRL.* **2015**, *1*, 28-31.
- (71) Singh, P.; Ravindra, N. M. Temperature Dependence of Solar Cell Performance-An Analysis. *Sol. Energy Mater. Sol. Cells.* **2012**, *101*, 36-45.
- (72) Chiang, S. Y.; Pearson, G. L. Properties of Vacancy defects in GaAs Single Crystals. *J. Appl. Phys.* **1975**, *46*, 2986-2991.
- (73) Wang, X.; Khan, M. R.; Gray, J. L.; Alam, A.; Lundstrom, M. S. Design of GaAs Solar Cells Operating Close to the Shockley-Queisser Limit. *IEEE J. Photovolt.* **2013**, *3*, 737-744.
- (74) Kurtz, S. R.; Allerman, A. A.; Jones, E. D.; Gee, J. M.; Banas, J. J.; Hammons, B. E. InGaAsN Solar Cells with 1.0 eV Band Gap, Lattice Matched to GaAs. *Appl. Phys. Lett.* **1999**, *74*, 729-731.
- (75) Moon, S.; Kim, K.; Kim, Y.; Heo, J.; Lee, J. Highly Efficient Single-Junction GaAs Thin-Film Solar Cell on Flexible Substrate. *Sci. Rep.* **2016**, *6*, 1-6.

- (76) Bauhuis, G. J.; Mulder, P.; Haverkamp, E. J.; Huijben, J. C. C. M.; Schermer, J. J. 26.1% Thin-Film GaAs Solar Cell using Epitaxial Lift-Off. *Sol. Energy Mater. Sol. Cells*. **2009**, *93*, 1488-1491.
- (77) Ratnaike, R. Acute and Chronic Arsenic Toxicity. *Postgrad Med. J.* **2003**, *79*, 391-396.
- (78) Burton, J. D.; Culkin, F.; Riley, J. P. The Abundances of Gallium and Germanium in Terrestrial Materials. *Geochim. Cosmochim. Acta*. **1959**, *16*, 151-180.
- (79) Chamberlain, G. A. Organic Solar Cells: A Review. *Sol. Cells*. **1983**, *8*, 47-83.
- (80) Scharber, M. C.; Sariciftci, N. S. Efficiency of Bulk-Heterojunction Organic Solar Cells. *Prog. Poly. Sci.* **2013**, *38*, 1929-1940.
- (81) Yeh, N.; Yeh, P. Organic Solar Cells: Their Developments and Potentials. *Renew. Sust. Energ. Rev.* **2013**, *21*, 421-431.
- (82) Qin, P.; Yang, X.; Chen, R.; Sun, L. Influence of π -Conjugation Units in Organic Dyes for Dye-Sensitized Solar Cells. *J. Phys. Chem. C*. **2007**, *111*, 1853-1860.
- (83) Facchetti, A. π -Conjugated Polymers for Organic Electronics and Photovoltaic Cell Applications. *Chem. Mater.* **2011**, *23*, 733-758.
- (84) Spanggaard, H.; Krebs, F. C. A Brief History of the Development of Organic and Polymeric Photovoltaics. *Sol. Energy Mater. Sol. Cells*. **2004**, *83*, 125-146.
- (85) Kallmann, H.; Pope, M. Photovoltaic Effect in Organic Crystals. *J. Chem. Phys.* **1959**, *30*, 585-586.
- (86) C. W. Tang. 1986. Two-layer organic photovoltaic cell. *Appl. Phys. Lett.* **1986**, *48*, 183-185.
- (87) Yu, G.; Gao, J.; Hummelen, J. C.; Wudl, F.; Heeger A. J. Polymer Photovoltaic Cells: Enhanced Efficiencies via a Network of Internal Donor-Acceptor Heterojunctions. *Science*. **1995**, *270*, 1789-1791.
- (88) Chen, J.-D.; Cui, C.; Li, Y.-Q.; Zhuo, L.; Ou, Q.-D.; Li, C.; Li, Y.; Tang, J.-X. Single Junction Polymer Solar Cells Exceeding 10% Power Conversion Efficiency. *Adv. Mater.* **2015**, *27*, 1035-1041.
- (89) Bredas, J.-L.; Norton, J. E.; Cornil, J.; Coropceanu, V. Molecular Understanding of Organic Solar Cells: The Challenges. *Acc. Chem. Res.* **2009**, *42*, 1691-1699.
- (90) Jana, B.; Ghosh, A.; Patra, A. Photon Harvesting in Conjugated Polymer-Based Functional Nanoparticles. *J. Phys. Chem. Lett.* **2017**, *8*, 4608-4620.
- (91) Durrant, J. R. Molecular Approaches to Solar Energy Conversion: The Energetic Cost of Charge Separation from Molecular-Excited States. *Philos. Trans. R. Soc. London, Ser. A*. **2013**, *371*, 1-10.
- (92) Neher, D.; Kniepert, J.; Elimelech, A.; Koster, L. J. A. A New Figure of Merit for Organic Solar Cells with Transport-Limited Photocurrents. *Sci. Rep.* **2016**, *6*, 1-9.

- (93) Van Franeker, J. J.; Voorthuijzen, W. P.; Gorter, H.; Hendriks, K. H.; Janssen, R. A. J.; Hadipour, A.; Andriessen, R.; Galagan, Y. All-Solution-Processed Organic Solar Cells with Conventional Architecture. *Sol. Energy Mater. Sol. Cells.* **2013**, *117*, 267-272.
- (94) Sondergaard, R.; Hoel, M.; Angmo, D.; Larsen-Olsen, T. T.; Krebs, F. C. Roll-to-Roll Fabrication of Polymer Solar Cells. *Mater. Today.* **2012**, *1*, 36-49.
- (95) Hoth, C. N.; Schilinsky, P.; Choulis, S. A.; Brabec, C. J. Printing Highly Efficient Organic Solar Cells. *Nano Lett.* **2008**, *8*, 2806-2813.
- (96) He, C.; He, Q.; He, Y.; Li, Y.; Bai, F.; Yang, C.; Ding, Y.; Wang L.; Ye, J. Organic Solar Cells Based on the Spin-Coated Blend Films of TPA-th-TPA and PCBM. *Sol. Energy Mater. Sol. Cells.* **2006**, *90*, 1815-1827.
- (97) Kalowekamo, J.; Baker, E. Estimating the Manufacturing Cost of Purely Organic Solar Cells. *Sol. Energy.* **2009**, *8*, 1224-1231.
- (98) Apaydin, D. H.; Yildiz, D. E.; Cirpan, A.; Toppare, L. Optimizing the Organic Solar Cell Efficiency: Role of the Active Layer Thickness. *Sol. Energy Mater. Sol. Cells.* **2013**, *113*, 100-105.
- (99) Nam, Y. M.; Huh, J.; Jo, W. H. Optimization of Thickness and Morphology of Active Layer for High Performanc of Bulk-Heterojunction Organic Solar Cells. *Sol. Energy Mater. Sol. Cells.* **2010**, *94*, 1118-1124.
- (100) Kirchartz, T.; Agostinelli, T.; Campoy-Quiles, M.; Gong, W.; Nelson, J. Understanding the Thickness-Dependent Performance of Organic Bulk Heterojunction Solar Cells: The Influence of Mobility, Lifetime, and Space Charge. *J. Phys. Chem. Lett.* **2012**, *3*, 3470-3475.
- (101) Sah, C-T.; Yamakawa, K. A.; Lutwack, R. Effect of Thickness on Silicon Solar Cell Efficiency. *IEEE Trans. Electron Devices.* **1982**, *29*, 903-908.
- (102) Zaki, A. A.; El-Amin, A. A. Effect of Cell Thickness on the Electrical and Optical Properties of Thin Film Silicon Solar Cell. *Opt. Laser Tech.* **2017**, *97*, 71-76.
- (103) Liao, H-C.; Ho, C-C.; Chang, C-Y.; Jao, M-H.; Darling, S. B.; Su, W-F. Additives for Morphology Control in High-Efficiency Organic Solar Cells. *Mater. Today.* **2013**, *16*, 326-336.
- (104) Kim, Y.; Choulis, S. A.; Nelson, J.; Bradley, D. D. C. Device Annealing Effect in Organic Solar Cells with Blends of Regioregular Poly(3-heyhlthiophene) and Soluble Fullerene. *Appl. Phys. Lett.* **2005**, *86*, 1-3.
- (105) Tamai, Y.; Fan, Y.; Kim, V. O.; Ziabrev, K.; Rao, A.; Barlow, S.; Marder, S. R.; Friend, R. H.; Menke, M. S. Ultrafast Long-Range Charge Separation in Nonfullerene Organic Solar Cells. *ACS Nano.* **2017**, *11*, 12473-12481.
- (106) Gu, K. L.; Zhou, Y.; Gu, X.; Yan, H.; Diao, Y.; Kurosawa, T.; Ganapathysubramanian, B.; Toney, M. F.; Bao, Z. Tuning Domain Size and Crystallinity in Isoindigo/PCBM Organic Solar Cells via Solution Shearing. *J. Org. Elec.* **2017**, *40*, 79-87.
- (107) Huang, Z.; Cheng, L.; Wu, B.; Wu, X. The Study of Optical and Electrical Properties of Solar Cells with Oblique Incidence. *IEEE Phot. Tech. Lett.* **2016**, *28*, 2047-2049.

- (108) Zhang, S.; Ye, L.; Zhang, H.; Hou, J. Green-Solvent-Processable Organic Solar Cells. *Mater. Today*. **2016**, *19*, 533-543.
- (109) Zeigler, D. F.; Chen, K-S.; Yip, H-Y.; Zhang, Y.; Jen, A. K.-Y. Tunable Light-Harvesting Polymers Containing Embedded Dipolar Chromophores for Polymer Solar Cell Applications. *J. Poly. Sci. A*. **2012**, *50*, 1362-1373.
- (110) Tang, A.; Zhan, C.; Yao, J. Comparative Study of Effects of Terminal Non-Alkyl Aromatic and Alkyl Groups on Small-Molecule Solar Cell Performance. *Adv. Energ. Mater.* **2015**, *5*, 1-9.
- (111) Xu, T.; Yu, L. How to Design Low Bandgap Polymers for Highly Efficient Organic Solar Cells. *Mater. Today*. **2014**, *17*, 11-15.
- (112) Kim, J-S.; Kim, J-H.; Lee, W.; Yu, H.; Kim, H. J.; Song, I.; Shin, M.; Oh, J. H.; Jeong, U.; Kim, T-S.; Kim, B. J. Tuning Mechanical and Optoelectronic Properties of Poly(3-hexylthiophene) through Systematic Regioregularity Control. *Macromolecules*. **2015**, *48*, 4339-4346.
- (113) Goldey, M. B.; Reid, D.; Pablo, J.; Galli, G. Planarity and Multiple Components Promote Organic Photovoltaic Efficiency by Improving Electronic Transport. *Phys. Chem. Chem. Phys.* **2016**, *18*, 31388-31399.
- (114) Lu, H-I.; Lu, C-W.; Lee, Y-C.; Lin, H-W.; Lin, L-Y.; Lin, F.; Chang, J-H.; Wu, C-I.; Wong, K-T. New Molecular Donors with Dithienopyrrole as the Electron-Donating Group for Efficient Small-Molecule Organic Solar Cells. *Chem. Mater.* **2014**, *26*, 4361-4367.
- (115) Crossley, D. L.; Cade, I. A.; Clark, E. R.; Escande, A.; Humphries, M. J.; King, S. M.; Vitorica-Yrezabel, I.; Ingleson, M. J.; Turner, M. L. Enhancing Electron Affinity and Tuning Band Gap in Donor-Acceptor Organic Semiconductors by Benzothiadiazole Directed C-H Borylation. *Chem. Sci.* **2015**, *6*, 5144-5151.
- (116) Zhou, Y.; Yan, Q.; Zheng, Y-Q.; Wang, J-Y.; Zhao, D.; Pei, J. New Polymer Acceptors for Organic Solar Cells: The Effect of Regio-Regularity and Device Configuration. *J. Mater. Chem. A*. **2013**, *1*, 6609-6613.
- (117) Vezie, M. S.; Few, S.; Meager, I.; Pieridou, G.; Dorling, B.; Ashraf, R.; Goni, A. R.; Bronstein, H.; McCulloch, I.; Hayes S. C.; Campoy-Quiles, M.; Nelson, J. Exploring the Origin of High Optical Absorption in Conjugated Polymers. *Nature Mater.* **2016**, *15*, 746-753.
- (118) Varotto, A.; Nam, C-Y.; Radivojevic, I.; Tome, J. P. C.; Cavaleiro, J. A. S.; Black, C. T.; Drain, C. M. Phthalocyanine Blends Improve Bulk Heterojunction Solar Cells. *J. Am. Chem. Soc.* **2010**, *132*, 2552-2554.
- (119) Ebenhoch, B.; Thomson, S. A. J.; Genevicius, K.; Juska, G.; Samuel, I. D. W. Charge Carrier Mobility of the Organic Photovoltaic Materials PTB7 and PC₇₁BM and its Influence on Device Performance. *Org. Elec.* **2015**, *22*, 62-68.
- (120) Tamai, Y.; Ohkita, H.; Benten, H.; Ito, S.; Exciton Diffusion in Conjugated Polymers: From Fundamental Understanding to Improvement in Photovoltaic Conversion Efficiency. *J. Phys. Chem. Lett.* **2015**, *6*, 3417-3428.

- (121) Kim, S. H.; Somorjai, G. A.; Surface Science of Single-Site Heterogeneous Olefin Polymerization Catalysts. *Proc. Nat. Acad. Sci. USA.* **2006**, *103*, 15289-15294.
- (122) Bryan, Z. J.; McNeil, A. J. Conjugated Polymer Synthesis via Catalyst-Transfer Polycondensation (CTP): Mechanism, Scope, and Applications. *Macromolecules.* **2013**, *46*, 8395-8405.
- (123) Tsai, C-H.; Fortney, A.; Qiu, Y.; Gil, R. R.; Yaron, D.; Kowalewski, T.; Noonan, K. J. T. Conjugated Polymers with Repeated Sequences of Group 16 Heterocycles Synthesized Through Catalyst-Transfer Polycondensation. *J. Am. Chem. Soc.* **2016**, *138*, 6798-6804.
- (124) Sontag, S. K.; Marshall, N.; Locklin, J. Formation of Conjugated Polymer Brushes by Surface-Initiated Catalyst-Transfer Polycondensation. *Chem. Comm.* **2009**, *23*, 3354-3356.
- (125) Cheng, P.; Zhan, X. Stability of Organic Solar Cells: Challenges and Strategies. *Chem. Soc. Rev.* **2016**, *45*, 2544-2582.
- (126) Turkovic, V.; Engmann, S.; Tsierkezos, N.; Hoppe, H; Madsen, M.; Rubahn, H-G.; Ritter, U.; Gobsch, G. Long-Term Stabilization of Organic Solar Cells Using UV Absorbers. *J. Phys. D: Appl. Phys.* **2016**, *49*, 1-7.
- (127) Leblebici, S. Y.; Chen, T. L.; Olalde-Velasco, P.; Yang, W.; Ma, B. Reducing Exciton Binding Energy by Increasing Thin Film Permittivity: An Effective Approach to Enhance Exciton Separation Efficiency in Organic Solar Cells. *ACS Appl. Energy Interfaces.* **2013**, *5*, 10105-10110.
- (128) Wagenpfahl, A. Mobility Dependent Recombination Models for Organic Solar Cells. *J. Phys.: Condens. Matter.* **2017**, *29*, 1-21.
- (129) Bagher, A. M. Comparison of Organic Solar Cells and Inorganic Solar Cells. *Int. J. Renew. Sus. Energy.* **2014**, *3*, 53-58.
- (130) Proctor, C. M.; Kuik, M.; Nguyen, T-Q. Charge Carrier Recombination in Organic Solar Cells. *Prog. Poly. Sci.* **2013**, *38*, 1941-1960.
- (131) Stegemann, B.; Kegel, J.; Mews, M.; Conrad, E.; Korte, L.; Sturzebecher, Uta.; Angermann, H. Evolution of the Charge Carrier Lifetime Characteristics in Crystalline Silicon Wafers During Processing of Heterojunction Solar Cells. *Energy Procedia.* **2014**, *55*, 219-228.
- (132) Jain, V.; Rajbongshi, B. K.; Mallajosyula, A. T.; Bhattacharjya, G.; Lyer, S. S. K.; Ramanathan, G. Photovoltaic Effect in Single-Layer Organic Solar Cell Devices Fabricated with Two New Imidazolin-5-one Molecules. *Sol. Energy Mater. Sol. Cells.* **2008**, *92*, 1043-1046.
- (133) Gommans, H. H. P.; Cheyns, D.; Aernouts, T.; Giroto, C.; Poortmans, J.; Heremans, P. Electro-Optical Study of Subphthalocyanine in a Bilayer Organic Solar Cell. *Adv. Func. Mater.* **2007**, *17*, 2653-2658.
- (134) Rim, S-B. Effect of Molecular Packing on the Exciton Diffusion Length in Organic Solar Cells. *Appl. Phys. Lett.* **2007**, *91*, 1-3.

- (135) Cuiffi, J.; Benanti, T.; Nam, W. J.; Fonash, S. Modeling of Bulk and Bilayer Organic Heterojunction Solar Cells. *Appl. Phys. Lett.* **2010**, *96*, 1-3.
- (136) Nelson, J. Polymer:Fullerene Bulk Heterojunction Solar Cells. *Mater. Today.* **2011**, *14*, 462-470.
- (137) Eftaiha, A. F.; Sun, J-P.; Hill, I. G.; Welch, G. C. Recent Advances of Non-Fullerene, Small Molecular Acceptors for Solution Processed Bulk Heterojunction Solar Cells. *J. Mater. Chem. A.* **2014**, *2*, 1201-1213.
- (138) Gerischer, H.; Michel-Beyerle, M.; Reberstrost, E.; Tributsch, H. (1968). Sensitization of Charge-Injection into Semiconductors with Large Band Gap. *Electrochim. Acta.* **1968**, *13*, 1509–1515.
- (139) O'Regan, B.; Grätzel, M. A low-cost, high-efficiency solar cell based on dye-sensitized colloidal TiO₂ films. *Nature.* **1991**, *353*, 737–740.
- (140) Bai, Y.; Cao, Y.; Zhang, J.; Wang, M.; Li, R.; Wang, P.; Zakeeruddin, S. M.; Grätzel, M. High-performance dye-sensitized solar cells based on solvent-free electrolytes produced from eutectic melts. *Nature Materials.* **2008**, *7*, 626–630.
- (141) Briscoe, J.; Dunn, S. Dye-Sensitized Solar Cells: The Future of Using Earth-Abundant Elements in Counter Electrodes Dye-Sensitized Solar Cells. *Adv. Mater.* **2016**, *28*, 3802-3813.
- (142) Wu, J.; Lan, Z.; Lin, J.; Huang, M.; Huang, Y.; Fan, L.; Luo, G. Electrolytes in Dye-Sensitized Solar Cells. *Chem. Rev.* **2015**, *115*, 2136-2173.
- (143) Burschka, J.; Pellet, N.; Moon, S.J.; Humphry-Baker, R.; Gao, P.; Nazeeruddin, M. K.; Gratzel, M. Sequential deposition as a route to high-performance perovskite-sensitized solar cells. *Nature.* **2013**, *499*, 316-319.
- (144) Ninsonti, H.; Chomkitichai, W.; Baba, A.; Wetchakun, N.; Kangwansupamonkon, W.; Phanichphant, S.; Kazunari, S.; Kato, K.; Kaneko, F. Au-Loaded Titanium Dioxide Nanoparticles Synthesized by Modified Sol-Gel/Impregnation Methods and Their Application to Dye-Sensitized Solar Cells. *Int. J. Photoenergy.* **2014**, *1*, 1-8.
- (145) Choi, M-C.; Kim, Y.; Ha, C-S. Polymers for Flexible Displays: From Material Selection to Device Applications. *Prog. Poly. Sci.* **2008**, *33*, 581-630.
- (146) Neville, R. G.; Mahoney, J. W.; MacDowall, K. R. Novel Thermally Stable and Chemically Resistant Epoxy Polymers derived from Phenylene Oxides. *Appl. Poly. Sci.* **1968**, *12*, 607-618.
- (147) Clark, E. S.; Scott, L. S. Superdrawn Crystalline Polymers: A New Class of High-Strength Fiber. *Poly. Eng. Sci.* **1974**, *14*, 682-686.
- (148) Müllekom, H. A. M.; Vekemans, J. A. J. M.; Havinga, E. E.; Meijer, E. W. Developments in the Chemistry and Band Gap Engineering of Donor-Acceptor Substituted Conjugated Polymers. *Mater. Sci. Eng. R.* **2001**, *32*, 1-40.
- (149) Kleinschmidt, A.; Root, S. E.; Lipomi, D. J. Poly(3-hexylthiophene) (P3HT): Fruit Fly or Outlier in Organic Solar Cell Research. *J. Mater. Chem. A.* **2017**, *5*, 11396-11400.

- (150) Rahimi, K.; Botiz, I.; Agumba, J. O.; Motamen, S.; Stingelin, N.; Reiter, G. Light Absorption of poly(3-hexylthiophene) Single Crystals. *Roy. Soc. Chem. Adv.* **2014**, *4*, 11121-11123.
- (151) Geiser, A.; Fan, B.; Benmansour, H.; Castro, F.; Heier, J.; Keller, B.; Mayerhofer, K. E.; Nuesch, F.; Hany, R. Poly(3-hexylthiophene)/C₆₀ heterojunction solar cells: Implication of Morphology on Performance and Ambipolar Charge Collection. *Sol. Energy Mater. Sol. Cells.* **2008**, *92*, 464-473.
- (152) Woo, C. H.; Thompson, B. C.; Kim, B. J.; Toney, M. F.; Frechet, J. M. J. The Influence of Poly(3-hexylthiophene) Regioregularity on Fullerene-Composite Solar Cell Performance. *J. Am. Chem. Soc.* **2008**, *130*, 16324-16329.
- (153) Zhang, Y.; Cao, K.; Zhu, X.; Li, X.; Qiao, X.; Tu, G.; Zhang, B.; Huang, D.; Shen, Y.; Wang, M.; Effect of the Molecular Weight of Poly(3-hexylthiophene) on the Performance of Solid-State Dye-Sensitized Solar Cells. *Roy. Soc. Chem. Adv.* **2013**, *3*, 14037-14043.
- (154) Dkhissi, A.; Ouhib, F.; Chaalane, A.; Hiorns, R. C.; Dagon-Lartigau, C.; Iratcabal, P.; Desbrieres, J.; Pouchan, C. Theoretical and Experimental Study of Low Band Gap Polymers for Organic Solar Cells. *Phys. Chem. Chem. Phys.* **2012**, *14*, 5613-5619.
- (155) Acevedo-Pena, P.; Baray-Calderon, A.; Hu, H.; Gonzalez, I.; Ugalde-Saldivar, V. M. Measurements of HOMO-LUMO Levels of Poly(3-hexylthiophene) Thin Films by a Simple Electrochemical Method. *J. Sol. State Electrochem.* **2017**, *21*, 2407-2414.
- (156) Laquindanum, J. G.; Katz, H. E.; Lovinger, A. J.; Dodabalapur, A. Benzodithiophene Rings as Semiconductor Building Blocks. *Adv. Mater. Com.* **1997**, *9*, 36-39.
- (157) Chuang, H-Y.; Hsu, S. L-C.; Le, P-I.; Lee, J-F.; Huang, S-Y.; Lin, S-W.; Lin, P-Y. Synthesis and Properties of a New Conjugated Polymer Containing Benzodithiophene for Polymer Solar Cells. *Poly. Bull.* **2014**, *71*, 1117-1130.
- (158) Jang, S.-Y.; Kim, I-B.; Kim, J.; Khim, D.; Jung, E.; Kang, B.; Lim, B.; Kim, Y-A.; Jang, Y-H.; Cho, K.; Kim, D-Y. New Donor-Donor Type Copolymers with Rigid and Coplanar Structures for High-Mobility Organic Field-Effect Transistors. *Chem. Mater. Comm.* **2014**, *26*, 6907-6910.
- (159) Brabec, C. J.; Heeney, M.; McCulloch, I.; Nelson, J. Influence of Blend Microstructure on Bulk Heterojunction Organic Photovoltaic Performance. *Chem. Soc. Rev.* **2011**, *40*, 1185-1199.
- (160) Lu, L.; Yu, L. Understanding Low Bandgap Polymer PTB7 and Optimizing Polymer Solar Cells Based on it. *Adv. Mater.* **2014**, *26*, 4413-4430.
- (161) Liu, X.; Shen, W.; He, R.; Luo, Y.; Li, M. Strategy to Modulate the Electron-Rich Units in Donor-Acceptor Copolymers for Improvements of Organic Photovoltaics. *J. Phys. Chem. C.* **2014**, *118*, 17266-17278.
- (162) Chen, H-Y.; Hou, J.; Zhang, S.; Liang, Y.; Yang, G.; Yang, Y.; Yu, Y.; Wu, Y.; Li, G. Polymer Solar Cells with Enhanced Open-Circuit Voltage and Efficiency. *Nature Photonics.* **2009**, *3*, 649-653.

- (163) Li, Y.; Cui, J.; Zhao, J.; Liu, J.; Song, P.; Ma, F.; Effect of Electronic Acceptor Segments on Photophysical Properties of Low-Band-Gap Ambipolar Polymers. *Sci. World. J.* **2013**, *1*, 1-8.
- (164) Sendur, M.; Balan, A.; Baran, D.; Karabay, B.; Toppare, L. Combination of Donor Characters in a Donor-Acceptor-Donor (DAD) Type Polymer Containing Benzothiadiazole as the Acceptor Unit. *Org. Elec.* **2010**, *11*, 1877-1885.
- (165) Golovnin, L.; Bakulin, A. A.; Zapunidy, S. A.; Nechvolodova, E. M.; Paraschuk, D. Y. Dramatic Enhancement of Photo-Oxidation Stability of a Conjugated Polymer in Blends with Organic Acceptor. *Appl. Phys. Lett.* **2008**, *92*, 1-3.
- (166) Schubert, M.; Preis, E.; Blakesley, J. C.; Pingel, P.; Scherf, U.; Neher, D. Mobility Relaxation and Electron Trapping in a Donor/Acceptor Copolymer. *Phys. Rev. B.* **2013**, *87*, 1-12.
- (167) Wu, F.; Chen, S.; Chen, L.; Chen, Y. Tuning Joint Sequence for Donor-Acceptor Polymers Based on Fluorinated Benzothiadiazole with Thiophene/Furan Bridged. *Polymer.* **2015**, *78*, 154-160.
- (168) Lee, C-H.; Lai, Y-Y.; Hsu, J-Y.; Huang, P-K.; Cheng, Y-C. Side-Chain Modulation of Dithienofluorene-Based Copolymers to Achieve High Field-Effect Mobilities. *Chem. Sci.* **2017**, 2942-2951.
- (169) Li, Y.; Fu, Y.; Tong, H.; Xie, Z.; Wang, L. Effect of Side-Chain Positions on Morphology and Photovoltaic Properties of Phenazine-Based Donor-Acceptor Copolymers. *J. Polym. Sci. A.* **2013**, *51*, 2910-2918.
- (170) Morse, G. E.; Tournebize, A.; Rivaton, A.; Chasse, T.; Taviot-Gueho, C.; Blouin, N.; Lozman, O. R.; Tierney, S. The effect of Polymer Solubilizing Side-Chains on Solar Cell Stability. *Phys. Chem. Chem. Phys.* **2015**, *17*, 11884-11897.
- (171) Gibson, G. L.; Seferos, D. S. "Heavy-Atom" Donor-Acceptor Conjugated Polymers. *Chem. Phys.* **2014**, *215*, 811-823.
- (172) Vazquez, R. J.; Kim, H.; Kobilka, B. M.; Hale, B. J.; Jeffries-EL, M.; Zimmerman, P.; Goodson, T. Evaluating the Effect of Heteroatoms on the Photophysical Properties of Donor-Acceptor Conjugated Polymers Based on 2,6-Di(thiophen-2-yl)benzo[1,2-b:4,5-b']difuran: Two-Photon Cross-Section and Ultrafast Time-Resolved Spectroscopy. *J. Phys. Chem. C.* **2017**, *121*, 14382-14392.
- (173) Wood, S.; Kim, J-H.; Wade, J.; Park, J. B.; Hwang, D-H.; Kim, J-S. Systematic Control of Heteroatoms in Donor-Acceptor Copolymers and its Effects on Molecular Conformation and Photovoltaic Performance. *J. Mater. Chem. C.* **2016**, *4*, 7966-7978.
- (174) Cansu-Ergun, E. G.; Akbayrak, M.; Akdag, A.; Onal, A. M. Effect of Thiophene Units on the Properties of Donor Acceptor Type Monomers and Polymers Bearing Thiophene-Benzothiadiazole-Scaffolds. *J. Electrochem. Soc.* **2016**, *163*, 153-158.
- (175) Zhou, H.; Yang, L.; Stoneking, S.; You, W. A Weak Donor-Strong Acceptor Strategy to Design Ideal Polymers for Organic Solar Cells. *ACS Appl. Mater. Interfaces.* **2010**, *2*, 1377-1383.

- (176) Biniak, L.; Schroeder, B. C.; Nielsen, C. B.; McCulloch, I. Recent Advances in High Mobility Donor-Acceptor Semiconducting Polymers. *J. Mater. Chem.* **2012**, *22*, 14803-14813.
- (177) Zong, K.; Reynolds, J. R. 3,4-Alkylenedioxyppyroles: Functionalized Derivatives as Monomers for New Electron-Rich Conducting and Electroactive Polymers. *J. Org. Chem.* **2001**, *66*, 6873-6882.
- (178) Wang, C.; Mueller, C. J.; Gann, E.; Liu, A. C. Y.; Thelakkat, M.; McNeill, C. R. EDOT-diketopyrrolopyrrole Copolymers for Polymer Solar Cells. *J. Mater. Chem. A.* **2016**, *4*, 3477-3486.
- (179) Bundgaard, E.; Krebs, F. C. Low band gap polymers for organic photovoltaics. *Sol. Energy Mater. Sol. Cells.* **2007**, *91*, 954-985.
- (180) Dennler, G.; Scharber, M. C.; Brabec, C. J. Polymer-Fullerene Bulk-Heterojunction Solar Cells. *Adv. Mater.* **2009**, *21*, 1-16.
- (181) Du, C.; Li, C.; Li, W.; Chen, X.; Bo, Z.; Veit, C.; Ma, Z.; Wuerfel, U.; Zhu, H.; Hu, W.; Zhang, F. 9-Alkylidene-9H-Fluorene-Containing Polymer for High-Efficiency Polymer Solar Cells. *Macromolecules.* **2011**, *44*, 7617-7624.
- (182) Kang, T. E.; Kim, T.; Wang, C.; Yoo, S.; Kim, B. J. Poly(benzodithiophene) Homopolymer for High-Performance Polymer Solar Cells with Open-Circuit Voltage of Near 1 V: A Superior Candidate to Substitute for Poly(3-hexylthiophene) as Wide Bandgap Polymer. *Chem. Mater.* **2015**, *27*, 2653-258.
- (183) Kastinen, T.; Niskanen, M.; Risko, C.; Cramariuc, O.; Hukka, T. I. Intrinsic Properties of Two Benzodithiophene-Based Donor-Acceptor Copolymers Used in Organic Solar Cells: A Quantum-Chemical Approach. *J. Phys. Chem. A.* **2016**, *120*, 1051-1064.
- (184) Holliday, S.; Li, Y.; Luscombe, C. K. Recent Advances in High Performance Donor-Acceptor Polymers for Organic Photovoltaics. *Prog. Poly. Sci.* **2017**, *70*, 34-51.
- (185) Mola, G. T.; Abera, N. Correlation between LUMO offset of Donor/Acceptor Molecules to an Open Circuit Voltage in Bulk Heterojunction Solar Cell. *Phys. B: Condens. Matter.* **2014**, *445*, 56-59.
- (186) Yuen, J. D.; Fan, J.; Seifert, J.; Lim, B.; Hufschmid, R.; Heeger, A. J.; Wudl, F. High Performance Weak Donor-Acceptor Polymers in Thin Film Transistors: Effect of the Acceptor on Electronic Properties, Ambipolar Conductivity, Mobility, and Thermal Stability. *J. Am. Chem. Soc.* **2011**, *133*, 20799-20807.
- (187) Lin, H-W.; Lee, W-Y.; Chen, W-C. Selenophene-DPP Donor-Acceptor Conjugated Polymer for High Performance Ambipolar Field Effect Transistor and Nonvolatile Memory Applications. *J. Am. Chem. Soc.* **2012**, *22*, 2120-2128.
- (188) Sonar, P.; Ng, G-M.; Lin, T. T.; Dodabalapur, A.; Chen, Z-K. Solution Processable Low Bandgap Diketopyrrolopyrrole (DPP) Based Derivatives: Novel Acceptors for Organic Solar Cells. *J. Mater. Chem.* **2010**, *20*, 3626-3636.
- (189) Li, W.; Hendriks, K. H.; Wienk, M. M.; Janssen, R. A. J. Diketopyrrolopyrrole Polymers for Organic Solar Cells. *Acc. Chem. Res.* **2016**, *49*, 78-85.

- (190) Stalder, R.; Mei, J.; Graham, K. R.; Estrada, L. A.; Reynolds, J. R. Isoindigo, a Versatile Electron-Deficient Unit for High-Performance Organic Electronics. *Chem. Mater.* **2014**, *26*, 664-678.
- (191) Wang, C.; Zhao, B.; Cao, Z.; Shen, P.; Tan, Z.; Li, X.; Tan, S. Enhanced Power Conversion Power Conversion Efficiencies in Bulk Heterojunction Solar Cells Based on Conjugated Polymer with Isoindigo Side Chain. *Chem. Commun.* **2013**, *49*, 3857-3859.
- (192) Liang, Y.; Xu, Z.; Xia, J.; Tsai, S. T.; Wu, Y.; Li, G.; Ray, C.; Yu, L. For the Bright Future-Bulk Heterojunction Polymer Solar Cells with Power Conversion Efficiency of 7.4%. *Adv. Energy Mater. Comm.* **2010**, *22*, 135-138.
- (193) Liu, J.; Li, X.; Zhang, S.; Ren, X.; Cheng, J.; Zhu, L.; Zhang, D.; Huo, L.; Hou, J.; Choy, W. C. H. Synergic effects of randomly aligned SWCNT mesh and self-assembled molecule layer for high-performance, low-bandgap, polymer solar cells with fast charge extraction. *Adv. Mater. Interfaces.* **2015**, *2*, 1-9.
- (194) Speller, E. M. The Significance of Fullerene Electron Acceptors in Organic Solar Cell Photo-Oxidation. *Mater. Sci. Tech.* **2017**, *33*, 924-933.
- (195) Larson, B. W.; Wiltaker, J. B.; Wang, X-B.; Popov, A. A.; Rumbles, G.; Kopidakis, N.; Strauss, S. H.; Boltalina. Electron Affinity of Phenyl-C₆₁-Butyric Acid Methyl Ester (PCBM). *J. Phys. Chem. C.* **2013**, *117*, 14958-14964.
- (196) Ryan, J. W.; Matsuo, Y. Increased Efficiency in Small Molecule Organic Solar Cells Through the Use of a 56- π Electron Acceptor- Methano Indene Fullerene. *Sci. Rep.* **2015**, *5*, 1-5.
- (197) Pensack, R. D.; Guo, C.; Vakhshouri, K.; Gomez, E. D.; Asbury, J. B. Influence of Acceptor Structure on Barriers to Charge Separation in Organic Photovoltaic Materials. *J. Phys. Chem. C.* **2012**, *116*, 4824-4831.
- (198) Liu, T.; Troisi, A. What Makes Fullerene Acceptors Special as Electron Acceptors in Organic Solar Cells and How to Replace Them. *Adv. Mater.* **2013**, *25*, 1038-1041.
- (199) Choutoulesi, E.; Mitzithra, C.; Hamilakis, S.; Kordatos, K.; Kollia, C.; Loizos, Z. Low-Cost Synthesis of Fullerene Derivatives. *Syn. Commun.* **2011**, *43*, 2042-2049.
- (200) Pavlovich, V. S.; Shpilevsky, E. M. Absorption and Fluorescence Spectra of C₆₀ Fullerene Concentrated Solutions in Hexane and Polystyrene at 77-300 K. *J. Appl. Spec.* **2010**, *77*, 335-342.
- (201) Wang, W.; Yan, C.; Lau, T-K.; Wang, J.; Liu, K.; Fan, Y.; Lu, X.; Zhang, X. Fused Hexacyclic Nonfullerene Acceptor with Strong Near-Infrared Absorption for Semitransparent Organic Solar Cells with 9.77% Efficiency. *Adv. Mater. Comm.* **2017**, *29*, 1-7.
- (202) Zhang, L.; Lin, B.; Ke, Z.; Chen, J.; Li, W.; Zhang, M.; Ma, W. A Universal Approach to Improve Electron Mobility without Significant Enlarging Phase Separation in IDT-based Non-Fullerene Acceptor Organic Solar Cells. *Nano Energy.* **2017**, *41*, 609-617.
- (203) Zhang, Z.; Li, M.; Liu, Y.; Zhang, J.; Feng, S.; Xu, X.; Song, J.; Bo, Z. Simultaneous Enhancement of the Molecular Planarity and the Solubility of Non-Fullerene Acceptors:

- Effect of Aliphatic Side-Chain Substitution on the Photovoltaic Performance. *J. Mater. Chem. A.* **2017**, *5*, 7776-7783.
- (204) Liu, X.; Ye, L.; Zhao, W.; Zhang, S.; Li, S.; Su, G. M.; Wang, C.; Ade, H.; Hou, J. Morphology Control Enables Thickness-Insensitive Efficient Nonfullerene Polymer Solar Cells. *Mater. Chem. Front.* **2017**, *1*, 2057-2064.
- (205) Ahmed, E.; Ren, G.; Kim, F. S.; Hollenbeck, E. C.; Jenekhe, S. A. Design of New Electron Acceptor Materials for Organic Photovoltaics: Synthesis, Electron Transport, Photophysics, and Photovoltaic Properties of Oligothiophene-Functionalized Naphthalene Diimides. *Chem. Mater.* **2011**, *23*, 4563-4577.
- (206) Wang, Y.-J.; Courtright, B. A.; Ferreira, A. S.; Tolbert, S. H.; Jenekhe, S. A. 7.7% Efficient All-Polymer Solar Cells. *Adv. Mater.* **2015**, *27*, 4578-84.
- (207) Yang, J.; Xiao, B.; Tajima, K.; Nakano, M.; Takimiya, K.; Tan, A.; Zhou, E. Comparison Among Perylene Diimide (PDI), Naphthalene Diimide (NDI), and Naphthodithiophene Diimide (NDTI) Based n-Type Polymers for All-Polymer Solar Cells Application. *Macromolecules.* **2017**, *50*, 3179-3185.
- (208) Guo, Y.; Li, Y.; Awartani, O.; Zhao, J.; Han, H.; Ade, H.; Zhao, D.; Yan, H. A Vinylene-Bridged Perylenediimide-Based Polymeric Acceptor Enabling Efficient All-Polymer Solar Cells Processed under Ambient Conditions. *Adv. Mater.* **2016**, *28*, 8483-8489.

Chapter 2

Experimental Theory and Techniques

2.1 Overview

The experimental theory and techniques used in this dissertation will be discussed. The experimental methods and experimental setups will be discussed. These techniques were used to investigate the linear and nonlinear properties of the organic light harvesting compounds. The understanding of these techniques will help in the elucidation and better understanding of the optical properties of the investigated compounds. Computational methods were utilized to complement the experimental techniques to better understand the underlying quantum mechanical properties responsible for the experimental results.

2.2 Steady-State Spectroscopy

Two steady-state techniques were used in these studies in order to investigate the fundamental linear spectroscopic properties of the light harvesting organic materials. The steady-state absorption was investigated with UV-VIS spectrophotometer and the steady-state emission was investigated with a fluorometer. Steady-state spectroscopy investigates the linear response of the light-matter interaction of materials. Steady-state spectroscopy investigates the long timescale averaged linear response of a material when irradiated with photons of the electromagnetic spectrum. The samples' steady-state spectroscopic properties were investigated with UV and visible light.

In UV-Vis absorption spectroscopy, the sample is irradiated with UV and visible light and the intensity of absorbed radiation by the sample is recorded as function of wavelength.¹

The samples in this study were investigated in the solution phase. The samples were dissolved in organic solvents. By dissolving the samples in organic solvent, the concentration of the solute can be uniformly controlled avoiding aggregation. The morphological properties and thickness of the solid state will not affect the intrinsic spectroscopic response of the sample.²⁻³ The solvent does not have a response to visible light and the UV response of the solvent can be subtracted from the sample-solvent response to give the response of the sample. Although steady-state absorption is “steady-state”, the steady-state absorption measures the transition from the ground state to the excited state by measuring how much light and which frequencies provide enough energy to promote an electron from the ground state of the molecule to excited state of the molecule.⁴ The absorption process is fast, it occurs over a few hundred femtoseconds, which is much faster than the detector can resolve.⁵⁻⁶ Thus, the detector response is an independent path function and only measures the absolute intensity change of the transmitted light without any time resolution.

The absorption process is dependent on the path length the light travels through the sample, the molar absorptivity coefficient, and the concentration of the sample in a given path length. These parameters are used to show the absorption per molecule. These parameters are described by the Beer-Lambert law which mathematically relates the absorption of light at a given wavelength, which is directly proportional to the concentration within the given path length, given in **Equation 2.2.1**.⁷

$$A = \log\left(\frac{I_0}{I}\right) = \epsilon \cdot l \cdot c \quad \text{Equation 2.2.1}$$

Where A is the absorption, I_0 is the initial intensity, I is the final intensity that reaches the detector after passing through the sample, ϵ is the molar absorptivity ($M^{-1}cm^{-1}$) which is the intrinsic property of how strongly a molecule absorbs light at a given wavelength, l is the path

length (cm) that the light travels through the sample, and c is the concentration (mol/l) within the path length. The concentration within the path length is considered the same concentration as the concentration of the solution due to uniform dispersion of the sample throughout the solution.

The molar absorptivity coefficient is a critical parameter for describing the absorption characteristics of organic light harvesting materials because it represents the absorbing strength of a molecule at a given wavelength.⁸ With typical molar absorptivity coefficients for conjugated light harvesting organic molecules are between 10^3 to $10^6 \text{ M}^{-1}\text{cm}^{-1}$.⁹⁻¹¹

The absorption per molecule can be represented with the one-photon absorption cross section, seen in **Equation 2.2.2**.¹²⁻¹³

$$\sigma = \frac{\alpha \cdot \epsilon \cdot c}{n} \quad \text{Equation 2.2.2}$$

Where α is the Napierian absorption coefficient which is equal to $\ln(10)$, ϵ is the molar extinction coefficient (molar absorptivity coefficient), c is the concentration (mol/l), and n is the number of absorbing molecules per centimeter cubed. An analogous term will be used to describe two-photon absorption cross-section in later sections.

The absorption was measured with an Agilent 8453 UV-visible spectrophotometer. The absorption data was collected with Agilent Chemstation software that was connected to the spectrophotometer. The spectrophotometer uses a deuterium-discharge lamp and tungsten lamp to irradiate the sample. The two lamp system provides light from ultraviolet wavelengths of the electromagnetic spectrum to infrared wavelengths of the electromagnetic spectrum (190 nm - 1100 nm). The light from the lamps is collimated by a source lens. The collimated light passes through the shutter or stray light filter into the sample located in the sample holder. 1 cm path length Starna Quartz cuvettes were used to hold the samples. Transmitted light is then

collimated by the spectrograph lens. The light then passes through a slit. The light is then dispersed onto the diode array via a holographic grating. This system can be seen in **Figure 2.2.1**.

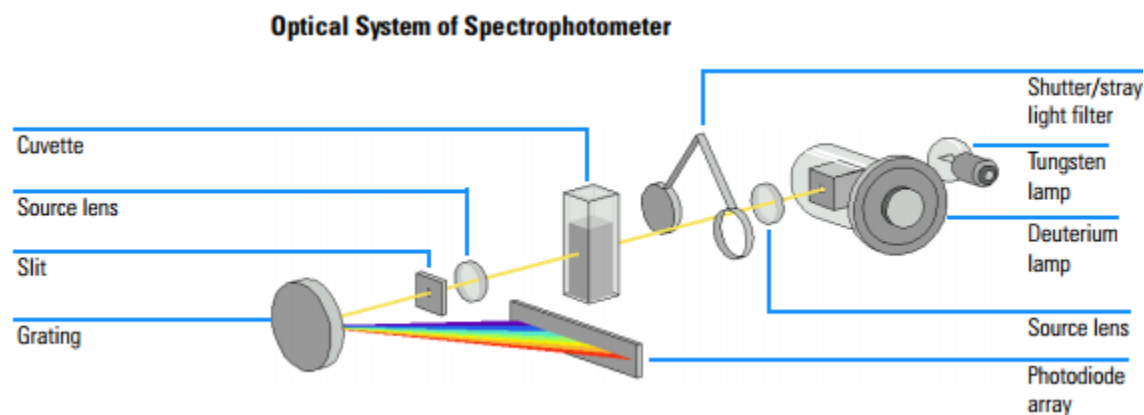


Figure 2.2.1. Agilent 8453 UV-Vis spectrophotometer schematic¹⁴

Ideally, all of the absorbed photons in light-harvesting would go into electricity generation, but this is not the case for most molecules because the energy from photons can be lost to other quantum processes like fluorescence. Steady-state emission spectroscopy is used to investigate the ratio of absorbed photons to emitted photons and the emitted photon's wavelength can give insight into other photophysical processes that may be taking place.¹⁵⁻¹⁷ The fluorescence intensity is given by **Equation 2.2.3**.

$$I_{flu} = I_0 \cdot \phi \cdot l \cdot \epsilon \cdot c \quad \text{Equation 2.2.3.}$$

Where I_{flu} is the fluorescence intensity, I_0 is the incident light intensity, ϕ is the quantum yield which will be discussed shortly, l is the path length (cm), ϵ is the molar absorptivity ($M^{-1}cm^{-1}$), and c is concentration in ($M=mol/L$). Most organic molecules have fluorescence lifetimes from femtoseconds to nanoseconds. Since absorption is much faster than fluorescence, the fluorescence steady state is reached almost instantly. Thus the steady-state fluorescence is proportional to the fluorescence lifetime of the molecule.

As discussed earlier, the absorption of a photon can lead to many different photophysical processes, which are accounted for by the quantum yield term in the fluorescence equation. The quantum yield is the ratio of the emitted photons to absorbed photons. The quantum yield can be described by **Equation 2.2.4**.

$$\phi = \frac{k_f}{k_f + k_i + k_{ec} + k_{ic} + k_{pd} + k_d} \quad \text{Equation 2.2.4.}$$

Where k_f is the fluorescence rate constant, k_i is the intersystem rate constant, k_{ec} is the external conversion rate constant, k_{ic} is the internal conversion rate, k_{pd} is the predissociation rate constant, and k_d is the dissociation rate constant. Thus the quantum yield is a critical parameter that can give insight of other photophysical processes.¹⁸⁻²⁰

The fluorescence quantum yields for the investigated compounds were determined by comparative methods. A standard with a well-known quantum yield and absorbs and emits in the same region as the sample being analyzed is chosen to determine quantum yield of the sample.²¹ The fluorescence quantum yield is calculated by **Equation 2.2.5**.

$$\Phi_{sam} = \Phi_{std} \cdot \left(\frac{Grad_{sam}}{Grad_{std}} \right) \cdot \left(\frac{\eta_{sam}}{\eta_{std}} \right)^2 \quad \text{Equation 2.2.5.}$$

Where sam denotes the sample, std denotes the standard, ϕ is the quantum yield, Grad is the gradient of the integrated fluorescence intensity versus the absorption, and η is the refractive index which accounts for of the solvent effects of the solvent used to make the solution.

The fluorescence spectrum measurement was done by Spex FluoroMax-2 fluorometer. The diagram can be seen in **Figure 2.2.2**. The data is recorded using DataMax software using a computer. The excitation source is a 150W continuous xenon lamp that is mounted vertically that produces light from 190 nm to 2000 nm. The light beam from the xenon lamp is focused on the entrance slit of an excitation spectrometer with an elliptical mirror. The

slit width is adjustable in order to avoid damaging the sample. Diffraction gratings in the excitation spectrometer allow single wavelength excitation of samples. A sample holder holds 1 cm path length Starna Quartz cuvettes. Fluorescence is measured by a photomultiplier tube (PMT) detector perpendicular to the excitation beam to eliminate scattering and signal from the excitation beam. The fluorescence from the samples enters the slits to an emission spectrometer. The slits can control how fluorescence reaches the detector in order to prevent saturating the detector or damaging the detector from strongly emissive species. Gratings in the emission spectrometer placed in front of the detector ensure efficient collection of each emission wavelength. The signal is then amplified by a photon counting amplifier which is then recorded by a computer.

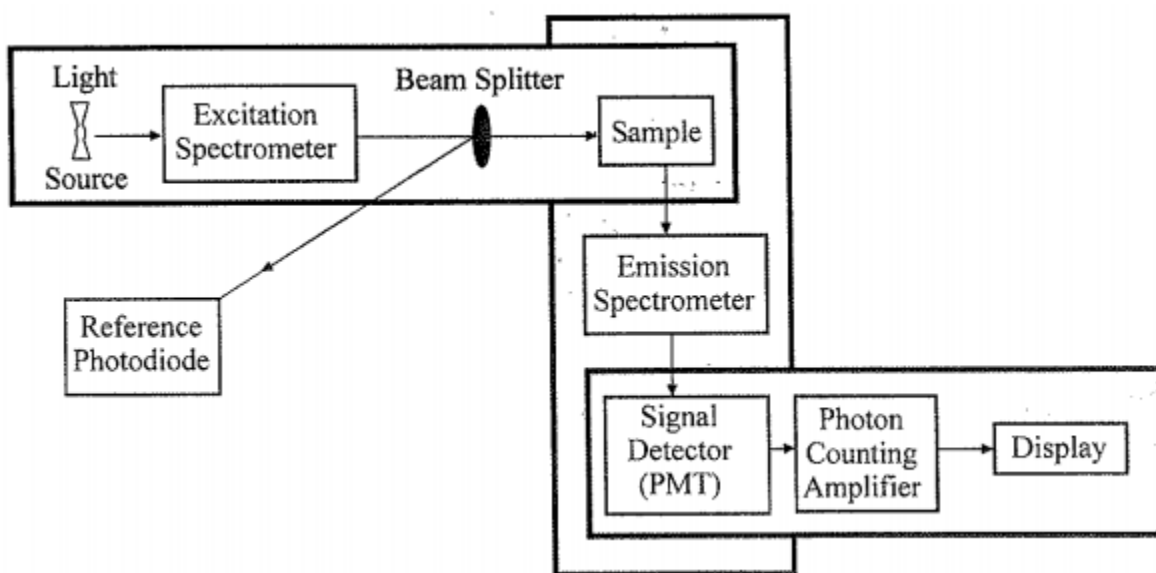


Figure 2.2.2. Fluoromax-2 schematic²²

2.3 Time-resolved fluorescence upconversion

The fluorescence lifetime of a molecule is the amount of time a molecule spends in the excited state before returning to the ground state and emitting a photon. The molecules in a solution are in the electronic ground state but in various rotational and vibrational energy states

which results in all of the molecules in a Boltzmann distribution of ground states.⁵ Thus the fluorescence lifetime constant represents when (1/e) (36.8%) of the molecules have returned to the ground state.²³ Organic molecules have fluorescence lifetimes from picoseconds to nanoseconds.²³ In order to investigate these fast lifetimes, a technique called fluorescence upconversion is used.

The time-resolved fluorescence experiments were performed using a fluorescence setup shown in **Figure 2.3.1**. The time-resolved fluorescence upconversion uses a diode pumped neodymium-doped yttrium vanadate (Nd:YVO₄) Millennia (Spectra Physics) continuous laser to generate a 532 nm beam of up to 5 W of power. The Millennia (Spectra Physics) pumps a Ti-sapphire Tsunami (Spectra Physics) which produces laser pulses of 110 fs between 790 to 810 nm of up to 800 mW at a repetition rate of 80 MHz. The Tsunami (Spectra Physics) generates the ultrafast pulses through a technique called passive mode-locking. The experiments used in these studies used an 800 nm beam. The 800 nm beam is directed into a FOG-100 (CDP inc) which is upconverted by a beta-barium borate (crystal) to produce a 400 nm beam. A beam splitter passes the fundamental 800 nm to an optical delay line and serves as an optical gate, and the 400 nm beam is reflected towards the sample in order to provide the excitation source. The sample is placed in a rotating sample holder with a path length of 1 mm containing two quartz lenses to prevent photodegradation. The fluorescence from the sample is then collected by focusing the emission and the residual 800 nm from the optical delay line on another BBO crystal, overlapping the two beams temporally and spatially and producing a sum frequency of the two beams. The sum frequency of the two beams is between 300 nm to 400 nm is then focused and directed into a monochromator where it is detected by a photomultiplier tube (PMT) (Hamamatsu R152P). The delay line can produce step sizes of ~6.25 femtoseconds resolution.

The experimental range of the delay line allows the fluorescence dynamics between 220 fs to 1 nanosecond to be resolved.

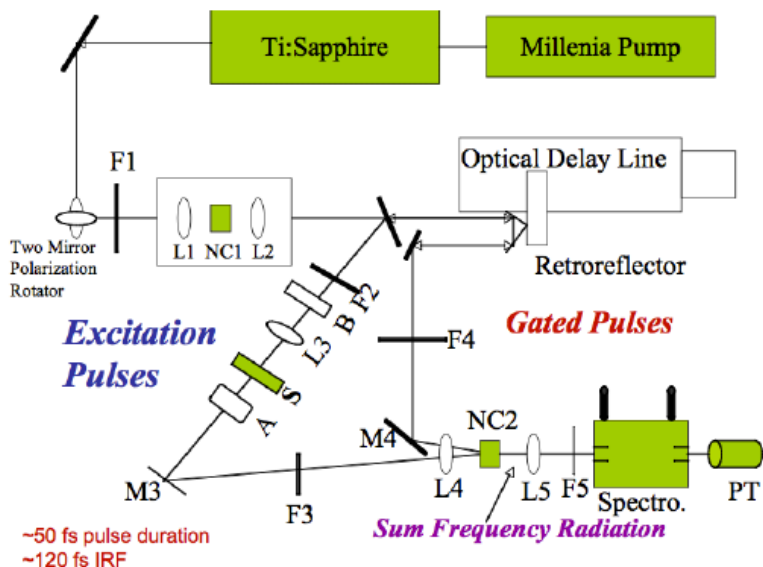


Figure 2.3.1. Fluorescence upconversion setup

The fluorescence upconversion setup can also be used to measure the fluorescence anisotropy of the investigated materials. Fluorescence anisotropy can give details on the rotational properties of a molecule or exciton dynamics in macromolecules.²⁴⁻²⁵ To conduct anisotropy measurements, a Berek compensator is used to control the polarization of the 400 nm beam that is used as the excitation source. The polarization of the 400 nm can be parallel polarized ($I_{//}$) or perpendicular polarized (I_{\perp}). In solution, the molecules are randomly orientated, so when excitation source is polarized in one direction, only molecules with absorption transition dipole parallel to the electric vector of the excitation source are excited. The anisotropy is calculated by **Equation 2.3.1.**

$$r(t) = \frac{I_{//} - g \cdot I_{\perp}}{I_{//} + 2g \cdot I_{\perp}} \quad \text{Equation 2.3.1.}$$

Where $r(t)$ is the fluorescence anisotropy at time t , $I_{//}$ is the parallel polarized light in respect to the laser polarization, I_{\perp} is the perpendicular polarized light in respect to the laser polarization, and g is the g factor which is used to correct for detector sensitivity of parallel polarized and perpendicular light.²⁶

The maximum initial anisotropy value that can be achieved for a two level system for a one-photon process is 0.4.²⁷ This happens when no depolarization from the excitation to the emission dipoles occurs. The initial anisotropy is calculated by **Equation 2.3.2**.

$$r = \frac{2}{5} \left(\frac{2\cos^2\theta - 1}{2} \right) \quad \text{Equation 2.3.2.}$$

Where r is the initial anisotropy, θ is the angle between the absorption and emission transition dipoles, and the constant of $2/5$ accounts for the transition probability.

2.4 Two-photon Absorption Spectroscopy

Two-photon absorption (TPA) is the simultaneous absorption of two photons with the same energy in order to excite a molecule from the ground state to the excited state. It is analogous to one photon absorption where a high energy photon is used to excite a molecule from the ground state to the excited state, whereas in two-photon absorption, two lower energy photons are used to excite a molecule from the ground state to the excited state.²⁸ Due to the simultaneous absorption of two photons, two-photon absorption quadratically is dependent on the intensity of the incident photon, whereas in one-photon absorption, a single photon is used to excite the molecule resulting in a linear dependence.²⁹ One of the benefits of TPA is that only a small portion of the sample is excited, at the focus of the beam. The phenomenon of TPA was theorized by Maria Goeppert-Mayer in 1931, but the experimental validation of TPA theory did not occur until the invention of high intensity lasers thirty years later.³⁰⁻³¹ Two different types of laser setups were used for these studies, one using a pulsed femtosecond laser and the other using

a pulsed nanosecond laser. Both laser setups used the TPEF method, which will be described later, to determine the TPA properties of the investigated materials.

In order to determine the TPA properties for the investigated compounds the TPEF method was utilized. The TPA cross-section can be determined by using the TPEF method by **Equation 2.4.1.**³²

$$F(t) = \frac{1}{2} \eta \delta [c] n \frac{g_p}{\pi f \lambda \tau} \phi \langle P(t) \rangle^2 \quad \text{Equation 2.4.1.}$$

Where $F(t)$ is the fluorescence photons collected per second, η is quantum yield, δ is the TPA cross-section for the sample, $[c]$ is the concentration, n is the refractive index of the solvent, g_p is the shape factor of the pulsed laser (0.66 for Gaussian shape), f is the frequency of the laser, λ is the excitation wavelength, τ is the pulse durations, ϕ is the collection efficiency, and $\langle P(t) \rangle$ is the input intensity. Since the same laser system is used for each sample in each study, the laser parameters can be neglected. The collection efficiency can be neglected if a standard is used that has known TPA cross-section and quantum yield. The logarithm of both sides can be taken to give **Equation 2.4.2.**

$$\log[F(t)] = 2 \log[\langle P(t) \rangle] + \log \left[\frac{1}{2} \eta \delta [c] n \frac{g_p}{\pi f \lambda \tau} \phi \right] \quad \text{Equation 2.4.2.}$$

The last term will be a constant. Therefore, the logarithm plot of the fluorescence intensity is proportional to 2 times the power plus a term that takes into account the experimental parameters. The values for the standard and sample can be substituted in the above equation to obtain **Equation 2.4.3.**

$$\log[F(t)_{samp}] - b_{samp} = \log[F(t)_{std}] - b_{std}; \quad b = \log \left[\frac{1}{2} \eta \delta [c] n \frac{g_p}{\pi f \lambda \tau} \phi \right] \quad \text{Equation 2.4.3.}$$

The relationship between the standard and sample can be established. It is important to note the b in **Equation 2.4.3** can be ascribed to the y-intercept. **Equation 2.4.3** is further manipulated to give **Equation 2.4.4**.

$$\log[F(t)_{samp}] - \log[F(t)_{std}] = b_{samp} - b_{std} \quad \text{Equation 2.4.4.}$$

With a little more manipulation the above equation can be used to solve for the two-photon absorption cross-section of the sample to give **Equation 2.4.5**.

$$\delta_{samp} = \frac{10^{(b_{samp}-b_{std})} \cdot \delta_{std} \eta_{std} [c]_{std} n_{std}}{\eta_{samp} [c]_{samp} n_{samp}} \quad \text{Equation 2.4.5.}$$

Where the quantum yields of the sample and standard, concentrations of the samples and standard, and refractive index of the solvents can easily be determined. The y-intercept or b value is determined by plotting the log-log plot of the fluorescence intensity versus power.

The ultrafast TPEF setup consists of diode-pumped Mai Tai (Spectra Physics) mode-locked pulsed Ti:sapphire laser that produces 100 fs pulses from 700nm- 980 nm of up to 2W at a repetition rate of 80 MHz. This can be used as the excitation source for the TPA experiments or the wavelength output from the Mai Tai can be extended by pumping a synchronously pumped parametric oscillator (OPO) (OPAL) with the output beam from Mai-Tai. The OPAL is capable of delivering tunable femtosecond pulses from 1100 nm to 1400 nm of 130 fs with up to 600 mw power. The beam is directed through a variable neutral density wheel that controls the power of the excitation beam for the experiment. An optical glass is used to direct about 10% of the incident beam into a high-speed silicon photodiode connected to a multimeter which gives connects to the computer interface in order for the intensity to be recorded as a function of voltage which can be calibrated to power in milliwatts. The beam is directed and focused onto a sample. The fluorescence is collected at a right angle to the excitation beam to avoid interference from the excitation beam. The monochromator is placed in front of a PMT to select

the fluorescence wavelength of interest which is then detected by a photomultiplier tube (R152P, Hamamatsu) connected to a computer via a photon-counting unit. The schematic can be seen in **Figure 2.4.1**.

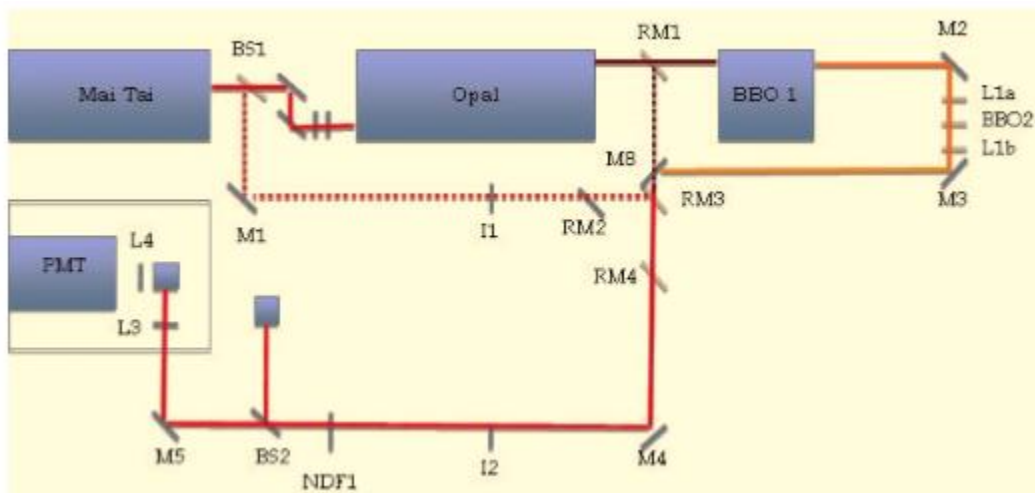


Figure 2.4.1. Ultrafast TPEF Setup

2.5 Transient absorption spectroscopy

Transient absorption (TA) spectroscopy is one of the most powerful spectroscopic techniques. TA spectroscopy is a pump-probe technique that investigates the chemical excited state dynamics. Steady-state spectroscopy can give information on the final state or initial state of the molecule, but does not give any information on intermediate processes. Fluorescence upconversion spectroscopy can give information on the fluorescence decay dynamics, but no information on the absorption process. TPA spectroscopy gives insight on the transition dipoles, but it is also a steady state technique as well. TA spectroscopy can give great insight on the excited state of the investigated materials. It can give insight into the absorption and emission properties, dark states, chemical species involved in transitions, vibrational cooling, bleach recovery, and singlet to triplet conversion.³³

TA spectroscopy uses a monochromatic ultrafast pulse ($\sim 120\text{fs}$) to excite the molecule (pump), and a pulsed white light continuum from 450-750 nm is used to probe the excited state. The white light continuum probe is time-delayed with respect to the pump pulse. The absorption measured by the probe is subtracted from the steady state absorption spectrum which produces a spectrum of the change in absorption ΔA versus time and wavelength. The pump excites the sample from the S_0 ground state to the first excited S_1 state, after a time delay the probe beams excites the molecule while it is in its S_1 state to S_n state, seen in **Figure 2.5.1**.

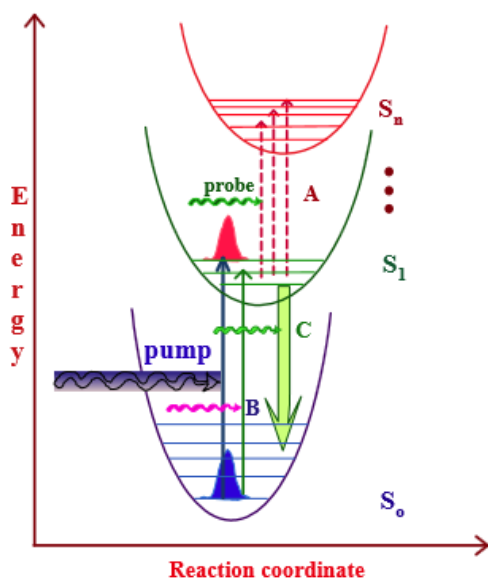


Figure 2.5.1. Pump-probe concept used in transient absorption spectroscopy. A is excited state absorption, B is a bleach state, and C is stimulated emission.

Upon excitation by the pump beam, the molecule can be excited to other higher excited states, which is called an Excited State Absorption (ESA) represented by a positive signal in the ΔA . Upon excitation by the pump beam, the ground state is partially depopulated and some of the molecules are promoted to the excited state. The ground state absorption signal disappears because there are fewer molecules in the ground state to excite to the excited state. This is called a ground state bleach (GSB) and signal becomes negative ($-\Delta A$). When the interaction of the

probe pulse with the excited molecule stimulates the repopulation of the ground state via emission of a photon, Stimulated Emission (SE) occurs, and the signal becomes negative ($-\Delta A$). The photons emitted by the molecules have exactly the same polarization, direction and wavelength as the photons that caused the molecules to drop from the excited to the ground state, thus it appears as a negative signal

The TA system uses diode pumped neodymium-doped yttrium vanadate (Nd:YVO₄) Millennia (Spectra Physics) continuous laser to generate a 532 nm beam of up to 5 W of power. The Millennia (Spectra Physics) pumps a Ti-sapphire Tsunami (Spectra Physics) which produces laser pulses of 20 fs between 790 to 810 nm of up to 300 mW at a repetition rate of 100 MHz. The Tsunami (Spectra Physics) generates the ultrafast pulses through a technique called passive mode-locking. The experiments used in these studies used an 800 nm beam as a seed beam. The pulse energy of the seed beam is a few nanoJoules. The seed pulses are amplified inside a regenerative amplifier (Spitfire Pro, Spectra Physics) in three stages. The first stage stretches the seed pulse. A retroreflecting mirror assembly slows the shorter end (blue) of the spectral pulse relative to the longer part of the spectral pulse (red). This results in a negative Group Velocity Dispersion (GVD) stretching the pulse temporally. Then the temporally stretched pulse is regenerative amplified. A Ti:Sapphire crystal is pumped by a 532 nm Nd: YLF laser (Empower, Spectra Physics) at 7.5W. This causes a population inversion of the gain medium. The stretched seed pulse then is injected into resonator via a Pockels cell. After a single pass through the crystal, the pulse energy of the seed is amplified by a factor of 3 to 4. But in order to get sufficient gain for the stretched pulse, the pulse is passed multiple times through the gain before the pulse energy level is high enough to eliminate the population inversion of the gain medium. Another Pockels cell allows the amplified stretched pulse to exit the resonator. The final step is

pulse compression. A retroreflecting mirror assembly slows the long end (red) of the spectral pulse relative to the shorter part of the spectral pulse (blue). Compressing the pulse back into a 130 fs pulse. The resulting output from the amplifier is at 800nm, 1 kHz, and ~100 fs pulse width with an average power of 800 mW. With a pulse energy on the order of microJoules.

The amplified output is split by a beam splitter. 20% of the pulse is directed into the Helios (Ultrafast systems) for white light generation probe beam, while 80% of the beam is directed into the Optical Parametric Amplifier (OPA, Spectra Physics). The OPA output is used as the pump beam for the experiment. The OPA uses various nonlinear frequency conversion processes to achieve a spectral range from 350 nm to 2000 nm. Inside the OPA, the beam from the amplifier is further split into two separate beams. One beam is used for white light generation and the other is used for optical parametric generation (preamp). The white light is generated by a Ti:Sapphire plate and is focused onto the main BBO Crystal (BBO1). Optical parametric generation (OPG) is used to amplify a specific wavelength of the white light inside BBO1. The preamp beam passes through a delay stage before arriving at BBO1. The pre-amp beam spatially and temporally overlaps the white light on BBO1 which produces a signal and idler beam. The signal is removed using dichroic mirrors and the returning idler beam is overlapped spatially and temporally with remaining 85% of the original 800 nm beam resulting in amplification of the idler beam. The residual 800 nm beam is dumped using a dichroic mirror. The idler beam is then passed through BBO2 and BBO3, where a spectral range of 300 nm to 2000 nm is generated by controlling the angles of BBOs.

The Helios unit, which generates the white light continuum probe, uses the output beam from the amplifier and directed into the optical delay line. The pulse is focused onto a Ti:Sapphire plate after the delay line to generate the white light continuum (450 nm to 750 nm)

probe. The probe beam is time delayed from the excitation beam with a computer controlled optical delay line. The white light is then overlapped with the pump beam in a 2 mm quartz cuvette containing the sample, the change in absorption of the probe light is collected by a CCD detector (Ocean optics 2000). Data acquisition is controlled by the software from Ultrafast Systems Inc. Typical power of the probe beam is $\sim 10 \text{ J/cm}^2$ while the pump beam is $\sim 1000 \text{ J/cm}^2$. Magic angle polarization is maintained between the pump and probe beam using a waveplate in order to avoid anisotropy contributions due to polarization. The sample is stirred with a rotating magnetic stirrer to prevent degradation. A diagram of the setup can be seen in **Figure 2.5.2.**

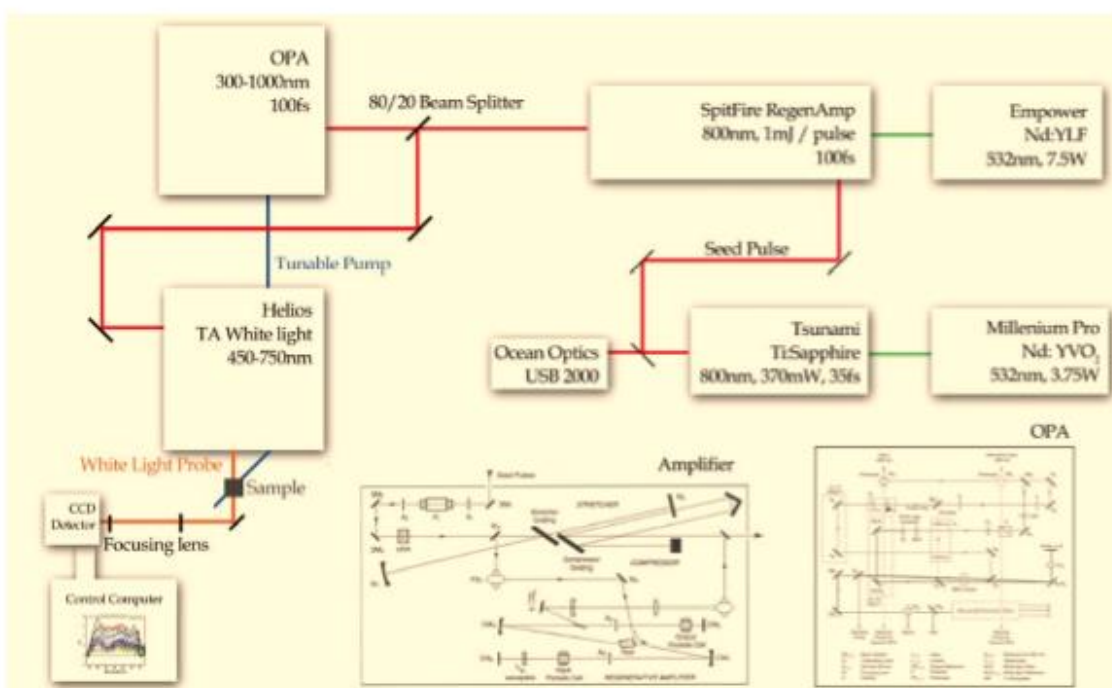


Figure 2.5.2. Ultrafast transient absorption setup.

2.6 Computational methods

In these studies, computational methods were used to elucidate the molecular structures responsible for the molecular processes in the optical experiments. The complex electronic

structures are too complex to find a closed form solution, so numerical methods must be used in order to determine the molecular orbitals that are reasonable for the molecular structures and optical properties.³⁴ Computational methods are rapidly becoming more popular and solving more complex problems because of rapid development in the computational theory and technology. Computer memory, speed, multiprocessing, threading, and improvements in computer theory have all led to this popularity. Computational methods were used to investigate the electronic structures, energy levels, excited state structures, ground state structures, and effects of polymerization. Although, there have been massive improvements in computational methods, it has still been difficult to perform accurate computations for large macromolecules.³⁵ For the large structures in these studies, the monomer and oligomers electronic structures were calculated and the extrapolated to the polymer case.

A computational investigation into the structural and electronic properties of the investigated polymers were carried out using Density Functional Theory (DFT) and Time Dependent Density Functional Theory (TDDFT) using GAMESS suite of programs. The B3LYP level of theory was used to calculate the geometry and orbital energy levels of monomer, dimer, trimer, and tetramer in order to approximate the geometry and orbital energy levels for the investigated conjugated polymers. B3LYP is a hybrid functional that uses Becke's 3 parameter(B3) exchange correlation functional which uses 3 parameters to mix in the exact Hartree-Fock exchange correlation and the Lee Yang and Parr(LYP) correlation functional that recovers dynamic electron correlation.³⁶ B3LYP has been used extensively in computational chemistry to describe geometry and orbital energy levels and has produced comparable orbital energy levels to experimentally obtained orbital energy levels.³⁷ It is particularly useful for donor acceptor polymers because of its ability to describe conjugation effects. Another hybrid

functional was also employed, wB97x-D, to compare the two levels of theory with split valence 6-31G(d) basis set. wB97x-D is a meta-GGA DFT functional that includes the second derivative of the electron density and contains empirical dispersion terms and long-range corrections to approximate the geometry and orbital energy levels.³⁸ Frequency calculations were also performed in order to ensure the minimum of the potential energy surface for the optimized ground state geometry at the same level of theory. Then excited state geometries and orbital energy levels were then performed by using TDDFT using the same level of theory. Absorption, emission, and TPA cross sections were then calculated using the same level of theory. The two levels of theory were then compared to orbital energy levels determined by cyclic voltammetry (CV).

References

- (1) Aljamali, N. M. Review in (NMR and UV-Vis) Spectra. *Int. J. Med. Res. Pharm. Sci.* **2015**, *2*, 28-36.
- (2) Gaudin, O. P. M.; Samuel, I. D. W.; Amriou, S.; Burn, P. L. Thickness Dependent Absorption Spectra in Conjugated Polymers: Morphology or Interference. *Appl. Phys. Lett.* **2010**, *96*, 1-3.
- (3) Amrutha, S. R.; Jayakannan, M. Probing the π -Stacking Induced Molecular Aggregation in π -Conjugated Polymers, Oligomers, and Their Blends of p-Phenylenevinylenes. *J. Phys. Chem. B.* **2008**, *112*, 1119-1129.
- (4) Kuhn, H. A Quantum-Mechanical Theory of Light Absorption of Organic Dyes and Similar Compounds. *J. Chem. Phys.* **1949**, *17*, 1198-1212.
- (5) Strickler, S. J.; Berg, R. A. Relationship between Absorption Intensity and Fluorescence Lifetime of Molecules. *J. Chem. Phys.* **1962**, *37*, 814-822.
- (6) Chen, Q.; Yang, J. W.; Osinsky, A.; Gangopadhyaya, S.; Lim, B.; Anwar, M. Z.; Khan, M. A.; Kusenkov, D.; Temkin, H. Schottky Barrier Detectors on GaN for Visible-Blind Ultraviolet Detection. *Appl. Phys. Lett.* **1997**, *70*, 2277-2279.
- (7) Swinehart, D. F. The Beer-Lambert Law. *J. Chem. Educ.* **1962**, *39*, 333-335.
- (8) Shalhoub, G. M. Visible Spectra Conjugated Dyes: Integrating Quantum Chemical Concepts with Experimental Data. *J. Chem. Educ.* **1997**, *74*, 1317-1319.
- (9) Lee, Y.; Jo, A.; Park, S. B. Rational Improvement of Molar Absorptivity Guided by Oscillator Strength: A Case Study with Furoindolizine-Based Core Skeleton. *Angew. Chem.* **2015**, *127*, 15915-15919.

- (10) Liu, X.; Xu, Z.; Cole, J. M. Molecular Design of UV-vis Absorption and Emission Properties in Organic Fluorophores: Toward Larger Bathochromic Shifts, Enhanced Molar Extinction Coefficients, and Greater Stokes Shifts. *J. Phys. Chem. C*. **2013**, *117*, 16584-16595.
- (11) Vezie, M. S.; Few, S.; Meager, I.; Pieridou, G.; Dorling, B.; Ashraf, R.; Goni, A. R.; Bronstein, H.; McCulloch, I.; Hayes S. C.; Campoy-Quiles, M.; Nelson, J. Exploring the Origin of High Optical Absorption in Conjugated Polymers. *Nature Mater.* **2016**, *15*, 746-753.
- (12) Day, P. N.; Nguyen, K. A.; Pachter, R.; Calculation of One-Photon and Two-Photon Absorption Spectra of Porphyrins Using Time-Dependent Density Functional Theory. *J. Chem. Theory Comput.* **2008**, *4*, 1094-1106.
- (13) Gagliardi, S.; Falconieri, M. Experimental Determination of the Light-Trapping-Induced Absorption Enhancement Factor in DSSC Photoanodes. *J. Nanotechnol.* **2015**, *6*, 886-892.
- (14) Agilent 8453 UV-visible Spectroscopy System Service Manual.
- (15) Hedley, G. J.; Ruseckas, A.; Samuel, D. W. Light Harvesting for Organic Photovoltaics. *Chem. Rev.* **2017**, *117*, 796-837.
- (16) Birks, J. B.; Dyson, D. J. The Relations between the Fluorescence and Absorption Properties of Organic Molecules. *Proc. R. Soc. A.* **1963**, *275*, 135-148.
- (17) Ware, W. R.; Baldwin, B. A. Absorption Intensity and Fluorescence Lifetimes of Molecules. *J. Chem. Phys.* **1964**, *40*, 1703-1705.
- (18) Resch-Genger, U.; Rurack, K. Determination of the Photoluminescence Quantum Yield of Dilute Dye Solutions (IUPAC Technical Report). *Pure Appl. Chem.* **2013**, *85*, 2005-2026.
- (19) Birks, J. B. Fluorescence Quantum Yield Measurements. *J. Res. Natl. Bur. Stand.* **1976**, *80*, 389-399.
- (20) Ni, T.; Melton, L. A. Two-Dimensional Gas-Phase Temperature Measurements Using Fluorescence Lifetime Imaging. *Appl. Spectrosc.* **1996**, *50*, 1112-1116.
- (21) Parker, C. A.; Rees, W. T. Correction of Fluorescence Spectra and Measurement of Fluorescence Quantum Efficiency. *Analyst.* **1960**, *85*, 587-600.
- (22) FluoroMax-2 Manual.
- (23) Berezin, M. Y.; Achilefu, S. Fluorescence Lifetime Measurements and Biological Imaging. *Cehm. Rev.* **2010**, *110*, 2641-2684.
- (24) Montilla, F.; Frutos, L. M.; Mateo, C. R.; Mallavia, R. Fluorescence Emission Anisotropy Coupled ot an Electrochemical System: Study of Exciton Dynamics in Conjugated Polymers. *J. Phys. Chem. C*. **2007**, *111*, 18405-18410.
- (25) Rusinova, E.; Tretyachenko-Ladokhina, V.; Vele, E. O.; Seneor, D. F.; Ross, J. B. A. Alexa and Oregon Green Dyes as Fluorescence Anisotropy Probes for Measuring Protein-Protein and Protein-Nucleic Acid Interactions. *Anal. Biochem.* **2002**, *308*, 18-25.

- (26) Canet, D.; Doering, K.; Dobson, C. M.; Dupont, Y. High-Sensitivity Fluorescence Anisotropy Detection of Protein-Folding Events: Application to α -Lactalbumin. *Biophys. J.* **2001**, *80*, 1996-2003.
- (27) Siegel, J.; Suhling, K.; Leveque-Fort, S.; Webb, S. E. D.; Davis, D. M.; Phillips, D.; Sabharwal, Y.; French, P. M. W. Wide-Field Time-Resolved Fluorescence Anisotropy Imaging (TR-FAIM): Imaging the Rotation Mobility of a Fluorophore. *Rev. Sci. Instrum.* **2003**, *74*, 182-192.
- (28) Svoboda, K.; Yasuda, R. Principles of Two-Photon Excitation Microscopy and Its Applications to Neuroscience. *Neuron.* **2006**, *50*, 823-839.
- (29) Rumi, M.; Perry, J. W. Two-Photon Absorption: An Overview of Measurements and Principles. *Adv. Opt. Photonics.* **2010**, *2*, 451-518.
- (30) Goppert-Mayer, von M. Uber Elementarakte Mit Xwei Quantensprungen. **1931**, *114*.
- (31) Kaiser, W.; Garrett, C. G. B. Two-Photon Excitation in CaF₂:Eu²⁺. *Phys. Rev. Lett.* **1961**, *7*, 229-232.
- (32) Xu, C.; Webb, W. W. Measurement of Two-Photon Excitation Cross Sections of Molecular Fluorophores with Data From 690 to 1050 nm. *J. Opt. Soc. Am. B.* **1996**, *13*, 481-491.
- (33) Berera, R.; van Grondelle, R.; Kennis, J. T. M. Ultrafast Transient Absorption Spectroscopy: Principles and Application to Photosynthetic Systems. *Photosynth. Res.* **2009**, *101*, 105-118.
- (34) Saad, Y.; Chelikowsky, J. R.; Shontz, S. Numerical Methods for Electronic Structure Calculations of Materials. *SIAM Rev.* **2010**, *52*, 3-54.
- (35) Hofer, T. S. From Macromolecules to Electrons-Grand Challenges in Theoretical and Computational Chemistry. *Front. Chem.* **2013**, *1*, 1-4.
- (36) Peverati, R.; Truhlar, D. G. Quest for a Universal Density Functional: The Accuracy of Density Functionals across a Broad Spectrum of Databases in Chemistry and Physics. *Phil. Trans. R. Soc. A.* **2014**, *372*, 1-52.
- (37) Tirado-Rives, J.; Jorgensen, W. L. Performance of B3LYP Density Functional Methods for a Large Set of Organic Molecules. *J. Chem. Theory Comput.* **2008**, *4*, 297-306.
- (38) Salzner, U.; Aydin, A. Improved Prediction of Properties of π -Conjugated Oligomers with Range-Separated Hybrid Density Functionals. *J. Chem. Theory Comput.* **2011**, *7*, 2568-2583.

Chapter 3

Ultrafast Spectroscopic Study of Donor-Acceptor Benzodithiophene Light Harvesting Organic Conjugated Polymers

The work in this chapter was accepted in the Journal of Physical Chemistry C (JPC) with the title:

“Ultrafast Spectroscopic Study of Donor-Acceptor Benzodithiophene Light Harvesting Organic Conjugated Polymers”

Bradley Keller, Alan McLean, Bong-Gi Kim, Kyeongwoon Chung, Jinsang Kim, Theodore Goodson III

Modifications were made to the manuscript to adapt it to the style of this dissertation. References and supporting information of the manuscript are included in this chapter.

3.1 Abstract

New light harvesting organic conjugated polymers containing 4,8-bis(2-ethylhexyloxy)benzo[1,2-b;3,4-b']dithiophene(BDT) donor groups and thiophene with various electron-withdrawing acceptor groups were investigated. Also investigated was poly[[4,8-bis[(2-ethylhexyl)oxy]benzo[1,2-b:4,5-b']dithiophene-2,6-diyl][3-fluoro-2-[(2-ethylhexyl)carbonyl]thieno[3,4-b]thiophenediyl]] (PTB7), which is one of the most efficient photovoltaic conjugated polymers. In this study, the steady state absorption, steady state emission, ultrafast fluorescent decay dynamics and nonlinear optical properties of these light harvesting conjugated polymers were probed in solution. All of the conjugated polymers investigated have significant absorption over much of the visible spectrum due to small bandgaps

due to low lying LUMO energies created by the electron-withdrawing groups.

Fluorescence upconversion studies on the conjugated polymers showed short decay dynamics for conjugated polymers with strong electron-withdrawing groups. Two-photon absorption spectroscopy showed large two-photon absorption cross-sections for the conjugated polymers with strong electron-withdrawing acceptors. Fluorescence decay anisotropy studies also showed short exciton migrations for the conjugated polymers with stronger electron-withdrawing acceptors.

3.2 Introduction

Increasing energy costs due to increasing globalization and energy consumption has led to the economic viability of alternative energy sources.¹⁻⁴ Solar energy harvesting has become an increasingly more viable method for power generation due to rising fossil fuel prices.⁵⁻⁷ Solar energy harvesting is cleaner, greener, and renewable, unlike fossil fuels which are traditionally used for power generation.⁸⁻¹⁰ With 43% of the power of sunlight in the visible region, it is advantageous to design photovoltaic materials that absorb photons in this region for maximum power generation.^{11,12} A significant portion of that power reaches the surface of the earth as visible light, with a maximum photon flux around 700 nm.¹³ Thus, it is imperative to develop efficient photovoltaic materials that can convert solar energy into useable energy.

Conjugated polymers have garnered great interest for applications in organic photovoltaic (OPV) materials. OPV materials are flexible, light weight, easily processed, low cost in processing, and an abundance of raw materials make them ideal candidates for solar energy conversion compared to their inorganic counterparts.¹⁴⁻¹⁶ OPVs have high thermal stability and are readily formed into thin films, making them ideal for many photovoltaic applications.^{17,18} Unfortunately, OPV devices reported so far have low power conversion efficiency compared to their inorganic

counterparts.¹⁹ Current OPVs have only reached slightly over 10.5% power conversion efficiency(PCE) in tandem solar cells of P3HT:CBAPDTP-PC₆₁BM, but the PCE of OPVs are rapidly improving.^{20,21}

One particular promising class of OPVs is donor-acceptor(DA) polymers. These conjugated polymers are composed of an electron rich donor subunit and an electron deficient acceptor subunit covalently linked. The design of these conjugated polymers focuses on tuning the optical bandgap of the conjugated polymer in order to maximize the collection of solar photons.²² Tuning of the bandgap is accomplished by orbital mixing of the electron rich donor subunit and the electron deficient subunit maximizes the open-circuit voltage for devices. Modulation of the energy levels can be accomplished by attaching electron-withdrawing groups to the acceptor subunit or attaching electron-donating groups to the donor subunit.²³ The donor and acceptor motif can also result in higher conjugation length, which allows the polymer to adopt a more planar structure, which leads to higher electron delocalization along the conjugated polymer backbone.²²

Current interest is focused on DA polymers that use thieno[3,4-b]thiophene(TT) electron-withdrawing subunits and benzodithiophene(BDT) electron-donating subunits. Thiophene based polymers have shown to efficiently generate charge carriers.²⁴ Thiophene based oligomers absorb near 400 nm and there is a shift in absorption with increasing conjugation and increasing strength of electron-withdrawing groups.²⁵ Thiophene based dendrimers have also shown interesting spectroscopic properties such as high two-photon absorption cross-sections indicating good charge transfer characteristics.²⁶⁻²⁸ The HOMO and LUMO levels of the polymers can be modulated by introducing electron-withdrawing groups on the acceptor TT subunit and electron-donating groups on the BDT donating subunit which has been shown in other conjugated

systems.²⁹ One of the leading BDT-TT D-A polymer, poly[[4,8-bis[(2-benzo[2-ethylhexyl)oxy]benzo[1,2-b:4,5-b']dithiophene-2,6-diyl][3-fluoro-2-[(2-ethylhexyl)carbonyl]thieno[3,4-b]thiophenediyl]] (PTB7), has a PCE of 9.2% which is a significant increase compared to P3HT devices and gets much closer to commercial viability.³⁰ The high PCE of PTB7 can be attributed to the low-lying HOMO and LUMO levels, good absorption in the visible spectrum, small bandgap, and good interfacial interaction with PC₆₁BM.³⁰ The increase in PCE is also attributed to the electron-withdrawing effect of the ester and fluorine group on the TT subunit, which enhances the dipole moment of PTB7.³¹ The increased dipole moment results in an increase in charge transfer in PTB7.

The donor monomers in D-A polymers also influence the properties of the D-A polymer. The HOMO level of the D-A is close to the HOMO level of the donor acceptor group.²² Designing strong electron-donating monomers is important for charge dissociation, although too strong of a donor can result in low ionization potentials which can lead to oxidative doping and decreased efficiency.³² Donor monomers also must have great hole mobility in order to have efficient charge separation and to prevent hole-electron annihilation.³³ Increasing the conjugation of the donor system has also shown to increase PCE for benzodithiophenes based donor systems.³⁴ Increasing the conjugation of the donor system allows the hole to delocalize which lowers the local charge density which decreases the Coulombic attraction between the electron and the hole of the conjugated polymer. Benzodithiophenes are also good choice for donor systems because they adopt conjugated planar structures and small steric hindrance between adjacent repeating units which is important for charge carrier mobility.³⁴⁻³⁶

In this work, we present the results of a spectroscopic study of PBTCT, PBT8PT, PBTT17T, and PBTfDO donor acceptor polymers in solution. These conjugated donor acceptor

polymers have a BDT donor and thiophene acceptor with various electron-withdrawing groups. The results of the spectroscopic studies of these new conjugated polymers are compared to those of PTB7, which is one of the most efficient BDT-TT conjugated donor acceptor polymers. These polymers were designed to find a reliable strategy for achieving specific HOMO and LUMO energy level modulation via alternating donor-acceptor monomer units in order to increase PCE.²² In order to understand the photophysical properties for efficient power generation in these donor acceptor polymers, the steady state fluorescence, steady state absorption, fluorescence anisotropy, two-photon absorption cross-section, and fluorescence decay excited state dynamics have been investigated in solution.

3.3 Experimental

3.3.1 Steady State UV-Vis and Emission Measurements

The steady state measurements and time resolved measurements of the samples were performed at room temperature in the solution state. Polymers were dissolved in 1,2-dichlorobenzene. Concentrations of 1.5×10^{-7} M to 3.0×10^{-5} were used for the measurements. The samples were placed in 4 mm quartz cuvettes. Steady state absorbance spectra were measured using an Agilent 8432 UV-visible absorption spectrophotometer. Steady state emission spectrum measurements were carried out with a Fluoromax-2 spectrophotometer. Absolute quantum yield of polymer films was measured by using QuantaMasterTM spectrofluorometer equipped with an integrating sphere.

3.3.2 Fluorescence Lifetime Measurements

The time-resolved fluorescence experiments were carried out using an ultrafast fluorescence set-up that has been previously described.³⁷⁻⁴⁰ A mode-locked Ti-sapphire femtosecond laser (Spectra-Physics Tsunami) was used to generate 80-fs pulses at 800 nm

wavelength with a repetition rate of 80 MHz. The Tsunami is pumped by a 532 nm continuous wave output laser (Spectra-Physics Millennia), which has neodymium-doped yttrium vanadate (Nd:YVO₄) gain medium. An excitation pulse of 400 nm was generated by accessing the second harmonic of a β -barium borate crystal and the residual 800 nm beam was made to pass through a computer-controlled motorized optical delay line. The polarization of the excitation beam was controlled by a berek compensator. The power of the excitation beam was 20 mW. The fluorescence emission by the sample was up-converted by a non-linear crystal of β -barium borate by using the residual 800 nm beam which had been delayed by the optical delay line with a gate step size of 6.25 fs giving temporal resolution. A monochromator is used to select the wavelength of the up-converted emission of interest and the selected emission is detected by a photomultiplier tube (R152P, Hamamatsu, Hamamatsu City, Japan). The photomultiplier tube converts the detected photons into photon counts by a voltage cascade which is read by a computer. Coumarin 153 and Cresyl violet dyes were used for aligning the laser. The instrument response function (IRF) has been determined from the Raman signal of water to have a pulse width at half max of 110 fs.³⁹ Lifetimes of fluorescence decay were obtained by fitting the fluorescence decay with multi-exponential decay functions convoluted with the IRF in MATLAB and Origin 8.

3.3.3 Two-Photon Absorption Measurements

Two-photon spectroscopy was performed using a mode-locked Ti:sapphire laser delivering 110 fs output pulses at a repetition rate of 80 MHz. Emission scans were performed at 800 nm excitation while scanning 525-700 nm emission. Two-photon spectroscopy was also performed using a mode-locked Ti:sapphire laser delivering 110 fs output pulses at a repetition rate of 80 MHz which pumps an Opal optical parametric oscillator (OPO) lithium borate (LBO)

crystal which allows for 1.3 μm and 1.5 μm output excitations. Emission scans were performed at 1300 nm excitation while scanning 600-900 nm emission. Two-photon power-dependent fluorescence intensity was utilized to determine two-photon absorption cross-section through the Two-photon emission fluorescence (TPEF) method.^{41,42} The TPEF setup utilized a Spectra-Physics Mai-Tai Diode-pumped Mode-Locked Ti:Sapphire laser which is tunable from 700 to 980 nm. A femtosecond synchronously pumped parametric oscillator (OPAL) laser was used in conjunction with the Mai-Tai laser in order to generate the 1300 nm excitation. The output pulses were less than 130 femtoseconds with a repetition rate of 80 MHz and an output power of 200 mW. Input power from the laser was varied using a variable neutral density filter. The emission detection wavelength during the power dependence scan was selected by the emission wavelength that produced the highest number of counts at 800 nm and 1300 nm excitation.

3.4 Results

3.4.1 Synthesis.

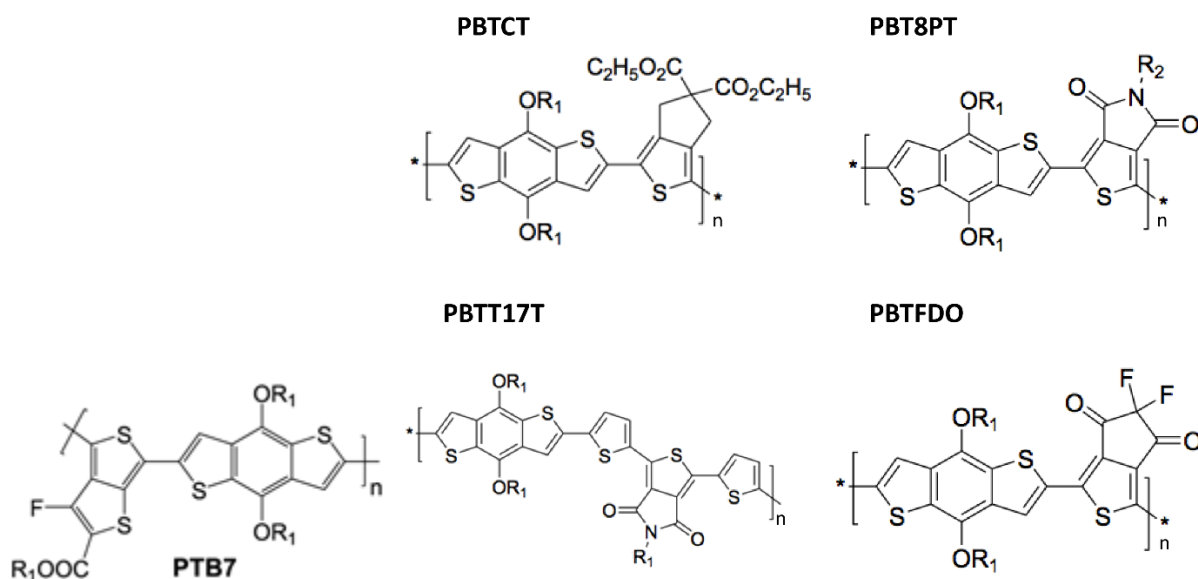
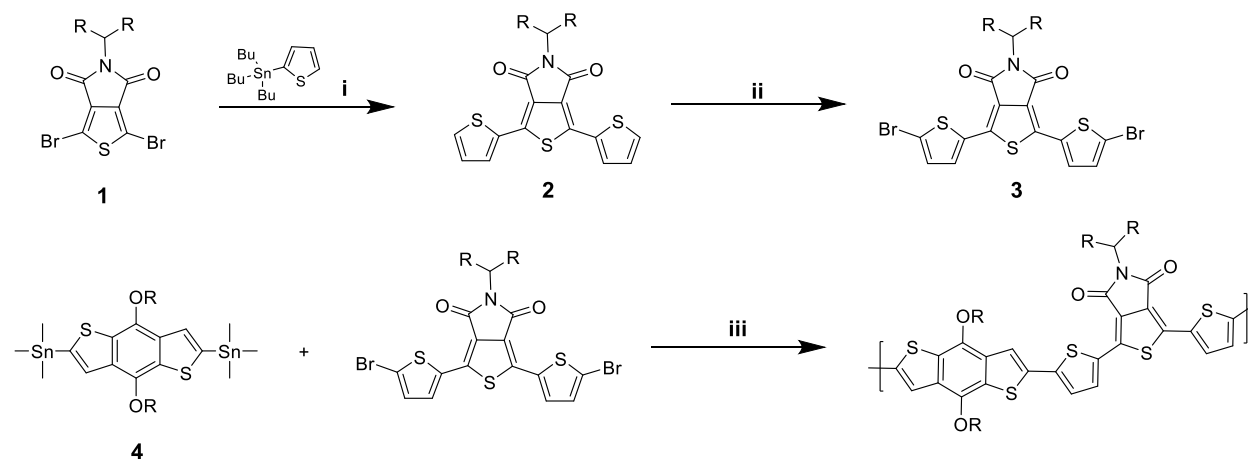


Figure 3.4.1. Investigated polymers. For PTB7, R_1 =2-ethylhexyl. For the other polymers, R_1 =2-ethylhexyl, and R_2 =4-octylphenyl. All starting materials were purchased from commercial supplier (Aldrich and Fisher Sci).²²



Scheme 3.4.1. Detailed synthetic scheme of PBTT17T. R indicates 2-ethylhexyl group, i) Pd(0), THF, reflux, 12 hours, ii) NBS, DMF, iii) Pd2(dba)₃, P(o-tolyl)₃, toluene, 110 °C, 48 hours.

Compound 2. Under Ar condition, compound **1** (1 g, 1.82 mmol) and 2-tributylstannyl thiophene (1.36 g, 3.0 eq) were dissolved into anhydrous THF. After adding

tetrakis(triphenylphosphine)palladium(0) (5 mol%), the mixture was heated up to 80 °C for 16 hours. Then, the mixture was poured into water and extracted with chloroform. The organic layer was dried with MgSO₄, and target compound (56 %) was obtained from column chromatography after elution with dichloromethane/n-hexane (1/2). ¹H-NMR (400MHz, CDCl₃) δ 8.09 (s, 2H), 7.46 (s, 2H), 7.18 (s, 2H), 4.22 (s, 1H), 2.14 (m, 2H), 1.58 (m, 4H), 1.30 (m, 16H), 0.86 (m, 12H) and m/z EIMS 556.

Compound 3. Under dark condition, compound **2** (1 g, 1.80 mmol) was dissolved into chloroform, and 2.3 equivalent of NBS (0.74 g, 4.14 mmol) was slowly added under ice bath. Then, the mixture was warmed up to room temperature and stirred for 6 hours. After adding water to the mixture, the organic layer was separated and dried with MgSO₄. Compound **3** (88 %) was obtained from column chromatography after elution of dichloromethane/n-hexane. ¹H-NMR (400MHz, CDCl₃) δ 7.68 (s, 2H), 7.08 (d, 2H), 4.38 (m, 1H), 2.08 (m, 2H), 1.58 (m, 4H), 1.30 (m, 16H), 0.86 (m, 12H) and m/z EIMS 714.

Polymerization of PBTT17T. Under inert conditions (Ar), compound 4 was dissolved into anhydrous toluene, and the equivalent amount of corresponding monomer (compound 3) was mixed. After adding Pd₂(dba)₃ (5 mol% to monomer) and P(o-toyl)₃ (3.5 eq to Pd(0)) to the mixture, it was stirred for 48 hours at 110 °C. Then, 2-tributylstannyl thiophene (39.5 μl) and 2-bromothiophene (12.5 μl) were added 3 hours intervals, one after the other, both for the termination of polymerization and chain end modification. The final polymer was collected via reprecipitation into methanol, and the solid was collected through 0.45 μm nylon filter. After washing the collected solid with methanol and acetone in a soxhlet apparatus, to remove the oligomers and catalyst residue, soluble part to chloroform was only obtained for next characterization. Then, the polymer solution was eluted through a column packed with Cellite/Florosil, and the obtained solution was reprecipitated from methanol after concentration in vacuo. Mn (17800), Mw (63720), and PDI (3.58)

3.5 Molecular Weight Determination.

Table 3.5.1. Molecular weight and steady state properties of studied polymers. Mw is the molecular weight of the polymers, PDI is the polydispersity index, N_{monomer} is the number of repeat units, λ_(abs)(nm) is the absorption peak wavelength, λ_(em)(nm) is the emission wavelength, Φ is quantum yield of the polymer samples

Polymers	M _w (kDa)	PDI	N _{monomer}	λ _(abs) (nm)	λ _(em) (nm)	Φ
PTB7	146.0	2.4	92	628, 671	736	0.0086
PBTCT	27.9	2.1	19	515, 552	600, 660	0.0910
PBT8PT	59.8	2.6	29	449, 551, 628	663, 717	0.0360
PBTT17T	63.7	3.58	19	536	600, 660	0.0490
PBTFDO	22.0	1.9	18	649, 703	780	0.0043

The molecular weight of the conjugated polymers used in this study was determined by gel permeation chromatography and is shown in **Table 3.5.1**, PTB7 had the highest weight

average molecular weight with 92 monomers per polymer chain. PBTCT had the third lowest weight average molecular weight with 19 monomers per polymer chain. PBT8PT had the third highest weight average molecular weight with 29 monomers per polymer chain. PBTT17T had the second highest weight average molecular weight, but had the broadest PDI and 19 monomers per polymer chain. PBTfDO had the lowest weight average molecular weight with 18 monomers per polymer chain.

3.6 Linear Absorption Spectra

Shown in **Figure 3.6.1** is the absorption spectra for the investigated polymers. A summary of the steady state properties of the polymers is provided in **Table 3.5.1**. All of the polymers studied have significant absorbance over much of the visible spectrum. The absorption maximum for PTB7 is at $14,800\text{ cm}^{-1}$ which is attributed to the $\pi\text{-}\pi^*$ transition between the thienothiophene (TT) and benzodithiophene (BDT) monomers and the small peak at $25,250\text{ cm}^{-1}$ can be attributed to a $S_0 \rightarrow S_1$ transition in the TT monomer.²³ PTB7 has a high extinction coefficient between $12,500\text{ cm}^{-1}$ - $17,700\text{ cm}^{-1}$ which is ideal for absorbing photons in the high solar flux region, this may contribute to PTB7's high power conversion efficiency.⁴³ PBTfDO and PBT8PT also had absorption maxima near $20,000\text{ cm}^{-1}$, with the bathochromic shift and greater absorption of low energy photons of PBTfDO attributed to the much stronger electron-withdrawing strength of its acceptor. PBTfDO and PTB7 have a strong electron-withdrawing fluorine atom and electron-withdrawing ester group on the acceptor monomer modulates the HOMO-LUMO energy gap, which results in narrowing of the optical bandgap compared to PBTCT and PBTT17T.^{22,44}

PBTCT and PBTT17T both are unable to utilize the lower energy photons of the high solar flux region, but for differing reasons. PBTCT fails at absorbing low energy photons in the

near IR region of the visible spectrum. PBTCT had the weakest electron-withdrawing acceptor of the investigated polymers leading to a large HOMO-LUMO energy gap resulting in no absorption in the near IR region of the visible spectrum. PBTT17T and PBT8PT had the same electron-withdrawing group on the acceptor, but PBT8PT was able to absorb lower energy photons. The poor absorption of low energy photons by PBTT17T is attributed to poor interaction between the donor and acceptor due to the additional thiophene linker resulting in a large HOMO-LUMO energy gap. This underlines the importance of the direct intramolecular interaction between the donor and acceptor for intramolecular charge transfer. The absorption spectra for the studied polymers illustrated that with increasing electron-withdrawing strength of the acceptor, there is a bathochromic shift of the maximum and leading edge of the absorption due to the lowering of LUMO energy level within the D-A polymer. The trailing edge of the absorption remained fairly unchanged along the series, which is due to the fact all of the D-A polymers having the same donor unit and thus similar HOMO energy levels.²² This modulation of the energy gap is due to the HOMO in the polymer corresponding to the donor group and the LUMO level corresponds with the acceptor group, thus the band gap is narrowed by introducing more electron-withdrawing groups that lower the LUMO which also correlates well with the DFT calculations conducted by Kim et al.²²

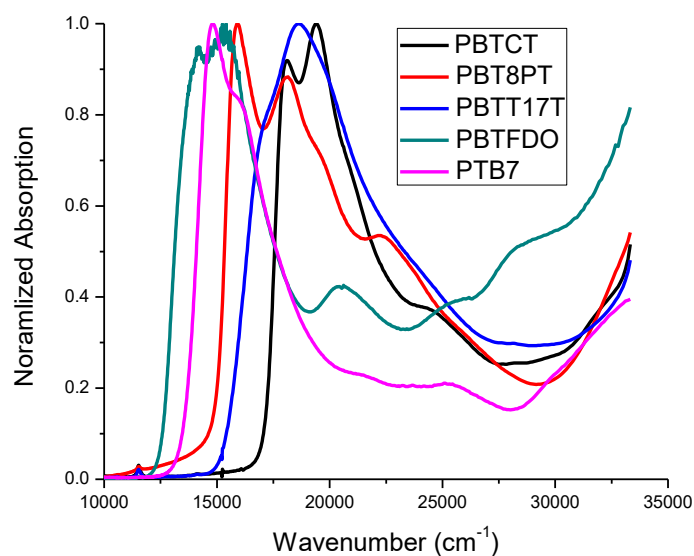


Figure 3.6.1. Absorption spectra of PBTCT, PBT8PT, PBTT17T, PBTFDO, and PTB7. The absorption spectra are normalized.

3.7 Fluorescence Spectra

Shown in **Figure 3.7.1** is the fluorescence spectra for the investigated polymers. PBTCT has a fluorescent peak at $16,700\text{cm}^{-1}$ and a prominent shoulder at $15,200\text{cm}^{-1}$. PBTT17T has a fluorescent peak at $15,100\text{cm}^{-1}$ and a shoulder at $13,900\text{cm}^{-1}$. The maximum peak of PBTT17T is 438nm red shifted as compared to PBT8PT's maximum but relatively unshifted compared to PBTCT, which is due to bulky side chain group on the PBTT17T thiophene acceptor, which is the same electron-withdrawing group of PBT8PT. The linker in PBTT17T results in less interaction between the thiophene acceptor and BDT donor as compared to PBT8PT due to the thiophene subunit decreasing the intramolecular interaction between the thiophene acceptor and BDT donor. The emission spectra for PBTFDO is the most red shifted, which is to the less bulky fluoro groups on the acceptor.

It is ideal to design light harvesting polymers with low quantum yields because higher quantum yields result in energy losses through radiative pathways which decreases the efficiency

of converting sunlight to electrical power in solar cell devices, although lower quantum yields may result in an increase non-radiative energy loss, thus other factors must be taken into consideration, such as emission decay dynamics, anisotropy, and two-photon absorption properties. The quantum yields for the investigated polymers is shown in **Table 3.5.1**. The studied polymers with the stronger electron-withdrawing groups had the lowest quantum yields. The stronger electron-withdrawing groups are able to activate non-radiative intramolecular photoinduced electron transfer(PET).⁴⁵ This causes the excited electron to be transferred to the acceptor more efficiently, which directly competes with electron hole pair annihilation which is responsible for fluorescence, resulting in a lower quantum yield. The low quantum yield of PBFTDO and PTB7 can be explained by the electron-withdrawing effect of fluorine, which is not only responsible for PET, but results in the changing of the redox potential and the excitation energy of the emitting subunit, which further changes the electron-accepting ability of the acceptor. Zhang⁴⁶ et al found that halogenation increases the rate constant of intramolecular PET according to Marcus electron transfer theory, which is consistent with the results of the studied polymers.⁴⁶ Thus, the low quantum yields of PBTFDO and PTB7 are quite desirable because of the reduced loss of energy through radiative pathways.

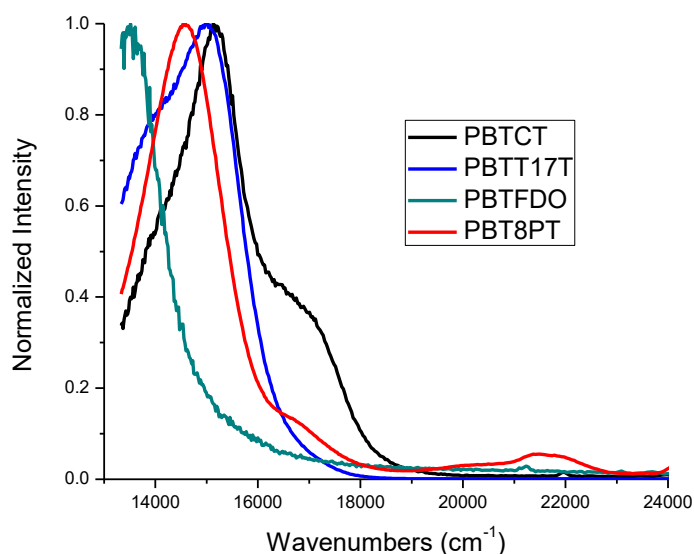


Figure 3.7.1. Emission(PBTCT, PBT8PT, PBTT17T: Excitation wavelength: 400nm. PBTfDO: Excitation wavelength: 450nm. PTB7: Excitation wavelength: 517 nm). Emission intensities are normalized.

3.8 Two-Photon Absorption Measurements

Table 3.8.1. TPA properties of studied polymers

Sample	δ (GM)	δ (GM)/monomer
PTB7	96,000	1044
PBTCT	3020	160
PBT8PT	87.2	3.0
PBTT17T	739	39
PBTfDO	3970	220

The two-photon cross section indicates the charge transfer character of the light-harvesting polymer.⁴⁷ For example, the repeating D-A units of the investigated polymers introduce nonlinearity that not only increases the two-photon absorption cross-section, but also increases charge transfer potential. As further elaboration, nonlinearity introduces asymmetry along the backbone, allowing for a distortion of the electron density along the backbone to provide a gradient for charge transfer to occur.

The two-photon excited fluorescence method was used to measure the two-photon absorption cross section, as shown in **Table 3.8.1**. The two-photon cross-section measures a standardized rate of bi-photon absorption. Hence, assuming equivalent efficiency, polymers with a higher two-photon cross-section are usually more ideal applied materials. An increase two-photon cross section was seen for the polymers that had strong electron-withdrawing groups on the acceptor. For example, PTB7 has a fluorine and ester group on its acceptor and PBTfDO has fluorine groups and dione groups. This suggests that strong electron-withdrawing groups can be used to increase two-photon cross section in order to promote charge transfer characteristics. Although there is a drop in two-photon cross-section per monomer for PBTfDO, which had the strongest electron withdrawing group, this drop per monomer has been seen in other polymers with extremely high dipole moments, which was attributed to electron trapping or recombination by Lu et al.^{44,48}

Next, comparing PBTT17T and PBT8PT, there was a 10-fold increase in two-photon absorption of the former, with the only difference in structure being a thiophene linker. Adding the linker added separation between the donor and acceptor to the polymer, which resulted in greater charge separation and is why the two-photon absorption cross-section increases. However, PBTT17T exemplifies that while adding a thiophene linker can provide circumstantial benefits, adding the linker does not necessarily create the better light-harvesting polymer or extend the conjugation, as PBTT17T has higher quantum yield (more loss due to radiation), and narrower one-photon absorption (less absorption of other wavelengths).

3.9 Fluorescence Upconversion Dynamics

The fluorescence decay dynamics were fitted to a multi-exponential decay functions. The decay dynamics for the investigated polymers are shown in **Figure 3.9.1** and **Figure 3.9.2**.

As seen in **Table 3.9.1**, the fluorescence lifetime measurements of the polymers indicate that the fluorescence lifetime is related to the electron-withdrawing strength of the acceptor. The investigated polymers with strong electron-withdrawing groups had short fluorescence lifetimes. The short total fluorescence lifetimes can be attributed to fluorescence quenching by the acceptor for PBTFDO and PTB7 resulting in quenching of the intermediate decay, whereas the weaker electron-withdrawing polymers PBTCT, PTB8PT, and PBTT17T do not quench the intermediate state leading to triexponential decay. This also was correlated with the smaller quantum yields exhibited by the investigated polymers with strong electron-withdrawing groups. The short component and long component of the decay dynamics of PTB7 and PBTFDO were quite similar which suggests similar relaxation processes. PBTT17T, PBTCT, PBT8PT had the longest decays of the investigated polymers which is attributed to the weaker electron-withdrawing strength of the acceptors in these polymers which suggests similar relaxation processes.

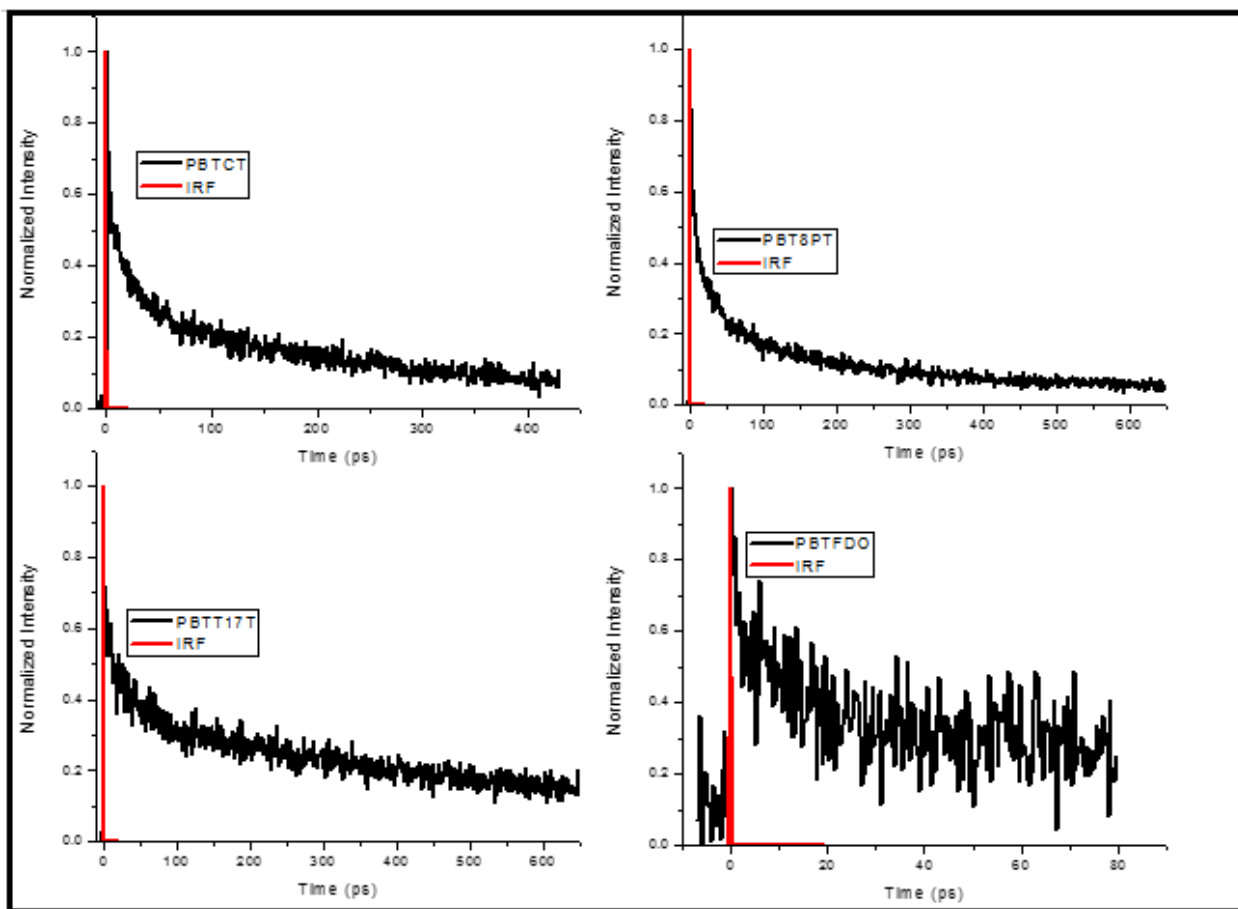


Figure 3.9.1. Fluorescence Upconversion of PBTCT(top left) at 400nm excitation and 600nm emission., PBT8PT(top right) at 400nm excitation and 650nm emission., PBTT17T(bottom left) at 400nm excitation and 650nm emission., and PBTEDO(bottom right) at 400nm excitation and 700nm emission.

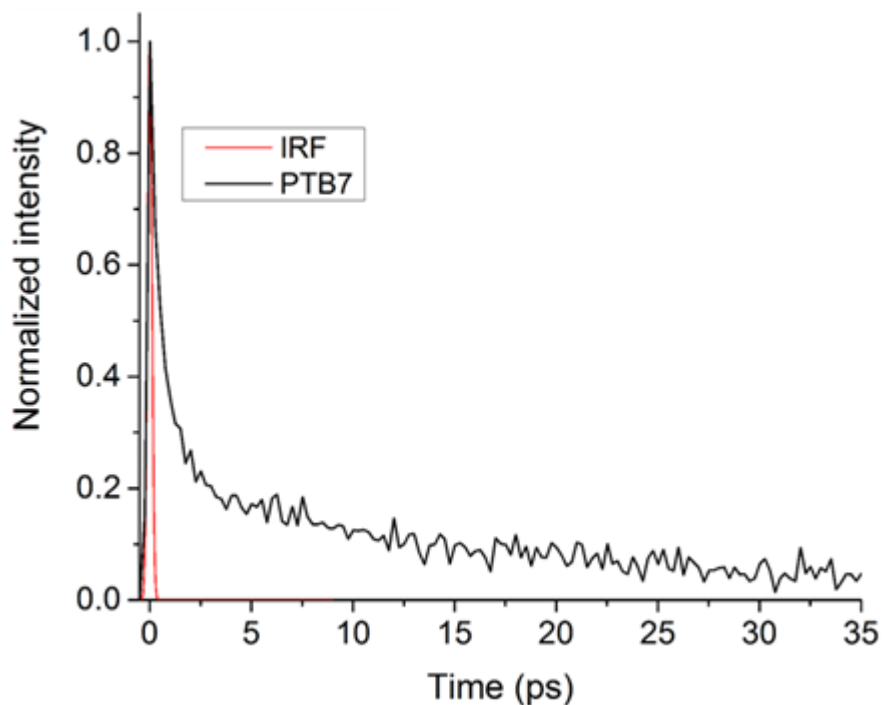


Figure 3.9.2. Fluorescence Upconversion of PTB7 at 400nm excitation and 700nm emission.²³

Table 3.9.1. Fluorescence lifetime of polymer samples

Polymer	A_1	τ_1 (ps)	A_2	τ_2 (ps)	A_3	τ_3 (ps)
PBTCT	0.405	0.749	0.552	15.7	0.259	207.14
PBT8PT	0.216	0.523	0.310	26.36	0.191	205.24
PBTT17T	0.391	0.583	0.34	7.67	0.31	159.97
PBTFDO	0.11	1.35	0.125	40.0		
PTB7	0.78	0.54	0.22	11.0		

Fluorescence anisotropy measurements were conducted for PBTCT, PBT8PT, PBTT17T, and PBTFDO. These can be seen in **Figure 3.9.3**. Fluorescence anisotropy measurements give information on conformational disorder and exciton hopping times along a polymer backbone.^{49,50} An initial anisotropy value of 0.4 is indicative of a two level state.⁵¹ Deviations from 0.4 for the initial anisotropy value can be attributed to multiple polarized transitions contributing to the anisotropy. The initial anisotropy value can also be affected by the resolution obtained using given experimental parameters.

Cho et al⁵² has found that PTB7 has an initial anisotropy of 0.4 and decay of 30 ps in toluene.⁵² The results found in this study for PTB7 in chloroform were an initial anisotropy of 0.09 with a decay of 48 ps which is comparable to the results found by Cho et al.⁵² The discrepancy between the results in this study and those found by Cho may be due to different conformations of PTB7 in different solvents, as well as the strong influence of excited state absorption seen for transient absorption anisotropy.

The initial anisotropy of the other investigated polymers were much lower than the 0.4 initial anisotropy expected of a two level system. The lower initial anisotropy values can be attributed to vibronic cooling that occurs faster than the resolution of the upconversion system. The anisotropic decay times for PTB7 and PBTfDO were 48ps and 8 ps, respectively. This fast decay can be associated with quick Förster energy transfer. PBTCT and PBT8PT had relatively long anisotropic decays of 130ps and 320ps, respectively, which is attributed to a much longer coherent energy transfer. Interestingly, PBTT17T, which has a linker separating the donor and acceptor, has an extremely short anisotropic decay of 0.08ps. Such a short decay can be attributed to Dexter-type energy transfer, unfortunately such a fast process is much faster than the resolution of the upconversion system.

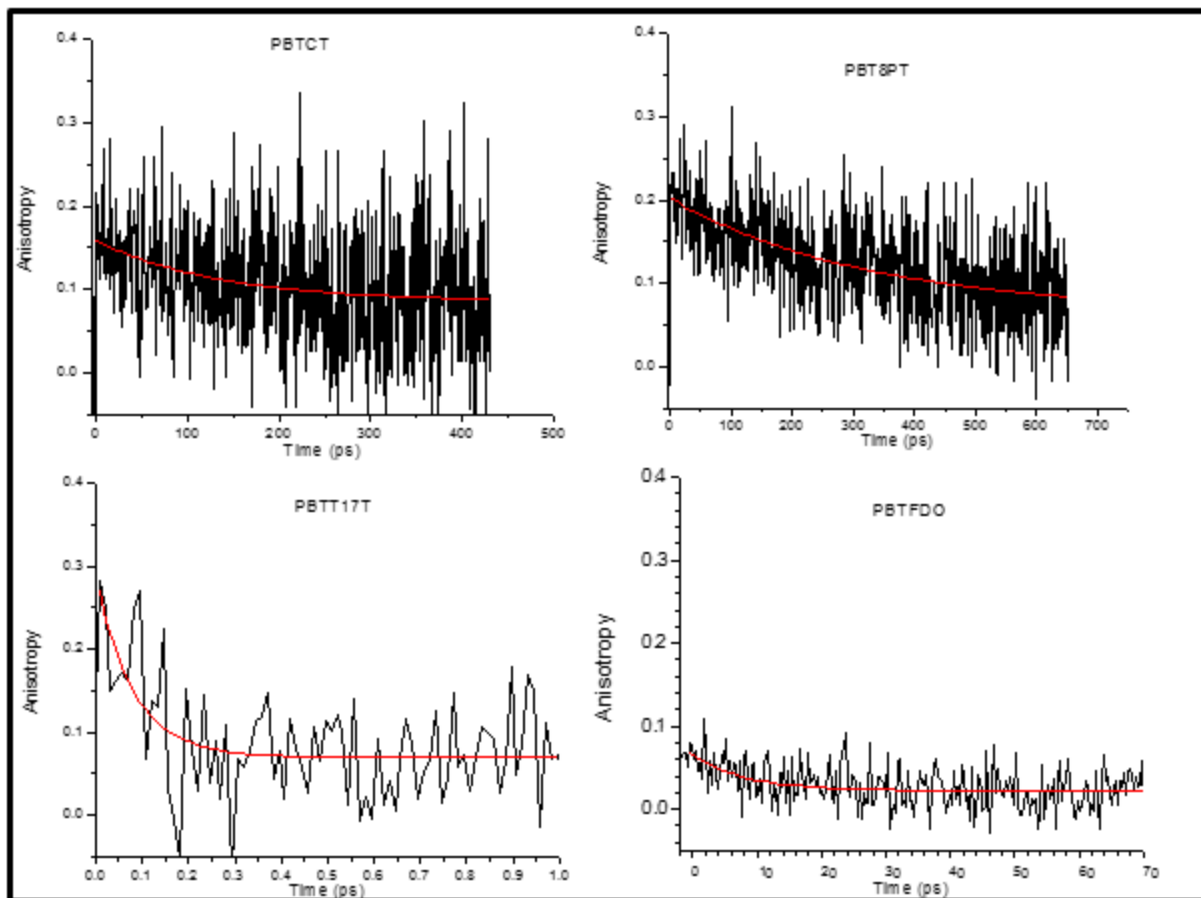


Figure 3.9.3. Anisotropic measurements. PBTCT (top left). PBT8PT (top right). PBTT17T (bottom left). PBTfDO (bottom right).

3.10 Discussion

The goal of this investigation was to probe the photophysical properties of light harvesting conjugated polymers in order to understand the fundamentals of organic light harvesting polymers. The conjugated polymers with the stronger electron-withdrawing monomers showed broad absorption due to lowering of the LUMO energy levels. Whereas conjugated polymers with the weaker electron-withdrawing monomers showed narrow absorption due to higher LUMO energy levels. Broad absorption in the visible spectrum is crucial for generation of higher free carrier concentrations which drastically impacts the performance of light harvesting conjugated polymers.⁴⁸ More charge carriers result in more conversion of photons into electrical work. The results from this study suggest that the donor-

acceptor conjugated polymers with the stronger electron-withdrawing monomers will be able to harvest a wide spectrum of photons which will result in more charge carrier generation which will increase the efficiency of the solar cell. The results show that conjugated polymers with strong electron-withdrawing monomers had low quantum yields due to fluorescent quenching which is desirable for efficient energy transfer along the polymer backbone. The excitation of the conjugated polymer results in a hole and electron pair that are attracted to each other by coulombic force, forming a quasiparticle exciton. Overcoming the coulombic attraction is imperative for OPV efficiency. If the donor-acceptor polymer cannot dissociate the electron-hole pair, electron-hole pair recombination will occur resulting in decreased efficiency and higher quantum yields.⁵³ The low quantum yields of the conjugated polymers in this study with strong electron-withdrawing monomers are indicative of sufficient exciton dissociation and reduction of charge recombination.

The conjugated polymers with strong electron-withdrawing monomers had large two-photon absorption cross-sections due to large transition dipoles. Conjugated polymers with weak electron-withdrawing monomers had much smaller two-photon absorption cross-sections. High two-photon absorption cross-sections are attributed to the repeating donor-acceptor units introducing nonlinearity which increases the transition dipole moment which increases the potential for charge transfer.²³ The two-photon absorption results further demonstrate the effect that strong electron-withdrawing monomers have on charge transfer.

The fluorescent dynamics showed that the polymers with strong electron-withdrawing monomers had very fast decay dynamics. Whereas polymers with weak electron-withdrawing monomers had much longer decay dynamics. The fast decay dynamics can be attributed to the strong electron-withdrawing effects, which creates a strong pull that results in a quick

delocalization and relaxation.²³ The longer decay dynamics for the weaker electron-withdrawing monomers may be a result of an absence of a pathway for energy to be delocalized and less driving force for the relaxation due to the weaker electron-withdrawing strength.⁵⁴ The fast decay dynamics are important for preventing charge recombination and allowing for efficient energy transfer.

Fluorescence anisotropic measurements were used to investigate energy transfer along the polymer backbone.^{50,55} The anisotropic decay times can be used to measure the time scales of the energy transfer.⁴⁹ Anisotropic decay times of <650 fs correspond to strong electronic coupling resulting in Dexter-type energy transfer. For longer time anisotropic decay times, over >650 fs, the migration can be described as incoherent hopping (~1-50ps), and coherent energy mechanisms that can last a few nanoseconds.⁵⁶ The anisotropic decay can be seen in **Table 3.10.1**. Augmenting the electron-withdrawing strength resulted in different relaxation processes to be activated for energy transfer. Strong electron-withdrawing acceptors had anisotropic decay times that were consistent with Förster energy transfer, whereas weaker withdrawing acceptors showed anisotropic decay times that were consistent with coherent energy transfer. Placing a linker between the donor and acceptor resulted in a very fast anisotropic decay which is consistent with Dexter-type energy transfer.

Table 3.10.1. Anisotropy and Power Conversion Efficiency.

Polymer	Initial Anisotropy Value	Anisotropic Decay Time (ps)	Power Conversion Efficiency (%)
PTB7	0.09	48	7.40
PBTCT	0.163	130	1.13
PBT8PT	0.22	320	6.78
PBTT17T	0.27	0.08	Not recorded
PBTFDO	0.07	8	0.27

3.11 Conclusions

The photophysical results from this study underline the complex nature of photon harvesting for electricity generation. In general, polymer designs that have low quantum yields, fast decay dynamics, reasonably large dipole moments, large two-photon absorption cross-sections, and efficient energy transfer, will produce photon harvesting devices that will have good PCE. These properties were augmented in this study by the addition of various electron withdrawing groups on the acceptor. The photophysical experiments on these polymers give insight into the complex mechanisms that are responsible for efficient light harvesting which can be useful for further improvement of PCE of light harvesting conjugated polymers.

Acknowledgement

This material is based upon work supported by the U.S. Department of Energy, Office of Science, Office of Basic Energy Sciences, Photochemistry, via Grant DE-SC0012482.

References

- (1) Snaith, H. J. Estimating the Maximum Attainable Efficiency in Dye-Sensitized Solar Cells. *Adv. Funct. Mater.* **2010**, *20*, 13-19.
- (2) Pelc, R.; Fujita, R. M. Renewable Energy from the Ocean. *Mar. Policy* **2002**, *26*, 471-479.
- (3) McKendry, P. Energy Production from Biomass (Part 1): Overview of Biomass. *Bioresour. Technol.* **2002**, *83*, 37-46.
- (4) Turner, J. A Realizable Renewable Energy Future. *Science* **1999**, *285*, 687-689.
- (5) Lewis, N. S.; Nocera, D. G. Powering the Planet: Chemical Challenges in Solar Energy Utilization. *Proc. Natl. Acad. Sci.* **2006**, *104*, 15729-15735.
- (6) Guter, W.; Schöne, J.; Philipps, S. P.; Steiner, M.; Siefert, G.; Wekkeli, A.; Welser, E.; Oliva, E.; Bett, A. W.; Dimroth, F. Current-Matched Triple-Junction Solar Cell Reaching 41.1% Conversion Efficiency under Concentrated Sunlight. *Appl. Phys. Lett.* **2009**, *94*, 1-3.
- (7) Liu, M.; Johnston, M. B.; Snaith, H. J. Efficient Planar Heterojunction Perovskite Solar Cells By Vapour Deposition. *Nature* **2013**, *501*, 395-398.

- (8) Glaser, P. E. Power From the Sun: Its Future. *Science* **1968**, *162*, 857-861.
- (9) Dresselhaus, M. S.; Thomas, I. L. Alternative Energy Technologies. *Nature* **2001**, *414*, 332-337.
- (10) Panwar, N. L.; Kaushik, S. C.; Kothari, S. Role of Renewable Energy Sources in Environmental Protection: A Review. *Renew. Sustain. Energy Rev.* **2011**, *15*, 1513-1523.
- (11) Thekaekara, M. P. Solar Energy Outside the Earth's Atmosphere. *Sol. Energy* **1973**, *14*, 109-127.
- (12) Gueymard, C.A. The Sun's Total and Spectral Irradiance for Solar Energy Applications and Solar Radiation Models. *Sol. Energy* **2004**, *76*, 423-453.
- (13) Kim, B.-G.; Chung, K.; Kim, J. Molecular Design Principle of All-organic Dyes For Dye-Sensitized Solar Cells. *Chemistry* **2013**, *19*, 5220-5230.
- (14) Lewis, N. S. Toward Cost-Effective Solar Energy Use. *Science* **2008**, *315*, 798-801.
- (15) Brabec, C. J.; Hauch, J. A.; Schilinsky, P.; Waldauf, C. Production Aspects of Organic Photovoltaics and Their Impact on the Commercialization of Devices. *MRS Bull.* **2005**, *30*, 50-52
- (16) Kim, B.-G.; Jeong, E. J.; Chung, J. W.; Seo, S.; Koo, B.; Kim, J. A Molecular Design Principle of Lyotropic Liquid-Crystalline Conjugated Polymers with Directed Alignment Capability For Plastic Electronics. *Nat. Mater.* **2013**, *12*, 659-664.
- (17) Jørgensen, M.; Norrman, K.; Krebs, F. C. Stability/Degradation of Polymer Solar Cells. *Sol. Energy Mater. Sol. Cells* **2008**, *92*, 686-714
- (18) Krebs, F. C. Fabrication and Processing of Polymer Solar Cells: A Review of Printing and Coating Techniques. *Sol. Energy Mater. Sol. Cells* **2009**, *93*, 687-702.
- (19) Green, M. A.; Emery, K.; Hishikawa, Y.; Warta, W.; Dunlop, E. D. Solar Cell Efficiency Tables (Version 45). *Prog. Photovoltaics Res. Appl.* **2015**, *23*, 1-9.
- (20) You, J.; Dou, L.; Yoshimura, K.; Kato, T.; Ohya, K.; Moriarty, T.; Emery, K.; Chen, C.-C.; Gao, J.; Li, G.; Yang, Y. A Polymer Tandem Solar Cell with 10.6% Power Conversion Efficiency. *Nat. Commun.* **2013**, *4*, 1-10.
- (21) Liu, Y.; Zhao, J.; Li, Z.; Mu, C.; Ma, W.; Hu, H.; Jiang, K.; Lin, H.; Ade, H.; Yan, H. Aggregation and Morphology Control Enables Multiple Cases of High-Efficiency Polymer Solar Cells. *Nat. Commun.* **2014**, *5*, 1-8.
- (22) Kim, B. G.; Ma, X.; Chen, C.; Ie, Y.; Coir, E. W.; Hashemi, H.; Aso, Y.; Green, P. F.; Kieffer, J.; Kim, J. Energy Level Modulation of HOMO, LUMO, and Band-Gap in Conjugated Polymers for Organic Photovoltaic Applications. *Adv. Funct. Mater.* **2013**, *23*, 439-445.

- (23) Adegoke, O. O.; Jung, I. H.; Orr, M.; Yu, L.; Goodson III, T. G. Effect of Acceptor Strength on Optical and Electronic Properties in Conjugated Polymers for Solar Applications. *J. Am. Chem. Soc.* **2015**, *137*, 5759-5769.
- (24) Reid, O. G.; Pensack, R. D.; Song, Y.; Scholes, G. D.; Rumbles, G. Charge Photogeneration in Neat Conjugated Polymers. *Chem. Mater.* **2014**, *26*, 561-575.
- (25) Oliva, M. M.; Casado, J.; Navarrete, J. T. L.; Patchkovskii, S.; Goodson, T.; Harpham, M. R.; Seixas De Melo, J. S.; Amir, E.; Rozen, S. Do [all]- S, S'-dioxide Oligothiophenes Show Electronic and Optical Properties of Oligoenes and/or of Oligothiophenes. *J. Am. Chem. Soc.* **2010**, *132*, 6231-6242.
- (26) Harpham, M. R.; Süzer, Ö.; Ma, C. Q.; Bäuerle, P.; Goodson, T. Thiophene Dendrimers as Entangled Photon Sensor Materials. *J. Am. Chem. Soc.* **2009**, *131*, 973-979.
- (27) Ramakrishna, G.; Bhaskar, A.; Bauerle, P.; Goodson, T. Oligothiophene Dendrimers as New Building Blocks for Optical Applications. *J. Phys. Chem. A* **2008**, *112*, 2018-2026.
- (28) Bhaskar, A.; Ramakrishna, G.; Hagedorn, K.; Varnavski, O.; Mena-Osteritz, E.; Bäuerle, P.; Goodson, T. Enhancement of Two-Photon Absorption Cross-Section in Macrocyclic Thiophenes with Cavities in the Nanometer Regime. *J. Phys. Chem. B* **2007**, *111*, 946-954.
- (29) Jung, I. H.; Lo, W.; Jang, J.; Chen, W.; Landry, E. S.; Lu, L.; Talapin, D. V.; Yu, L.; Zhao, D. Synthesis and Search for Design Principles of New Electron Accepting Polymers for All-Polymer Solar Cells. *Chem. Mater.* **2014**, *26*, 3450-3459.
- (30) He, Z.; Zhong, C.; Su, S.; Xu, M.; Wu, H.; Cao, Y. Enhanced Power-Conversion Efficiency in Polymer Solar Cells Using an Inverted Device Structure. *Nat. Photonics* **2012**, *6*, 593-597.
- (31) Carsten, B.; Szarko, J. M.; Son, H. J.; Wang, W.; Lu, L.; He, F.; Rolczynski, B. S.; Lou, S. J.; Chen, L. X.; Yu, L. Examining the Effect of the Dipole Moment on Charge Separation in Donor-Acceptor Polymers for Organic Photovoltaic Applications. *J Am Chem Soc* **2011**, *133*, 20468-20475.
- (32) Zhang, X.; Shim, J. W.; Tiwari, S. P.; Zhang, Q.; Norton, J. E.; Wu, P.-T.; Barlow, S.; Jenekhe, S. A.; Kippelen, B.; Brédas, J.-L.; Marder, S. R. Dithienopyrrole–Quinoxaline/Pyridopyrazine Donor–Acceptor Polymers: Synthesis and Electrochemical, Optical, Charge-Transport, and Photovoltaic Properties. *J. Mater. Chem.* **2011**, *21*, 4971-4982.
- (33) Gedefaw, D.; Tessarolo, M.; Zhuang, W.; Kroon, R.; Wang, E.; Bolognesi, M.; Seri, M.; Muccini, M.; Andersson, M. R. Conjugated Polymers Based on Benzodithiophene and Fluorinated Quinoxaline for Bulk Heterojunction Solar Cells: Thiophene Versus Thieno[3,2-b]thiophene as π -Conjugated Spacers. *Polym. Chem.* **2014**, *5*, 2083-2093.
- (34) Son, H. J.; Lu, L.; Chen, W.; Xu, T.; Zheng, T.; Carsten, B.; Strzalka, J.; Darling, S. B.;

- Chen, L. X.; Yu, L. Synthesis and Photovoltaic Effect in Dithieno[2,3-d:2',3'-d']Benzo[1,2-b:4,5-b']dithiophene-Based Conjugated Polymers. *Adv. Mater.* **2013**, *25*, 838-843.
- (35) Zhou, H.; Yang, L.; You, W. Rational Design of High Performance Conjugated Polymers for Organic Solar Cells. *Macromolecules* **2012**, *45*, 607-632.
- (36) Hou, J.; Park, M.-H.; Zhang, S.; Yao, Y.; Chen, L.-M.; Li, J.-H.; Yang, Y. Bandgap and Molecular Energy Level Control of Conjugated Polymer Photovoltaic Materials Based on Benzo[1,2-b:4,5-b']dithiophene *Macromolecules* **2008**, *41*, 6012-6018.
- (37) Varnavski, O.; Yan, X.; Mongin, O.; Blanchard-Desce, M.; Goodson, T. Strongly Interacting Organic Conjugated Dendrimers with Enhanced Two-Photon Absorption. *J. Phys. Chem. C* **2007**, *111*, 149-162.
- (38) Varnavski, O.; Leanov, A.; Liu, L.; Takacs, J.; Goodson III, T. Large Nonlinear Refraction and Higher Order Nonlinear Optical Effects in a Novel Organic Dendrimer. *J. Phys. Chem. B* **2000**, *104*, 179-188.
- (39) Flynn, D. C.; Ramakrishna, G.; Yang, H.; Northrop, B. H.; Stang, P. J.; Goodson, T. Ultrafast Optical Excitation in Supramolecular Metallacycles with Charge Transfer Properties. *J Am Chem Soc* **2010**, *132*, 1348-1358.
- (40) Xu, C.; Webb, W. W. Measurement of Two-Photon Excitation Cross Sections of Molecular Fluorophores with Data from 690 to 1050 nm. *J. Opt. Soc. Am. B* **1996**, *13*, 481-491.
- (41) Clark, T. B.; Orr, M. E.; Flynn, D. C.; Goodson, T. Synthesis and Optical Properties of Two-Photon Absorbing GFP-Type Probes. *J. Phys. Chem. C* **2011**, *115*, 7331-7338.
- (42) Furgal, J. C.; Jung, J. H.; Goodson, T.; Laine, R. M. Analyzing Structure – Photophysical Property Relationships for Isolated T 8 , T 10 , and T 12 Stilbenevinylsilsesquioxanes. *J Am Chem Soc* **2013**, *135*, 12259-12269.
- (43) Liang, Y.; Xu, Z.; Xia, J.; Tsai, S. T.; Wu, Y.; Li, G.; Ray, C.; Yu, L. For the Bright Future-Bulk Heterojunction Polymer Solar Cells with Power Conversion Efficiency of 7.4%. *Adv. Mater.* **2010**, *22*, 135-138.
- (44) Lu, L.; Yu, L. Understanding Low Bandgap Polymer PTB7 and Optimizing Polymer Solar Cells Based on it. *Adv. Mater.* **2014**, *26*, 4413-4430.
- (45) Zhang, X.-F. The Effect of Phenyl Substitution on the Fluorescence Characteristics of Fluorescein Derivatives via Intramolecular Photoinduced Electron Transfer. *Photochem. Photobiol. Sci.* **2010**, *9*, 1261-1268.
- (46) Zhang, X.-F.; Zhang, I.; Liu, L. Photophysics of Halogenated Fluoresceins: Involvement of Both Intramolecular Electron Transfer and Heavy Atom Effect in the Deactivation of Excited States. *Photochem. Photobiol.* **2010**, *86*, 492-498.

- (47) Norman, P.; Luo, Y.; Ågren, H. Large Two-Photon Absorption Cross Sections in Two-Dimensional, Charge-Transfer, Cumulene-Containing Aromatic Molecules. *J. Chem. Phys.* **1999**, *111*, 7758-7765.
- (48) Son, S. K.; Kim, Y.-S.; Son, H. J.; Ko, M. J.; Kim, H.; Lee, D.-K.; Kim, J. Y.; Choi, D. H.; Kim, K.; Kim, B. Correlation between Polymer Structure and Polymer:Fullerene Blend Morphology and Its Implications for High Performance Polymer Solar Cells. *J. Phys. Chem. C* **2014**, *118*, 2237-2244.
- (49) Grage, M. M. L.; Pullerits, T.; Ruseckas, A.; Theander, M.; Inganäs, O.; Sundström, V. Conformational Disorder of a Substituted Polythiophene in Solution Revealed by Excitation Transfer. *Chem. Phys. Lett.* **2001**, *339*, 96-102.
- (50) Grage, M. M. L.; Wood, P. W.; Ruseckas, A.; Pullerits, T.; Mitchell, W.; Burn, P. L.; Samuel, I. D. W.; Sundström, V. Conformational Disorder and Energy Migration in MEH-PPV with Partially Broken Conjugation. *J. Chem. Phys.* **2003**, *118*, 7644-7650.
- (51) Martinsson, P.; Sundström, V.; Åkesson, E. An Ultrafast Time-Resolved Anisotropy Study of Bacteriochlorophyll a in Pyridine. *FEBS Lett.* **2000**, *465*, 107-109.
- (52) Cho, S.; Rolczynski, B. S.; Xu, T.; Yu, L.; Chen, L. X. Solution Phase Exciton Diffusion Dynamics of a Charge-Transfer Copolymer PTB7 and a Homopolymer P3HT. *J. Phys. Chem. B* **2015**, *119*, 7447-4756.
- (53) Lemaire, V.; Steel, M.; Beljonne, D.; Brédas, J. L.; Cornil, J. Photoinduced Charge Generation and Recombination Dynamics in Model Donor/Acceptor Pairs for Organic Solar Cell Applications: A full Quantum-Chemical Treatment. *J. Am. Chem. Soc.* **2005**, *127*, 6077-6086.
- (54) Lahankar, S. A.; West, R.; Varnavski, O.; Xie, X.; Goodson, T.; Sukhomlinova, L.; Twieg, R. Electronic Interactions in a Branched Chromophore Investigated by Nonlinear Optical and Time-Resolved Spectroscopy. *J. Chem. Phys.* **2004**, *120*, 337-344.
- (55) Westenhoff, S.; Daniel, C.; Friend, R. H.; Silva, C.; Sundström, V.; Yartsev, A. Exciton Migration in a Polythiophene: Probing the Spatial and Energy Domain by Line-Dipole Förster-Type Energy Transfer. *J. Chem. Phys.* **2005**, *122*, 1-8.
- (56) Grage, M.; Zaushitsyn, Y.; Yartsev, A.; Chachisvilis, M.; Sundström, V.; Pullerits, T. Ultrafast Excitation Transfer and Trapping in a Thin Polymer Film *Phys. Rev. B* **2003**, *67*, 1-5.

Chapter 4

The Role of Donor Conjugation Length on the Optical Properties of Donor-Acceptor Light Harvesting Conjugated Polymers: An Investigation of Thiophene Additions to s-Indacene Donors with Diketopyrrolopyrrole, Isoindigo, and Thienothiophene Acceptors

Bradley Keller, Hyungjun Kim, Zhengxu Cai, Audrey Eshun, Luping Yu, Theodore Goodson III

4.1 Abstract

New donor-acceptor light harvesting polymers with either a 4,4,9,9-tetrakis(4-hexylphenyl)-4,9-dihydro-s-indaceno[1,2-b:5,6-b']dithiophene (**IDT**) or a 4,4,9,9-tetrakis(4-hexylphenyl)-4,9-dihydro-s-indaceno[1,2-b:5,6-b']dithienothiophene (**IDTT**) donor subunit with either a 2-(nonadecan-9-yl)-5-(2-octyldodecyl)-3,6-di(thiophen-2-yl)-2,5-dihydropyrrolo[3,4-c]pyrrole-1,4-dione (**DPP**), (E)-1,1'-bis(2-octyldodecyl)-[3,3'-biindolinylidene]-2,2'-dione (**II**), or 3-ethyl-1-(thieno[3,4-b]thiophen-2-yl)heptan-1-one (**TT**) acceptor were synthesized. In this study the effects of donor conjugation length and donor-acceptor combination on the optical properties were investigated with ultrafast spectroscopic techniques and computational methods. The polymers with the extended conjugated donor had significantly enhanced absorption near 400 nm. Fluorescence upconversion experiments revealed that the donor conjugation length increased the fluorescence lifetimes for the extended conjugated polymers. Two-Photon Absorption (TPA) experiments and computational methods showed that the extended conjugated donor polymers exhibited enhanced charge transfer characteristics. Transient Absorption (TA) investigations revealed new optical species for the extended donor polymers. This study has shown the considerable effect that donor conjugation has on the optical properties of donor-

acceptor light-harvesting conjugated polymers. The results from this work can be used in the design and synthesis of new donor-acceptor polymers for organic photovoltaics.

4.2 Introduction

Global population has seen rapid growth and with this growth, there has been a growth in energy demand and consumption.^{1,2} With this increase in consumption, there has been an increase in climate change due to the pollution that is attributed to the burning of fossil fuels for energy generation.³ This has led to interest in cleaner, renewable, and greener sources of energy, such as solar energy harvesting.⁴ Indeed, solar energy harvesting systems have seen an average annual growth in global photovoltaic capacity of 40%.⁵ The most prominent solar harvesting systems are solar cells. Solar cells consist of electron rich and electron poor active material that absorb sunlight, converting photonic energy into electron and hole charge carriers that are responsible for electricity generation.⁶ Traditionally, solar cell absorbing active materials have used inorganic semiconductors for light harvesting, but these materials are brittle, inflexible, have low optical absorption coefficients in the visible region of electromagnetic spectrum, require high temperature and pressures for manufacturing, or contain toxic elements.⁷⁻¹⁰ This has limited the number of applications that these materials can be used in and contribute to the overall cost of using these technologies.

This has led to interest in organic light harvesting materials that can improve upon the drawbacks of their inorganic counterparts. Organic solar harvesting materials have high optical absorption coefficients, flexible, lightweight, easily tunable band gaps, and are readily solution processable.¹¹⁻¹⁴ In organic solar cells an absorbing organic layer is sandwiched between two conducting electrodes, typically a conducting glass on the top and a metallic electrode on the bottom. Light is absorbed by the absorbing organic layer forming a tightly bound exciton, an

electron-hole pair. Another organic layer is used to overcome the binding energy of the exciton to dissociate the electron from the hole, forming free charge carriers that then flow to the electrodes, with the electrons flowing to the cathode and the holes flowing to the anode. The most promising organic solar harvesting devices have incorporated low band gap organic donor-acceptor (D-A) conjugated polymers that serve as the photon absorbing material and hole transporting material, and an organic acceptor material that has high electron affinity in order for charge separation and electron transport.¹⁵

Donor-acceptor polymers have a relatively simple motif, but finding suitable donor and acceptor monomers that lead to high power conversion efficiencies is no easy task. There have been a few promising donor monomers that have been incorporated in light harvesting D-A polymers that have resulted in high efficiencies. Benzodithiophene (BDT) has shown great promise as the electron rich donor subunit in D-A polymers. BDT is a planar conjugated monomer composed of a central benzene and a fused thiophene unit on both ends of the central benzene unit. It is relatively easy to synthesize and easily modified.¹⁶ The planar conjugated backbone of the BDT unit is excellent for device π - π stacking and high hole mobilities.¹⁷ Donor-acceptor polymers that have incorporated BDT units have shown high power conversion efficiencies.^{18,19} Another promising donor monomer is carbazole. Carbazole has a central pyrrolidine unit with a benzene fused on each side. The nitrogen atom of the pyrrolidine is easily functionalized to increase solubility and the lone pairs increase the donating ability of the donor monomer, and the benzene rings can be functionalized to augment the solubility or donating ability of the monomer.^{20,21} D-A Polymers that have incorporated carbazole donors have also shown high power conversion efficiencies.²² One of the most promising donor subunit is the indacenodithiophene donor monomer. Indacenodithiophene aromatic fused-ring system provides

a rigid structure that promotes planarity for extended conjugation, and restricts twisting and out of plane rotation due to steric hindrance.²³ The IDT structure provides great tunability with modification of the bridging atom, introduction of electronic influencing groups, and introduction of side groups. IDT polymers have shown high hole mobilities.²⁴ DA polymers that have incorporated IDT have shown high power conversion efficiencies (PCE) of more than 12%.²⁵

As important as the donor monomer is to the D-A polymer, the acceptor monomer is as equally as important and much research has been devoted to designing electron-withdrawing acceptors. One promising acceptor monomer is diketopyrrolopyrole (DPP). DPP is a strong electron withdrawing acceptor that has demonstrated high electron and hole mobilities.^{26,27} The introduction of thiophene subunits on both ends of DPP connects the DPP to the donor monomer as well as creates a Donor-Acceptor-Donor motif between the electron deficient DPP and electron rich thiophenes.²⁸ D-A polymers that have incorporated DPP have seen high PCEs of up to 10%.²⁹ Another promising acceptor monomer is isoindigo. Isoindigo consists of two oxindole rings centrosymmetrically conjugated to each other at their 3-carbons by a central double bond that binds two electron-withdrawing carbonyls and two electron-rich benzene rings in trans confirmation. It has good electron-withdrawing properties, two amides that are readily functionalized, the phenyl rings have sites for conjugation elongation, high hole mobilities, planar backbone, and strong interchain interactions due to the rigidity of the isoindigo core.^{30,31} Isoindigo also has the advantage of large scale availability from natural sources which leads to a greener overall synthetic pathway.³² Polymers that have incorporated isoindigo as acceptor units have seen efficiencies of up to 8%.³³ One of the most studied and most commonly incorporated acceptor monomer is thienothiophene.^{18,34} Thienothiophene is composed of two thiophene rings

fused to each other. The fused ring promotes planarity and enhances conjugation along the monomer backbone. Thienothiophene has four isomers: thieno[2,3-b]thiophene, thieno[3,4-c]thiophene, thieno[3,2-b]thiophene, and thieno[3,4-b]thiophene; with thieno[3,4-b]thiophene proving to be the most successfully incorporated isomer as an acceptor in donor-acceptor polymers because it introduces an anisotropic charge distribution that is good for charge transport.^{35,36} The doubly unsaturated cyclopentadiene does not show aromaticity, but aromaticity is achieved by substituting the central carbon with a heteroatom with a lone pair that contributes to the π resonancy. When incorporating sulfur as the heteroatom, the highest resonance energy is achieved of 29 kcal mol⁻¹ compared other heteroatom unsaturated pentacyclics which is important for charge transport characteristics.³⁴ One of the best aspects of the thienothiophene is its ease of functionalization. The conjugation length can be extended or electron-withdrawing groups can be attached to the monomer to impart optical and electronic changes to the structure.^{37,38} D-A polymers that have incorporated thienothiophene acceptors have achieved high power conversion efficiencies, in fact the seminal work of Liang et al demonstrated the great potential these acceptors can have on the optoelectronic properties of D-A polymers.¹⁹

Much research has focused on synthesizing new donor materials and acceptor materials, device architectures, morphologies, optical properties of devices, electrical properties of devices, but limited attention has been on the dynamic fundamental optical properties of the D-A conjugated polymers light absorbing materials.³⁹⁻⁴³ In fact, there is still much debate on the mechanisms that lead to the optoelectronic properties of these materials.⁴⁴⁻⁴⁶ Numerous studies have investigated the optoelectronic properties of bulk heterojunction donor-acceptor systems, but a deeper understanding of the dynamic optical properties of D-A conjugated polymers that

are used as the donating materials in organic solar cells will go a long way in unraveling the mysteries responsible for high power conversion efficiency organic solar cells.⁴⁷⁻⁴⁹

There have been many studies that have focused on the effects that the acceptor monomer has on the optical properties of donor-acceptor polymers. The electron-withdrawing strength of the acceptor has significant influence on the electronic and optical properties of the donor-acceptor polymer. From electrochemical studies and computations, it is known that the LUMO of the acceptor closely matches the LUMO of the donor-acceptor polymer.^{50,51} By introducing electron-withdrawing groups to the acceptor monomer, the band gap of the donor-acceptor polymer can be easily tuned.⁵² Acceptor strength has also had profound effects on the optical properties of light-harvesting D-A polymers. D-A Polymers with strong acceptors have seen an enhancement of light absorbing capabilities in the high solar flux regions of the visible spectrum,⁵³ greater charge transfer, and quenched fluorescence. This has led to high power conversion efficient donor-acceptor polymers such as PTB7.⁵⁴ But effects of acceptor strength on optoelectronic properties are not so clear cut, D-A polymers with strong acceptors with great charge transfer characteristics, quenched fluorescence, and good absorption properties have also produced low power conversion efficiencies due to local exciton trapping preventing efficient transfer along the polymer backbone.⁵⁵ Thus more investigation is needed in order to get a better understanding of the influence of acceptors on the fundamental optoelectronic properties of light harvesting donor-acceptor polymers.

Studies that focus on the donor influence on the optical properties of light harvesting donor-acceptor polymers are relatively sparse. Electron-rich donors with strong acceptors are imperative in promoting charge transfer along the polymer backbone. The HOMO of donor significantly influences the HOMO of the polymer, and the polymer HOMO and acceptor

material LUMO offset determine the open circuit voltage.⁵⁶ Strong donors have lower onset oxidation potentials and contribute to lower band gaps.⁵⁷ But too strong of a donor results in poor charge carrier extraction due to poor energy level mismatch in the device. Attempts have been made to enhance the donating ability of donor monomer increase the power efficiency of donor-acceptor devices. One method has focused on increasing the donor conjugation, but too large of a conjugated donor system results in out of plane twisting of the donor in respect to the acceptor resulting in poorer power efficiencies.⁵⁸ Donating groups have also been added to the donor monomer to increase the donating ability, but often times the donating groups can also increase steric hindrance between donor and the acceptor decreasing the conjugation length along the polymer backbone.⁵⁹⁻⁶¹ Thus designing donor monomers is no easy task as well.

In this study, six donor-acceptor polymers were synthesized and their optical properties were investigated. Each polymer had a 4,4,9,9-tetrakis(4-hexylphenyl)-4,9-dihydro-s-indaceno[1,2-b:5,6-b']dithiophene (**IDT**) or a 4,4,9,9-tetrakis(4-hexylphenyl)-4,9-dihydro-s-indaceno[1,2-b:5,6-b']dithienothiophene (**IDTT**) donor with either a 2-(nonadecan-9-yl)-5-(2-octyldodecyl)-3,6-di(thiophen-2-yl)-2,5-dihydropyrrolo[3,4-c]pyrrole-1,4-dione (**DPP**), (E)-1,1'-bis(2-octyldodecyl)-[3,3'-biindolinylidene]-2,2'-dione (**II**), or 3-ethyl-1-(thieno[3,4-b]thiophen-2-yl)heptan-1-one (**TT**) acceptor. The extended conjugation of the donor should promote a more planar, linear, and rigid structure while not introducing steric hindrance between the donor and acceptor unit. The introduction of different strength and size acceptors will give a better insight into the interaction between the donor and acceptor and its effect on the optical properties. Optical properties were investigated using steady state spectroscopy. All of D-A polymers exhibited a high and low energy absorption. The conjugation extension had little effect on peak absorption maximum, but there was a significant increase in molar absorptivity for wavelengths

<500 nm. Polymers with stronger acceptors had red-shifted absorption maxima. Polymers with extended donor system had higher quantum yields (QY). The optical and nonlinear properties were investigated using ultrafast spectroscopic techniques. Ultrafast fluorescence upconversion technique was used to investigate the fluorescence lifetime of the D-A polymers. D-A polymers with the extended conjugation show longer fluorescence lifetimes indicating longer lived excitonic states. Two-photon absorption (TPA) properties were investigated utilizing ultrafast Two-Photon Excitation Fluorescence (TPEF) method in order to investigate the charge transfer characteristics of the polymers. The polymers with stronger acceptors had the highest TPA cross-sections compared to their corresponding analogue indicating improved charge transfer characteristics. Ultrafast transient absorption experiments were employed to investigate the excited state dynamics of the investigated polymers. Transient absorption experiments revealed significant changes in the excited state dynamics. In particular, new species are seen for the extended conjugated donors with additional bleached or ESA states in the transient spectra. Computational methods were used to investigate the effect that polymerization and donor conjugation length had on the optical properties of the investigated polymers. These experiments have shown the profound impact that donor conjugation length has on the optical properties of the investigated polymers.

4.3 Experimental

4.3.1 Steady State UV-Vis and Emission Measurements

The investigated polymers were dissolved in chloroform for all steady state experiments. Concentrations of 3.0×10^{-6} M were used for all steady state experiments and concentrations of 3.0×10^{-6} M or lower were used for quantum yield experiments. Steady state absorption spectra were measured using an Agilent 8432 UV-visible absorption spectrophotometer. Steady state

emission spectrum measurements were carried out with a Fluoromax-2 spectrophotometer. Styryl 9m ($\phi = 0.54$) in chloroform was used as the fluorimetric standard for the calculation of the fluorescence quantum yield for P2 and P5 using the well-known comparative method.^{62,63} Zinc phthalocyanine ($\phi = 0.30$) in pyridine was used as the fluorimetric standard for quantum yield determination of P1, P3, P4, and P6.⁶⁴ The quantum yields were measured at 430 nm excitation.

4.3.2 Two-Photon Absorption (TPA) Experiments

The two-photon-absorption (TPA) cross sections were measured using the two-photon excited fluorescence (TPEF) method.⁶⁵ The setup employs a mode-locked Spectra-Physics femtosecond Mai Tai laser, which is tunable from 700 to 900 nm, to generate 110-fs pulses. For the experiments in this study, the Spectra-Physics Mai Tai laser generated a 775 nm with 110-fs pulsewidth to pump a Spectra-Physics femtosecond synchronously pumped optical parametric oscillator (OPAL), which produced 1250 nm (for P3 and P6 excitation) or 1300 nm (for P1, P2, P4, and P5 excitation) with 150-fs excitation pulses. The beam was directed into a solution in a sample cell (quartz cuvette, 1 cm path length), and the resultant fluorescence was collected in a direction perpendicular to the incident beam. A lens was used to direct the collected fluorescence into a monochromator. The output from the monochromator was directed into a photomultiplier tube (PMT), and the photons were converted into counts by a photon counting unit. The photomultiplier tube was connected to the computer through a photon counting unit (Hamamatsu) for signal recording. Zn 2,9,16,23-tetra-tert-butyl-29H,31H-phthalocyanine and Styryl 9m have known TPA cross-sections and were used as standards for comparative method determination of TPA cross-sections.⁶⁶

4.3.3 Fluorescence Upconversion Experiments

The time-resolved fluorescence experiments were performed using a fluorescence setup that had previously been described.⁶⁷ A femtosecond Mode-locked Ti-sapphire pulsed laser (Spectra Physics Tsunami) was used to generate 80 fs pulses at 800 nm wavelength with a repetition rate of 82 MHz. The Tsunami was pumped by a 532 nm continuous wave Millennia (Spectra Physics) laser. An excitation pulse of 400 nm was generated by a second harmonic BBO crystal, and the residual 800 nm beam was used as an optical gate by a computer-controlled motorized optical delay line. The polarization of the excitation beam was controlled by a birefringent compensator. The fluorescence signal of the sample was up-converted by a BBO crystal by using the residual 800 nm beam, which is delayed by the optical delay line with a gate step size of 6.25 fs. This allows the fluorescence decay dynamics to be measured temporally. A monochromator is used to select the wavelength of the up-converted signal which is detected by a photomultiplier tube (R152P, Hamamatsu). The instrument response function (IRF) has been determined from the Raman signal of water to have a width of 110 fs.

4.3.4 Transient Absorption Experiments

The femtosecond transient absorption experiment setup has been described previously.⁶⁸ The femtosecond transient absorption investigations were carried out using ultrafast pump-probe techniques with detection in the visible region. The laser system produces 1-mJ, 100-fs pulses at 800 nm with a repetition rate of 1 kHz that were obtained from a Nd:YLF(Spectra Physics Empower)-pumped Ti:Sapphire regenerative amplifier (Spectra Physics Spitfire) with the input from a continuous wave Nd:YVO4 (Spectra Physics Millennia)-pumped Ti:Sapphire oscillator (Spectra Physics Tsunami). The output of laser beam was split to generate pump and probe beam pulses with a beam splitter (85% and 15%, respectively). The pump beam was generated by an

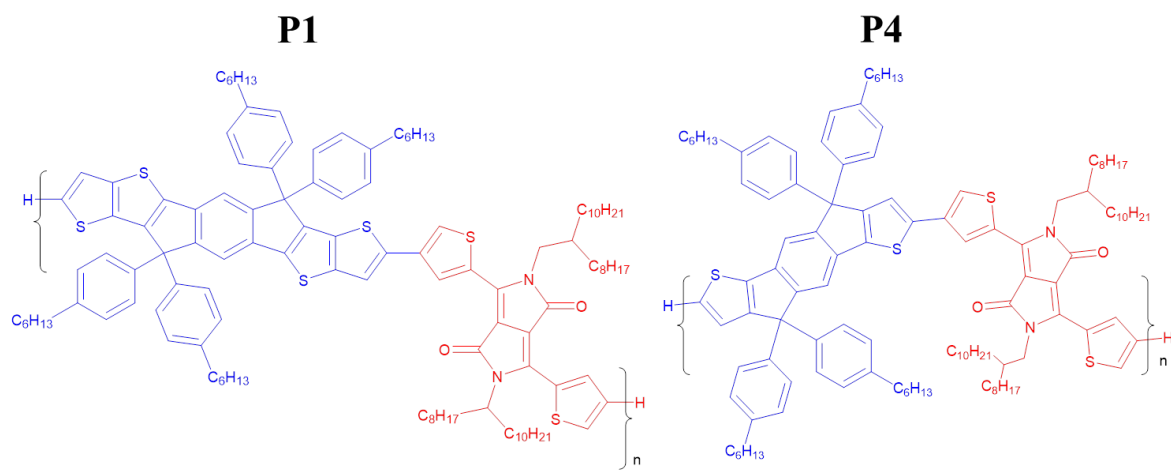
optical parametric amplifier (Spectra Physics OPA-800). The 400 nm pump beam was produced from the second harmonic of the idler beam using a BBO. The white light continuum probe beam was generated from the amplified beam by a Helios system (Ultrafast Systems Inc). The probe beam was generated by a 2 mm sapphire plate generating a white light continuum from 450 nm to 750 nm. The time delay between the pump and probe was controlled with a computer-controlled motion controller. The white light and the pump beam were overlapped in a 2 mm quartz cuvette containing the sample with a magnetic stirrer. The typical energy probe beam is $< 0.1 \mu\text{J}$, while the pump beam energy is $\sim 1 - 2 \mu\text{J}$ per pulse. Magic angle polarization is kept consistent between the pump and probe using a polarizer. The change in absorbance as a function of time for the signal was collected by a CCD detector (Ocean Optics). Data acquisition was controlled by software from Ultrafast Systems Inc.

4.4 Molecular Structures and Molecular Properties

The molecular properties of the investigated properties can be seen in **Table 4.4.1** and the molecular structures can be seen in **Figure 4.4.1**. All of the polymers had a polydispersity (PDI) near 2 except for P3, which had a slightly higher PDI of 2.61. The average number molecular weight (M_n) for all the polymers was between 20 kDa and 40 kDa. The weight average molecular weight (M_w) was between 40 kDa to 90 kDa. The number of repeat units varied from 13 repeat units (RPU) to 24 RPU. The number of repeat units was fairly close between polymers with the same acceptor type, except for P2 and P5, where P2 has two times the number of repeat units in P5. The two polymers are still comparable because the persistence length of conjugated light harvesting polymers are much smaller than the length of the polymer, and optical properties can be normalized to the number of repeat units.

Table 4.4.1. Molecular Properties

Polymer	Mn (Da)	Mw (Da)	PDI	RPU
P1	25900	48200	1.86	14
P2	42500	88400	2.08	23
P3	22600	59100	2.61	17
P4	34100	62800	1.84	19
P5	22600	42800	1.90	13
P6	28300	55500	1.96	24



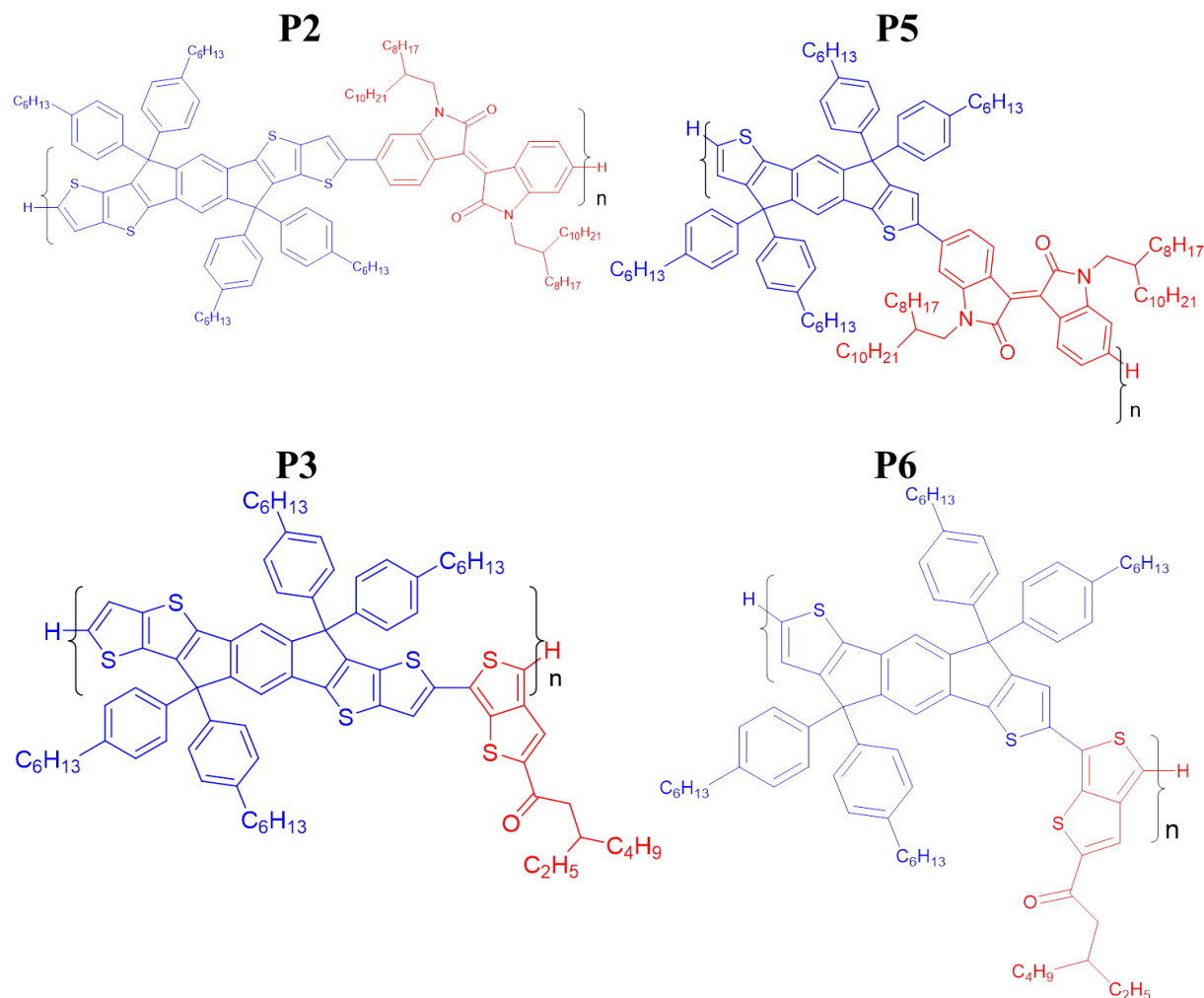


Figure 4.4.1. Polymer Structures (blue portion is the donor and red portion is the acceptor).

4.5 Steady State

4.5.1 Absorption

The steady state absorption spectra of the investigated polymers were performed in chloroform solutions at concentrations of 3×10^{-6} M. This concentration was chosen in order to minimize internal sample reabsorption while maximizing signal to noise ratio. The normalized steady state absorption spectra for all of the investigated polymers can be seen in **Figure 4.5.1.1**. All of the investigated polymers have broad absorption in the visible spectral region with distinct absorption peaks in the 400-500 nm region and absorption maxima in the 600-800 nm region.

The broad absorption and absorption maxima in the 600-800 nm region make them ideal candidates for light harvesting for photovoltaics to match the high photon flux region of the Sun. Poly(4,9-Dihydro-s-indaceno[1,2-b:5,6-b']dithiophene) polymers generally absorb in the 500 nm region, poly(bithienyl diketopyrrolopyrole) polymers have a weak absorption peak near 450 nm and broad maxima near 700-800 nm, poly(Isoindigo) polymers have weak absorption at 450 nm and broad maxima near 700 nm, and polymers with thienothiophene acceptors have an absorption maxima near 650 nm, which makes each subunit ideal for incorporation in a donor-acceptor polymer.^{18,27,33,69-71} The strong absorption in the 400-500 nm region of the 4,9-Dihydro-s-indaceno[1,2-b:5,6-b']dithiophene donor subunit, and the overlap of the weak absorption of the Isoindigo, thienothiophene, and the bithienyl diketopyrrolopyrole acceptor subunits in the 400-500 nm region with strong absorption in the 600-800 nm region makes a stronger absorbing polymer and potentially introduces unique optical properties for the investigated polymers.

The steady state absorption properties of the investigated polymers can be seen in **Table 4.5.1.1**. The polymers with longer conjugated donors had higher molar absorptivities for the higher energy transitions, whereas the lower energy molar absorptivity was relatively unaffected by the donor conjugation length. The higher molar absorptivities for the lower energy transition for the more conjugated donor polymers could be due to the more conjugated system enhancing delocalization or may be due to the additional rigidity that promotes planarity along the polymer backbone.^{72,73} This suggests that the donor may have a higher contribution than the acceptor to the lower energy absorption transition. The polymers with the stronger acceptors had higher molar absorptivities for the low energy transition and no effect on the high energy transitions, which suggests that the acceptor contributes more to the low energy transition.⁷⁴

The polymers with the bithienyl diketopyrrolopyrrole and isoindigo acceptor moieties showed distinct absorption peaks, whereas the polymers with the thienothiophene acceptor moiety had an overlap of the lower energy and higher energy absorption peaks, regardless of donor subunit conjugation length. For both polymer series P1-P3 and P4-P6, a bathochromic shift of the lower energy absorption peak is seen with increasing strength of the acceptor, which is typically seen for polymers with stronger acceptors.⁵⁵ With about 20-30 nm bathochromic shift of the low energy absorption of the polymers with the BTDPP acceptor compared to the polymers with II acceptor, and 70-100 nm bathochromic shift of the low energy absorption of polymers with BTDPP acceptor compared to the polymers with the TT acceptor. The higher energy absorption peak is less affected by the acceptor strength, with red shifts of 30-40 nm for the peak absorption for the more conjugated donor polymers with stronger acceptors and up to ~60 nm bathochromic shift for the less conjugated donor polymers with stronger acceptors. This suggests that the acceptor strength has more influence on the lower energy absorption than the higher energy absorption.

The donor conjugation length had a modest effect on the peak absorption wavelength for the high energy transition. The polymers with the longer donor conjugation had 10-20 nm red shift of the high energy absorption peak maxima. This result as well as the increase in molar absorptivity of the higher energy transitions agrees with a greater contribution of the donor in this transition. The donor conjugation length had a small effect on the peak absorption wavelength for the low energy transition with a red shift of ~10 nm blue shift of the low energy absorption peak maxima. Interestingly, for P1 and P6, there was a drastic change in the low energy absorption peak maxima of a ~40 nm blue shift for the longer conjugated donor polymer. This may be due to steric hindrance introduced by the additional thiophene units of the donor

that is alleviated in the smaller donor polymer. This pronounced effect is not seen in the other series of polymers because the acceptor monomers in those polymers are more bulky than the TT acceptors, which results in structures that relieve the steric hindrance in both the longer conjugated donor and the less conjugated donor of the same series of acceptors..

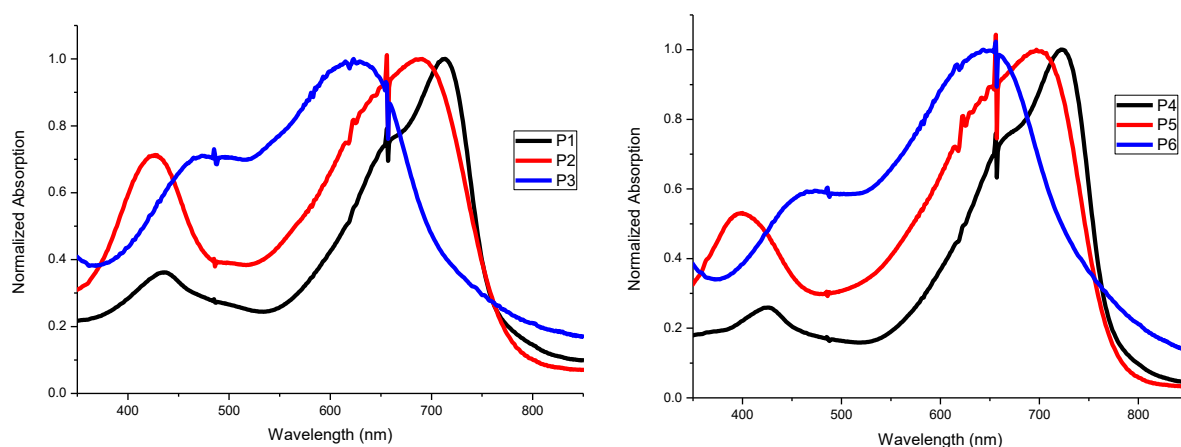


Figure 4.5.1.1. Normalized steady state absorption of more conjugated donor polymer series P1-P3(left) and less conjugated polymer series P4-P6(right).

Table 4.5.1.1. Steady state absorption properties(Molar absorptivities: $\epsilon/10^4 \text{ L mol}^{-1} \text{ cm}^{-1}$)

Polymer	High Energy Absorption (nm)	ϵ	Low Energy Absorption (nm)	ϵ
P1	436	5.970	715	17.285
P2	424	7.605	692	10.115
P3	470	5.150	620	6.960
P4	429	4.345	725	17.670
P5	404	5.160	696	10.130
P6	461	4.375	657	6.690

4.5.2 Fluorescence

The steady state fluorescence spectra of the investigated polymers were performed in chloroform solutions at the same concentrations that were used for the steady state absorption

experiments. The normalized steady state fluorescence spectra for all of polymers were excited using 430 nm excitation and >600 nm excitation, which can be seen in **Figure 4.5.2.1**. In order to establish that we are not selectively exciting a specific emission maxima, the polymers were excited using 430 nm and >600 nm excitation to target the donor monomer and acceptor monomer of the polymer, respectively. The emission maxima are independent of the excitation wavelength, which is congruent with Kasha's rule.⁷⁵ The fluorescence spectra are narrower than the absorption spectra for the investigated polymers. This is attributed to different absorption units that occur in polymers due to bending or twisting that cause different conjugation absorbing segments of the polymer. Whereas the emission is attributed to longer conjugated segments, with excitons migrating from the higher energy shorter segments to the lower energy longer conjugated segments that serve as the major emitters.⁷⁶

All of the polymers exhibit steady state fluorescence maxima in the near-infrared region of the electromagnetic spectra, ~700 nm – 800 nm, with minor peaks near 500 nm for P2 and P5, and a minor peak near 550nm for P6. The emission maxima can be attributed to the relaxation of the lower energy transition of the polymer. The minor peaks near 500 nm and 550 nm can be attributed to the relaxation of high energy states from hot excitons that recombine during relaxation before the energy can migrate to the lower energy transition to be emitted. P1 and P4 only had one emission peak near 740 nm, lacking the 500 nm emission seen in the other series of polymers. This suggests that this donor-acceptor motif, regardless of the donor conjugation length, can suppress other fluorescence pathways that are seen in the other investigated polymers. The 500 nm emission is more pronounced in P2 than in P5, which suggests that the longer conjugation donor of P2 promotes other radiative pathways. The 550 nm emission for P6 is attributed to the promotion of the higher energy transition state.

The emission maxima for polymers with comparative donors were relatively unaffected by the increase in donor length conjugation, with the largest shifts amounting to only ~10 nm shift suggesting that the donor conjugation length does not have significant influence on the lower energy fluorescence transition. The polymers with stronger acceptors had emissions that more red shifted, which is typical for donor-acceptor polymers due to the narrowing of the bandgap which is often dominated by the acceptor strength.^{53,55} The Stokes shifts for comparative donor analogues were also relatively unaffected by the increase in donor length conjugation, although P3 did have larger Stokes shifts compared to P6 which is due to better planarity of polymer backbone of P3 due to the longer conjugated donor system.

Since the polymer's followed Kasha's rule, 430 nm excitation was used for the Quantum Yield(QY) determination. This wavelength is useful for exploring the direct excitation of the higher energy transition as well as investigating the lower energy major emission maxima, thus the contribution of the lower energy emission can be analyzed, if present, to the overall emission behavior. The steady state fluorescence properties are summarized in **Table 4.5.2.1**.

There were significant differences between the polymer donor analogues in terms of their QYs. Studies have investigated the effect of donor conjugation length on the optical properties of organic donor acceptor systems. Yamaguchi et al found that longer conjugated systems and longer conjugated donor-acceptor systems of the same type had an increase in both QY and emission maximum.⁷⁷ Whereas, Kurowska et al found in small molecule donor-acceptor systems, that the QY decreased and the emission maximum increased with an increase in donor ratio.⁷⁸ Surprisingly, there has not been much investigation of conjugation length of the donor in donor-acceptor polymers with tailored donor and acceptor subunits. The polymers in this study with longer donor conjugation lengths had higher QYs than their corresponding shorter donor

polymer analogues. This suggests that the two additional fused thiophenes promotes radiation relaxation pathways compared to their less conjugated donor polymers. The emission maxima for the polymers increased with increasing acceptor strength due to the narrowing of the optical bandgap, which is typically seen with polymers with strong acceptors.⁷⁹ Interestingly, quenching of the fluorescence was not seen with increasing acceptor strength for the investigated polymers, which is also typically seen with polymers with strong acceptors.⁸⁰ This suggests that the acceptors are strong enough to promote exciton formation, but too strong where the exciton is trapped and then quenched. In order to have efficient solar harvesting polymers, the exciton must be able to survive long enough to eventually get to the donor polymer and acceptor interface for the exciton dissociation. The optical lifetimes will be thoroughly discussed in the time resolved experiments sections of this paper.

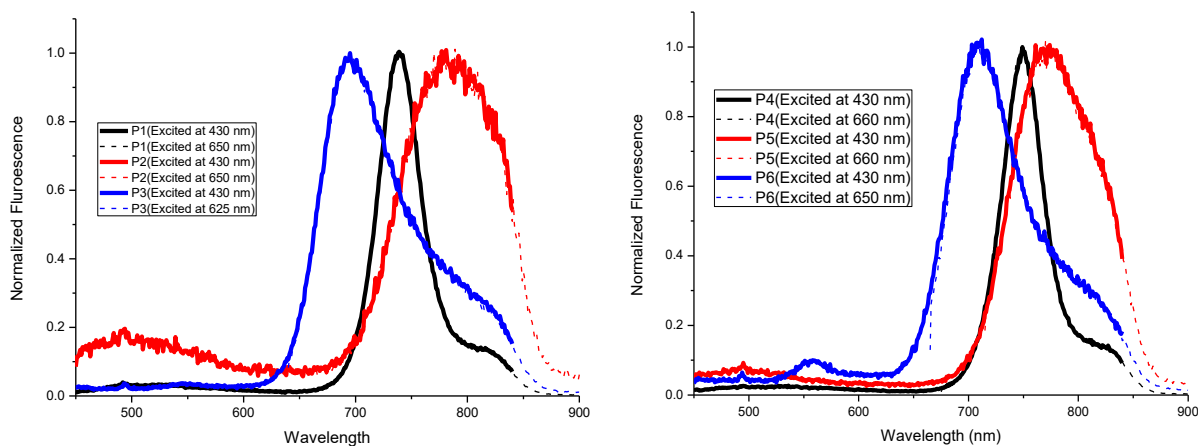


Figure 4.5.2.1. Normalized steady state fluorescence of P1-P3(Left) and P4-P6(Right) at 430 nm excitation for donor excitation (solid line) and >600 nm excitation for acceptor excitation(dashed line)

Table 4.5.2.1. Steady state fluorescence properties

Polymer	Max Fluorescence(nm)	QY	Stokes Shift (nm)
P1	738	0.82 \pm 0.05	23
P2	780	0.19 \pm 0.08	88
P3	695	0.44 \pm 0.08	75
P4	749	0.65 \pm 0.12	24
P5	772	0.14 \pm 0.04	76
P6	709	0.13 \pm 0.03	52

4.6 Quantum-Mechanical Calculations

4.6.1 Basis Set and Level of Theory

A computational investigation into the structural and electronic properties of the investigated polymers in chloroform were carried out using Density Functional Theory (DFT) and Time Dependent Density Functional Theory (TDDFT) using GAMESS suite of programs. The B3LYP level of theory was used to calculate the geometry and orbital energy levels of monomer, dimer, trimer, and tetramer in order to approximate the geometry and orbital energy levels of the investigated conjugated polymers. B3LYP is a hybrid functional that uses Becke's 3 parameter(B3) exchange correlation functional which uses 3 parameters to mix in the exact Hartree-Fock exchange correlation and the Lee Yang and Parr(LYP) correlation functional that recovers dynamic electron correlation. B3LYP has been used extensively in computational chemistry to describe geometry and orbital energy levels for conjugated polymers and has produced comparable orbital energy levels to experimentally obtained orbital energy levels. It is particularly useful for donor acceptor polymers because of its ability to describe conjugation effects.⁸¹ Another hybrid functional was also used, wB97x-D, to compare the two levels of theory with split valence 6-31G(d) basis set. wB97x-D is a meta-GGA DFT functional that

includes the second derivative of the electron density and contains empirical dispersion terms and long-range corrections to approximate the geometry and orbital energy levels. Frequency calculations were also performed in order to ensure the minimum of the potential energy surface for the optimized ground state geometry at the same level of theory. Then excited state geometries and orbital energy levels were then performed by using TDDFT using the same level of theory. Absorption, emission, and TPA cross sections were then calculated using the same level of theory. The two levels of theory used to investigate the effects of structure property relationships, as well as the effect of polymerization on the molecular orbital energy levels.

4.6.2 Computation

The linear and branched alkyl solubility side chains were replaced with methyl groups to reduce computational time as well as to maintain conformational constraints introduced by the side chains, this is a reasonable modification because it has been shown that the side chains do not contribute to the polymer backbone electronic properties.

4.6.3 Molecular Orbital Energies of Monomers

B3LYP was used to determine the molecular orbital energies for the monomers of the investigated polymers. B3LYP is one of the most commonly used functionals to investigate the molecular orbital energy levels of donor-acceptor polymers.⁸² Because of the vast computational costs of simulating the energy levels for large macromolecules, often times a repeat unit or a few repeat units are used to model the electronic system. This a reasonable compromise when the electronic properties are due to small number of repeat units, but fails for electronic systems that are due to many repeat units or have significant energy level modulation due to polymerization. The molecular orbital diagram for the monomers of the investigated polymers can be seen in **Figure 4.6.3.1**. All of the polymers had low lying HOMO energy levels with high lying LUMO

energy levels. The polymers with longer conjugated donors had slightly higher HOMO and LUMO energy levels ~ 0.05 eV, with larger discrepancies seen for the HOMO energy levels which are more correlated with donor subunit HOMO. The polymers with the more electron-withdrawing acceptors had deeper lying LUMOs which resulted in smaller bandgaps. The HOMO, LUMO, and bandgaps can be seen in **Table 4.6.3.1**.

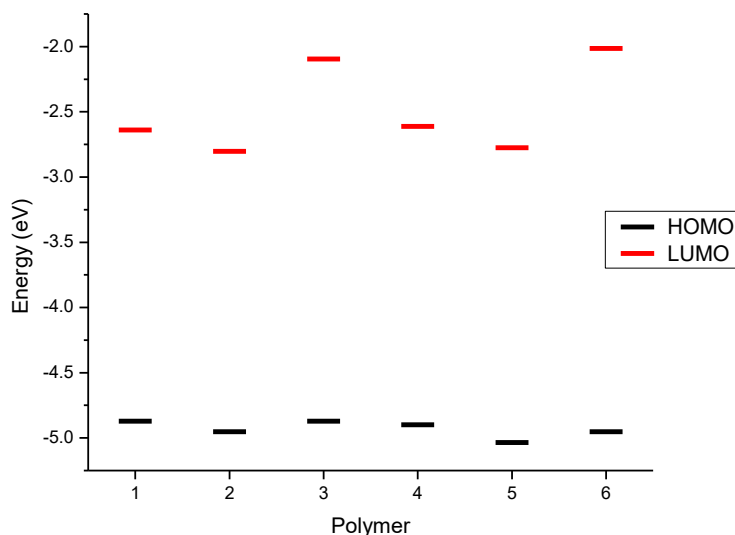


Figure 4.6.3.1. Molecular orbital energy diagram of monomers of polymers P1-P6 using B3LYP functional.

Table 4.6.3.1. HOMO, LUMO and Bandgap energies for monomers of polymers P1-P6 using B3LYP functional

Polymer	HOMO (eV)	LUMO (eV)	Bandgap (eV)
P1	-4.87	-2.64	-2.23
P2	-4.95	-2.80	-2.15
P3	-4.87	-2.10	-2.78
P4	-4.90	-2.61	-2.29
P5	-5.03	-2.78	-2.26
P6	-4.95	-2.01	-2.94

Unfortunately, the calculated bandgaps were not well correlated with the optical bandgaps determined from experiments. This may be due to the failure of B3LYP to account for dispersive forces and charge transfer character, or could be due to the monomeric unit not being

a good representation of the electronic system. To account for dispersive forces and charge transfer, wB97x-D was used to calculate the molecular orbital energies of the monomer, which can be seen in **Figure 4.6.3.2**. The HOMO and LUMO energies follow similar trends as those calculated by B3LYP. The HOMO energy levels calculated by wB97x-D are close to the HOMO energy levels calculated by B3LYP, with the largest discrepancy of 0.04 eV. However, the LUMO energy levels calculated by wB97x-D are much lower than the LUMO energy levels calculated by B3LYP, with discrepancies of up to 0.24 eV. As a result the bandgap, as seen in **Table 4.6.3.2**, is much closer to the experimentally obtained bandgap. Although there is still a large discrepancy between the calculated and experimentally obtained bandgaps, which suggests dispersive forces and charge transfer do not fully account for the electronic properties of the system.

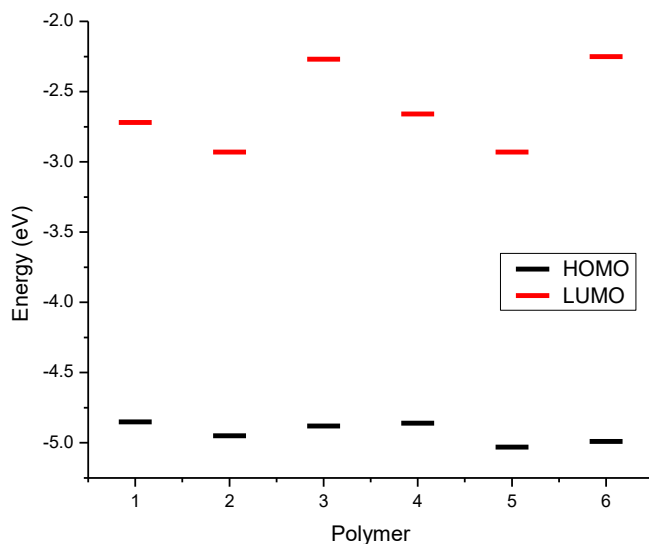


Figure 4.6.3.2. Molecular orbital energy diagram of monomers of polymers P1-P6 using wB97x-D functional.

Table 4.6.3.2. HOMO, LUMO and Bandgap energies for monomers of polymers P1-P6 using wB97x-D functional.

Polymer	HOMO (eV)	LUMO (eV)	Bandgap (eV)
P1	-4.85	-2.72	-2.13
P2	-4.95	-2.93	-2.02
P3	-4.88	-2.27	-2.61
P4	-4.86	-2.66	-2.20
P5	-5.03	-2.93	-2.10
P6	-4.99	-2.25	-2.74

4.7 Polymerization Effects on Molecular Orbital and Electronic Structure Calculations

4.7.1 Polymerization Effect on Bandgap

WB97-D was better able to estimate the optical bandgap compared to B3LYP, but still failed to accurately account for the effects that polymerization has on energy level modulation. In order to study the effects of polymerization on the energy levels, the molecular energy levels for the monomer, dimer, trimer, and tetramer were calculated. As seen in **Figure 4.7.1.1**, the bandgap rapidly decreases from the monomer to the tetramer, with small change in bandgap from the trimer to the tetramer. Indeed, the calculated bandgaps are similar to the experimentally determined bandgaps, seen in **Table 4.7.1.1**.

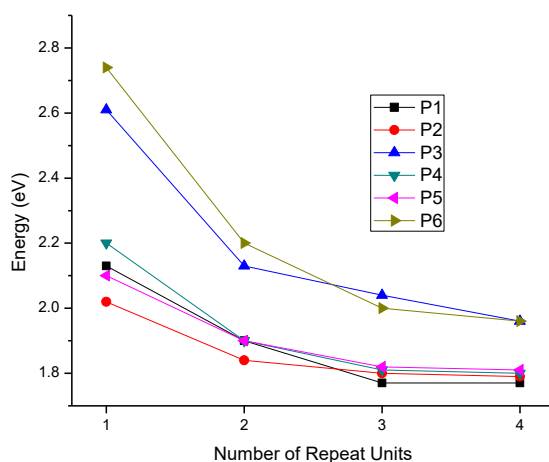


Figure 4.7.1.1. Bandgap of monomer, dimer, trimer, and tetramer of P1-P6 using wB97x-D functional.

Table 4.7.1.1. Bandgap of monomer, dimer, trimer, and tetramer of polymers P1-P6 using wB97x-D functional in eV

	Monomer	Dimer	Trimer	Tetramer	Elec(CV)	Opt
p1	2.13	1.90	1.77	1.77	1.90	1.64
p2	2.02	1.84	1.80	1.79	2.01	1.62
p3	2.61	2.13	2.04	1.96	2.16	1.74
p4	2.20	1.90	1.81	1.80	2.01	1.61
p5	2.10	1.90	1.82	1.81	1.99	1.61
p6	2.74	2.20	2.00	1.96	2.03	1.71

4.7.2 Polymerization Effects on Electronic Structure Calculations

The HOMO, LUMO, HOMO-1, and LUMO+1 geometries for the monomers were calculated and can be seen in **Figure 4.7.2.1**. The HOMO for P1 is concentrated on the acceptor subunit with little electron density distributed on the donor. The little electron density that is distributed on the donor is concentrated on the two fused thiophene units of the donor nearest to the acceptor, with even less electron density on the rest of the donor. The LUMO for P1 is also concentrated on the acceptor and is similar to how the electron density is distributed for the HOMO, except there is almost no electron density on the rest of the donor subunit with the two periphery thiophene units having no contribution to the HOMO. The HOMO-1 is delocalized across both the donor and acceptor subunit, with small electron density on the periphery thiophene linker of the acceptor. The LUMO+1 electron density is also delocalized across the polymer, including the periphery thiophene linker of the acceptor. For P4, a similar trend is seen for HOMO, LUMO, HOMO-1, and LUMO+1. Although, with two fewer thiophenes in the donor subunit, more electron density is delocalized across the whole donor subunit which is not the case for the two periphery thiophene in the donor subunit for P1, a trend seen for all of the more conjugated donor analogues.

The HOMO for P2 and P5 is more concentrated on the donor subunit with less electron density distributed on the acceptor, which is in stark contrast to how electron density is distributed in the HOMO of P1 and P4. The LUMO for P2 and P5 is almost entirely concentrated on the acceptor subunit, with some electron density on the thiophenes on the donor closest to the acceptor subunit. The HOMO-1 for P2 and P5 is well delocalized across the polymer backbone. Interestingly, the electron density distribution of LUMO+1 for P2 and P5 is similar to the HOMO for P2 and P5 with the electron density predominately delocalized over the donor subunit.

The HOMO, LUMO, HOMO+1, and LUMO-1 for P3 and P6 is well delocalized over the entire polymer backbone. This symmetric distribution of the electron density for the HOMO, LUMO, HOMO+1, and LUMO-1 is very different from the anti-symmetrical electron density distribution seen for the other investigated polymers, suggesting a less pronounced charge transfer.

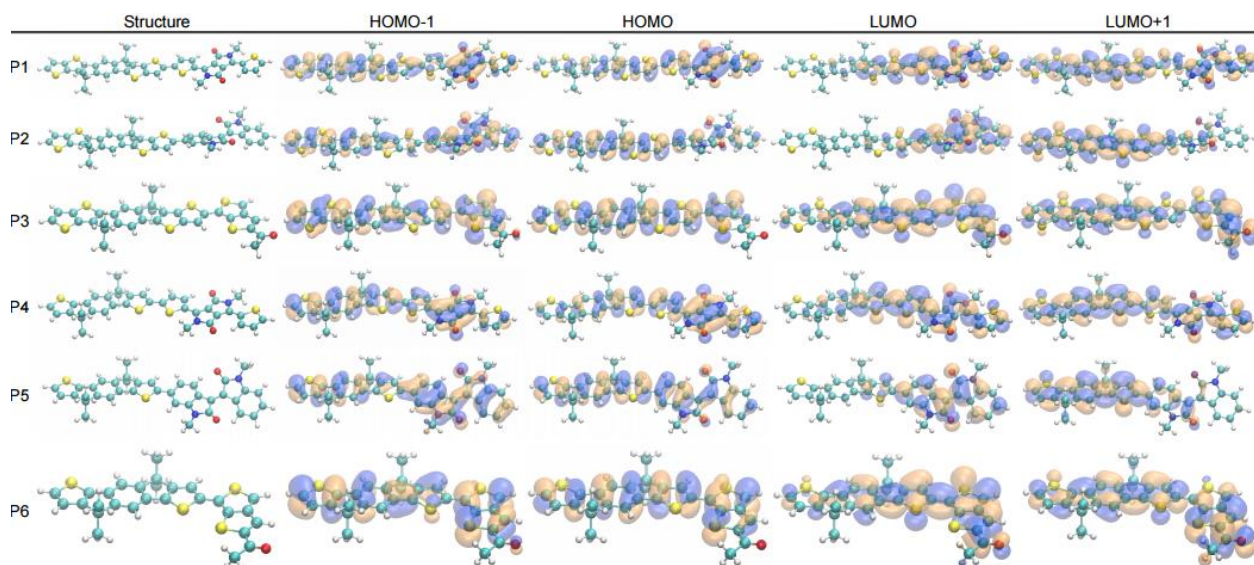
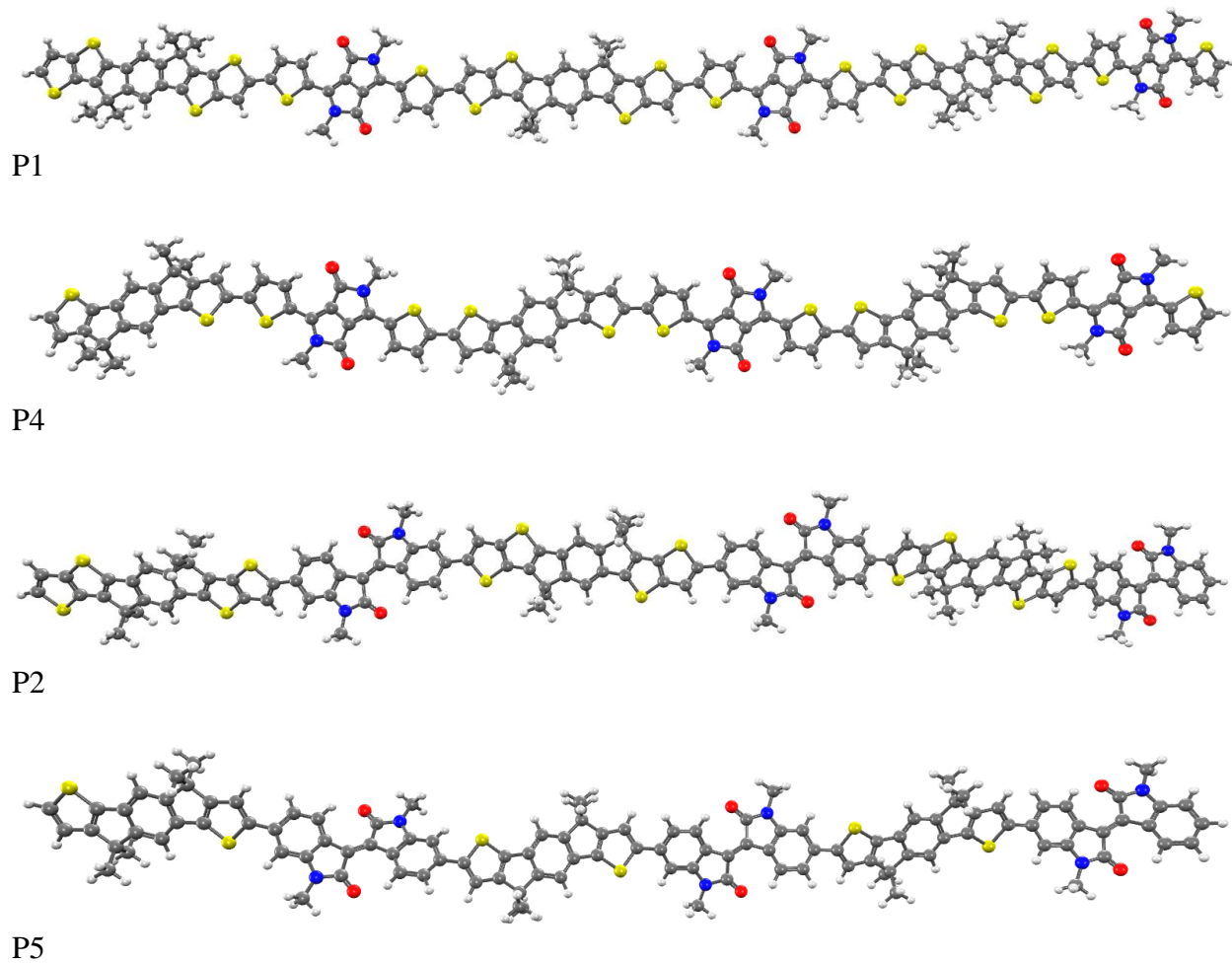
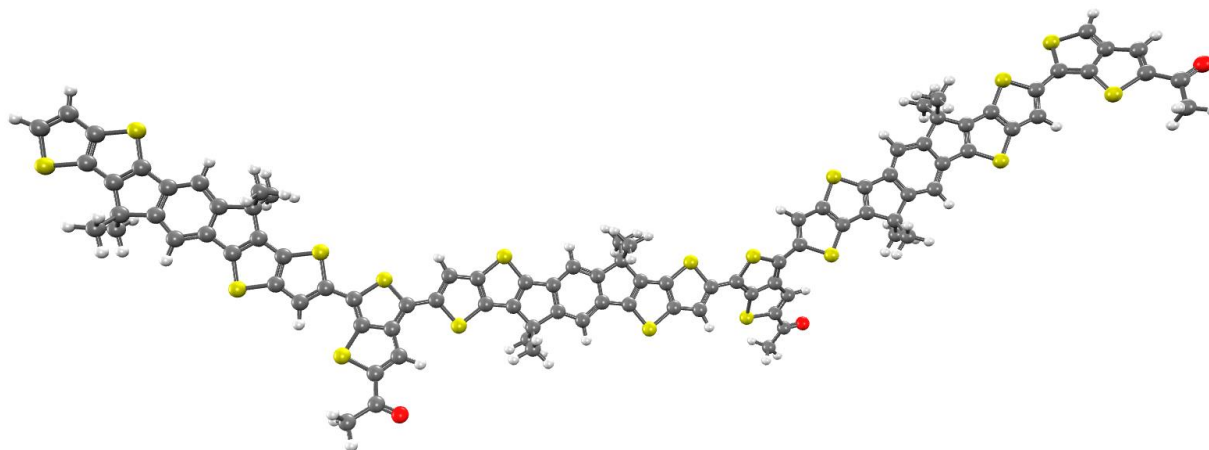


Figure 4.7.2.1. Electronic geometries for donor-acceptor monomers.

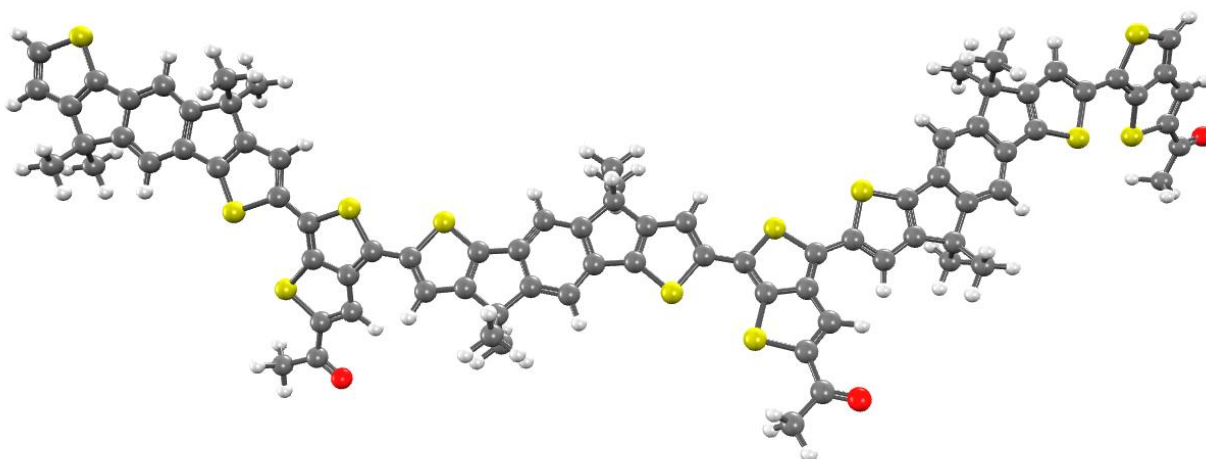
4.7.3 Polymer Electronic Structure Absorption Calculations

The electronic structure calculations for the trimers for P1-P6 were calculated seen in **Figure 4.7.3.1**. P1, P2, P4, and P5 series of trimers have linear backbones while P3 and P6 are bent. Since the difference between the trimer and the tetramer energies for P1-P6 are small, and due to computational limits, the trimer electronic structure calculations were used to represent the polymer electronic structures for P1-P6.





P3



P6

Figure 4.7.3.1. The electronic structure calculations for the trimers for P1-P6.

The low energy absorption from S_0 to S_1 involves different electronic redistributions for P1 and P4. For P1, the low energy absorption from S_0 to S_1 for P1 involves two major electronic structure contributions. The first electronic structure contributes 85% to the transition. This electronic structure has the electron density delocalized across two donor-acceptor subunits in the ground state. In the excited state the electron density is still delocalized across two donor-acceptor subunits but there is significantly more electron density localized on two acceptors. The second electronic structure contributes 12% to the transition. This electronic structure has the electron density on two alternating donor-acceptor subunits with little to no density on a third

donor monomer that separates the electron density from the two alternating donor-acceptor subunits and a third acceptor that separates the electron density on another two alternating donor-acceptor subunits in the ground state. In the excited state, the electron density is primarily localized on the two acceptors that had electron density in the ground state, but still no electron density between the two acceptor monomers. Whereas, for P4, the low energy absorption from S_0 to S_1 for P4 involves one major electronic structure contribution, which contrasts with P1 which had two major electronic structures contributing to the low energy transition. This electronic structure contributes 88% to the transition. This electronic structure has the electron density delocalized across two donor-acceptor subunits with little electron density on the third donor-acceptor subunits in the ground state. In the excited state, the electron density is primarily delocalized across two donor-acceptor subunits.

The difference in electronic structures for P1 and P4 for the low energy absorption from S_0 to S_1 is attributed to the effect of the two additional thiophene units fused to the donor in P1. The two additional thiophene units fused to the donor not only promotes a more planar donor structure, but it also promotes a more planar polymer backbone. P1 has a more planar polymer backbone compared to P4 and as a result, the electronic transition from the ground state to the excited state involves a transition from a delocalized state to a more localized state with most of the electron density on two acceptor units in P1 whereas for P4, there is still significant electron density on the donor subunit between the two acceptor units which can be seen in **Figure 4.7.3.2**.

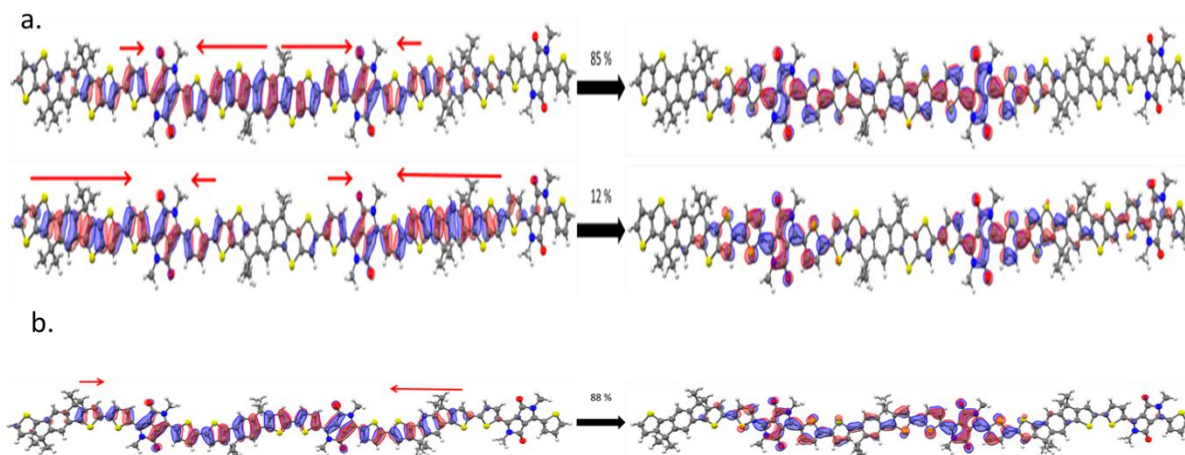


Figure 4.7.3.2. Electronic structure for the ground state (left) and excited state (right) that contribute to the low energy S_0 to S_1 transition for P1 (a.) and P4 (b.). The red arrows represent the qualitative magnitudes of the electron density change.

The high energy absorption involves different electronic states for P1 and P4. The high energy absorption for P1 involves a transition from S_0 to S_{24} , whereas the high energy absorption for P4 involves a transition from S_0 to S_{22} . The higher energy absorption transition from S_0 to S_{24} for P1 involves four major electronic contributions. The first electronic structure contributes 39% to the transition. This electronic structure has the electron density delocalized on two adjacent donor-acceptor subunits with most of the electron density on the donor monomers with little electron density on the two acceptors in the ground state. In the excited state, the electron density is delocalized across one donor-acceptor subunit with some additional electron density on a portion of a second donor-acceptor unit with little electron density shared between the two. The second electronic structure contributes 34% to the transition. This electronic structure has the electron density delocalized across one donor-acceptor subunit with additional electron density on a periphery donor in the ground state. In the excited state, the electron density is delocalized across one donor-acceptor subunit and on an adjacent acceptor with most of the density localized on one acceptor. The third electronic structure contributes 11% to the transition. This electronic structure has the electron density delocalized across two alternating

donor-acceptor subunits in the ground state with little to no electron density shared between the two in the ground state. In the excited state the electron density is transferred to the other half of the trimer with the electron density delocalized across two donor-acceptor subunits. The fourth electronic structure contributes 10% to the transition. The electron density is delocalized most of the trimer with significant density localized on one donor-acceptor subunit in the ground state. In the excited state the electron density is localized on one donor-acceptor subunit with a little electron density located on a periphery acceptor. The higher energy absorption transition from S_0 to S_{22} for P4 was also different from the lower energy absorption transition for P4. The higher energy absorption involves 2 major electronic contributions. The first electronic structure contributes 71% to the transition. This electronic structure has the electron density localized on one donor-acceptor subunit and a little electron density on a second acceptor monomer in the ground state. In the excited state, the electron density is delocalized across two donor-acceptor subunits. The second electronic structure contributes 12% to the transition. This electronic structure has the electron density delocalized across one donor-acceptor subunit and on an adjacent acceptor. In the excited state, the electron density is localized on two acceptor monomers.

The high energy absorption transitions for P1 and P4 are quite different. For P1, the electron density is localized in alternating segments in the ground state and are delocalized across one continuous segment in the excited state. Whereas for P4, the main transition is localized mainly on one donor-acceptor unit in the ground state and delocalized in the excited state and the minor transition is localized on half of the trimer with localization on two acceptors in the excited state. Taken as a whole, the P1 high energy absorption transition is composed of a dispersed electron density across the trimer in the ground state followed by localization on

continuous segment of the trimer, whereas P4 is primarily composed of delocalization of the electron density with some localization on two acceptors in the trimer in the excited state. The additional conjugation of the donor in P1 results in delocalization of the ground state across the polymer backbone, whereas P4 has most of the electron density localized on two acceptors in the ground state which can be seen in **Figure 4.7.3.3**.

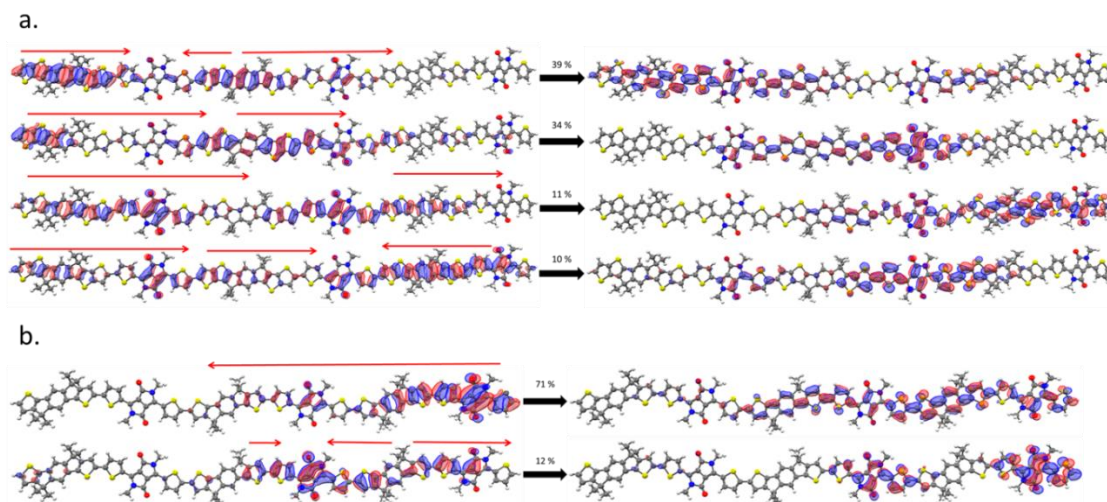


Figure 4.7.3.3. Electronic structure for the ground state (left) and excited state (right) that contribute to the high energy transition for P1 (a.) and P4 (b.). The red arrows represent the qualitative magnitudes of the electron density change.

The low energy absorption for P2 and P5 involves a transition from S_0 to S_1 for both trimers. The low energy absorption transition for both P2 and P5 are quite similar with the electron density delocalized across two donor monomers in the ground state and the electron density localized on two adjacent acceptors in the excited state seen in **Figure 4.7.3.4**. The longer conjugated donor of P2 does not have a pronounced effect on the electronic structures like what was seen for P1 and P4, which may be due to bulky II acceptor having similar interaction with both donor types due to the steric hindrance introduced by II acceptor that is not seen with the less bulky DPP acceptor.

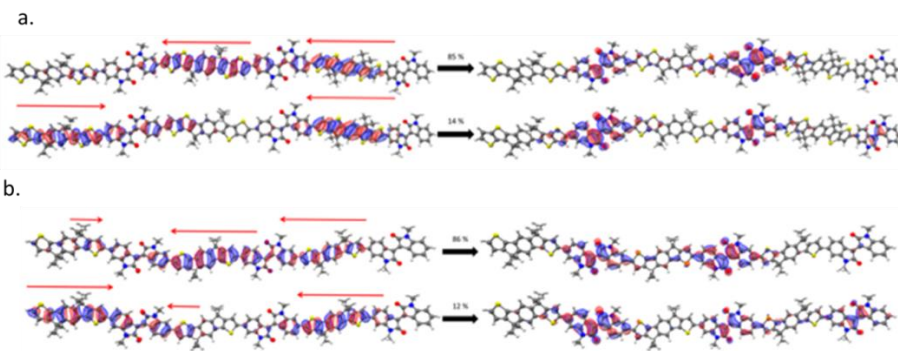


Figure 4.7.3.4. Electronic structure for the ground state (left) and excited state (right) that contribute to the low energy S_0 to S_1 transition for P2 (a.) and P5 (b.). The red arrows represent the qualitative magnitudes of the electron density change.

The high energy absorption transition saw the greatest difference in electronic structures for P2 and P5. The higher energy absorption involves the transition from S_0 to S_{22} for both P2 and P5. For P2, the higher energy absorption involves 2 major electronic contributions. The first electronic structure contributes 81% to the transition. This electronic structure has the electron density delocalized on one donor-acceptor subunit with little electron density on an acceptor monomer on the periphery in the ground state. In the excited state, the electron density is localized on one acceptor subunit with little electron density on an adjacent acceptor monomer in the excited state. The second electronic structure contributes 11% to the transition. The second electronic structure has electron density localized on two adjacent acceptor monomers in the ground state. In the excited state, the electron density is localized on one acceptor monomer with little electron density on an adjacent acceptor. Whereas in P5, the higher energy absorption involves 3 major electronic contributions. The first electronic structure contributes 86% to the transition. This electronic structure has the electron density delocalized on the three acceptor monomers. In the excited state, the electron density is localized on one central acceptor. The second electronic structure contributes 15% to the transition. The second electronic structure has electron density delocalized on one donor-acceptor and an adjacent acceptor monomer in the ground state. In the excited state, the electron density is delocalized on one donor-acceptor

subunit with more electron density on the acceptor monomer. The third electronic structure contributes 13% to the transition. The third electronic structure has the electron density delocalized on one donor-acceptor subunit and an adjacent acceptor monomer. In the excited state, the electron density is delocalized across one donor-acceptor monomer with most of the electron density on the donor monomer.

The influence of the extended conjugation donor on the electronic structures for P2 and P5 can easily be seen for the ground state and excited state structures for the high energy absorption. For P2, with the extended conjugated donor, much of the electron density is localized on the donor in the ground state of the major contributor with the minor contributor having the electron density localized on two acceptors in the ground state. In the excited state for P2, the electron density is localized on one acceptor. Whereas, the dominant electronic structure for P5 has the electron density localized on the three acceptors in the ground state and the minor contributors having the electron density delocalized across a donor-acceptor unit and an additional acceptor in the ground state. The excited state structure has much of the electron density localized on one acceptor but it also has two minor contributors with delocalization across a donor-acceptor unit. Thus the donor has a greater influence in the ground state for P2 and the acceptor in the excited state, whereas the acceptor has greater influence in the ground state for P5 and the donor in the excited state for the high energy absorption which can be seen in **Figure 4.7.3.5**.

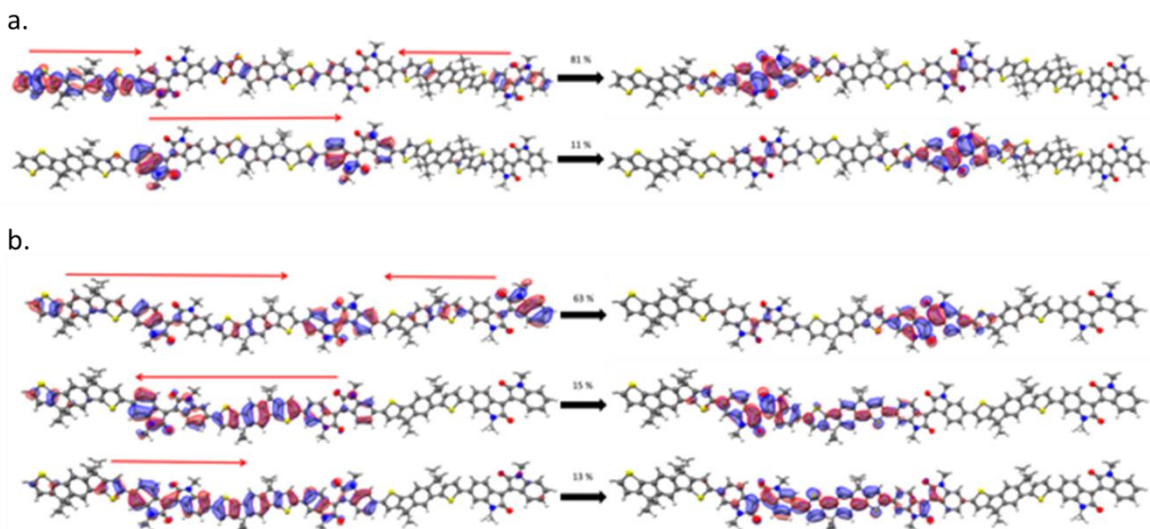


Figure 4.7.3.5. Electronic structure for the ground state (left) and excited state (right) that contribute to the high energy S_0 to S_{22} transition for P2 (a.) and P5 (b.). The red arrows represent the qualitative magnitudes of the electron density change.

The low energy absorption from S_0 to S_1 for P3 and P6 had different electron densities distributed across the trimer backbone. The low energy absorption from S_0 to S_1 for P3 involves one major electronic structure contribution. This electronic structure contributes 91% to the transition. This electronic structure has the electron density delocalized across two donor-acceptor subunits. In the excited state, the electron density is delocalized on one donor-acceptor subunit and an adjacent acceptor. Whereas, the low energy absorption from S_0 to S_1 for P6 involves one major electronic structure contribution. This electronic structure contributes 93% to the transition. This electronic structure has the electron density delocalized across three donor-acceptor subunits. In the excited state, the electron density is delocalized on two donor-acceptor subunits.

Both ground state electronic structures for the S_0 to S_1 transition for P3 and P6 have the electronic density delocalized across the trimer backbone, but in P3 the electronic density is more delocalized across the polymer than it is for P6. This suggests that the longer conjugation of the donor for P3 does not increase the orbital overlap along the backbone. The excited state

electronic structures are quite similar for P3 and P6 with the electron density delocalized over two donor-acceptor units seen in **Figure 4.7.3.6**.

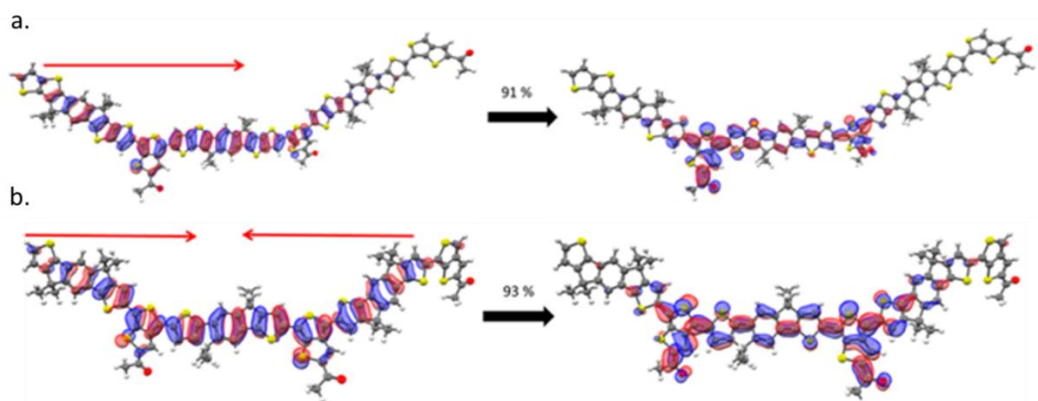


Figure 4.7.3.6. Electronic structure for the ground state (left) and excited state (right) that contribute to the low energy S_0 to S_1 transition for P3 (a.) and P6 (b.). The red arrows represent the qualitative magnitudes of the electron density change.

The high energy absorption from S_0 to S_9 for P3 and P6 had markedly different electronic structures in the ground and excited state. The high energy absorption from S_0 to S_9 for P3 involves one major electronic structure contribution. This electronic structure contributes 86% to the transition. This electronic structure has the electron density delocalized across two donor-acceptor subunits in the ground state. In the excited state, the electron density is delocalized on one donor-acceptor subunit. Whereas the higher energy absorption for P6 involves two major electronic contributions. The first electronic structure contributes 65% to the transition. This electronic structure has the electron density delocalized on two donor-acceptor subunits in the ground state. In the excited state, the electron density is delocalized on two donor-acceptor subunits with most of the density localized on the acceptor monomers. The second electronic structure contributes 23% to the transition. The second electronic structure has electron density localized on three donor-acceptor subunits with little electron density on two of the acceptor monomers in the ground state. In the excited state, the electron density is localized on two acceptor monomers that had little electron density in the ground state.

The high energy absorption from S_0 to S_9 for P3 had the electron density delocalized over fewer donor-acceptor units compared to the ground state electronic structure of P6. Again, the extended conjugation of the donor of P3 fails to increase the orbital mixing across the entire trimer that is seen in P6 for the high energy absorption. While in the excited state, the electron density is localized on one donor-acceptor subunit for P3 whereas the electron density is more localized on the two acceptors with some electron density located on the donor subunits. This demonstrates the different influence that the extended conjugation has on the excited and ground state high energy absorption which can be seen in **Figure 4.7.3.7**.

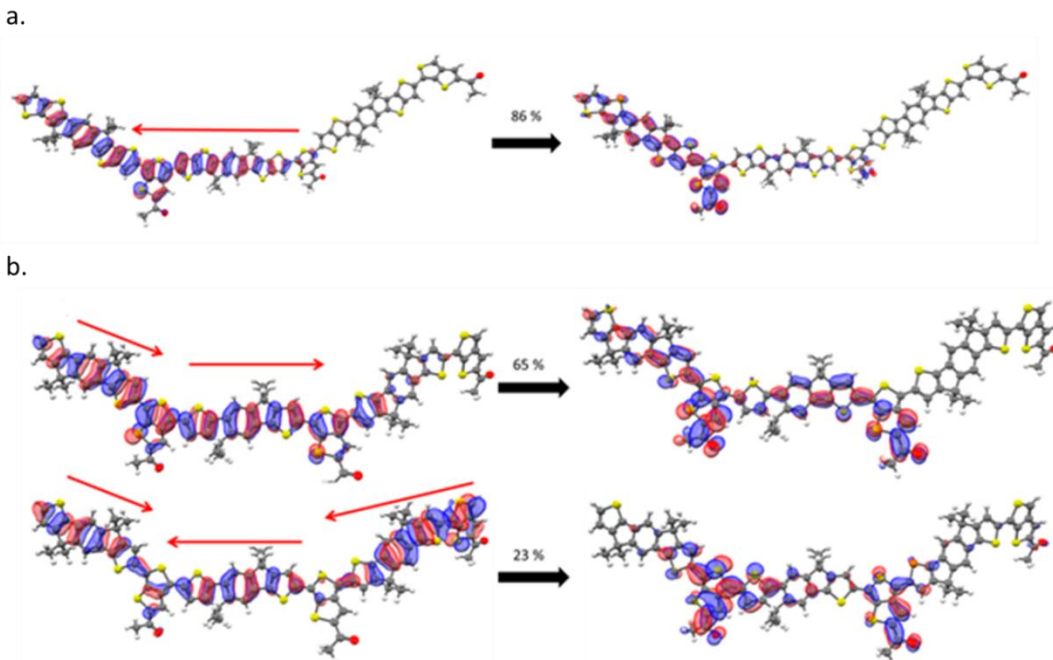


Figure 4.7.3.7. Electronic structure for the ground state (left) and excited state (right) that contribute to the high energy S_0 to S_9 transition for P3 (a.) and P6 (b.). The red arrows represent the qualitative magnitudes of the electron density change.

The acceptor strength did not have an effect on the electron distribution in the ground state for comparative donor analogue trimers for the low energy absorption transition. Whereas the ground state electronic structures had majority of the electron density localized on the donors, in the excited state for the low energy absorption, the electron density is primarily

localized on the acceptors. Indeed, the stronger acceptor polymers had the localization on the acceptors in the excited state, but the weaker electron acceptor polymer had electron density delocalized across a donor-acceptor unit, demonstrating the effect the acceptor strength has on the excited state electron density distribution for the low energy absorption transition. The acceptor strength did not have a discernible pattern for the high energy absorption transition, the ground states were delocalized and the excited states were localized with no apparent trend.

4.8 Two-Photon Absorption

Although electronic structures calculations can give great insight charge transfer within the polymer backbone, two-photon absorption spectroscopy can be used to quantify the charge characteristics of the donor-acceptor polymers.⁸³ The TPA cross sections were determined by using the TPEF method as discussed in the experimental section. An excitation wavelength of 1300 nm was used for P1, P2, P4, P5, and styryl 9m; and emission was collected at 740 nm. The excitation wavelength was chosen for these polymers because they exhibit one photon absorption maxima near 650 nm, and emission was collected at 740 nm after performing wavescans and identifying the emission maxima, which can be blue or red shifted from the one photon emission maxima. An excitation wavelength of 1250 nm was used for P3, P6, and zn-tetra-tert-pc; and the emission was collected at 695 nm. The excitation wavelength was chosen for these polymers because they exhibit one photon absorption maxima near 625 nm, and emission was collected at 695 nm.

The two-photon excited fluorescence as a function of power for the TPA standards and investigated polymers can be seen in **Figure 4.8.1**. The two-photon cross-sections calculated using the comparative method can be seen in **Table 4.8.1**. P1, P2, P4, and P5, the polymers with diketopyrrolopyrrole and isoindigo acceptors, had the highest two photon cross sections as well as the highest two-photon cross-section per repeat unit compared to P3 and P6 with the weaker

acceptors, which is consistent with the trend seen with the calculated TPA cross-sections calculated with BHLYP, seen in **Table 4.8.1**, and with other reports for strong acceptor donor-acceptor organic conjugated molecules.⁸⁴ Whereas P3, which has a weaker dithiophene acceptor, had the lowest TPA cross-section and TPA per repeat unit. The TPA cross-section could not be determined for P6 due to a likely smaller TPA cross-section and smaller QY of P6. Calculations showed that P6 would have the lowest TPA cross-section, and if P6 follows the same trend seen for P1, P2, and P3; it is likely that the P6 would have an even lower TPA cross-section than P3.

The effect of donor conjugation on the TPA cross-section was not so obvious. Calculations have indicated that the extended conjugated donor polymers should have a higher TPA cross-section than their corresponding analogues. Indeed, P1 has a larger TPA cross-section than P3 and presumably P4 has a higher cross-section than P6, according to calculations. But this trend is not seen for P2 and P5. The discrepancy is most likely due to two factors. The emission maxima for P2 and P5 are much further in the NIR, which means the emission collection for the TPEF is collected at the tail of the emission which affects the accuracy of the TPA determination. The efficiency of the PMT also decreases as detection wavelength shifts towards the red, which makes collection difficult. Thus the effects of donor conjugation on the TPA cross section are not clear.

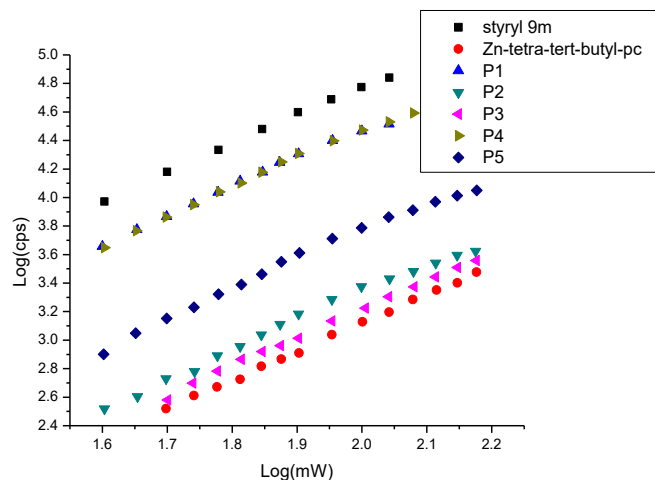


Figure 4.8.1. Logarithmic plot of the quadratic dependence(counts per second vs power) for standards styryl 9m, zn-tetra-tert-butyl-pc, and the investigated polymers. 1300 nm excitation was used for P1, P2, P4, P5, and styryl 9m. 1250 nm excitation was used for P3 and P6(not shown), and zn-tetra-tert-butyl-pc. All have a slope ~ 2 and $R^2 > 0.99$.

Table 4.8.1. TPA cross-section

Sample	TPA cross-section (GM)	BHHLYP TPA cross-section	TPA/RPU
P1	549	52.9	37.2
P2	132	14.9	5.73
P3	0.07	1.0	0.0041
P4	518	42.3	27.2
P5	367	11.4	28.2
P6	-	0.2	-

4.9 Time Resolved Fluorescence

Fluorescence decay dynamics of the investigated polymers were performed in chloroform solutions at the same concentrations that were used for the steady state experiments. The samples were excited at 400 nm and the fluorescence decay dynamics were investigated at 680 nm. The decay dynamics were investigated at 680 nm in order to investigate the polymer's emission maxima as well as avoid the upconverting of the 800 nm gate signal which interferes

with collection at longer sample emission wavelengths due to the upconverting crystal angle. The donor fluorescence decay dynamics were also investigated between 500 nm – 550 nm, but the emission was too weak for the upconverting and collection process. Thus, our study focused on the major emission decay dynamics. Unfortunately, the decay dynamics for P2 and P5 were not able to be investigated due to low quantum yields and their emission maxima were too far into the near-infrared where the gate upconversion signal made it impossible to investigate. To rule out emissive irregularities due to degradation of the sample, steady state absorptions were taken before and after the upconversion experiment. No change in intensity or spectral changes were seen between the steady state absorptions before and after the upconversion experiment, thus no degradation was observed. The decay dynamics can be seen in **Figure 4.9.1**.

The fluorescence decay dynamics were fitted using biexponential functions, the decay times can be seen in **Table 4.9.1**. The investigated polymers had a short initial decay (<3ps) and a longer second decay component. P1 and P4 had the longest long-lived decay components compared to polymers with weaker acceptors, 745 ps and 37 ps, respectively. P3 and P6, which had the weakest acceptors of the investigated polymers, had the shortest long-lived decay components within their respective donor series, 129 ps and 19 ps, respectively. The short initial decay was relatively unaffected by the donor conjugation length and acceptor strength. The short decay component has been attributed to relaxation of the hot excited singlet state and conformational relaxation, and the longer decay component has been attributed to the relaxation of the charge transfer state.^{55,85-88} The polymers with the longer donor conjugation all had significantly longer long-lived decay components compared to their corresponding analogue, about an order of magnitude larger. This is consistent with what others have reported, where the fluorescence rate increases for longer conjugated systems of the same type.⁸⁹ The longer long-

lived decay can be explained by the charge separation that occurs in the excited state and has been seen for other conjugated donor-acceptor systems.⁹⁰ In the excited state, the charge transfer states localize on specific segments, so the probability of recombining for emission is lower for states that are more separated, which occurs when the longer conjugated donor is taken into account resulting in longer fluorescence decay lifetimes.

The importance of the acceptor strength cannot be understated. Too strong of an acceptor can result in electron trapping and exciton trapping.^{55,91-93} Too weak of an acceptor, the exciton lifetime will be too short for the exciton dissociation by an organic accepting material.^{94,95} The polymers with stronger acceptors within the same donor series showed longer exciton life-times than their weaker acceptor counterparts. The DPP acceptor is strong enough to sufficiently promote the charge transfer along the polymer, while not being too strong where the charge is not able to migrate along the polymer backbone before recombining. The TT acceptor is also able to promote the charge transfer, but not to the extent that is seen with the DPP acceptor. This is consistent with the results of the two-photon absorption spectroscopy and electronic structure calculations, with larger charge transfer seen with the polymers with the stronger acceptors.

Table 4.9.1. Fluorescence decay dynamics.

Polymer	τ_1 (ps)	τ_2 (ps)
P1	0.79	745
P3	1.27	129
P4	0.64	37
P6	2.04	19

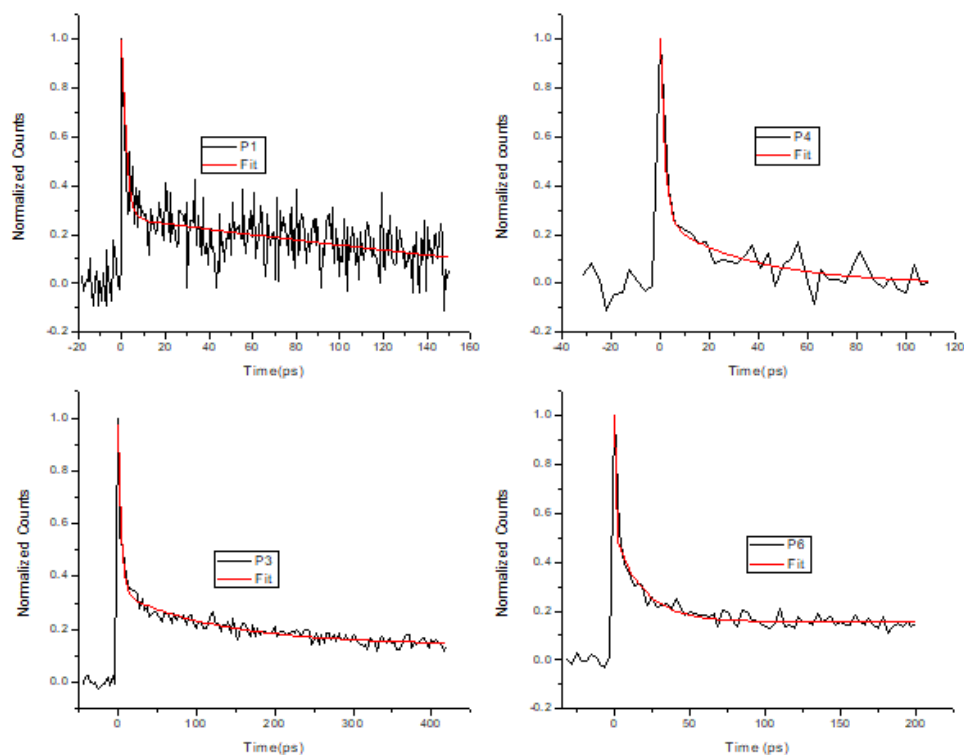


Figure 4.9.1. Fluorescence upconversion of P1 (top left), P4 (top right), P3 (bottom left), and P6 (bottom right) at 400 nm excitation and 680 nm emission.

4.10 Ultrafast Transient Absorption

Ultrafast transient absorption experiments were performed in chloroform solutions at the same concentrations that were used for the steady state experiments. Experiments were carried out by exciting the polymer samples with 400 nm femtosecond pulses and probing the excited state with a white light continuum at different delays, giving insight into the ultrafast excited-state dynamics of the investigated polymers. The transient absorption spectra for P1 and P4 can be seen in **Figure 4.10.1** and the fitted lifetimes can be seen **Table 4.10.1**. The transient absorption spectra for P1 and P4 are quite similar, with a ground state bleach (GSB) near 650 nm and a stimulated emission (SE) near 730 nm with overlap between the two bands. This matches well with the steady state absorption and steady state fluorescence for both polymers. The GSB at ~650 nm for both polymers exhibited a biexponential decay and the SE at ~730 nm for both

polymers exhibited a biexponential decay. The initial decay component of the GSB for both polymers was ~20 ps and is attributed to a hot relaxation to the S_1 state. This was followed by a ~500 ps relaxation from S_1 state to the charge transfer state. This is followed by a <100 ps relaxation from a hot charge transfer state, CT_1 , to a relaxed charge transfer state, CT_0 via SE. This was followed by a relaxation of the charge transfer state to the ground state via SE. The energy level diagrams for the overall photophysical processes for P1 and P4 can be seen in **Figure 4.10.2**. The ground state recovery for the GSB near 650 nm for both polymers was ~500 ps, suggesting that extended conjugation of the donor of P1 had a marginal effect on the ground state recovery. The fast emission process has been attributed to structural relaxation of the polymers, before a slow decay of the charge transfer state back to the ground state.⁹⁶ The SE lifetime of P4 was more than two times longer than the SE of P1, suggesting a greater influence of the donor on the SE dynamics. Interestingly, P1 had a fast GSB with a monoexponential decay at 453 nm of 69 ps, whereas no such process exists for P4, suggesting that the GSB is a result of the extension of the conjugation donor unit changes the relaxation process for the polymer.

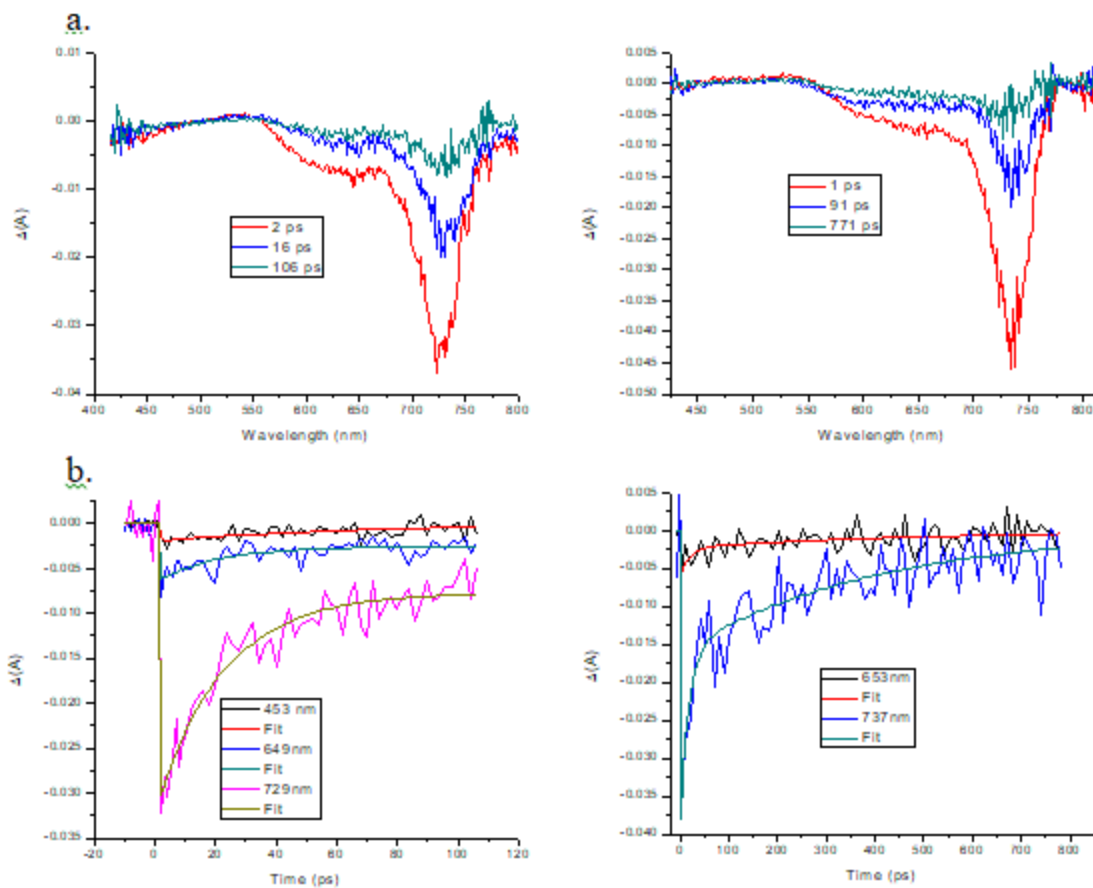


Figure 4.10.1. Transient absorption spectra and kinetic fits of P1 (a.) and P4 (b.).

Table 4.10.1. Transient absorption kinetic fits at selected wavelengths for P1 and P4

P1	Wavelength Nm	τ_1 (ps)	τ_2 (ps)	P4	Wavelength (nm)	τ_1 (ps)	τ_2 (ps)
	453	69	-		453	-	-
	649	20	658		653	19	488
	729	22	435		737	65	1028

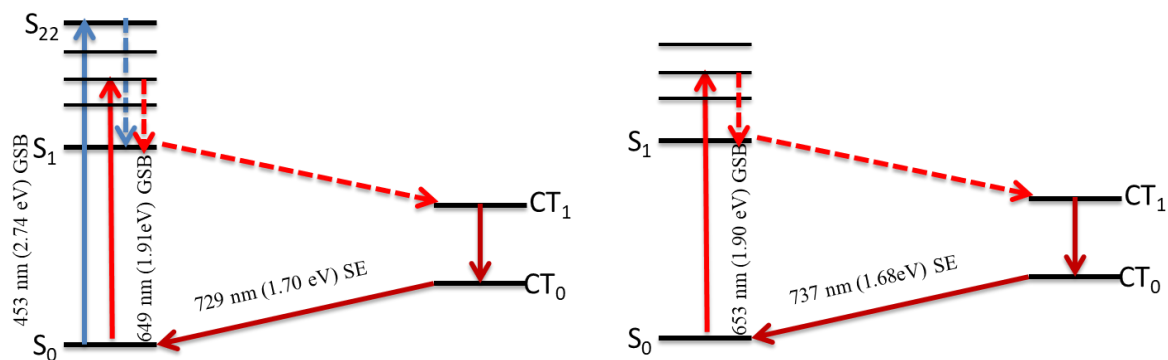


Figure 4.10.2. Energy level diagrams of transient absorption processes for P1 (left) and P4 (right).

The transient absorption spectra for P2 and P5 can be seen in **Figure 4.10.3** and the fitted lifetimes can be seen **Table 4.10.2**. P2 and P5 had a ground state bleach(GSB) near 435 nm and 620 nm and a stimulated emission (SE) near 700 nm with overlap between the later GSB and SE emission peaks. This matches well with the steady state absorption and steady state fluorescence for both polymers. Both polymers also had an ESA at 779 nm that overlaps with the fluorescence seen in the steady state emission spectra. P2 also had an ESA near 500 nm that was not seen for P5. The high energy GSB lifetimes for both polymers were fitted to exponential to monoexponential decays of 531 ps and 644 nm, respectively. The high energy GSB lifetimes were 3 times longer than the lower energy GSB, suggesting two different recovery mechanisms. Both low energy GSB lifetimes exhibited monoexponential decays of approximately 200 ps. The SE for both polymers had a decay time of 200 ps, with a monoexponential decay for P2 and a biexponential decay for P5. The biexponential decay of P5 has a short component of 41 ps that can be attributed to a hot relaxation in the excited state. Interestingly, both polymers had a biexponential ESA at 779 nm of 6ps and ~200 ps, which is the same wavelength that these polymers had fluorescence in the steady state. The energy level diagrams for the overall photophysical processes for P1 and P4 can be seen in **Figure 4.10.4**. The lack of SE at this

wavelength, and strong ESA indicates that excited state absorption cross-section must be larger than the emission cross section at the same wavelength. The changes in the transient absorption spectra of P2 and P5 compared to the other investigated polymers demonstrate the effect that the conjugation of the donor has on the optical properties of these polymers, but also how donor and acceptor interaction can produce major changes to the optical properties.

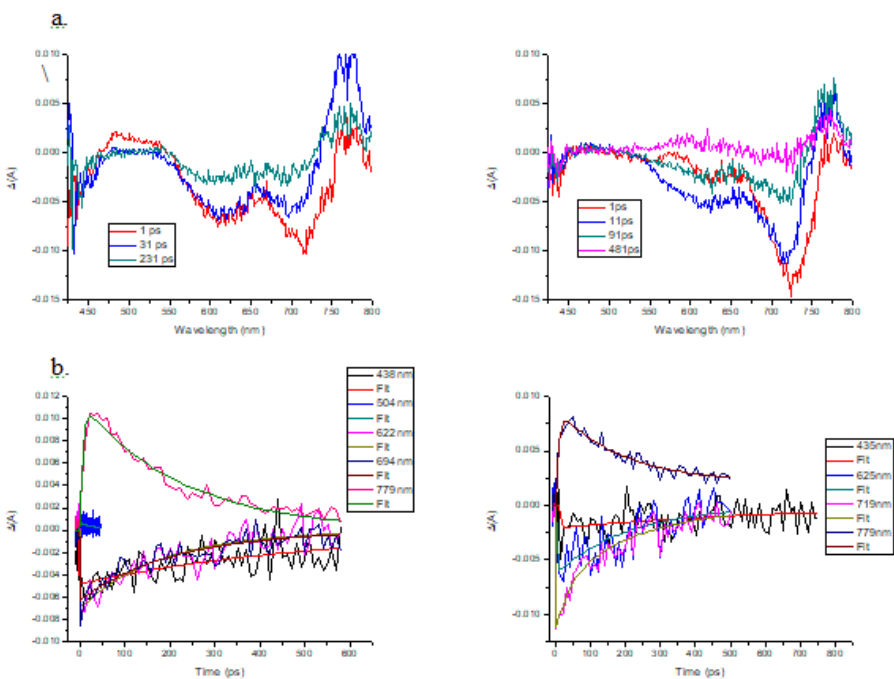


Figure 4.10.3. Transient absorption spectra and kinetic fits of P2 (a.) and P5 (b.).

Table 4.10.2. Transient absorption kinetic fits at selected wavelengths for P2 and P5

P2	Wavelength Nm	τ_1 (ps)	τ_2 (ps)	P5	Wavelength (nm)	τ_1 (ps)	τ_2 (ps)
	438	531	-		435	644	-
	504	45	-		504	-	-
	622	184	-		625	212	-
	694	210	-		719	41	243
	779	6	222		779	6	193

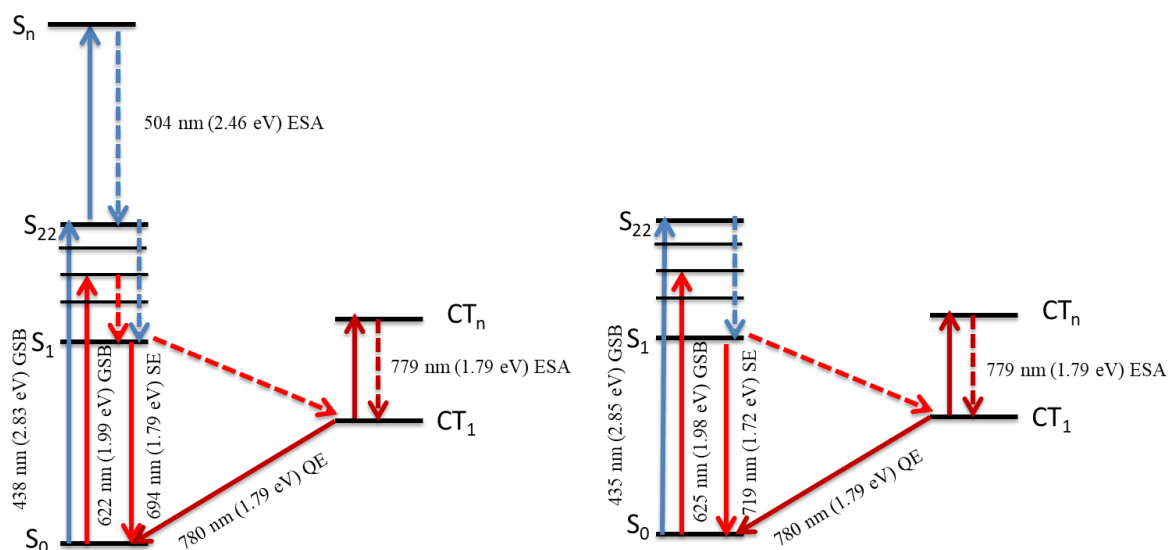


Figure 4.10.4. Energy level diagrams of transient absorption processes for P2 (left) and P5 (right).

The transient absorption spectra for P3 and P6 can be seen in **Figure 4.10.5** and the fitted lifetimes can be seen **Table 4.10.3**. The transient absorption spectra for P3 and P6 are quite similar, with a ground state bleach(GSB) near 460 nm and a GSB near 600 nm with overlap between the two bands, which matches the steady state absorption. There is a weak tail at ~700

nm for P6 that may be stimulated emission, which would match well with the steady state fluorescence, but it is not well resolved due to the strength of the GSB, which is also the case for P3 where the SE, if present, is masked by the strong GSB. The GSB at ~460 nm and ~600 nm for both polymers exhibited a biexponential decay and the SE at ~700 nm for P6 exhibited a biexponential decay. For both GSBs and for both Polymers, the first decay component is ~150 ps and is attributed to the relaxation of the hot excited state to the first excited state, followed by a long decay to the charge transfer state that is longer than the experimental window of this experimental set up. The energy level diagrams for the overall photophysical processes for P3 and P6 can be seen in **Figure 4.10.6**. This is followed by a decay of the hot charge transfer state to a relaxed charge transfer state, which then relaxes to the ground state. The biexponential nature and similar time constants of the GSB at ~460 nm and ~600 nm for both polymers suggests that the extended conjugation of the donor of P3 does not have an effect on the relaxation dynamics. This is a striking finding compared to the stronger acceptor polymers where the extend conjugation donors had other relaxation pathways compared to their less conjugated counterparts. This may be due to the weaker acceptor strength of P3 and P6 as well as the less bulky acceptor compared to polymers with the stronger acceptors. The more bulky acceptor polymers are more constrained due to steric hindrance, whereas the smaller TT acceptors are not impinged by the extended conjugation of the larger donors.

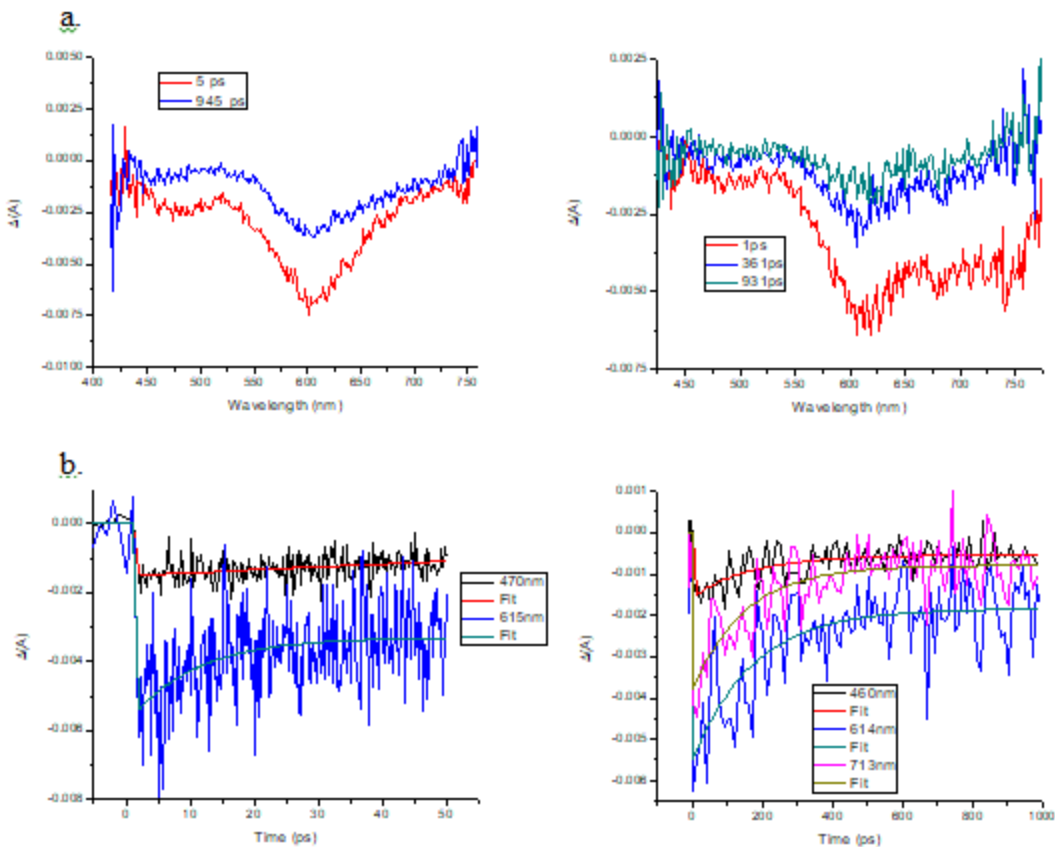


Figure 4.10.5. Transient absorption spectra and kinetic fits of P3 (a.) and P6 (b.).

Table 4.10.3. Transient absorption kinetic fits at selected wavelengths for P3 and P6

P3	Wavelength (nm)	τ_1 (ps)	τ_2 (ps)	P6	Wavelength (nm)	τ_1 (ps)	τ_2 (ps)
	470	151	inf		460	173	inf
	615	159	inf		614	172	inf
	693	-	-		713	150	inf

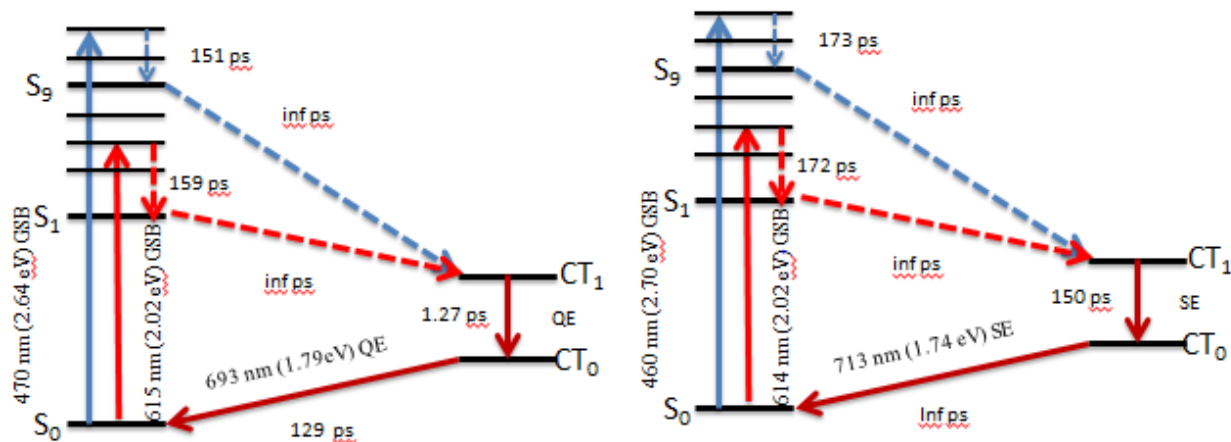


Figure 4.10.6. Energy level diagrams of transient absorption processes for P3 (left) and P6 (right).

4.11 Nanosecond Transient Absorption

As important as the ultrafast photophysical properties are to photovoltaic properties of light harvesting polymers, longer lived excited species also contribute to the overall photophysical properties. Nanosecond transient absorption experiments were conducted in chloroform solution using a LP980 (Edinburgh) system using a Spectra Physics QuantaRay Nd:YAG nanosecond pulsed laser and a GWU Optical Parametric Oscillator (OPO) tunable from 250 nm to 2600 nm. For this investigation 415 nm excitation beam was used as a pump and pulsed xenon lamp white light continuum was used for the probe.

The ultrafast and nanosecond transient absorption spectra for P1 and P4 can be seen in **Figure 4.11.1**. No additional excited states are seen from the ultrafast regime to the longer nanosecond to microsecond regime. This suggests that the larger donor system for this donor-acceptor motif does not result contribute to other excited species at longer timescales in the visible region, although there may be charge separated states or evidence of polaron changes at wavelengths longer than 870 nm, the limitation of the detector.

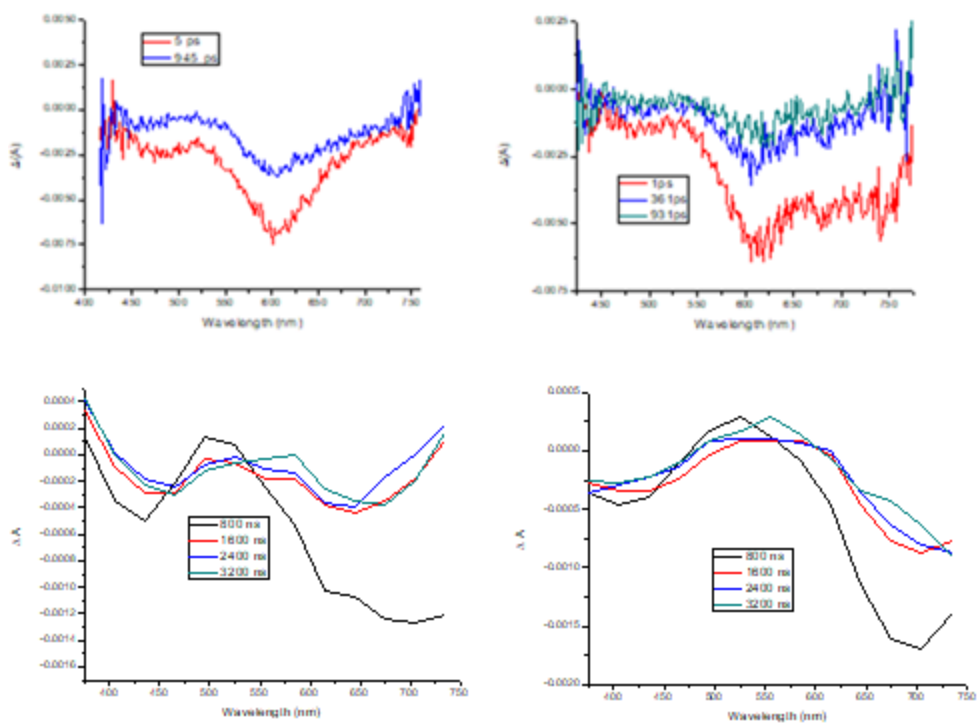


Figure 4.11.1. Ultrafast transient absorption spectra (top) for P1 (left) and P4 (right). Nanosecond transient absorption spectra (bottom) for P1 (left) and P4 (right).

The ultrafast and nanosecond transient absorption spectra for P2 and P5 can be seen in **Figure 4.11.2**. Whereas there was no notable difference in ultrafast and nanosecond transient for the P1 and P4 with the stronger acceptor system, there are significant differences between P2 and P5 in the ultrafast regime and nanosecond regime, and between the two polymers. For P2 in the ultrafast there is a bleach at 430 nm, an ESA at ~500 nm, and a bleach and SE from 600 nm to 750 nm. Whereas in the longer than a nanosecond regime, a bleach at 430 nm and an ESA from 500 nm to 700 nm. This suggests that after the initial singlet state is formed, a long lived triplet state is formed at lower energies. Whereas for P5 an excited state absorption is not seen at lower wavelengths in the ultrafast regime and in the nanosecond regime the bleach in the low energy and high energy regions still persists. This suggests that the larger donor system of P2 contributes to the promotion of the triplet state which is not seen for P5.

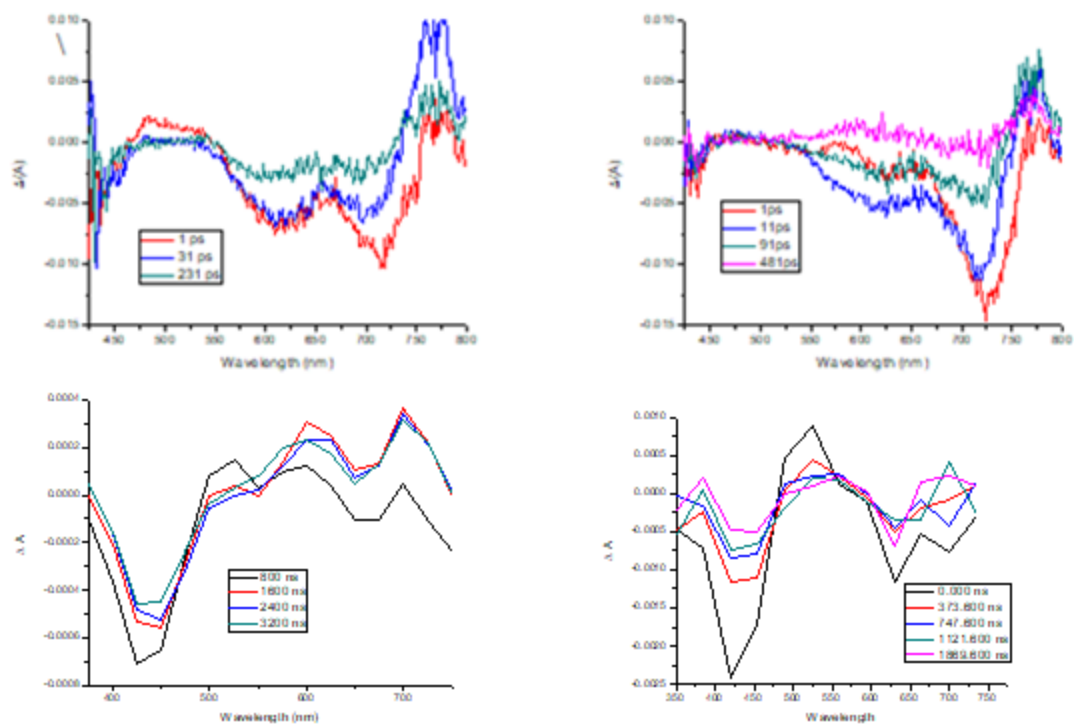


Figure 4.11.2. Ultrafast transient absorption spectra (top) for P2 (left) and P5 (right). Nanosecond transient absorption spectra (bottom) for P2 (left) and P5 (right).

The ultrafast and nanosecond transient absorption spectra for P3 and P6 can be seen in **Figure 4.11.3**. There are significant differences between P3 and P6 in the nanosecond regime, whereas the dynamics are quite similar in the ultrafast regime. In the ultrafast regime, there is a bleach in the 430 nm region and 630 nm region for both polymers. In the nanosecond transient absorption spectra, P3 has a bleach from 400 nm to 650 nm, but there is an excited state absorption near 700 nm, whereas for P6 there is only a bleach from 400 nm to 800 nm. This suggests that the larger donor of P3 also contributes to triplet state which is not seen for P6. This is similar to the results obtained for P2, suggesting that the donor system has more influence on the triplet state for weaker acceptor systems.

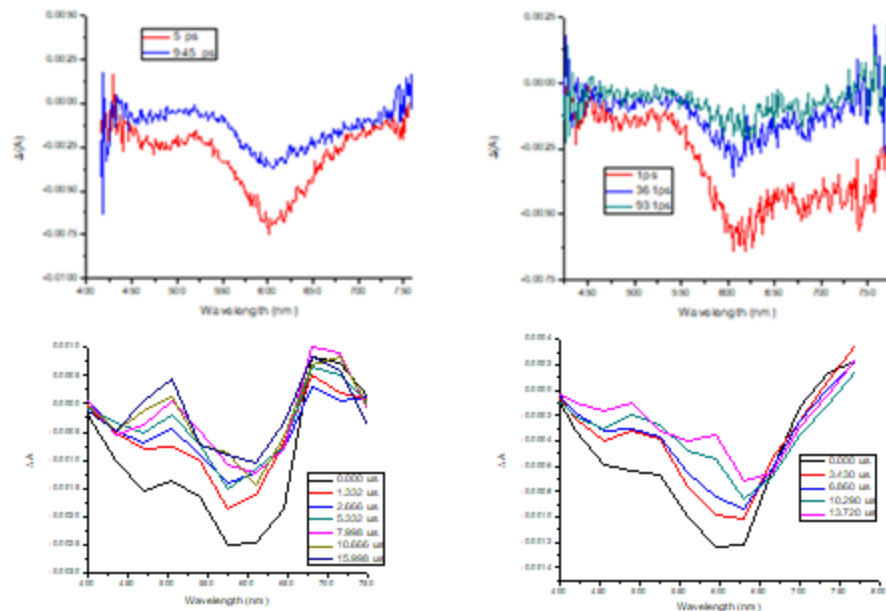


Figure 4.11.3. Ultrafast transient absorption spectra (top) for P3 (left) and P6 (right). Nanosecond transient absorption spectra (bottom) for P3 (left) and P6 (right).

4.12 Conclusion

Solar harvesting is the future for energy generation. Currently there is a rapid increase in technology improvements and mass implementation around the world. Light harvesting donor-acceptor polymers are going to play a significant role in this market because they are lightweight, easily processable, strong absorption properties, and ease of manufacturing. In this study the optical properties of six polymers were investigated. The polymers consisted of either a DPP, II, or TT acceptor with a s-indacene donors with a thiophene fused on either end or with a thienothiophene fused on either end, increasing the conjugation length of the donor. The polymers with the extended conjugated donor had significantly enhanced absorption capabilities. The fluorescence upconversion results showed longer excitonic lifetimes for the extended conjugated donor systems. Computations and TPA experiments showed that the extended conjugated polymers had enhanced charge transfer characteristics. Investigation of the excited state dynamics showed new optical species for the extended donor polymers. This work has

shown the pronounce effect that donor conjugation has on the optical properties of donor-acceptor light-harvesting conjugated polymers, which will help in the design and synthesis of new donor-acceptor polymers for organic photovoltaics.

References

- (1) Wolfram, C.; Shelef, O.; Gertler, P. How Will Energy Demand Develop in the Developing World? *J. Econ. Perspect.* **2012**, *26* (1), 119–138.
- (2) Walker, R. J. Population Growth and Its Implications for Global Security. *Am. J. Econ. Sociol.* **2016**, *75* (4), 980–1004.
- (3) Withagen, C. Pollution and Exhaustibility of Fossil Fuels. *Resour. Energy Econ.* **1994**, *16*, 235–242.
- (4) Gibson, L.; Wilman, E. N.; Laurance, F. How Green Is “ Green ” Energy ? *Trends Ecol. Evol.* **2017**, *32* (12), 922–935.
- (5) Ragoussi, M.-E.; Torres, T. New Generation Solar Cells Concepts, Trends. *Chem. Commun.* **2015**, *51*, 3957–3972.
- (6) Miles, R. W.; Hynes, K. M.; Forbes, I. Photovoltaic Solar Cells : An Overview of State-of-the-Art Cell Development and Environmental Issues. *Prog. Cryst. Growth Charact. Mater.* **2005**, *51*, 1–42.
- (7) Paggi, M.; Berardone, I.; Infuso, A.; Corrado, M. Fatigue Degradation and Electric Recovery in Silicon Solar Cells Embedded in Photovoltaic Modules. *Sci. Rep.* **2014**, *4*, 1–7.
- (8) Shi, G.; Kioupakis, E. Electronic and Optical Properties of Nanoporous Silicon for Solar-Cell Applications. *ACS Photonics* **2015**, *2* (2), 208–215.
- (9) Deligiannis, D.; Vasudevan, R.; Smets, A. H. M.; van Swaaij, R. A. C. M. M.; Zeman, M. Surface Passivation of c-Si for Silicon Heterojunction Solar Cells Using High-Pressure Hydrogen Diluted Plasmas. *AIP Adv.* **2015**, *5* (9), 1–8.
- (10) Babayigit, A.; Ethirajan, A.; Muller, M.; Conings, B. Toxicity of Organometal Halide Perovskite Solar Cells. *Nat. Mater.* **2016**, *15* (3), 247–251.
- (11) Günes, S.; Neugebauer, H.; Sariciftci, N. S. Conjugated Polymer-Based Organic Solar Cells. *Chem. Rev.* **2007**, *107* (4), 1324–1338.
- (12) Vezie, M. S.; Few, S.; Meager, I.; Pieridou, G.; Dörling, B.; Ashraf, R. S.; Goñi, A. R.; Bronstein, H.; Mcculloch, I.; Hayes, S. C.; et al. Exploring the Origin of High Optical Absorption in Conjugated Polymers. *Nat. Mater.* **2016**, *15*, 746–753.
- (13) Seo, J. H.; Um, H. D.; Shukla, A.; Hwang, I.; Park, J.; Kang, Y. C.; Kim, C. S.; Song, M.; Seo, K. Low-Temperature Solution-Processed Flexible Organic Solar Cells with PFN/AgNWs Cathode. *Nano Energy* **2015**, *16*, 122–129.
- (14) Zhong, H.; Li, Z.; Buchaca-Domingo, E.; Rossbauer, S.; Watkins, S. E.; Stingelin, N.; Anthopoulos, T. D.; Heeney, M. Low Band Gap Dithienogermolodithiophene Copolymers

- with Tunable Acceptors and Side-Chains for Organic Solar Cells. *J. Mater. Chem. A* **2013**, *1* (47), 14973–14981.
- (15) Huang, H.; Yang, L.; Sharma, B. Recent Advances in Organic Ternary Solar Cells. *J. Mater. Chem. A* **2017**, *5* (23), 11501–11517.
 - (16) Zhang, Z. G.; Wang, J. Structures and Properties of Conjugated Donor – Acceptor Copolymers for Solar Cell Applications. *J. Mater. Chem* **2012**, *22*, 4178–4187.
 - (17) Pai, R. K.; T. N., A.; B., H. Rational Design of Benzodithiophene Based Conjugated Polymers for Better Solar Cell Performance. *RSC Adv.* **2016**, *6* (28), 23760–23774.
 - (18) Homyak, P. D.; Tinkham, J.; Lahti, P. M.; Coughlin, E. B. Thieno [3 , 4 - B] Thiophene Acceptors with Alkyl , Aryl , Perfluoroalkyl , and Perfluorophenyl Pendants for Donor – Acceptor Low Bandgap Polymers. *Macromolecules* **2013**, *46*, 8873–8881.
 - (19) Liang, Y.; Xu, Z.; Xia, J.; Tsai, S. T.; Wu, Y.; Li, G.; Ray, C.; Yu, L. For the Bright Future-Bulk Heterojunction Polymer Solar Cells with Power Conversion Efficiency of 7.4%. *Adv. Mater.* **2010**, *22*, 135–138.
 - (20) Akbayrak, M.; Önal, A. M. Synthesis and Electrochemical Polymerization of Diketopyrrolopyrrole Based Donor–acceptor–donor Monomers Containing 3,6- and 2,7-Linked Carbazoles. *Polym. Chem.* **2016**, *7* (39), 6110–6119.
 - (21) Xie, H.; Zhang, K.; Duan, C.; Liu, S.; Huang, F.; Cao, Y. New Acceptor-Pended Conjugated Polymers Based on 3,6- and 2,7-Carbazole for Polymer Solar Cells. *Polymer (Guildf)*. **2012**, *53* (25), 5675–5683.
 - (22) Jiaoli, Li, Andrew C., G. Carbazole-Based Polymers for Organic Photovoltaic Devices. *Chem. Soc. Rev.* **2010**, *39* (7), 2399–2410.
 - (23) Li, Y.; Gu, M.; Pan, Z.; Zhang, B.; Yang, X. Indacenodithiophene : A Promising Building Block for High Performance Polymer Solar Cells. *J. Mater. Chem. A Mater. energy Sustain.* **2017**, *5*, 10798–10814.
 - (24) Zhang, X.; Bronstein, H.; Kronemeijer, A. J.; Smith, J.; Kim, Y.; Kline, R. J.; Richter, L. J.; Anthopoulos, T. D.; Sringhaus, H.; Song, K.; et al. Molecular Origin of High Field-Effect Mobility in an Indacenodithiophene- Benzothiadiazole Copolymer. *Nat. Commun.* **2013**, *4*, 1–9.
 - (25) Zhao, W.; Qian, D.; Zhang, S.; Li, S.; Inganäs, O.; Gao, F. Fullerene-Free Polymer Solar Cells with over 11 % Efficiency and Excellent Thermal Stability. *Adv. Mater.* **2016**, 4734–4739.
 - (26) Falzon, M.-F.; Zoombelt, A. P.; Wienk, M. M.; Janssen, R. A. J. R. a J. Diketopyrrolopyrrole-Based Acceptor Polymers for Photovoltaic Application. *Phys. Chem. Chem. Phys.* **2011**, *13* (19), 8931–8939.
 - (27) Turbiez, M.; Leeuw, D. M. De; Janssen, A. J. Poly (Diketopyrrolopyrrole - Terthiophene) for Ambipolar Logic and Photovoltaics. *J am chem Soc Commun.* **2009**, *131*, 16616–16617.
 - (28) Mori, H.; Suetsugu, M.; Nishinaga, S.; Chang, N.; Nonobe, H.; Okuda, Y.; Nishihara, Y. Synthesis, Characterization, and Solar Cell and Transistor Applications of phenanthro[1,2-

- B*:8,7-*B'*]dithiophene-Diketopyrrolopyrrole Semiconducting Polymers. *J. Polym. Sci. Part A Polym. Chem.* **2015**, *53* (5), 709–718.
- (29) Li, W.; Hendriks, K. H.; Wienk, M. M.; Janssen, R. A. J. Diketopyrrolopyrrole Polymers for Organic Solar Cells. *Acc. Chem. Res.* **2016**, *49*, 78–85.
- (30) Grand, C.; Baek, S.; Lai, T. H.; Deb, N.; Zajaczkowski, W.; Stalder, R.; Müllen, K.; Pisula, W.; Bucknall, D. G.; So, F.; et al. Structure-Property Relationships Directing Transport and Charge Separation in Isoindigo Polymers. *Macromolecules* **2016**, *49* (11), 4008–4022.
- (31) Estrada, L. A.; Stalder, R.; Abboud, K. A.; Risko, C.; Brédas, J. L.; Reynolds, J. R. Understanding the Electronic Structure of Isoindigo in Conjugated Systems: A Combined Theoretical and Experimental Approach. *Macromolecules* **2013**, *46* (22), 8832–8844.
- (32) Duan, C.; Huang, F.; Cao, Y. Recent Development of Push–pull Conjugated Polymers for Bulk-Heterojunction Photovoltaics: Rational Design and Fine Tailoring of Molecular Structures. *J. Mater. Chem.* **2012**, *22* (21), 10416–10434.
- (33) Stalder, R.; Mei, J.; Graham, K. R.; Estrada, L. A.; Reynolds, J. R. Isoindigo, a Versatile Electron-Deficient Unit For High-Performance Organic Electronics. *Chem. Mater.* **2014**, *26*, 664–678.
- (34) Cinar, M. E.; Ozturk, T. Thienothiophenes, Dithienothiophenes, and Thienoacenes: Syntheses, Oligomers, Polymers, and Properties. *Chem. Rev.* **2015**, *115*, 3096–3140.
- (35) Deka, B. C.; Purkayastha, S. K.; Sharma, H.; Bhattacharyya, P. K. Ground and Excited States of Neutral and Cationic thieno[3,2-*B*]thiophene: A DFT Study. *Comput. Theor. Chem.* **2016**, *1091*, 41–48.
- (36) Singh, R.; Pagona, G.; Gregoriou, V. G.; Tagmatarchis, N.; Toliopoulos, D.; Han, Y.; Fei, Z.; Katsouras, A.; Avgeropoulos, A.; Anthopoulos, T. D.; et al. The Impact of Thienothiophene Isomeric Structures on the Optoelectronic Properties and Photovoltaic Performance in Quinoxaline Based Donor–acceptor Copolymers. *Polym. Chem.* **2015**, *6* (16), 3098–3109.
- (37) Výprachtický, D.; Demirtas, I.; Dzhabarov, V.; Pokorná, V.; Ertas, E.; Ozturk, T.; Cimrová, V. New Copolymers with thieno[3,2-*B*]thiophene or dithieno[3,2-*b*:2',3'-*D*]thiophene Units Possessing Electron-Withdrawing 4-Cyanophenyl Groups: Synthesis and Photophysical, Electrochemical, and Electroluminescent Properties. *J. Polym. Sci. Part A Polym. Chem.* **2017**, *55* (16), 2629–2638.
- (38) Niimi, K.; Shinamura, S.; Osaka, I.; Miyazaki, E.; Takimiya, K. Dianthra[2,3-*b*:2',3'-*F*]thieno[3,2-*B*]Thiophene (DATT): Synthesis, Characterization, and FET Characteristics of New π -Extended Heteroarene with Eight Fused Aromatic Rings. *J. Am. Chem. Soc.* **2011**, *133* (22), 8732–8739.
- (39) Chochos, C. L.; Kalogirou, A. S.; Ye, T.; Tatsi, E.; Katsouras, A.; Zissimou, G. A.; Gregoriou, V. G.; Avgeropoulos, A.; Koutentis, P. A. 4H-1,2,6-Thiadiazine-Containing Donor-Acceptor Conjugated Polymers: Synthesis, Optoelectronic Characterization and Use in Organic Solar Cells. *J. Mater. Chem. C* **2017**, 1–10.
- (40) Nagarjuna, P.; Bagui, A.; Garg, A.; Gupta, V.; Singh, S. P. One-Step Synthesis of New

- Electron Acceptor for High Efficiency Solution Processable Organic Solar Cells. *J. Phys. Chem. C* **2017**, *121*, 26615–26621.
- (41) Adam, G.; Munkhbat, B.; Denk, P.; Ulbricht, C.; Hrelescu, C.; Scharber, M. C. Different Device Architectures for Bulk-Heterojunction Solar Cells. *Front. Mater.* **2016**, *3*, 1–10.
- (42) Ltaief, A.; Davenas, J.; Bouazizi, A.; Chaâbane, R. Ben; Alcouffe, P.; Ouada, H. Ben. Film Morphology Effects on the Electrical and Optical Properties of Bulk Heterojunction Organic Solar Cells Based on MEH-PPV/C60 Composite. *Mater. Sci. Eng. C* **2005**, *25* (1), 67–75.
- (43) Erb, T.; Zhokhavets, U.; Gobsch, G.; Raleva, S.; Stühn, B.; Schilinsky, P.; Waldauf, C.; Brabec, C. J. Correlation between Structural and Optical Properties of Composite Polymer/fullerene Films for Organic Solar Cells. *Adv. Funct. Mater.* **2005**, *15* (7), 1193–1196.
- (44) Trukhanov, V. A.; Bruevich, V. V.; Paraschuk, D. Y. Fill Factor in Organic Solar Cells Can Exceed the Shockley-Queisser Limit. *Sci. Rep.* **2015**, *5*, 1–10.
- (45) Street, R. A. Carrier Mobility, Structural Order, and Solar Cell Efficiency of Organic Heterojunction Devices. *Appl. Phys. Lett.* **2008**, *93* (13), 1–3.
- (46) Kupijai, A. J.; Behringer, K. M.; Schaeble, F. G.; Galfe, N. E.; Corazza, M.; Gevorgyan, S. A.; Krebs, F. C.; Stutzmann, M.; Brandt, M. S. Bipolar Polaron Pair Recombination in Polymer/fullerene Solar Cells. *Phys. Rev. B - Condens. Matter Mater. Phys.* **2015**, *92* (24), 1–8.
- (47) Street, R. A. Electronic Structure and Properties of Organic Bulk-Heterojunction Interfaces. *Adv. Mater.* **2016**, *28* (20), 3814–3830.
- (48) Larson, B. W.; Reid, O. G.; Coffey, D. C.; Avdoshenko, S. M.; Popov, A. A.; Boltalina, O. V.; Strauss, S. H.; Kopidakis, N.; Rumbles, G. Inter-Fullerene Electronic Coupling Controls the Efficiency of Photoinduced Charge Generation in Organic Bulk Heterojunctions. *Adv. Energy Mater.* **2016**, *6* (24), 1–11.
- (49) Serbenta, A.; Kozlov, O. V.; Portale, G.; Van Loosdrecht, P. H. M.; Pshenichnikov, M. S. Bulk Heterojunction Morphology of Polymer:fullerene Blends Revealed by Ultrafast Spectroscopy. *Sci. Rep.* **2016**, *6*, 1–11.
- (50) Kose, M. E. Evaluation of Acceptor Strength in Thiophene Coupled Donor – Acceptor Chromophores for Optimal Design of Organic Photovoltaic Materials. *J. Phys. Chem. A* **2012**, *116*, 11503–12509.
- (51) Creamer, A.; Casey, A.; Marsh, A. V.; Shahid, M.; Gao, M.; Heeney, M. Systematic Tuning of 2,1,3-Benzothiadiazole Acceptor Strength by Monofunctionalization with Alkylamine, Thioalkyl, or Alkoxy Groups in Carbazole Donor-Acceptor Polymers. *Macromolecules* **2017**, *50* (7), 2736–2746.
- (52) Kim, B. G.; Ma, X.; Chen, C.; Ie, Y.; Coir, E. W.; Hashemi, H.; Aso, Y.; Green, P. F.; Kieffer, J.; Kim, J. Energy Level Modulation of HOMO, LUMO, and Band-Gap in Conjugated Polymers for Organic Photovoltaic Applications. *Adv. Funct. Mater.* **2013**, *23* (4), 439–445.
- (53) Adegoke, O. O.; Jung, I. H.; Orr, M.; Yu, L.; Goodson III, T. G. Investigations of the

- Effect of the Acceptor Strength on the Optical and Electronic Properties in Conjugated Polymers for Solar Applications. *J. Am. Chem. Soc.* **2015**, 150407115828001.
- (54) Wan, Q.; Guo, X.; Wang, Z.; Li, W.; Guo, B.; Ma, W.; Zhang, M.; Li, Y. 10.8% Efficiency Polymer Solar Cells Based on PTB7-Th and PC71BM via Binary Solvent Additives Treatment. *Adv. Funct. Mater.* **2016**, 26 (36), 6635–6640.
- (55) Keller, B.; McLean, A.; Kim, B.-G.; Chung, K.; Kim, J.; Goodson, T. Ultrafast Spectroscopic Study of Donor–Acceptor Benzodithiophene Light Harvesting Organic Conjugated Polymers. *J. Phys. Chem. C* **2016**, acs.jpcc.6b01727.
- (56) Cravino, A. Origin of the Open Circuit Voltage of Donor-Acceptor Solar Cells: Do Polaronic Energy Levels Play a Role? *Appl. Phys. Lett.* **2007**, 91 (24), 1–4.
- (57) Chen, S.; Zhang, D.; Wang, M.; Kong, L.; Zhao, J. Donor–acceptor Type Polymers Containing the 2,3-bis(2-Pyridyl)-5,8-Dibromoquinoxaline Acceptor and Different Thiophene Donors: Electrochemical, Spectroelectrochemistry and Electrochromic Properties. *New J. Chem.* **2016**, 40 (3), 2178–2188.
- (58) Osaka, I.; Abe, T.; Shimawaki, M.; Koganezawa, T.; Takimiya, K. Naphthodithiophene-Based Donor-Acceptor Polymers: Versatile Semiconductors for OFETs and OPVs. *ACS Macro Lett.* **2012**, 1 (4), 437–440.
- (59) Beaujuge, P. M.; Subbiah, J.; Choudhury, K. R.; Ellinger, S.; McCarley, T. D.; So, F.; Reynolds, J. R. Green Dioxythiophene-Benzothiadiazole Donor-Acceptor Copolymers for Photovoltaic Device Applications. *Chem. Mater.* **2010**, 22 (6), 2093–2106.
- (60) Gokce, G.; Karabay, B.; Cihaner, A.; Icli Ozkut, M. [1,2,5]thiadiazolo[3,4-G]quinoxaline Acceptor-Based Donor–acceptor–donor-Type Polymers: Effect of Strength and Size of Donors on the Band Gap. *J. Polym. Sci. Part A Polym. Chem.* **2017**, 55 (20), 3483–3493.
- (61) Zhao, D.; Li, L.; Lo, W.; Zhang, N.; Goodson, T.; Yu, L. Two Photon Absorption Study of Low-Bandgap, Fully Conjugated Perylene Diimide-Thienoacene-Perylene Diimide Ladder-Type Molecules. *Chem. Mater.* **2017**, 29, 6726–6732.
- (62) Berezin, M. Y.; Zhan, C.; Lee, H.; Joo, C.; Akers, W. J.; Yazdanfar, S.; Achilefu, S. Two-Photon Optical Properties of near-Infrared Dyes at 1.55 Mm Excitation. *J. Phys. Chem. B* **2011**, 115 (39), 11530–11535.
- (63) Williams, A. T. R.; Winfield, S. A.; Miller, J. N. Relative Fluorescence Quantum Yields Using a Computer-Controlled Luminescence Spectrometer. *Analyst* **1983**, 108, 1067–1071.
- (64) Seybold, P. G.; Gouterman, M. Porphyrins. *J. Mol. Spectrosc.* **1969**, 31, 1–13.
- (65) McLean, A. M.; Socher, E.; Varnavski, O.; Clark, T. B.; Imperiali, B.; Goodson, T. Two-Photon Fluorescence Spectroscopy and Imaging of 4-Dimethylaminonaphthalimide Peptide and Protein Conjugates. *J. Phys. Chem. B* **2013**, 117 (50), 15935–15942.
- (66) Makarov, N. S.; Drobizhev, M.; Rebane, A. Two-Photon Absorption Standards in the 550–1600 Nm Excitation Wavelength Range. *Opt. Express* **2008**, 16 (6), 4029–4047.
- (67) Adegoke, O. O.; Ince, M.; Mishra, A.; Green, A.; Varnavski, O.; Martínez-Díaz, M. V.; Bäuerle, P.; Torres, T.; Goodson, T. Synthesis and Ultrafast Time Resolved Spectroscopy

- of Peripherally Functionalized Zinc Phthalocyanine Bearing Oligothiénylene-Ethynylene Subunits. *J. Phys. Chem. C* **2013**, *117*, 20912–20918.
- (68) Flynn, D. C.; Ramakrishna, G.; Yang, H.; Northrop, B. H.; Stang, P. J.; Iii, T. G. Ultrafast Optical Excitation in Supramolecular Metallacycles with Charge Transfer Properties. *J. Am. Chem. Soc.* **2010**, No. 14, 1348–1358.
- (69) Shin, N.; Yun, H.; Yoon, Y.; Son, H. J.; Ju, S.; Kwon, S.; Kim, B.; Kim, Y. Highly Stable Polymer Solar Cells Based on Poly (Dithienobenzodithiophene- Co -Thienothiophene). *Macromolecules* **2015**, *48*, 3890–3899.
- (70) Teng, W.; Ye, Q.; Ting, T.; Jin, S.; Xu, J. 4,9-Dihydro-S-indaceno[1,2-b:5,6-B']dithiophene-Embedded Electrochromic Conjugated Polymers with High Coloration Efficiency and Fast Coloration Time. *Sol. Energy Mater. Sol. Cells* **2015**, *136*, 92–99.
- (71) Schneider, J. A.; Dadvand, A.; Wen, W.; Perepichka, D. F. Tuning the Electronic Properties of Poly(thienothiophene Vinylene)s via Alkylsulfanyl and Alkylsulfonyl Substituents. **2013**.
- (72) Gettinger, C. L.; Heeger, A. J.; Drake, J. M.; Pine, D. J. THE EFFECT OF INTRINSIC RIGIDITY ON THE OPTICAL PROPERTIES OF PPV. *Mol. Cryst. Liq. Cyst.* **1994**, *256*, 507–512.
- (73) Nijegorodov, D. The Influence of Planarity and Rigidity on the Absorption and Fluorescence Parameters and Intersystem Crossing Rate Constant in Aromatic Molecules. *J. Phys. Chem. B* **1994**, *98*, 5639–5643.
- (74) Salzner, U. Effect of Donor – Acceptor Substitution on Optoelectronic Properties of Conducting Organic Polymers. *J. Chem. Theory Comput.* **2014**, *10*, 4921–4937.
- (75) Demchenko, A. P.; Tomin, V. I.; Chou, P. Breaking the Kasha Rule for More Efficient Photochemistry. *Chem. Rev.* **2017**, *117*, 13353–13381.
- (76) Lim, T.; Hsiang, J.; White, J. D.; Hsu, J. H.; Fan, Y. L.; Lin, K. F.; Fann, W. S. Single Short-Chain Conjugated Polymer Studied with Optical Spectroscopy : A Donor-Acceptor System. *Phys. Rev. B* **2007**, *75*, 1–9.
- (77) Yamaguchi, Y.; Matsubara, Y.; Ochi, T.; Wakamiya, T.; Yoshida, Z. How the π Conjugation Length Affects the Fluorescence Emission Efficiency. *J am chem Soc Commun.* **2008**, *130*, 13867–13869.
- (78) Zheleznova, Y.; Andryukhova, K. V; Fisyuk, A. S. Effect of Donor to Acceptor Ratio on Electrochemical and Spectroscopic Properties of Oligoalkylthiophene 1,3,4-Oxadiazole Derivatives. *Phys. Chem. Chem. Phys.* **2017**, *19*, 30261–30276.
- (79) Mi, S.; Wu, J.; Liu, J.; Zheng, J.; Xu, C. Donor – P -Bridge – Acceptor Fluorescent Polymers Based on Thiophene and Triphenylamine Derivatives as Solution Processable Electrochromic Materials. *Org. Electron.* **2015**, *23*, 116–123.
- (80) Khetubol, A.; Van Snick, S.; Clark, M. L.; Fron, E.; Couti??o-Gonz??lez, E.; Cloet, A.; Kennes, K.; Firdaus, Y.; Vlasselaer, M.; Leen, V.; et al. Improved Spectral Coverage and Fluorescence Quenching in Donor-Acceptor Systems Involving indolo[3-2-B]carbazole and Boron-Dipyrromethene or Diketopyrrolopyrrole. *Photochem. Photobiol.* **2015**, *91* (3), 637–653.

- (81) McCormick, T. M.; Bridges, C. R.; Carrera, E. I.; Dicarmine, P. M.; Gibson, G. L.; Hollinger, J.; Kozycz, L. M.; Seferos, D. S. Conjugated Polymers: Evaluating DFT Methods for More Accurate Orbital Energy Modeling. *Macromolecules* **2013**, *46*, 3879–3886.
- (82) Casey, A.; Dimitrov, S. D.; Shakya-tuladhar, P.; Fei, Z.; Nguyen, M.; Han, Y.; Anthopoulos, T. D.; Durrant, J. R.; Heeney, M. Effect of Systematically Tuning Conjugated Donor Polymer Lowest Unoccupied Molecular Orbital Levels via Cyano Substitution on Organic Photovoltaic Device Performance. *Chem. Mater.* **2016**, *28*, 5110–5120.
- (83) Huang, X.; Shi, Q.; Chen, W.; Zhu, C.; Zhou, W.; Zhao, Z. Low-Bandgap Conjugated Donor - Acceptor Copolymers Based on Porphyrin with Strong Two-Photon Absorption. **2010**, 9620–9626.
- (84) Boujtita, M.; Zales, R.; Vivas, M. G.; Silva, D. L.; Bartkowiak, W.; Canuto, S.; Boni, L. De; Mendonca, C. R. Molecular Structure – Optical Property Relationships for a Series of Non-Centrosymmetric Two-Photon Absorbing Push-Pull Triarylamine Molecules. *Sci. Rep.* **2014**, *4*, 1–11.
- (85) Scarongella, M.; Laktionov, A.; Rothlisberger, U.; Banerji, N. Charge Transfer Relaxation in Donor-Acceptor Type Conjugated Materials. *J. Mater. Chem. C* **2013**, *1* (12), 2308–2319.
- (86) Banerji, N.; Angulo, G.; Barabanov, I.; Vauthey, E. Intramolecular Charge-Transfer Dynamics in Covalently Linked Perylene - Dimethylaniline and Cyanoperylene - Dimethylaniline. *J. Phys. Chem. A* **2008**, *112*, 9665–9674.
- (87) Pigliucci, A.; Duvanel, G.; Daku, L. M. L.; Vauthey, E. Investigation of the Influence of Solute–Solvent Interactions on the Vibrational Energy Relaxation Dynamics of Large Molecules in Liquids. *J. Phys. Chem. A* **2007**, *111* (28), 6135–6145.
- (88) Hu, Z.; Willard, A. P.; Ono, R. J.; Bielawski, C. W.; Rossky, P. J.; Bout, D. A. Vanden. An Insight into Non-Emissive Excited States in Conjugated Polymers. *Nat. Commun.* **2015**, *6*, 1–9.
- (89) Bixon, M.; Jortner, J.; Heitele, H. Energy Gap Law for Nonradiative and Radiative Charge Transfer in Isolated and in Solvated. *J. Mater. Chem.* **1994**, *98*, 7289–7299.
- (90) Jiang, J.; Alsam, A.; Wang, S.; Aly, S. M.; Pan, Z.; Mohammed, O. F.; Schanze, K. S. Effect of Conjugation Length on Photoinduced Charge Transfer in π - Conjugated Oligomer-Acceptor Dyads. *J. Mater. Chem. A* **2017**, *121*, 4891–4901.
- (91) Mikhnenko, O. V; Kuik, M.; Lin, J.; Kaap, N. Van Der; Nguyen, T.; Blom, P. W. M. Trap-Limited Exciton Diffusion in Organic Semiconductors. *Adv. Mater.* **2014**, *26*, 1912–1917.
- (92) Collado-fregoso, E.; Bou, P.; Fei, Z.; Gann, E.; Ashraf, S.; Li, Z.; Mcneill, C. R.; Durrant, J. R.; Heeney, M. Increased Exciton Dipole Moment Translates into Charge-Transfer Excitons in Thiophene-Fluorinated Low-Bandgap Polymers for Organic Photovoltaic Applications. *Chem. Mater.* **2015**, *27*, 7934–7944.
- (93) Revoju, S.; Biswas, S.; Eliasson, B.; Sharma, G. D. Effect of Acceptor Strength on

- Optical, Electrochemical and Photovoltaic Properties of Phenothiazine-Based Small Molecule for Bulk Heterojunction Organic Solar Cells. *Dye. Pigment.* **2018**, *149*, 830–842.
- (94) Lim, S. H.; Zhou, Y.; Su, H.; Ong, S. A Stable Solution-Processed Polymer Semiconductor with Record High-Mobility for Printed Transistors. *Sci. Rep.* **2012**, *2*, 1–9.
- (95) Carsten, B.; Szarko, J. M.; Son, H. J.; Wang, W.; Lu, L.; He, F.; Rolczynski, B. S.; Lou, S. J.; Chen, L. X.; Yu, L. Examining the Effect of the Dipole Moment on Charge Separation in Donor–Acceptor Polymers for Organic Photovoltaic Applications. **2011**, 20468–20475.
- (96) Matsuzaki, H.; Furube, A.; Katoh, R.; Singh, S. P.; Sonar, P. Excited-State Dynamics in Diketopyrrolopyrrole-Based Copolymer for Organic Photovoltaics Investigated by Transient Optical Spectroscopy Excited-State Dynamics in Diketopyrrolopyrrole-Based Copolymer for Organic Photovoltaics Investigated by Transient Opti. *Jpn. J. Appl. Phys.* **2014**, *53*, 1–5.

Chapter 5

Nanosecond Two-Photon Excitation Fluorescence Design of Experiment and Preliminary Data

5.1 Introduction

The ease of wavelength tunability and broad wavelength selection from ~410 nm to ~1200 nm revolutionizes the TPEF capabilities for the Goodson Group. To utilize the full potential of this system, I have designed and created a new experimental system and procedure for the TPEF experiments. The Quanta-Ray and GWU OPO is used for the excitation source. A Hamamatsu R928 PMT is used to collect the fluorescence. A SRS 250 gated integrator is used to record the fluorescence response from the PMT. I coded a custom program using the Labview environment to record the signal output from gated integrator and for digitalization via computer. The saved data and program are stored on the computer that is connected to the SRS 250 via GPIB. The TPEF method then can be used to determine the two-photon properties of the investigated materials.

5.2 Experimental

A new nanosecond laser system has been installed and new experimental system and procedure were developed in order to investigate TPA properties of compounds using nanosecond pulses. A Lab Series 170 neodymium-doped yttrium aluminium garnet (Nd:YAG) Quanta-Ray (Spectra Physics) laser that can produce 10 ns pulses of 1064 nm beam with a power of 850 mW, 532 nm beam with a power of 450 mW, and 355 nm with 220 mW of power at a repetition rate of 10 Hz was used as a pump. The Quanta-Ray (Spectra Physics) generates a

1064 nm beam by using a pump chamber assembly with two xenon flash lamps that pump Nd:YAG rods that are water cooled by an internal water reservoir that uses a heat exchanger with an external water source to ensure that rods do not overheat. The external water supply is supplied by the building. The supply water source is hooked up to the chiller using a grey garden hose via the heat exchanger to provide the water that is used to exchange the heat from the internal water reservoir. A grey return garden hose is connected to heat exchanger and the water is returned to the return line of the building. The pressure differential between the two lines is approximately 10 PSI, but is determined by the overall building water usage and cannot be augmented by the user. When the internal water temperature reaches 31°C, a ceramic valve opens in the heat exchanger that allows heat from the internal water supply to exchange across tubing to the external water in the heat exchanger. Both the internal water supply and the external water supply are isolated from each other. This prevents any contaminants or possible debris from the building water from mixing with the distilled water in the internal reservoir, ensuring the longevity of the cooling system. It should be noted that when Spectra Physics first installed the system, the ceramic valve failed. When this occurred the water temperature would exceed 31°C. This was replaced by Spectra Physics and no further issues have been observed.

A standing wave condition is achieved with a high reflector and an output coupler mirror at the end of the pump chamber, creating a laser resonator. The high reflector reflects photons that are emitted parallel to the optical axis of the cavity, which get reflected by the output coupler. This causes the number of photons to be geometrically increased inside of the resonator. The output coupler reflects most of photons, but a small fraction of the photons are transmitted, resulting in the escaping photons to become the output beam of the laser. The flash lamps pump the Nd:YAG in the red and near infrared absorption bands. The excited electrons of

Nd:YAG quickly drop to the upper lasing transition, where they remain for approximately 230 μs before falling to the lower lasing transition, which emits a photon at 1064 nm. There are also other lasing transitions from the same upper lasing state, 1319, 1338, and 946 nm but the gain for these wavelengths are much smaller and the emission cross section for these wavelengths are much lower resulting in the selection of 1064 nm for the oscillations. An external nitrogen supply is used in order to ensure the hygroscopic Nd:YAG rods do not absorb water which would reduce the efficiency of the gain medium.

In order to obtain short pulses, a Q-switch at the end of pump chamber is used in order to generate the 10 ns pulses. A Q-switch is composed of a polarizer, a quarter-wave plate, and a Pockels cell. If the laser was just composed of the gain medium and resonator, the laser pulse would be on the same order of magnitude of the flash lamp, resulting in a long pulse duration and a low peak power. Thus a Q-switch is added to the resonator to shorten the pulse duration and increase the peak power. In normal mode, a Q-switch delay circuit fires a fixed delay which triggers the Marx bank. The Marx bank is a circuit that generates a high-voltage pulse from a DC voltage source. It accomplishes the high-voltage pulse by charging a number of capacitors in parallel, then quickly connecting them in series after they are fully charged. The capacitors are charged in parallel by the supply voltage through a resistor for each capacitor. A spark gap between each capacitor is used to connect each capacitor in series. The spark gaps have a breakdown voltage that is higher than the supply voltage and are open while the capacitors are charging. When the capacitors are charged, the lowest spark gap breaks down, which increases the voltage across the next spark gap, thus connecting the first two capacitors in series and triggering the next spark gap, which continues until all the capacitors are connected in series to the load. When all the spark gaps are broken down, the impedance is low, which causes all the

capacitors to discharge a high voltage pulse when connected to the load that is equal to the voltage times the number of the capacitors. After the capacitors discharge, the spark gaps stop being conductive, and the capacitors begin to charge again.

The high voltage pulse is used to trigger a Pockels cell to generate the short laser pulses. The Pockels cell is an electro-optical crystal that controls light propagation through it by controlling the phase delay of the crystal by applying a variable voltage. The Pockels cell introduces high loss into the laser resonator in order to generate high peak power pulses. The high cavity loss prevents oscillation while the population inversion builds. Then the Pockels cell is switched to a low loss state, which allows a high peak power pulse to be generated. When no voltage is applied to the Pockels cell, the polarizer horizontally polarizes the light entering the Q-switch and the quarter-wave plate converts the polarization to circular polarization. The circularly polarized light reflects off of the high reflector and the quarter-wave plate converts the circularly polarized light to vertically polarized light. The polarizer only allows horizontally polarized light to be transmitted, thus the vertically polarized light is reflected out of the resonator, resulting in high cavity loss. When the high voltage pulse triggers the Pockels cell, the polarization of the Pockels cell changes, cancelling the polarization retardation of the quarter-wave plate, allowing horizontally polarized light to exit the Q-switch, resulting in the high peak power pulse of tens of megawatts of <10 ns.

The high peak power pulse of the 1064 nm fundamental beam from the Nd:YAG is used to pump a harmonic generator. The harmonic generator at the output of the pump chamber uses potassium dideuterium phosphate (KD*P) crystals with nonlinear susceptibility to generate the 355 nm and 532 nm beams while passing 1064 nm as well. The 1064 nm beam excites the atomic dipoles of the crystal. At low intensities the polarization change is linearly dependent on

the electric field of the incident light and it is proportional to the magnitude of the electric field of the incident light. While at high intensities, the polarization change is nonlinearly dependent on intensity of the incident light. This polarization contains an oscillation term at twice the frequency of the incident light, resulting in the frequency doubling of the 1064 nm fundamental. The 355 nm beam is generated by sum-frequency mixing of the 1064 nm fundamental with the 532 nm second harmonic beam. The setup for the Quanta-Ray (Spectra Physics) can be seen in **Figure 5.2.1.**



Figure 5.2.1. Quanta-Ray Laser System¹

To ensure efficient and consistent operation of the Quanta-Ray, I have developed a Standard Operating Procedure (SOP) for the laser system. This SOP will ensure consistent day to day operation as well as the overall longevity of the laser system. The SOP is as follows:

NS Laser SOP

Start Up Procedure

1. Turn on water flow to chiller by turning the red handles of the building water main perpendicular to the floor.

2. Increase nitrogen flow to the laser from 0.2 to 0.5 on the nitrogen control apparatus on the laser table.
3. Press the enable button on the controller for the Quanta Ray,
4. Watch for the simmer lights to blink a few times and then turn off, and then the oscillator simmer indicator glows orange.
5. Then wait for water temperature to increase from $\sim 22^{\circ}\text{C}$ to $25\text{-}27^{\circ}\text{C}$, ~ 30 minutes for the water to circulate in the chiller. I have installed a remote thermometer in the water reservoir to monitor the temperature at all times. This ensures that there smaller temperature changes when the flash lamp is turned on.
6. Make sure that the single shot is selected on the controller and the laser is in long pulse mode. The single shot/rep switch sets the laser to one pulse at a time when it is switched to single shot. In long pulse mode, the voltage is applied to the Pockels cell as soon as the flash lamp fires, and the Q-switch is held open the entire lamp firing. This results in a train of pulses of about $200\ \mu\text{s}$ long, with a separation of 2 to $4\ \mu\text{s}$ between individual pulses. This results in the total energy of the pulse train to be similar to that of a single Q-switched pulse. This ensures that that the laser pulse energies are low while the system is warming up.
7. The flash lamps are then turned on by turning the OSC knob to the 9 o'clock position and wait ~ 10 minutes for the temperature to stabilize.
8. Then turn the OSC knob to 12 o'clock position and wait for the temperature of the chiller to reach 31°C .
9. Then turn OSC knob to start to turn off the flash lamps and then turn the Mode knob to Q-switch and hit the button to switch from single shot to Rep mode, then turn OSC knob

back to 9 o'clock position. Wait 10 minutes. The first few pulses in this mode are high energy, following this procedure prevents initial surges from damaging anything downstream.

10. Then turn the OSC knob to the 12 o'clock position. Wait 10 minutes.
11. Then turn the OSC knob to the 3 o'clock position. You should start to see the green flash of the signal coming through the middle output of the OPO.
12. Allow the laser to warm up for 60 minutes.
13. There is defocusing of the KD*P from the 355 nm that reflects back from the OPO that affects the power. The two black knobs on the Harmonic Generator (HG) can be used to increase the power after warm up.

Shut Down is accomplished by:

Shutdown Procedure

1. Turn OSC knob to start.
2. Press Rep button to single shot.
3. Turn Mode Knob to LP.
4. Let the chiller run for 10 minutes, then hit the stop button.
5. Decrease the nitrogen flow to 0.2.
6. Shutoff the water mains by turning the red handles parallel to the floor.

The Quanta-Ray (Spectra Physics) is used to pump a Beta Barium Borate (BBO) crystal in an Optical Parametric Oscillator (OPO) (GWU versascan). The 532 nm and 1064 nm beams are dumped into beam dumps within the GWU versascan and the 355 nm beam is used to pump the BBO crystal of the OPO. For optical parametric oscillation, the pump photon in the nonlinear BBO crystal splits into two lower-energy photons that add up to the energy of the

pump photon. The pump photon is polarized in the direction of the optical axis, extraordinary, and the resulting low-energy photons are polarized perpendicular to the optic axis, ordinary. The BBO crystal is a birefringent, which means the index of refraction of an extraordinary wave varies with the direction of propagation, negative uniaxial crystal, which means the index of refraction decreases continuously from that equal to the ordinary wave in the propagation direction along the optical axis to a minimum value in the orthogonal direction. Thus, as the BBO crystal is rotated, the index of refraction changes, resulting in unique frequency output of the two low energy photons, resulting in a signal photon and an idler photon. The BBO crystal is in a resonator cavity where standing wave conditions are achieved in order to produce a signal beam (412 nm – 709 nm) and idler beam (710 nm – 3300 nm) of laser pulses of 5 ns – 9 ns of up to 600 mw of power. The beam dumps can also be removed and the 532 nm and 1064 nm beams can be used in experiments for excitation sources. A diagram of the OPO can be seen in **Figure 5.2.2.**²

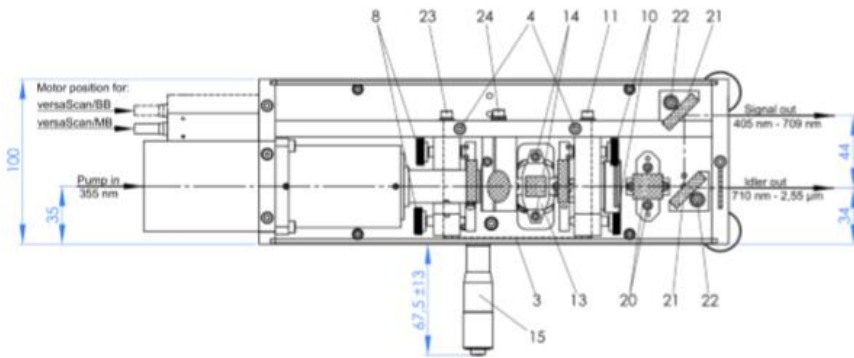


Figure 5.2.2. Schematic setup of OPO VersaScan²

To get the desired signal or idler wavelength output, the angle of the BBO crystal is tuned via an electric motor via computer using Spectra Physics supplied software. The electric motor position must be calibrated to produce the correct angle to produce the desired wavelength. The calibration is accomplished by the following procedure:

Electric Motor Calibration

1. The calibration can be accessed by opening the ScanMaster SHG GWU program on the desktop. Seen in **Figure 5.2.3**.

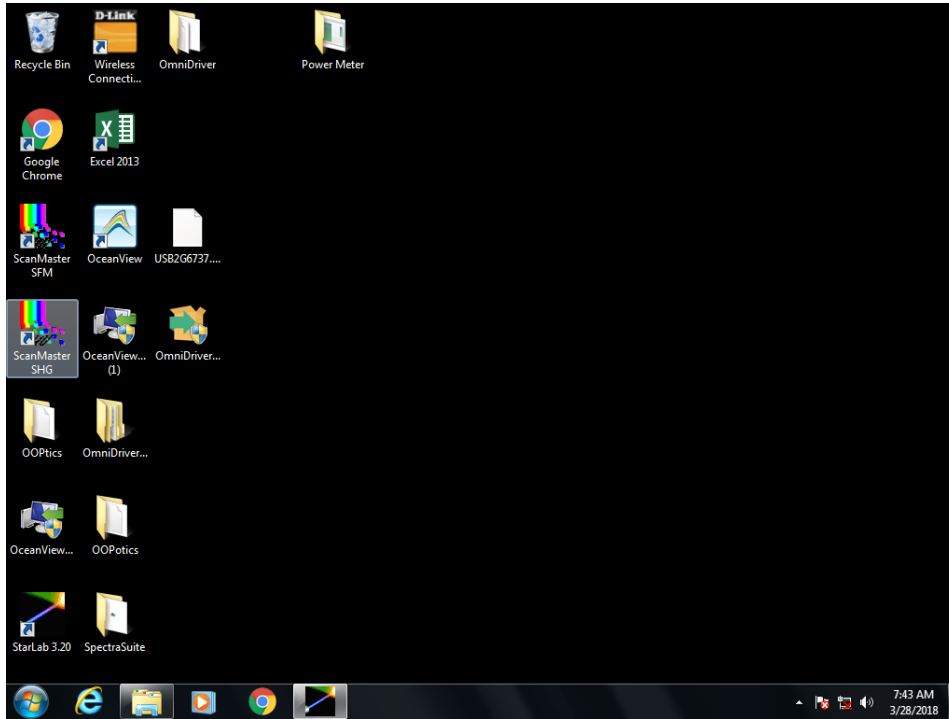


Figure 5.2.3. Desktop location for ScanMaster SHG

2. Then click on Config then open the calibration wizard. Seen in **Figure 5.2.4**.

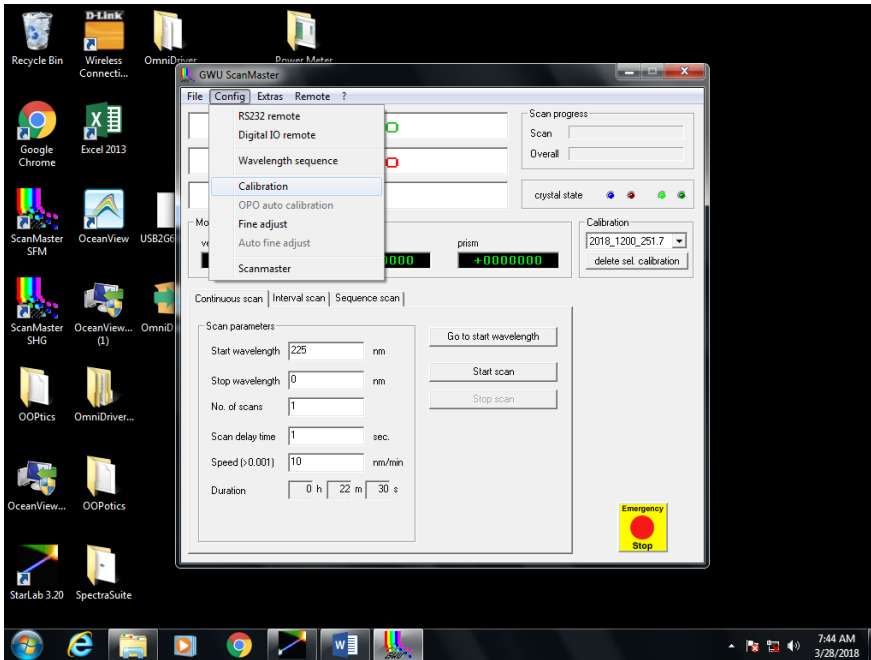


Figure 5.2.4. Location of the calibration wizard

3. After clicking on calibration, the base calibration window opens with a drop down menu for selecting which calibrations will be modified. To modify the calibration for the OPO, 2018_257_354 calibration file should be selected then click OK. Seen in **Figure 5.2.5.**

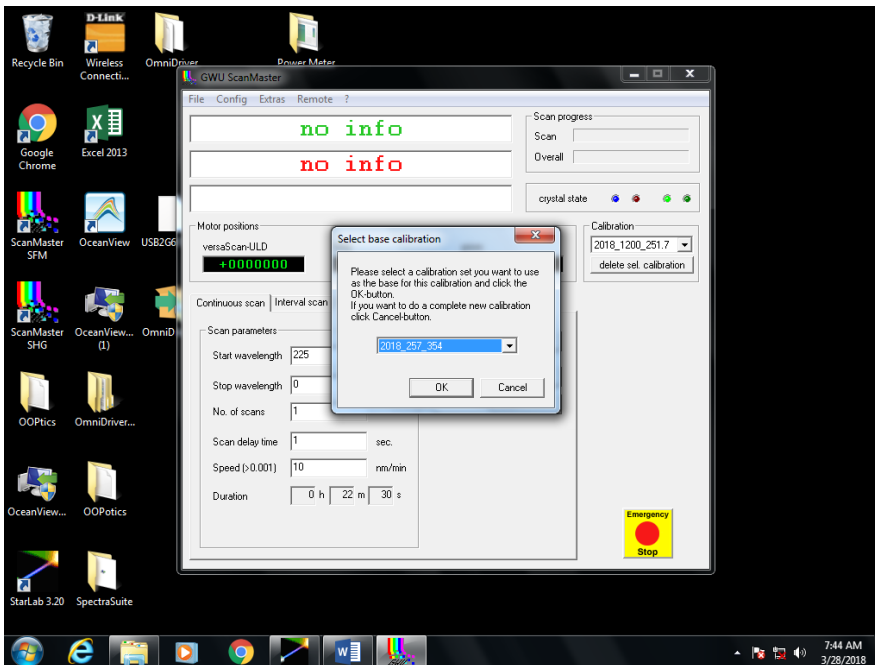


Figure 5.2.5. Base calibration selection

- This then opens the window for crystal configuration. To calibrate the motor positions for signal beam (409 nm – 708 nm) and idler beam (710 nm – 1200 nm), UV-L crystal configuration for stage 1 must be selected and then click OK. Seen in **Figure 5.2.6**.

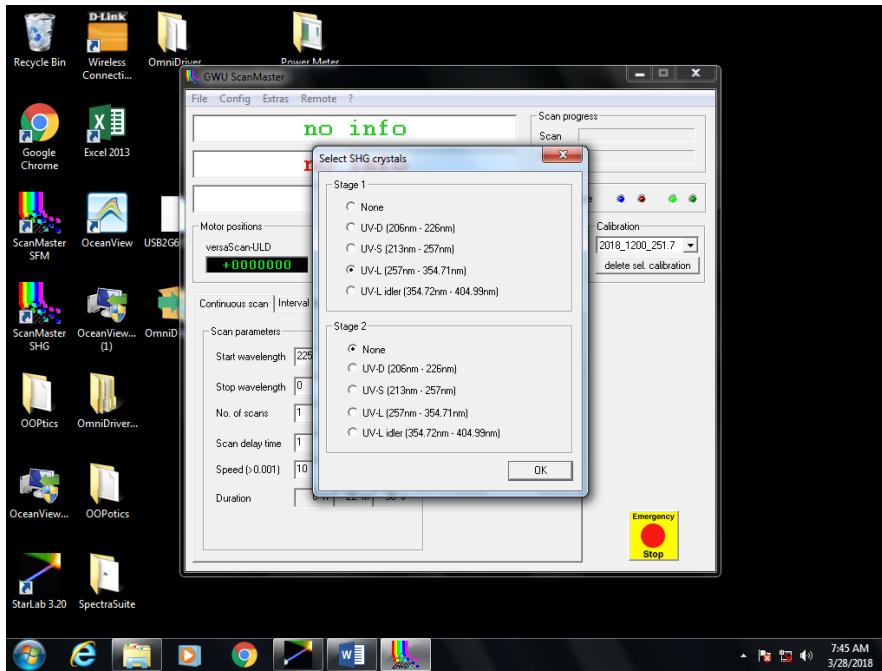


Figure 5.2.6. Crystal configuration selection window

- This finally opens the calibration wizard to calibrate the electric motor position for electronic control of the signal and idler wavelengths of the OPO. Seen in **Figure 5.2.7**.

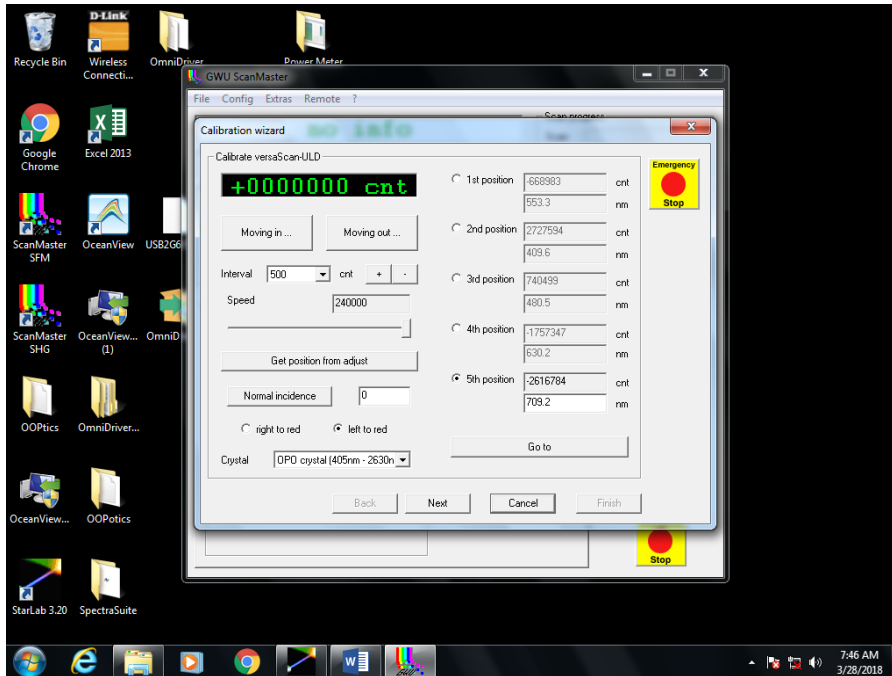


Figure 5.2.7. Calibration wizard window

6. To begin calibration, a five point calibration table is constructed.
7. For the first position, a wavelength is selected that is in the middle of the range of the crystal, in this case 550 nm. Then click Go to. This will roughly move the motor position to a wavelength of 550 nm. The wavelength is monitored by measuring a weak reflection of the output beam using a fiber with cosine corrector with an optical diffuser connected to an Ocean Optics spectrometer and recorded via OceanView software via computer. The power is monitored with a Coherent J-50MB-YAG: ENERGYMAX SENSOR with a Coherent LabMax-TOP energy meter.
8. The power is maximized by clicking the moving in and moving out buttons, the speed of motor position search is controlled by the sliding bar under the moving in and moving out buttons. When the maximum power is obtained, the exact output wavelength is recorded from the OceanView software. This is inputted in the wavelength window for the first position. This position is saved by clicking on Get position from adjust button.

9. For the second position, a wavelength is selected that is the start of the range of the crystal, in this case 410 nm. Then click Go to. This will roughly move the motor position to a wavelength of 410 nm. The procedure that was used to get the first position is then followed to obtain the second motor position for 410 nm.
10. For the third position, a wavelength is selected that is roughly the middle of 410 nm and 550 nm, in this case 480 nm. The third motor position was obtained by similar procedure used for first and second position.
11. For the fourth position, a wavelength is selected that is roughly the middle of 550 nm and 709 nm, in this case 630 nm. The fourth motor position was obtained by similar procedure used for the other motor positions.
12. For the fifth position, a wavelength is selected that is the end of the range of the crystal, in this case 709 nm. The fifth motor position was obtained by similar procedure used for the other motor positions.
13. Then click next. Then the similar procedure is used for the SHG crystal positions and prism positions for second harmonic generation, these wavelengths can be used for future experiments but are not used for TPA experiments.
14. Then to save the calibration, click finish.

The experimental setup for the nanosecond TPEF can be seen in **Figure 5.2.8**. The OPO output beam is passed through an iris to maintain a consistent beam diameter for all wavelengths. The signal and idler is then passed through an optical glass that reflects 10% of the beam to a Thorlabs silicon photodiode that is protected by a 2.5 OD and 0.4 OD neutral density filters. The photodiode is used to trigger the SRS 250 gated integrator, which will be discussed shortly. A beam dump is placed behind the reflecting glass to collect back reflection from the reflecting

glass. The remaining signal and idler beam is passed through a beam attenuator that can attenuate wavelengths >1000 nm. Two beam dumps are placed on either side of the beam attenuator to collect residual beams that are perpendicular to the propagating beam that result from the attenuation of the propagating beam. Finally the signal or idler is selected by placing either a GWU Vis filter option is used to get idler beam only, or 700 nm lowpass filters to block idler wavelengths for signal use. A reflecting mirror is used to direct the excitation beam into the sample. A neutral density wheel is used to control the power of the excitation beam. A focusing lens after the neutral density wheel is used to focus the beam onto the sample. A beam dump is placed behind the sample to collect the residual excitation beam. The fluorescence from the sample is collected perpendicular to the excitation beam. A focusing beam is used to collimate the fluorescence onto the PMT. A series of filters are used to block scattering from the excitation beam. The PMT fluorescence response output is connected to the SRS 250 gated integrator. The SRS 250 is connected to a computer via a GPIB where a custom program is used to record the data.

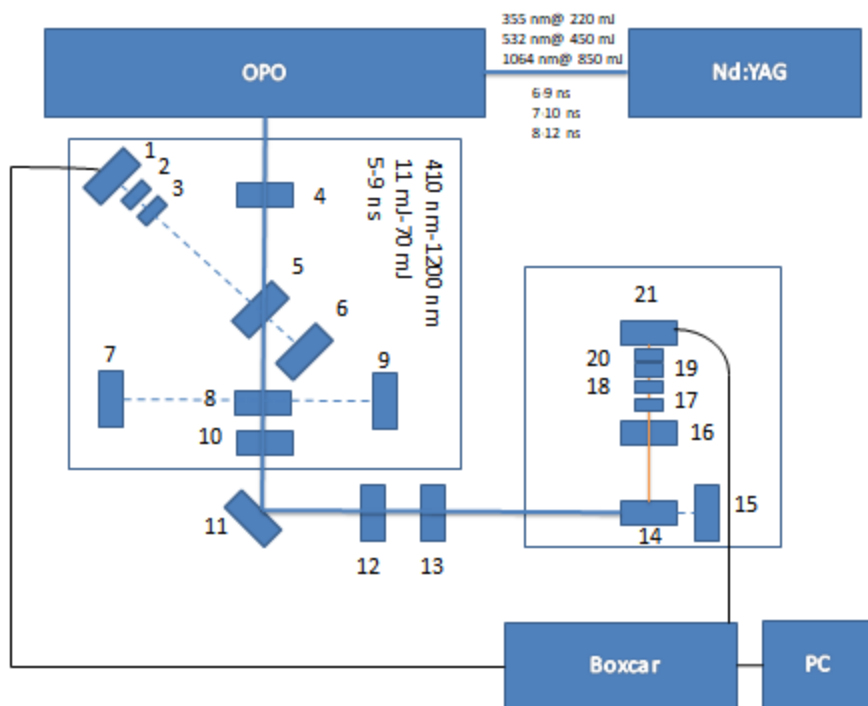


Figure 5.2.8. Nanosecond TPA Setup. 1: Photodiode for trigger. 2: 2.5 OD ND filter. 3: 0.4 OD ND filter. 4: Iris. 5: Reflecting glass. 6, 7, 9, 15: Beam dumps. 8: Beam attenuator(for wavelengths >1000nm). 10: Filter(GWU Vis filter option used to get Idler only, or 700 nm lowpass filters to block Idler wavelengths for Signal use). 12: ND wheel. 13, 16: Focusing lens. 14: Sample holder. 17-20: PMT filters (975 nm Lowpass filters for excitation wavelengths >975 nm, or 700 nm cut-off filters for excitation wavelengths <975 nm). 21: PMT. Solid blue lines are laser beams. Dashed blue lines are reflected laser beams. Solid orange line is fluorescence. Solid black lines are wires.

The SRS 250 gated integrator is the key component for the TPEF data collection. The SRS 250 consists of a gate generator and a fast gated integrator. The gate generator is triggered externally by the Thorlabs silicon photodiode. The gate generator generates a gate that is adjustably delayed from a few nanoseconds to 100 milliseconds, generating a continuously adjustable gate of 2 nanoseconds to 15 microseconds. The fast gated integrator integrates the input signal from the PMT during the gate. The output from the integrator is then normalized by the gate width to provide a voltage that is proportional to the average of the input signal during the sampling gate. The SRS 250 gated integrator can be seen in **Figure 5.2.9**.



Figure 5.2.9. SRS 250 gated integrator

The gated integrator analyzes an input analogue signal and produces an analogue output signal, which is not convenient for data analysis. To make data collection easier and easily manipulated, I coded a custom program to record and collect the TPEF signal. The first part of my program initializes the SRS 250 and prepares it to receive commands from my program. It sets the address that the SRS 250 and the computer will interact through, in this case the two are connected by GPIB with address 3. It also designates which front input will be reporting the data to the computer. A wait function is then employed to ensure that the ports and addresses are set before the data collection portion of the code is ran. This can be seen in **Figure 5.2.10.**

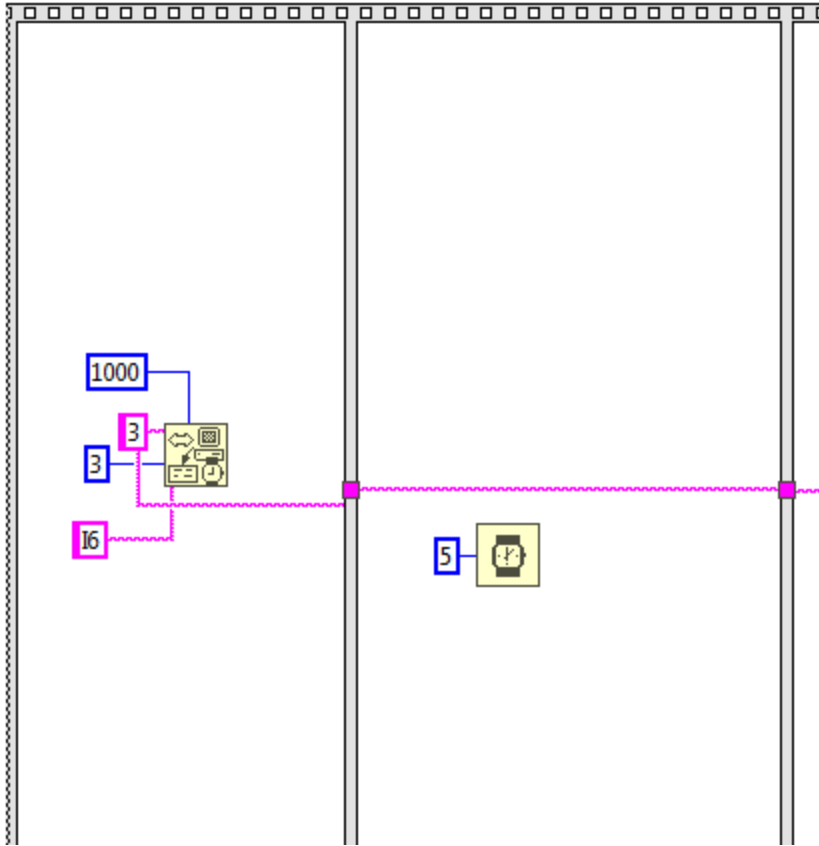


Figure 5.2.10. Block diagram of initialization of custom data collection program

The second part of my program is responsible for the data collection. It consists of two for loops. The inner for loop is responsible for setting how many samples will be recorded. The inner loop requests the voltage value from the SRS 250 after the fluorescence signal has been integrated and then it waits 100 ms for the next pulse to collect the fluorescence signal again. This is repeated for how many times the program is set to record. It then adds all of the signals together and divides it by the number of samples that were recorded. This can be seen in **Figure 5.2.11.**

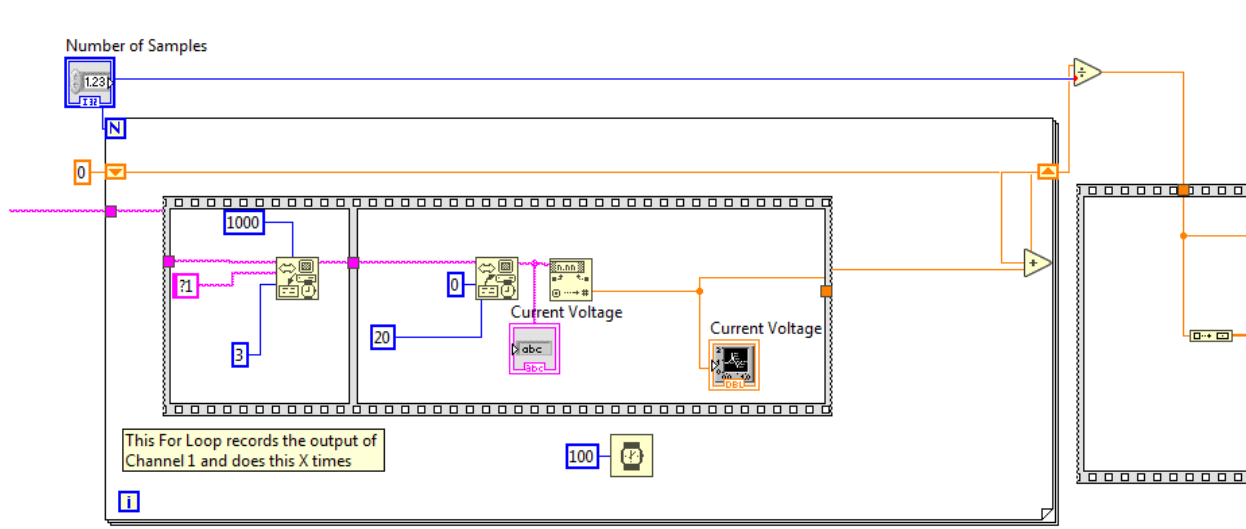


Figure 5.2.11. Block diagram data collection for first for loop

The outer for loop is used to set the number of scans and to create a break between scans so the user can change the power for the next scan. This can be seen in **Figure 5.2.11.** and

Figure 5.2.12.

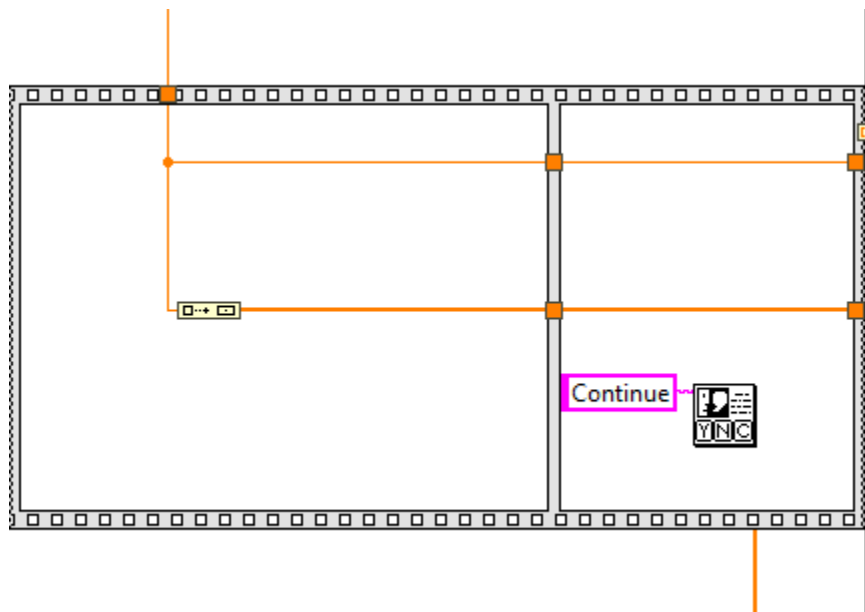


Figure 5.2.12. Block diagram for sequence that creates a user interface for scan s

The last part of the program plots the collected data and then creates a file with the values stored. Seen in **Figure 5.2.13.**

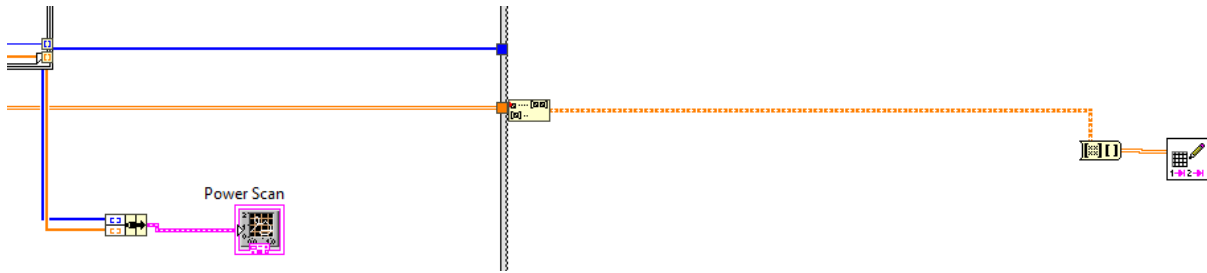


Figure 5.2.13. Block diagram for sequence that plots and saves the data to a file

This code is then responsible for the GUI for the user seen in **Figure 5.2.14**. The first user input controls the total of number scans that will be used for the experiment. The second user input controls the number of samples that will be collected for each scan. The GUI has 3 outputs for real time data visualization. The first graph plots the current voltage vs the pulse that generated the fluorescence signal. The second graph plots the average voltage vs each scan. The Current Voltage output gives the numerical value of the voltage after each laser pulse.

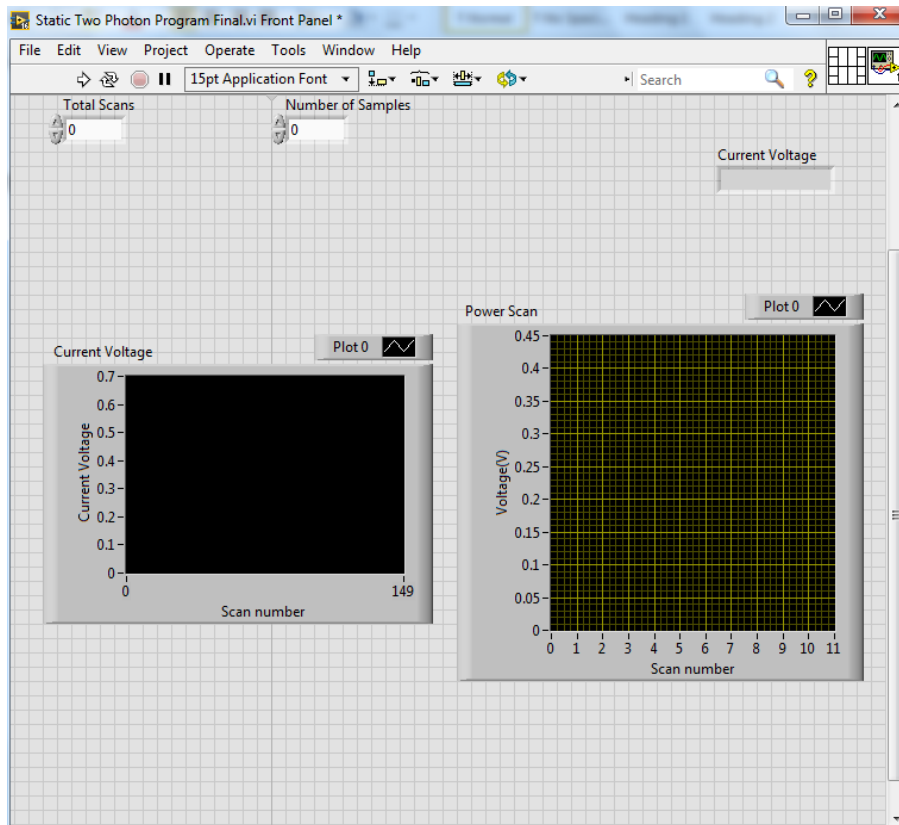


Figure 5.2.14. User interface for the TPEF collection program.

For accurate data collection, the collection program must be turned on before the SRS 250 is turned on. The user parameters must be inputted before the SRS 250 is turned on. As seen in **Figure 5.2.15**, where 14 scans of 600 pulses each will be conducted. Then the power can be turned on for the SRS 250. This prevents the GPIB write and read from timing out due to conflicts between the SRS 250 and the data collection program. Then the PMT can be turned on. To avoid drift of the background, which is intrinsic to the SRS 250, allow the whole collecting system to warm up for 60 mins. After this, experiments can be carried out.

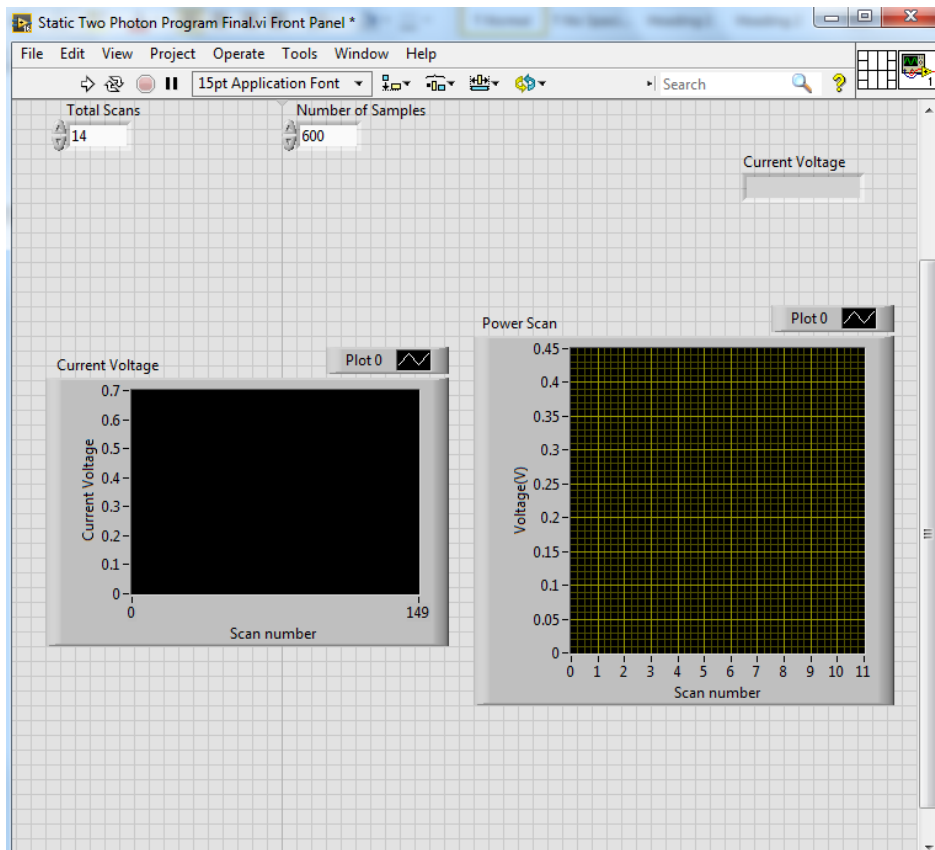


Figure 5.2.15. User parameters inputted before turning on SRS 250.

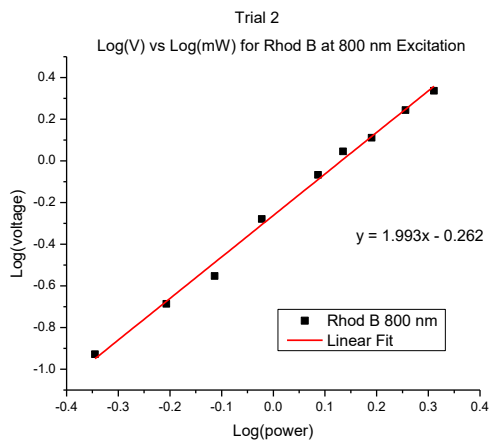
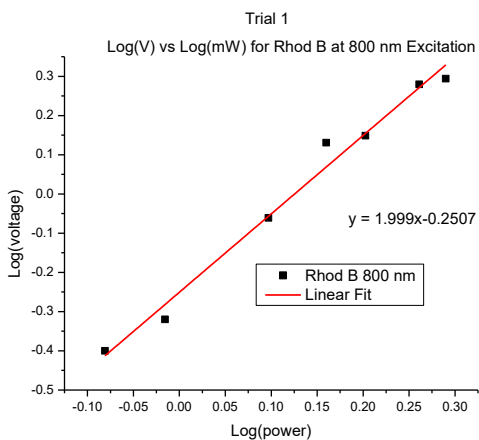
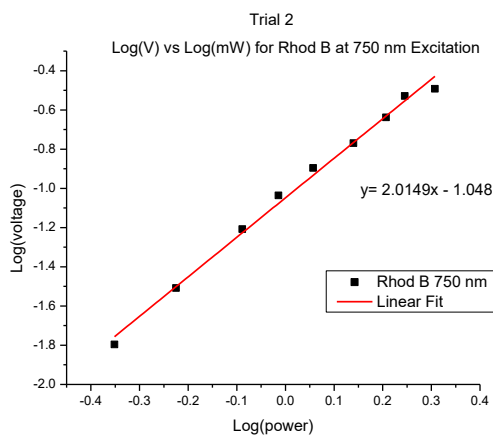
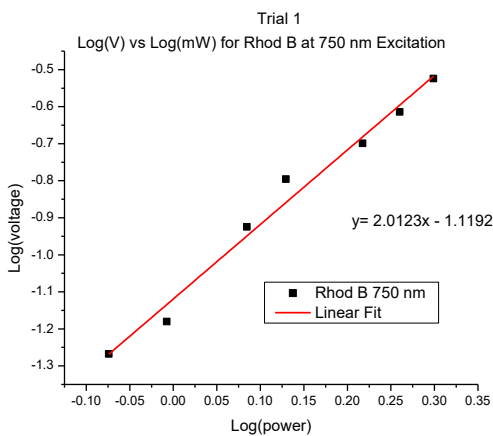
5.3 Preliminary Data

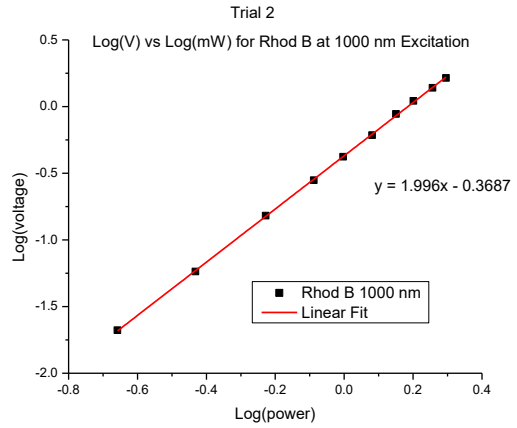
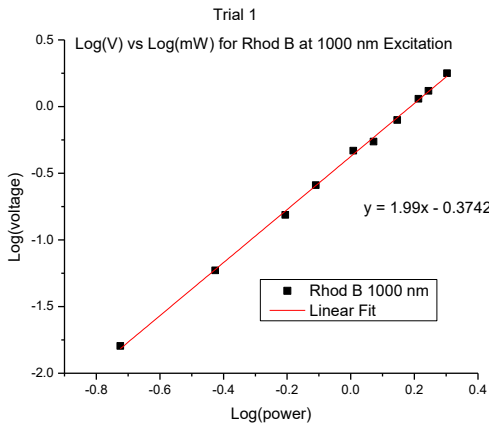
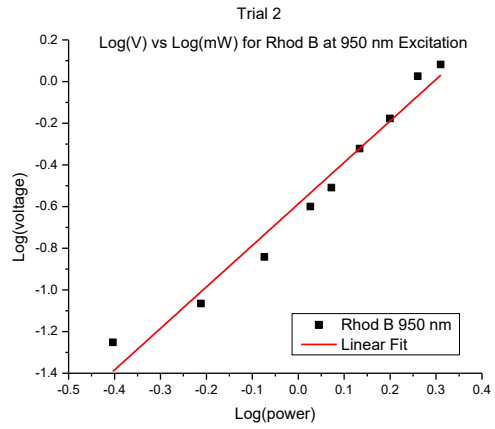
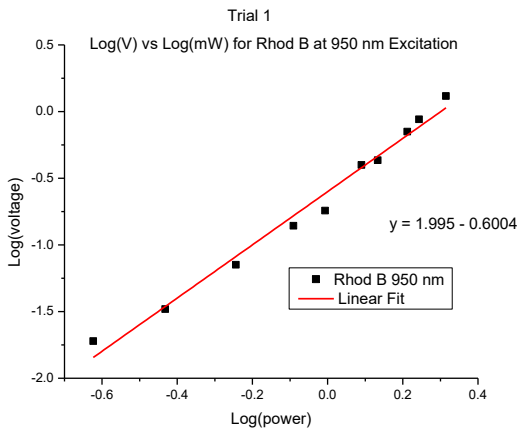
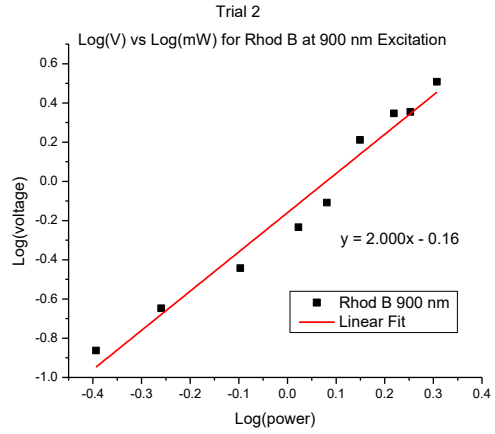
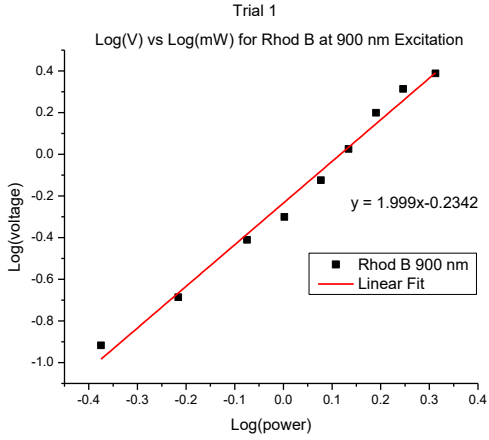
In order to verify that the experimental design is viable and that custom program is working, TPEF experiments were carried out using excitation wavelengths from 800 nm to 1100 nm using well studied two-photon absorbing dyes. Acridine Orange is a well-known two-photon absorbing dye. It was used to verify TPEF using 850 nm excitation. Rhodamine B is also a well-known two-photon absorbing dye. It was used to verify TPEF for 750 nm-1100 nm excitation, using 50 nm increments to confirm the TPEF at each wavelength.

The operation and experimental procedure described in **5.2** above was used. Additionally, a few more details are necessary to carry out these experiments. The optical density of dye solutions were kept below 0.1 OD. This was necessary to prevent fluorescence re-absorption. It also prevented saturation of the PMT. The dyes used in these experiments have large two-photon absorption cross-sections and high quantum yields which can easily produce high fluorescence intensities that can saturate the PMT, which will interfere with the TPEF experiments. The excitation powers were also kept below 2 mW. Higher powers would not only lead to saturation of the PMT but it would also lead to optical limiting conditions that would prevent two-photon absorption identification. Also, high responses from the PMT would saturate the integrating circuit in the gated integrator. Thus the concentration and the powers were kept low.

Experiments were carried out using 14 scans and 600 samples per scan. Two background scans were taken at the beginning of each experiment in order to establish the background level of the experiments. Two additional background scans were taken at the end of the experiment in order to monitor any drift of the background over the course of the experiment. The power level was controlled by the neutral density wheel. Scans were carried out from 0.2 mW to 2.0 mW

using increments of 0.2 mW. 600 samples were taken per scan in order to obtain the fluorescence as well as avoiding excessive exposure of the sample to the excitation beam which can lead to degradation. The experimental results from 750 nm to 1100 nm for Rhodamine B can be seen in **Figure 5.3.1** and the experimental results at 850 nm for Acridine Orange can be seen in **Figure 5.3.2**.





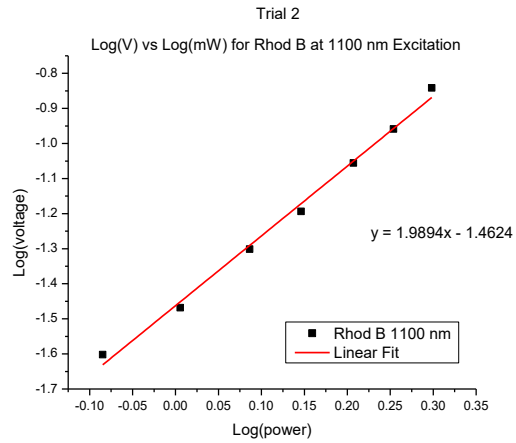
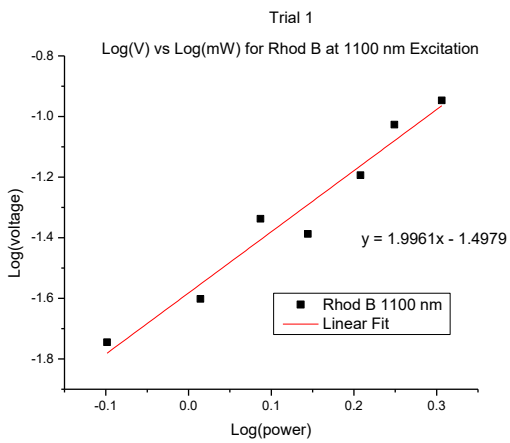
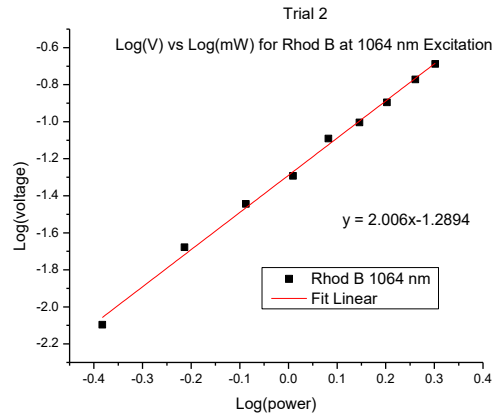
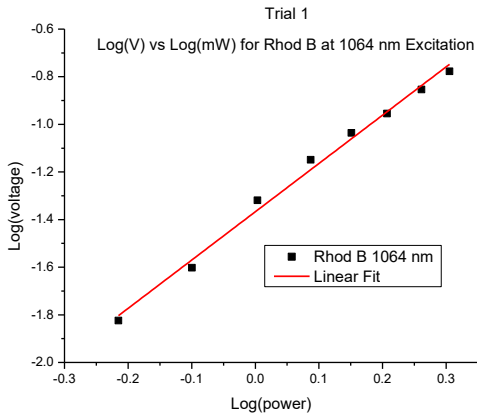


Figure 5.3.1 Two-photon absorption results from 750 nm to 1100 nm for Rhodamine B

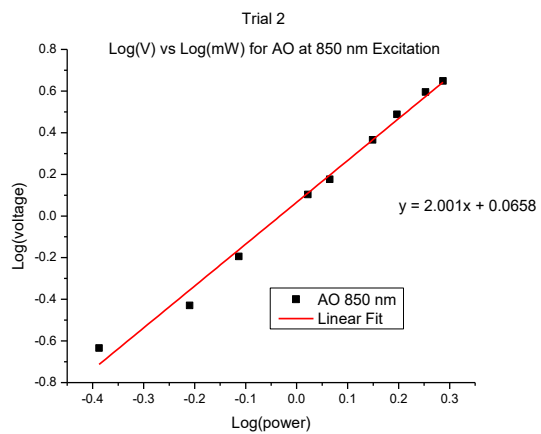
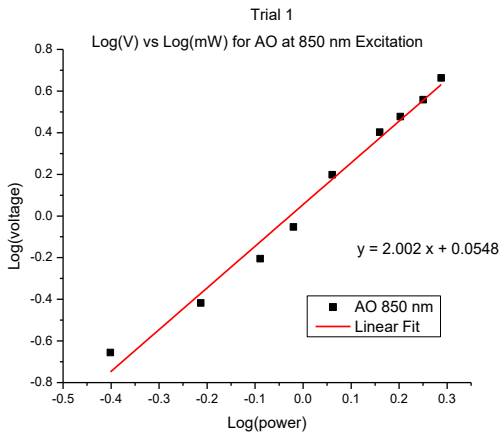


Figure 5.3.2 Two-photon absorption results from 850 nm for Acridine Orange

5.4 Conclusion

A new nanosecond laser has been introduced and described. The principles and standard operating procedures have been discussed. A new nanosecond laser system has been successfully installed that has a wide bandwidth of tunability. A new two-photon absorption system has been designed and tested. A PMT with a gated integrator with a custom program is used to collect the signal. Preliminary results of two-photon absorbing dyes have shown the successful operation of this new experimental system. There is still room for improvement for this system. The results using excitations above 900 nm had less scattering than the results from 700 nm – 900 nm. The PMT has high quantum efficiencies in the 700 nm - 900 nm range, thus longer wavelength scattering will not contribute to experimental error as much. Filters have been placed in front of the PMT to decrease the scattering from the excitation beam, but the two-photon results have shown that there is still scattering influencing the data. Although, good results have been obtained, the scattering does add some error to the TPA cross-section determinations. Additional filters can be added to the experimental setup to decrease the scattering even more, and an iris can be placed in front of the PMT aperture to cut down on the scattering.

References

- (1) Quanta-Ray Lab-Series: Pulsed Nd:YAG Lasers User's Manual.
- (2) GWU VersaScan. Beta-Barium Borate. Optical Parametric Oscillator User Manual.

Chapter 6

Nanosecond Transient Absorption Experiment and Preliminary Data

6.1 Introduction

The new nanosecond laser, described in Chapter 5, has also opened new and exciting opportunities for the investigation of long timescale photophysical processes. The new nanosecond laser can provide excitations of 250 nm to 2600 nm, providing a breadth of wavelengths to excite molecules of interest. A new fully automated spectrometer (LP980, Edinburgh) has been installed in order to record nanosecond transient absorption spectra and kinetics. The LP980 provides a pulsed probe beam that produces a continuous excitation from 190 to 2600 nm. Using the new nanosecond laser as a pump source and the LP980 probe source and using complex electronics and software, transient species can be investigated from 10s of nanoseconds to 100s of second, bringing a new era of exploration to the Goodson Group.

6.2 Experimental

The nanosecond transient absorption setup consists of an excitation laser used as the pump source and the LP980 spectrometer as the data collection device and probe source. The experimental setup can be seen in **Figure 6.1**. The operation and detailed description of the new nanosecond laser (QuantaRay, Spectra Physics, and OPO, GWU) is described in a previous chapter. For the nanosecond transient absorption experiment, the sample is excited from the ground state to an excited state by the nanosecond pulsed laser and a xenon lamp within the LP980 is used as a broadband light source to probe the excited state as depicted in **Figure 6.2**. The 150 W ozone-free, xenon arc lamp produces 6 ms pulses of a continuous spectrum from 190

nm to 2600 nm. The probe pulse excites the sample perpendicular to the laser excitation which maximizes the change in absorption while minimizing scattering and fluorescence. Transient species only occur in the overlapped region which reduces triplet-triplet annihilation and photodegradation. After passing through the sample at a right angle to the excitation beam, the light is directed to a monochromator. The light is then measured by a PMT (Hamamatsu R928) with a spectral range from 185 to 870 nm. The transmission response of the sample before, during, and after the excitation pulse is converted by the PMT into electrical signals that are measured by a TDS3052B Model oscilloscope. The Edinburgh supplied software converts the electrical signal into change of optical density.

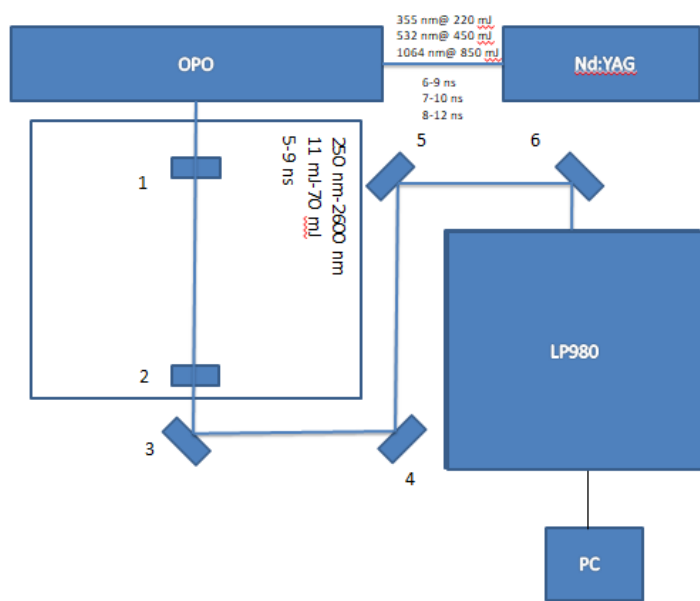


Figure 6.1. Nanosecond transient absorption setup. 1: Iris. 2: Filters (optional). 3-6: Prisms for directing the beam.

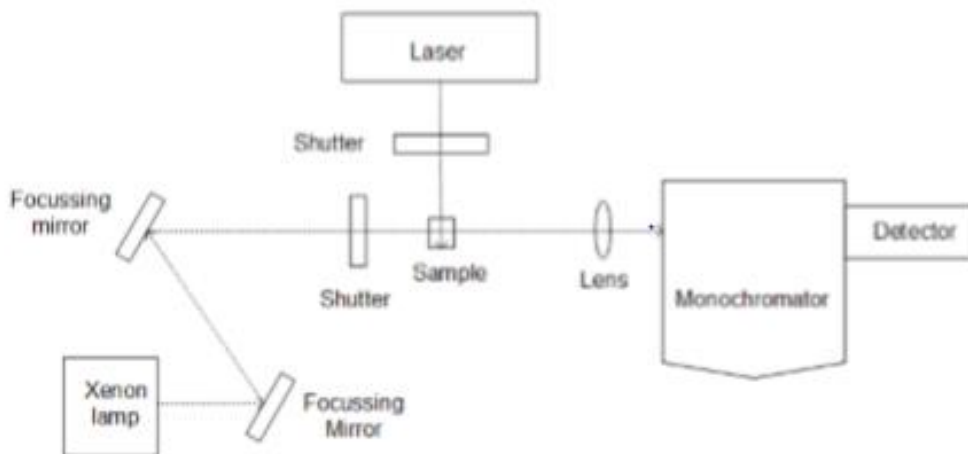


Figure 6.2. LP980 setup


To ensure efficient and consistent operation of the LP980 system and the nanosecond transient absorption experiment, I have developed a Standard Operating Procedure (SOP) for the system. This SOP will ensure consistent day to day operation as well as the overall longevity of the system. The SOP is as follows:

Nanosecond Transient Absorption SOP

Start Up Procedure

1. Warm up the QuantaRay and OPO using same procedure described in the nanosecond TPA chapter.
2. Turn on the computer that has the LP980 software and Turn on the Oscilloscope. Then turn on the Power Hub (PH1). Wait for the Probe Control on the LP980 to display “ready to start”, then press the silver button.
3. Open the L900 software on the computer. Allow the lamp to warm up for a half an hour for stable probe light.
4. Wait for the laser and lamp to warm up.

Sample Measurement and System Operation

5. Turn the Osc knob to Start on the QuantaRay controller. Turn the Source knob to External and Mode knob to External. Then turn the Osc to 9/10 power. This allows for full control of the laser system by the LP980 software.
6. In the L900 software window go to Setup → Kinetic Abs Setup or click on  in the tool bar and select Setup. The Kinetic Absorption Setup window can be seen in **Figure 6.3**. In order to conduct experiments, laser, laser shutter, and probe shutter need to be in timed configuration. Then ensure that the probe is in pulsed mode. Select the wavelength of interest under the detector monochromator tab and start with a bandwidth of 1 nm. Select “Apply” then press “Start”. Observe the probe background then press “Stop”. Adjust the bandwidth until the probe background is over 500 mV but less than 600 mV.

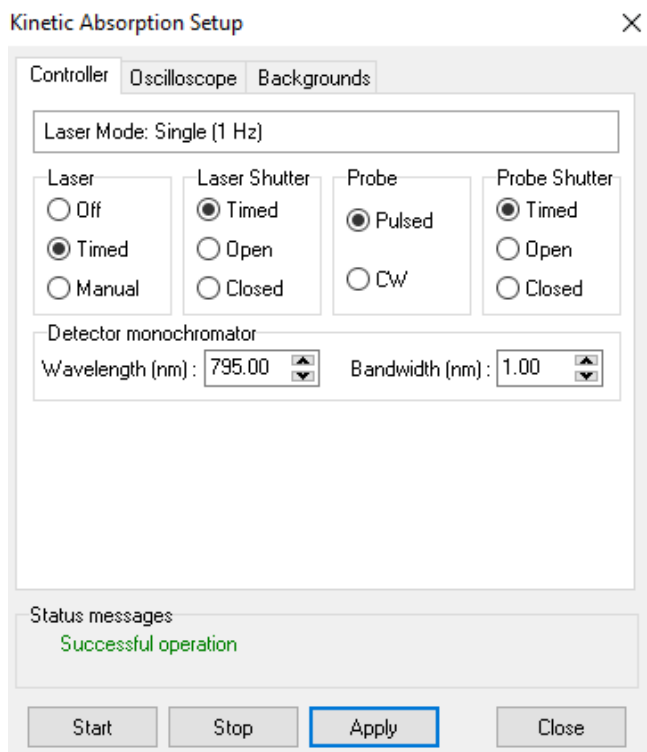


Figure 6.3. Kinetic Absorption Setup window

7. In the Kinetic Absorption Setup window, click on the Oscilloscope tab, seen in **Figure 6.4**, and set time range approximately 10 times longer than the sample's expected lifetime. If the sample's lifetime is unknown, set the time range to 4000 ns. Set the shift at 10% and start with the voltage range (under the PMT channel (Ch1) range tab) at 400 mV. Click on "Apply" and "Start", and then stop the scan once the signal appears. Optimize the slit, voltage, and time range in order to make sure the signal does not exceed 600 mV.

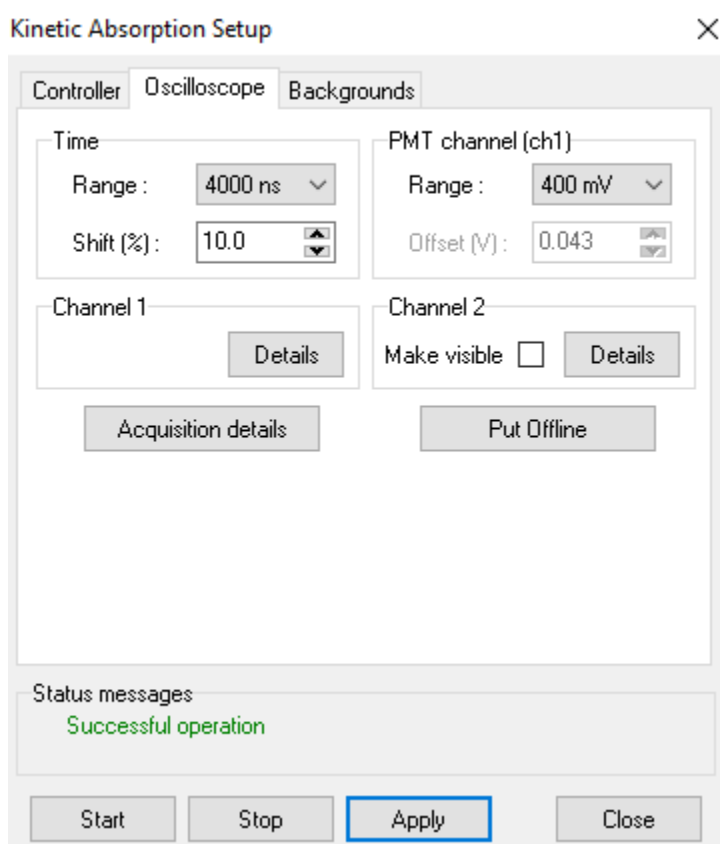



Figure 6.4. Oscilloscope tab

8. When the maximum possible signal is obtained, press "Apply" and then press "Close" on the Kinetic Abs Setup window. Click  and select Multiple for kinetic data at selected wavelength. Select desired number of averages per measurement under the Measurement

tab, seen in **Figure 6.5**. Select the number of laser shots to be discarded at 3. Select the background tabs and select the appropriate background subtraction, seen in **Figure 6.6**. Select probe background for measurements longer than 20 microseconds, and select fluorescence background when the sample has fluorescence at the monitoring wavelength to remove it. Click on “Apply” and “Start”.

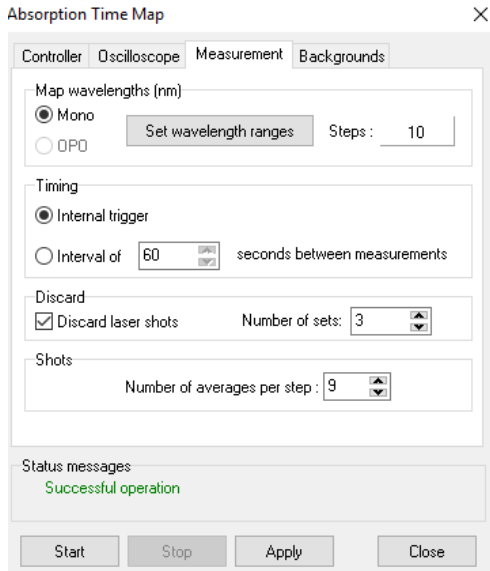


Figure 6.5. Measurement tab

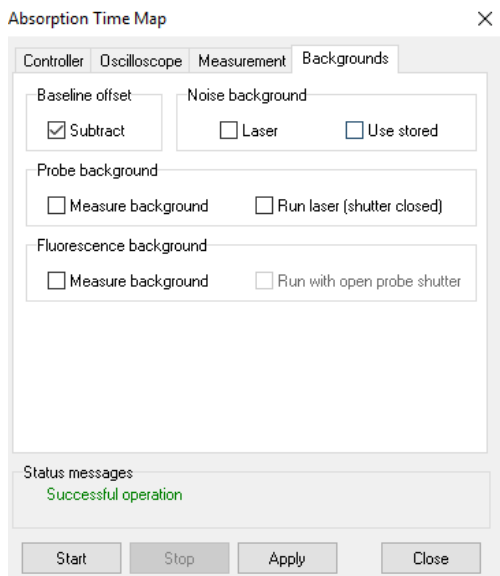




Figure 6.6. Background tab

9. To save the data, click on “File” and “Save”. This will save the data as files that can be read by the software. The data also must be saved by exporting to ASCII for data that can be read by excel and Origin 8. To export the the data in ASCII format by click “File” and “Export Data”.
10. To fit a negative Multi OD data go to Data in the toolbar and select scale and put -1 in the scale. This inverts the data so that the software can fit the kinetics. This inversion is not necessary for positive Multi OD data. Then click on “Data” and “exponential fit” and “Tail Fit”. Then save raw data and the fitted data can and export the fitted data using ASCII format.
11. To get kinetic data at multiple wavelengths, use Map measurements. Click  and select Setup and Kinetic Abs Setup. Under the controller tab, set the wavelength at 500 nm (where the lamp signal is most intense) and, if applicable, at a wavelength where the sample’s emission is maximum and then vary the slit width to get about 500 mV signal. Under the oscilloscope tab, use the same time and shift that was used for multiple in step 8, and then use voltage range at 160 mV. Once the voltage level of 500 mV is reached, set the wavelength (under detector monochromator tab) to the start wavelength that will be used as the initial wavelength for the map measurement. Click “Apply” and “Start”. Click “Stop” once the software has found the baseline at the start wavelength. Close the window.
12. Then click  and select Map. Under the measurement tab set your wavelength range for the map, seen in **Figure 6.7**, and set number of scans per each wavelength. The maximum possible wavelength range for map measurements is 300 nm to 860 nm. Select steps (interval) that give good resolution while avoiding sample degradation, avoid

mapping at laser excitation wavelength. Under the background tab set background as needed as discussed above. Click “Apply” and “Start”.

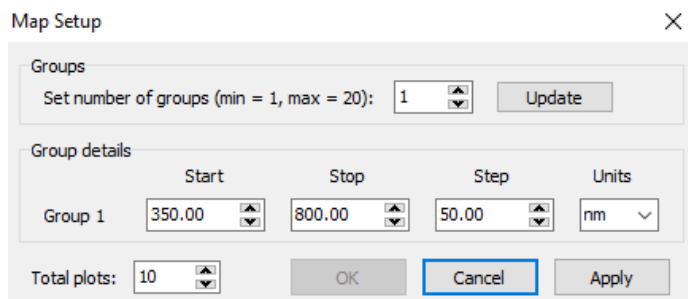


Figure 6.7. Wavelength selection window

13. Once data acquisition is complete, save both raw as well as the ΔOD data. Export the data in ASCII format. Move the cursor to the starting point of the signal in the ΔOD data, right click and set to time zero.
14. To get kinetic data at each wavelength, click “Data” and “Data Slicing”. Start the slicing range at zero and stop the slicing where the kinetic is complete. Select the desired number of slices that give a good representation of the kinetic decay, seen in **Figure 6.8**. Save data and export in ASCII format as previously described.

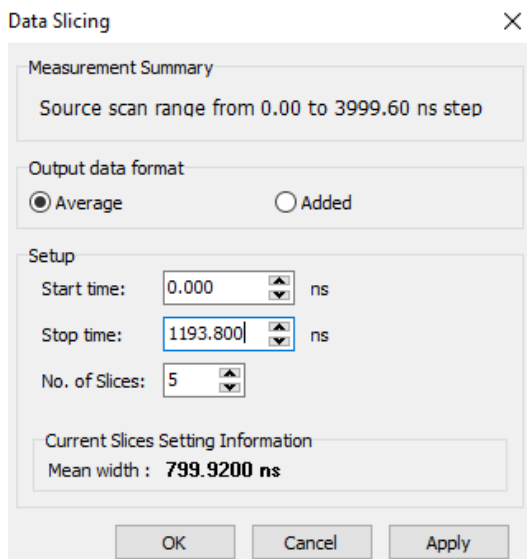


Figure 6.8. Data slicing window

Laser Alignment

15. Tris(bipyridine)ruthenium(II) chloride (RuBPY) is used to align the laser. Place the RuBPY (Standard) in the sample holder. Click on “kinetic abs setup”. Under the Controller tab select Open under the Laser shutter tab and hit “Apply”, as seen in **Figure 6.9**. Check that the beam is level with the prism outside the sample chamber and that is level with sample chamber. The beam height should be approx. 17 cm at the prism outside the sample chamber. The ideal beam diameter is approx. 7 mm. The Laser power should be below 5mJ just before the sample. This can be controlled by the Osc knob on the QuantaRay controller. Alignment is achieved when fluorescence is observed from the sample and the laser passes through the hole in the sample holder.

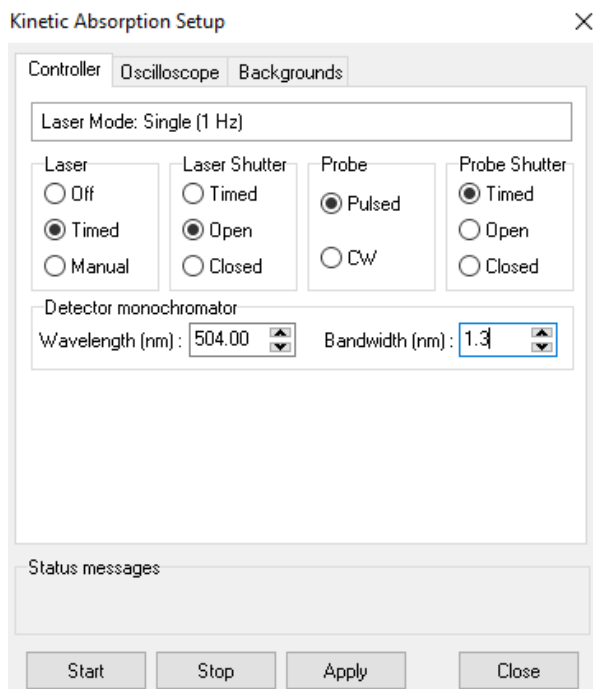


Figure 6.9. Kinetic absorption setup for RuBPY

16. Turn the Osc knob to Start on the QuantaRay controller. Turn the Source knob to External and Mode knob to External. Then turn the Osc to 9/10 power. This allows for full control of the laser system by the LP980 software.
17. Click laser icon in the L900 software to ensure the Laser setting is set to Mode1 (1 Hz) as seen in **Figure 6.10**.

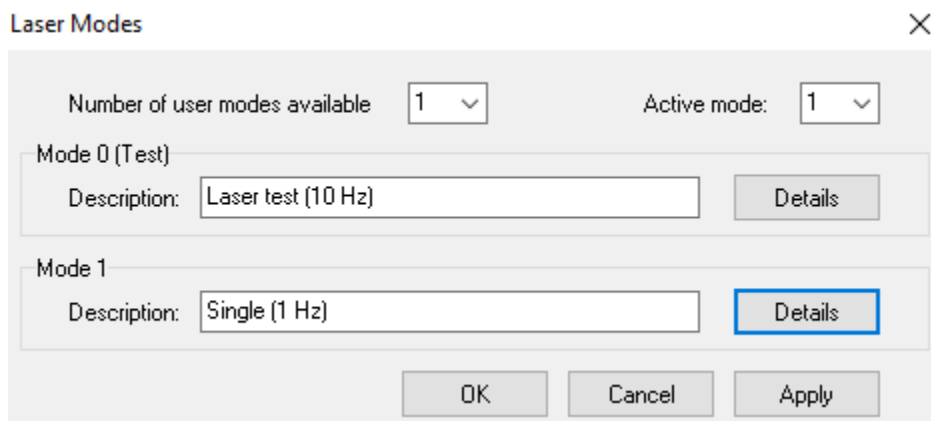



Figure 6.10. Laser mode window

18. Click  and select Setup. Under the Controller window keep laser-timed, Laser shutter-timed, Probe-pulsed, Probe shutter-timed.
19. Under the Controller tab, set the wavelength at the transient absorption wavelength (370 nm) of the standard. Keep the bandwidth between 1 to 2 nm, click “Apply” and “Start”.
20. Under the Oscilloscope tab, set the time to 4000ns, the shift to 10%, and the voltage range to 400 mV.
21. Two people are needed in order to override the interlocks of the laser compartment in the LP980 spectrometer seen in **Figure 6.11**. Small adjustments can be made using the tuning screws of the last prism before the sample to maximize the transient signal.

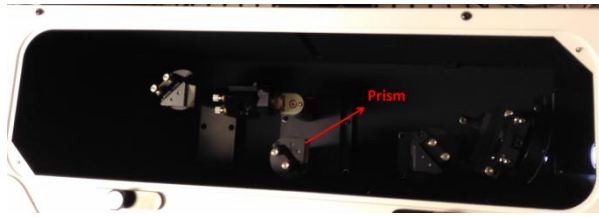


Figure 6.11. Prism compartment for adjusting laser alignment to the sample

Lamp Alignment

22. For lamp alignment, remove all samples. Set the iris next to the sample chamber in the vertical position seen in **Figure 6.12**. The lamp can be accessed by removing the lamp housing lid seen in **Figure 6.13**.



Figure 6.12. Sample compartment with iris

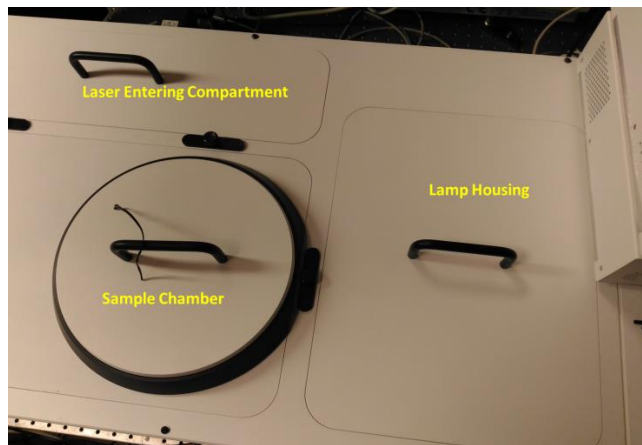


Figure 6.13. Lamp housing chamber

23. For lamp alignment, go to kinetic abs setup in the software. Under the Controller tab, set the laser to timed, laser shutter to closed, the probe pulse to CW, and the probe shutter to timed mode as seen in **Figure 6.14**. Set the wavelength to 500 nm, and the bandwidth to 1nm. Under the Oscilloscope tab, set the time range to 4000 ns, the shift at 10%, and the voltage range to 160 mV. Then press “Apply” and then “start”.

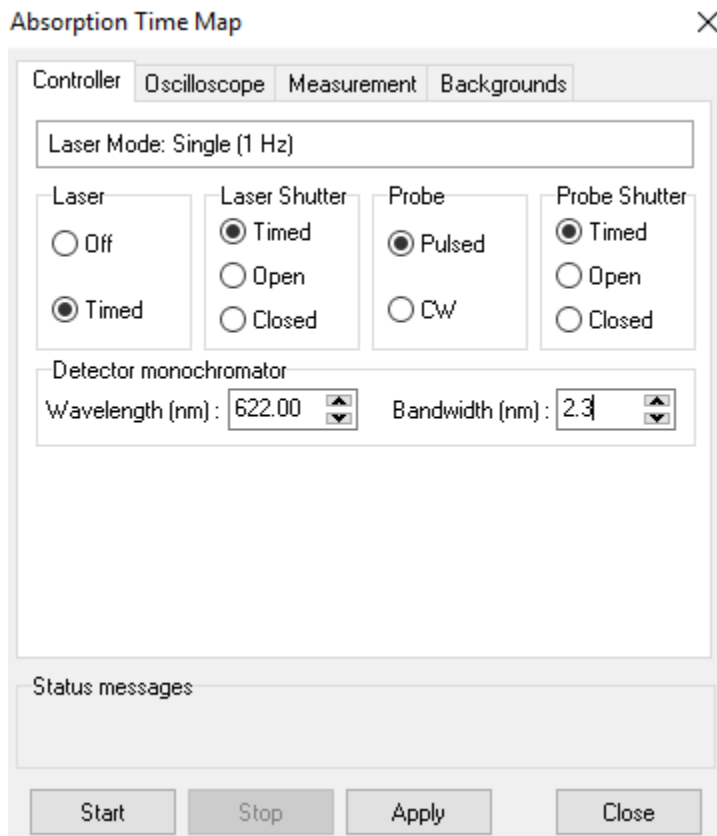


Figure 6.14. Configuration for Lamp alignment

24. With two people, override the interlocks. Unlock the mirror screws in the back of the mirror seen in **Figure 6.15**. Then use the alignment screws to achieve the highest voltage; this will be approx. 40 mV at peak. Then, carefully re-lock the screws on the mirror to “finger tight” and close the lid. After the lamp alignment repeat final laser alignment procedure.

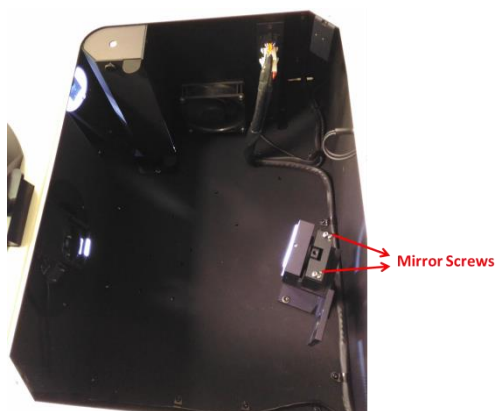


Figure 6.15. Mirror screws for adjustments

Shut Down SOP

25. Close all the active windows in the software.
26. Close the L900 software.
27. Turn off the Oscilloscope.
28. Click the silver button on the Probe Lamp Indicator. Wait for the indicator to read “ready to start”, then turn off PH1.
29. Turn the Osc knob to start, source knob to fixed and mode to LP.
30. Then press off button on QuantaRay controller.
31. If the system is not going to be used for a while (weeks or months) turn off LP1 and then turn off the switch at the backside of the instrument.

Preliminary Data

In order to verify the successful alignment and operation of the new nanosecond transient absorption system, $\text{Ru}(\text{BPY})_3$ was used as a standard. $\text{Ru}(\text{BPY})_3$ is a well-studied metal-organic dye that has long-lived excited states. $\text{Ru}(\text{BPY})_3$ has a d to d transition at 370 nm of up to 650 ns, a metal to ligand charge transfer (MLCT) at 450 nm up to 358 ns, and a singlet

emission at 620 nm.¹ Ru(BPY)₃ was excited using 415 nm beam and probed from 325 nm to 700 nm.

The operation and experimental procedure described above was used for mapping for Ru(BPY)₃. The optical density of the solution was kept at 0.4 OD. Experiments were carried out using increments of 20 nm from 325 to 700 nm. The excitation power was 4.2 mJ. The experimental results for Ru(BPY)₃ can be seen in **Figure 6.16**.

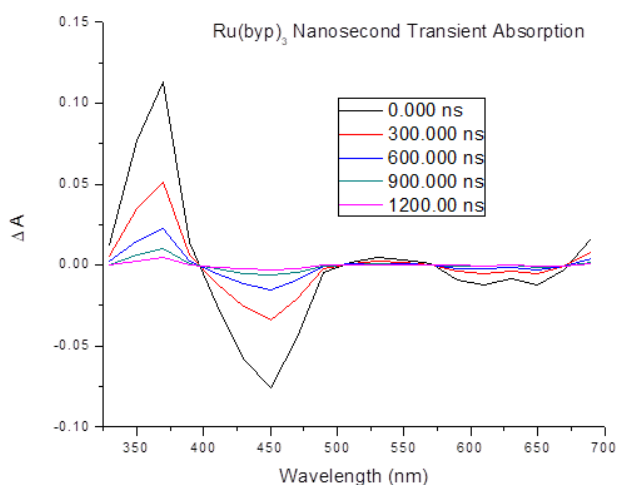


Figure 6.16. Nanosecond transient absorption of Ru(BPY)₃

The obtained results for Ru(BPY)₃ match well with the literature values. The obtained results exhibited a transition at 370 nm with a time constant of 381.51 ns, which is comparable to up to 650 ns found in literature, a transition at 450 nm with a time constant of 354.53 ns, which is comparable to 358 ns found in literature, and a singlet emission seen at 620 nm.¹ These results confirm the successful installation and operation of the new nanosecond transient absorption system.

Conclusion

A new nanosecond transient absorption experiment has been introduced and described. The principles and standard operating procedures have been discussed. Preliminary results of Ru(BPY)₃ dye have shown the successful operation of this new experimental system. There is still room for improvement for this system. An additional R5108 PMT unit that has spectral range from 400 nm to 1200 nm can be used instead of the RP928. This will allow for optical processes in the IR region to be studied. Maximizing the signal while avoiding sample degradation is of utmost importance. A stir bar can be placed in the sample cuvette and an external stirrer can be used to reduce degradation. A flow cell can also be implemented to reduce sample degradation. Purging the sample with Argon can and then using a flow cell can reduce the deactivation of the excited state by singlet oxygen. For samples that have temperature dependent transitions, a cryostat can be used to investigate these processes. This new nanosecond transient absorption system has given access to timescales and processes that are unprecedented in the Goodson Group. This will help in the understanding of electronic processes of the studied compounds.

References

1. Kalyanasundaram, K. Photophysics, photochemistry and solar energy conversion with tris(bipyridyl)ruthenium(II) and its analogues. *Coord. Chem. Reviews*, **1982**, *46*, 159–244.

Chapter 7

Overall Summary and Future Direction

7.1 Overall Summary

The world is rapidly growing and changing, and with this growth and change we have seen greater energy consumption. Currently, the main methods of energy generation combust some sort of fossil fuel to produce heat that is then used for electricity generation. These methods have many drawbacks. On a purely thermodynamics standpoint, much of the heat that is generated is lost and does not go towards electricity generation. The extraction and processing pose environmental hazards and risk. Fossil fuels are a finite resource. There is a financial limitation on how much oil or natural gas that can be extracted. Disregarding the financial limitation, there is also a practical limitation. They are being depleted at a rate that is much faster than what realistically could be ever be replenished. And the biggest issue with fossil fuels is harmful pollutants it releases into the atmosphere causing climate change.

This has led politicians, world leaders, corporations, and scientists to investigate alternative methods of energy production to meet these greater needs using various policies and technologies to satisfy these demands as well as providing a secure and practical source of energy that is less harmful to the environment. To this end, scientists have investigated different methods, materials, processes, technologies, designs, and theories to address these energy demands. One method of energy generation that has garnered a lot of interest, is solar energy harvesting. Solar energy has the benefit of being infinite, as long as the sun exists, and does not produce pollutants in order to generate energy. Much research has focused on this method of

energy generation from inventing new materials to improving device designs in order to become cost competitive with fossil fuels.

One of the most promising solar harvesting materials is organic light harvesting materials. Organic light harvesting materials are easily synthesized, the precursors can be easily obtained, processing and manufacturing is cheaper and less complex than other solar harvesting materials, flexible, have molar absorptivities, and can be made from renewable resources. Researchers have focused on designing organic materials that have good light absorption and high charge carrier mobilities. Researchers have also focused on synthesizing organic materials that promote charge separation and high electron mobilities. There has also been much research in device designs. In this work, the optical properties of organic light harvesting materials were investigated. Understanding the fundamental structure property relationships are key in designing efficient organic light harvesting materials. Chapter 1 of this dissertation introduced the motivations for my research and provided the background needed to understand the importance of my research. An overview of the current and future trends for energy production and energy consumption was discussed. The history of solar harvesting was discussed. Then the principles of solar harvesting were discussed in order to lay a base for understanding how light harvesting devices work. The earliest and most adapted type of light harvesting material was introduced. The benefits and drawbacks of inorganic materials were discussed. New inorganic light harvesting materials were introduced and discussed. Then organic light harvesting material properties were introduced. The advantages and disadvantages were presented. Device architectures were described to give an ideal how the materials are used in order to generate electricity. Various organic light harvesting materials were discussed. Then conjugated donor-acceptor polymers were introduced and each component of the donor-acceptor system was

discussed. Then organic acceptors were introduced and discussed. Chapter 2 explained the theory behind the techniques that were used to investigate the light harvesting materials. The experimental methods were presented and discussed.

In Chapter 3, the ultrafast optical properties of donor-acceptor polymers with benzodithiophene donors and different strength acceptors were investigated. The steady state absorption, steady state emission, ultrafast fluorescent decay dynamics and nonlinear optical properties of these light harvesting conjugated polymers were investigated in solution state. All of the conjugated polymers investigated had broad absorption in the visible spectrum due to small bandgaps due to the low lying LUMO energies created by the electron-withdrawing groups. Fluorescence upconversion studies on the conjugated polymers showed short decay dynamics for conjugated polymers with the stronger electron-withdrawing groups. Two-photon absorption spectroscopy showed large two-photon absorption cross-sections for polymers with the stronger electron-withdrawing acceptors. Fluorescence decay anisotropy studies also indicated the polymers with the stronger electron-withdrawing acceptors had shorter exciton migrations.

In Chapter 4, the influence of the donor conjugation length on the optical properties of new donor-acceptor polymers was investigated. Six new donor-acceptor polymers were synthesized. The polymers consisted of either a DPP, II, or TT acceptor with a s-indacene donors with a thiophene fused on either end or with a thienothiophene fused on either end, increasing the conjugation length of the donor. The polymers with the extended conjugated donor had higher molar absorptivities. The fluorescence upconversion results showed longer fluorescence lifetimes for the extended conjugated donor systems. Computations and TPA experiments showed that the extended conjugated polymers had enhanced charge transfer characteristics

compared to their shorter conjugated counterparts. Investigation of the excited state dynamics showed new ESA and bleached state at higher energies for the extended donor polymers.

In Chapter 5, a new nanosecond laser system was installed and a new nonlinear experiment was designed. This new system generates nanosecond pulses, which is the first for the Goodson Group. This new system is tunable from 400 nm to 2600 nm, which opens up the possibility to measure different photophysical processes that are not offered by many of the ultrafast systems in the Goodson Group. A new two-photon absorption experiment was designed implementing a SRS 250 gated integrator to record the two-photon excited fluorescence response of a PMT. TPA experiments were conducted from 750 nm to 1100 nm using samples with known TPA cross-sections. Preliminary results demonstrated the successful design of this new experimental setup.

In Chapter 6, the new nanosecond laser system was installed and a new nanosecond transient absorption experiment was designed. This new system generates nanosecond pulses, which is the first for the Goodson Group. This new system is tunable from 400 nm to 2600 nm, which opens up the possibility to measure different photophysical processes that are not offered by many of the ultrafast systems in the Goodson Group. A new two-photon absorption experiment was designed implementing a SRS 250 gated integrator to record the two-photon excited fluorescence response of a PMT. TPA experiments were conducted from 750 nm to 1100 nm using samples with known TPA cross-sections. Preliminary results demonstrated the successful design of this new experimental setup.

7.2 Future Directions

All of the experiments in this dissertation were conducted in the solution phase. This is quite important because the experiments give a better understanding of the fundamental

properties of the investigated organic materials, whereas in the solid state, the influence of packing, morphology, processing, and additives can all affect the observed behavior of the organic materials. Also different types of solvents can be used to see solvation effects on the organic materials. Knowing the fundamentals is important in predicting device characteristics, but it cannot account for properties that affect device performance such as morphology and packing behavior. Thus, it is important to investigate the optical properties of these materials in the solid state, because at the end of the day the organic materials are in the solid state in devices. The various organic components can be investigated in the solid state, then mixtures of the components can be investigated in order to investigate the effect of different compositions have on the photophysical properties.

Computations methods are invaluable for investigating these new materials. There have been rapid development in computational methods, theories, and technology that has made computations even more powerful tools for discovering new processes and new organic materials. But there are significant limitations to computational methods. Computations are unable to account for the various differences in local environment that these materials have in the solution and solid state. Computations also have trouble with systems that have many atoms in a molecule. Indeed, in this study smaller oligomers were used as model systems for the investigated polymers because the polymers were too large to investigate with current methods because the memory required, computational time required, and expense. New techniques, technology, methods, and theories are needed in order to investigate these larger systems.

All of the time resolved experiments in this dissertation were conducted at ultrafast timescales of less than a nanosecond, but charge separation, charge transport, and charge collection occur at much longer timescales from 100s of nanoseconds to microseconds. The new

nanosecond system I have installed and designed is going to be a game changer in the Goodson Group. With this new system, all of these longer processes can be investigated. The Gated Integrator can be used to longer timescale optical processes such as thermally activated delayed fluorescence, phosphorescence, and chemiluminescence. Longer fluorescence dynamics can now be investigated with the nanosecond laser and Gated Integrator. Installation of a new nanosecond transient absorption experiment can be used to investigate long lived states such as triplet states. Triplet-triplet annihilation can be investigated. Two-photon absorption properties can already be investigated with the new system. Microwave spectroscopy in conjunction with nanosecond laser excitation can be used to investigate the charge carrier mobilities. This system is going to allow much deeper understanding of the optical properties of these materials and will give a better picture of the whole optical processes involved in light harvesting materials.

Appendices

Appendix A. Enacting Two-Electron Transfer from a Single-Photon-Excited Chromophore

I conducted femtosecond transient absorption experiments in order to investigate two-electron transfer from QOT2 to anthraquinone. New photoproducts were identified and related to calculations conducted by Hyungjun Kim and compared to literature.

The work in this chapter was accepted in Journal of American Chemical Society communication (JACS) with the title:

“Enacting Two-Electron Transfer from a Single-Photon-Excited Chromophore”

Hyungjun Kim, Bradley Keller, Rosina H. Wu, Neranga Abeyasinhe, Ricardo J. Vázquez, Theodore Goodson III, Paul M. Zimmerman

Modifications were made to the manuscript to adapt it to the style of this dissertation. References and supporting information of the manuscript are included in this chapter.

A.1 Abstract

A simulation-led strategy enacts two-electron transfer between a single-photon-excited chromophore (tetracyanobithiophene) and multi-electron acceptor (anthraquinone). The thermodynamic plausibility of electron transfer and the absorption spectra of electron transfer products are predicted using quantum chemical simulation. These predictions are consistent with experimental observations of reduced lifetimes in time-resolved fluorescence spectroscopy, decreased transmission, and appearance of new absorption bands in transient absorption spectroscopy, all of which are consistent with multi-electron transfer. A maximum internal quantum efficiency of 137 % is estimated.

A.2 Introduction

Singlet fission (SF) produces two excited electrons from a single photon.¹⁻³ In materials that enable SF, the multi-electron excited state can be conceived as an entangled double-triplet⁴⁻⁷ and thus denoted TT , which eventually evolves into separated triplets, $2\times T_1$. Although SF may well be used to generate triplets for individual extraction in solar harvesting materials, the correlation between the two triplets makes TT a unique state that is not identical in character to $2\times T_1$.^{8,9} Towards the goals of understanding TT states in more detail and achieving efficient solar energy harvesting, we considered whether the excited electrons of TT could be transferred in a bimolecular, 2-electron process.

SF materials, mostly films,¹⁰ crystals,¹¹ and covalently linked dimers,¹² have been studied extensively in recent years. While multi-electron extraction per photon has been demonstrated in intermolecular SF chromophores (xSF),^{11,13-15} attaining high charge extraction yields remains difficult. Intramolecular SF (iSF) offers several advantages over xSF such as a high degree of tunability of molecular and electronic structure, and relative independence from molecular packing arrangements.¹⁶⁻¹⁸

A.3 Results and Discussion

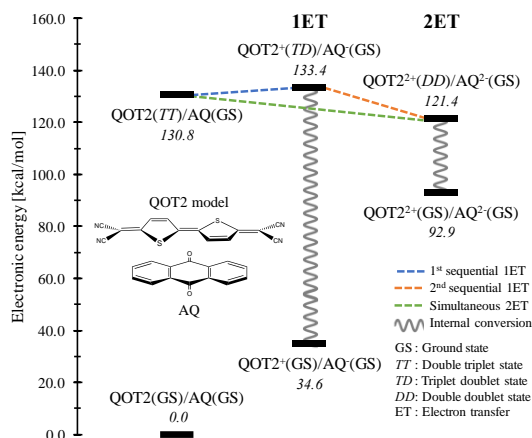


Figure A.3.1. Jablonski diagram for the states of intramolecular singlet fission, 1ET, and 2ET with chemical structures of QOT2/AQ.

While most iSF materials are based on acenes, our groups have revealed that monomers of tetracyanomethylene quinoidal bithiophene (QOT2) have characteristics that closely relate to a key SF intermediate, the TT state.¹⁷ This quinoidal molecule (**Figure A.3.1**, see SI) has a large one-photon absorption cross-section, a low-lying T_1 state, and a multiply excited state with TT character that can be generated via single-photon absorption.^{4,17} As a monomer with a single, tightly coupled π system, QOT2 is highly unusual among iSF chromophores because its triplets cannot separate into $2 \times T_1$. While such confinement of the TT state has not been possible in related SF materials, this special property is advantageous because it provides an opportunity to trap the double triplet and achieve simultaneous multi-electron extraction.¹³ In principle, two-electron transfer (2ET) from an entangled TT state may be advantageous for efficient energy harvesting, as competing relaxation channels will be outcompeted. Herein, the possibility of multi-electron transfer in iSF will be realized by a detailed quantum chemical study of the photoelectrochemical properties of the QOT2 TT state, and its coupling to a suitable acceptor for the two electrons.

The search for suitable acceptor molecule centered on anthraquinones, a plausible energy storage unit with $2e^-$ redox properties.¹⁹⁻²² Our prior study of a variety of these materials indicated that 9,10-anthraquinone (AQ) has a 2-electron affinity of 5.99 eV,²³ which is within range of acceptance of electrons from the QOT2 TT state. Chien *et al.* reported that the QOT2 TT state is dominated by double triplet character, with some contribution from triplet coupling components.⁴ Ionization of QOT2 TT state will likely produce QOT2⁺ TD and QOT2²⁺ DD states with +1 charge localized on each half of QOT2, where D represents a local doublet. Based on this model of QOT2 ionization, a four-point charge approximation gives the thermodynamic driving force as $\Delta E = \text{DIP}_{\text{QOT2}} + \text{DEA}_{\text{AQ}} - \sum_i 1/R_i + \sum_j 1/R_j$, where DIP and DEA indicate double ionization potential and double electron affinity, respectively, and the last two terms are Coulomb attraction and repulsion.²⁴ Quantum chemical simulations give 10.27 eV as an estimate of QOT2 TT state double IP. This analysis predicts 2ET from the QOT2 TT state is thermodynamically viable ($\Delta E = -0.69$ eV), but unfavorable from the ground state QOT2 ($\Delta E = +3.39$ eV, see SI).

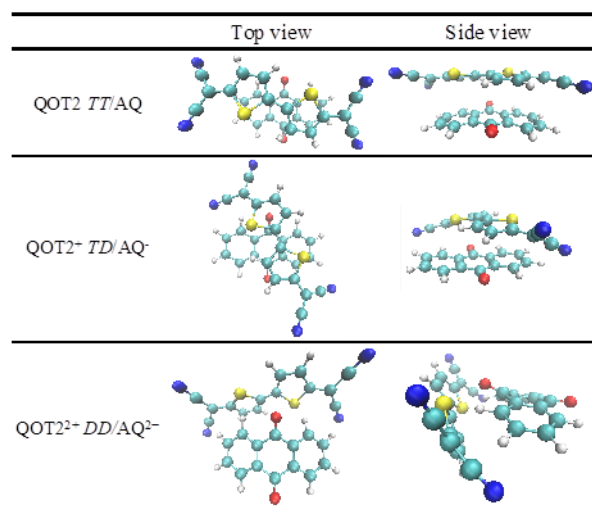


Figure A.3.2. Optimized structure of QOT2/AQ before ET (top panel; QOT2 TT /AQ), after 1ET (middle panel; QOT2⁺ TD /AQ⁻), and after 2ET (bottom panel; QOT2²⁺ DD /AQ²⁻) described by CDFT. Color scheme: hydrogen atom, white; carbon atom, cyan; nitrogen atom, blue; oxygen atom, red; sulfur atom, yellow.

Atomistic simulations were employed to examine the mechanistic feasibility of 2ET. For the key ET step, constrained density functional theory²⁵ (CDFT) was used to estimate the plausibility of this reaction. The molecular structures before ET (QOT2 *TT*/AQ), after 1ET (QOT2⁺ *TD*/AQ⁻), and after 2ET (QOT2²⁺ *DD*/AQ²⁻), are described in **Figure A.3.2**. QOT2/AQ complex forms π - π stacking structures as expected. 1ET, with nearly thermoneutral driving force ($\Delta G = 2.6$ kcal/mol), is followed by thermodynamically favorable second ET ($\Delta G = -9.4$ kcal/mol) and results in two total electrons transferred. Each ET is considered to ionize one of the two triplets in the *TT* state, leading to a *TD* state after the first ET, and a *DD* assignment after 2ET. Ionization of triplets to doublet states in CDFT allows the system to avoid the Marcus inversion region of large driving force (see oxidized QOT2(GS) species in **Figure A.3.1**). This result implies that 2ET can be achieved via two sequential 1ET steps (blue and orange lines in **Figure A.3.1**) and/or one simultaneous 2ET step (green line in **Figure A.3.1**). After 2ET, electrostatic attractions caused by the multi-electron transfer dominate over van der Waals interaction, and side-on binding to maximize Coulombic interaction is predicted (**Figure A.3.2**). (see SI)

Having evidence from simulation that 2ET from QOT2 to AQ has plausible pathways, the absorption spectra of ET products were also examined. The spectra of reduced AQ are available from the literature.²⁶ The absorption spectra of oxidized QOT2 *TT*, however, is not trivial to obtain. From quantum chemical simulations using XMS-CASPT2 and Spin-Flip RAS methods, the electronic state of neutral QOT2 *TT*, and singly and doubly oxidized QOT2 *TT*, are assigned to have 2^1A_g , 1^2B_g , and 1^1B_u symmetries, respectively (see SI). Starting from these states, transition wavelengths and dipole moments were computed (**Figure A.3.3**) to provide a baseline for subsequent spectroscopic experiments. Due to the wide range of wavelengths that

characterize these intermediates, multiple spectroscopic techniques were needed to identify these signatures.

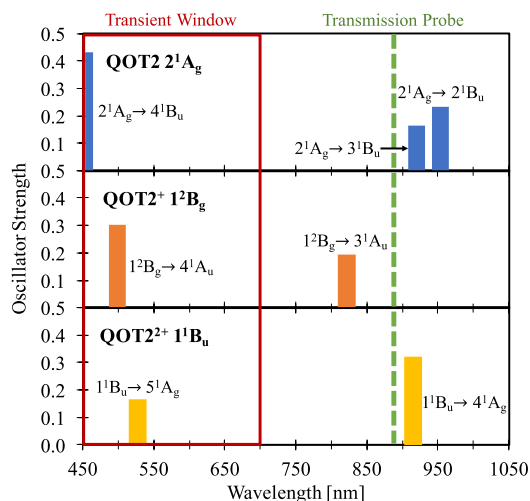


Figure A.3.3. Absorption spectra predicted by XMS-CASPT2 and Spin-Flip RAS for (top) QOT2 2^1A_g state, and (middle and bottom) its oxidized forms, QOT2⁺ 1^2B_g and QOT2²⁺ 1^1B_u states.

With these spectra peaks from simulation in hand, time-resolved fluorescence anisotropy was used to monitor the lifetime of the QOT2 singlet excited state in QOT2/AQ mixture (**Figure S**). In the mixture, the short and long fluorescence timescales decreased to 66% and 23% compared to pure QOT2, respectively (**Table S**). The faster decay of the mixture indicates the appearance of non-radiative sink that can consume exciton population, with ET being a possible cause.²⁷ The initial dynamics (< 25 ps), however, are similar in the QOT2 solution with or without AQ, indicating that the initial ultrafast formation of the *TT* state is unperturbed.

To support these initial indications, transmission measurements quantified the yield of *TT* using QOT2's excited state absorption (ESA) from 2^1A_g at 880 nm.¹⁷ Significant reduction of transmitted power is observed at high power, giving transmission of 0.47 in QOT2 sample (**Figure A.3.4**). Using a procedure established in a prior study of QOT2,¹⁷ a yield for the *TT* state (α_{TT}) is measured to be 84 % for QOT2 without AQ present, indicating 0.84 *TT* states per

absorbed photon. (see SI) In the mixture, ET will change the transmission profile due to the formation of $\text{QOT2}^+ 1^2\text{B}_g$ and $\text{QOT2}^{2+} 1^1\text{B}_u$, which have different absorption spectra compared to the $\text{QOT2 } TT$ state. In the QOT2/AQ mixture, the transmitted power is significantly reduced, by $\sim 0.1\text{mW}$. To explain this change, **Figure A.3.3** shows that $\text{QOT2}^{2+} 1^1\text{B}_u$ has absorption peak near the probe wavelength with a large oscillator strength, almost double that of neutral $\text{QOT2 } TT$ state. In contrast, singly ionized QOT2 ($\text{QOT2}^+ 1^2\text{B}_g$) is predicted to be less likely to absorb at the probe wavelength. The reduction in transmission with AQ present is therefore consistent with 2ET through the formation of the $\text{QOT2}^{2+} 1^1\text{B}_u$ state.

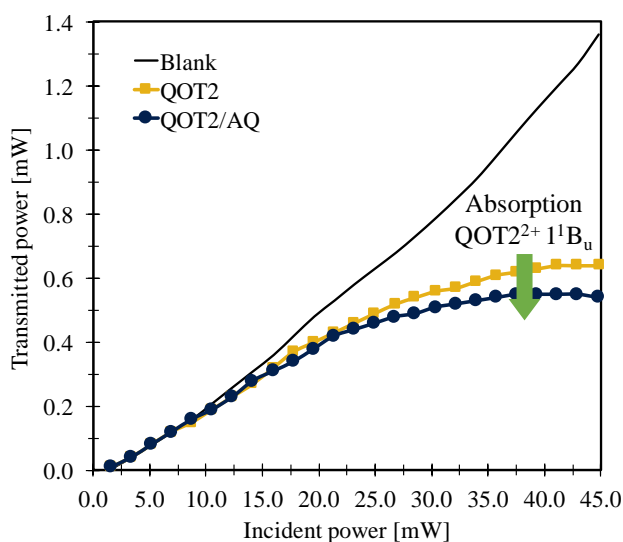


Figure A.3.4. Transmission profile of pure acetonitrile (Blank, black line), QOT2 (yellow square), and QOT2/AQ (blue circle) for the probe light of 880 nm as the function of the pump power at 440 nm.

Transient absorption spectroscopy (TAS) was performed to provide evidence of multi-electron transfer beyond the fluorescence and transmission experiments. Within its available spectral window of 450 – 700 nm, TAS provides a detailed viewpoint of the electronic structure of excited states as they evolve, and provides evidence for ET by detecting the photoactive ET products. TAS of QOT2 exhibits two characteristic bands: ground state bleach (GSB) at 450 – 560 nm and ESA I at 560 – 700 nm, in good agreement with previous studies¹⁷ (**Figure S**).

Characteristic bands of neutral QOT2 decay smoothly and disappear after 20 ps. In addition to these features, three new ESA bands arise when AQ is added to the mixture: ESA II at ~ 488 nm, ESA III at ~ 528 nm, and ESA IV at ~ 569 nm (**Figure A.3.5**).

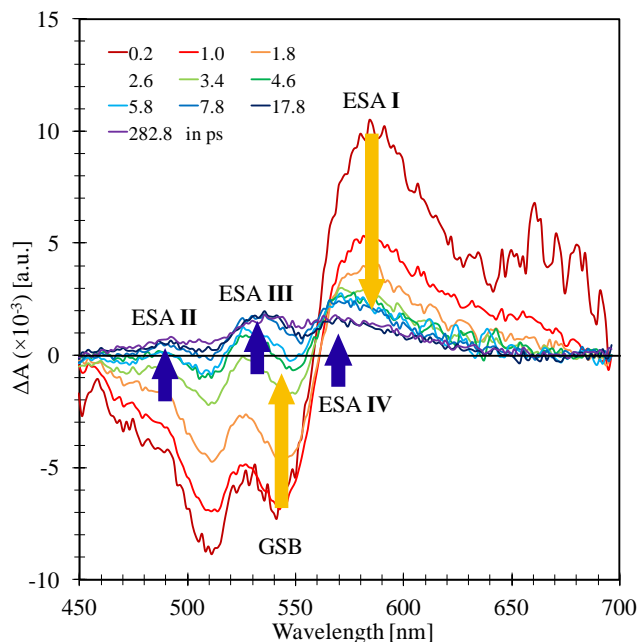


Figure A.3.5. Transient absorption spectrum of QOT2/AQ at selected decaying time as the function of probe wavelength. The characteristic bands of QOT2 (GSB and ESA I) are marked with yellow arrows, and newly arising features (ESA II, III, and IV) are indicated with blue arrows.

The assignment of new signals is made using the simulated absorption peaks (vide supra) for the oxidized QOT2 *TT* species alongside experimental signals for AQ anions²⁶ (**Table A.3.1**). The occurrence of ESA II can be understood by formation of QOT2⁺ 1²B_g and/or doubly reduced AQ ion, which are close to the observed absorption peak near 488 nm. According to simulation, QOT2²⁺ 1¹B_u absorbs light at 529 nm, which overlaps with ESA III. The last feature, ESA IV, is centered at 569 nm and assigned to the single ET product, AQ⁻, which is known to absorb at 550 nm. These results indicate the presence of mixture of species arising from 1ET and 2ET. TAS therefore supports the theoretical predictions of ET from QOT2 *TT* to AQ, and suggests that 2ET

is facile. Additional bands from ion-ion interactions are not detectable in the current transient window, since these likely exist only in the IR region.²⁸

Table A.3.1. Assignment of Characteristic Bands Present in the Transient Absorption Spectra Depending on One- or Two-Electron Transfer

Bands	Wavelength ^a	1ET	2ET
GSB	450 – 560	QOT2 GSB	
ESA I	560 – 700	QOT2 ESA	
ESA II	~ 488	QOT2 ⁺ 1 ² B _g (498)	AQ ²⁻ (470)
ESA III	~ 528	–	QOT2 ²⁺ 1 ¹ B _u (529)
ESA IV	~ 569	AQ ⁻ (550)	–

a) The position of absorption peak is given in nm unit.

The yield of charge carrier extraction from the *TT* state (β_{CE}) defined as $1 \times (\text{yield of 1ET at } TT) + 2 \times (\text{yield of 2ET at } TT)$, is estimated using the transmission profile and predicted molar extinction coefficient (see SI). This quantity is expressed as the function of the yield of 1ET, since the available spectroscopies cannot measure the yield of 1ET products directly. This analysis gives $\beta_{CE,max}$ to be as high as 163 %, where all *TT* states are involved in ET (37 % of *TT* states via 1ET and 63 % of *TT* states via 2ET pathways). The maximum internal quantum efficiency (IQE) given as $\alpha_{TT} \times \beta_{CE,max}$ is therefore approximately 137 %, ~1.4 electrons per photon absorbed. This IQE suggests that constructing molecules with tightly coupled *TT* states may be a strong design principle to overcome the Shockley-Queisser limit and create highly efficient, easily processable solar cells.²⁹

A.4 Conclusion

In summary, this study demonstrates the first theoretically designed molecular system that can harvest multi electrons from strongly correlated *TT* states. Instrumental to this

development were the characterization of QOT2's *TT* state⁴ and screening of $2e^-$ redox acceptors²³, which paved the way for the present study. Future studies will examine the mechanism of 2ET in more detail, in order to provide useful, robust guidelines for designing molecular species for multi-electron transfer.

ASSOCIATED CONTENT

Experimental and computational details. The Supporting Information is available free of charge on the ACS Publications website.

AUTHOR INFORMATION

Corresponding Author

*tgoodson@umich.edu

*paulzim@umich.edu

References

- (1) Smith, M. B.; Michl, J. *Chem. Rev.* **2010**, *110* (11), 6891.
- (2) Zimmerman, P. M.; Zhang, Z.; Musgrave, C. B. *Nat. Chem.* **2010**, *2* (8), 648.
- (3) Stern, H. L.; Musser, A. J.; Gelinas, S.; Parkinson, P.; Herz, L. M.; Bruzek, M. J.; Anthony, J.; Friend, R. H.; Walker, B. J. *Proc. Natl. Acad. Sci.* **2015**, *112* (25), 7656.
- (4) Chien, A. D.; Molina, A. R.; Abeyasinghe, N.; Varnavski, O. P.; Goodson, T.; Zimmerman, P. M. *J. Phys. Chem. C* **2015**, *119* (51), 28258.
- (5) Piland, G. B.; Burdett, J. J.; Dillon, R. J.; Bardeen, C. J. *J. Phys. Chem. Lett.* **2014**, *5* (13), 2312.
- (6) Weiss, L. R.; Bayliss, S. L.; Kraffert, F.; Thorley, K. J.; Anthony, J. E.; Bittl, R.; Friend, R. H.; Rao, A.; Greenham, N. C.; Behrends, J. *Nat. Phys.* **2016**, *13* (2), 176.
- (7) Yong, C. K.; Musser, A. J.; Bayliss, S. L.; Lukman, S.; Tamura, H.; Bubnova, O.; Hallani, R. K.; Meneau, A.; Resel, R.; Maruyama, M.; Hotta, S.; Herz, L. M.; Beljonne, D.; Anthony, J. E.; Clark, J.; Siringhaus, H. *Nat. Commun.* **2017**, *8* (May).
- (8) Chien, A. D.; Zimmerman, P. M. *J. Chem. Phys.* **2017**, *146* (1).
- (9) Rao, A.; Friend, R. H. *Nat. Rev. Mater.* **2017**, *2*, 17063.
- (10) Le, A. K.; Bender, J. A.; Roberts, S. T. *J. Phys. Chem. Lett.* **2016**, *7*, 4922.
- (11) Congreve, D. N.; Lee, J.; Thompson, N. J.; Hontz, E.; Yost, S. R.; Reuswig, P. D.; Bahlke, M. E.; Reineke, S.; Voorhis, T.; Baldo, M. A. *Science* (80-.). **2013**, *340* (6130), 334.
- (12) Sanders, S. N.; Kumarasamy, E.; Pun, A. B.; Steigerwald, M. L.; Sfeir, M. Y.; Campos, L. M. *Angew. Chemie Int. Ed.* **2016**, *55* (10), 3373.

- (13) Chan, W.-L.; Ligges, M.; Jailaubekov, A.; Kaake, L.; Miaja-Avila, L.; Zhu, X.-Y. *Science* (80-.). **2011**, *334* (December), 1541.
- (14) Chan, W. L.; Tritsch, J. R.; Zhu, X. Y. *J. Am. Chem. Soc.* **2012**, *134* (44), 18295.
- (15) Thompson, N. J.; Congreve, D. N.; Goldberg, D.; Menon, V. M.; Baldo, M. A. *Appl. Phys. Lett.* **2013**, *103* (26), 263302.
- (16) Pun, A. B.; Sanders, S. N.; Kumarasamy, E.; Sfeir, M. Y.; Congreve, D. N.; Campos, L. M. *Adv. Mater.* **2017**, *1701416*, 1701416.
- (17) Varnavski, O.; Abeyasinghe, N.; Aragón, J.; Serrano-Pérez, J. J.; Ortí, E.; López Navarrete, J. T.; Takimiya, K.; Casanova, D.; Casado, J.; Goodson, T. *J. Phys. Chem. Lett.* **2015**, *6* (8), 1375.
- (18) Low, J. Z.; Sanders, S. N.; Campos, L. M. *Chem. Mater.* **2015**, *27* (16), 5453.
- (19) Oraziatti, M.; Kuss-Petermann, M.; Hamm, P.; Wenger, O. S. *Angew. Chemie - Int. Ed.* **2016**, *55* (32), 9407.
- (20) Kuss-Petermann, M.; Oraziatti, M.; Neuburger, M.; Hamm, P.; Wenger, O. S. *J. Am. Chem. Soc.* **2017**, *139* (14), 5225.
- (21) Huskinson, B.; Marshak, M. P.; Suh, C.; Er, S.; Gerhardt, M. R.; Galvin, C. J.; Chen, X.; Aspuru-Guzik, A.; Gordon, R. G.; Aziz, M. J. *Nature* **2014**, *505* (7482), 195.
- (22) Er, S.; Suh, C.; Marshak, M. P.; Aspuru-Guzik, A. *Chem. Sci.* **2015**, *6* (2), 885.
- (23) Kim, H.; Goodson, T.; Zimmerman, P. M. *J. Phys. Chem. C* **2016**, *120* (39), 22235.
- (24) Dreuw, A.; Weisman, J. L.; Head-Gordon, M. *J. Chem. Phys.* **2003**, *119* (6), 2943.
- (25) Kaduk, B.; Kowalczyk, T.; Van Voorhis, T. *Chem. Rev.* **2012**, *112* (1), 321.
- (26) Babaei, A.; Connor, P. A.; McQuillan, A. J.; Umaphathy, S. *J. Chem. Educ.* **1997**, *74* (10), 1200.
- (27) Lee, S.; Hwang, D.; Jung, S. Il; Kim, D. *J. Phys. Chem. Lett.* **2017**, *8* (4), 884.
- (28) Dereka, B.; Koch, M.; Vauthey, E. *Acc. Chem. Res.* **2017**, *50* (2), 426.
- (29) Lee, J.; Jadhav, P.; Reusswig, P. D.; Yost, S. R.; Thompson, N. J.; Congreve, D. N.; Hontz, E.; Van Voorhis, T.; Baldo, M. A. *Acc. Chem. Res.* **2013**, *46* (6), 1300.

A.5 Supporting Information

A.5.1 QOT2 Structure

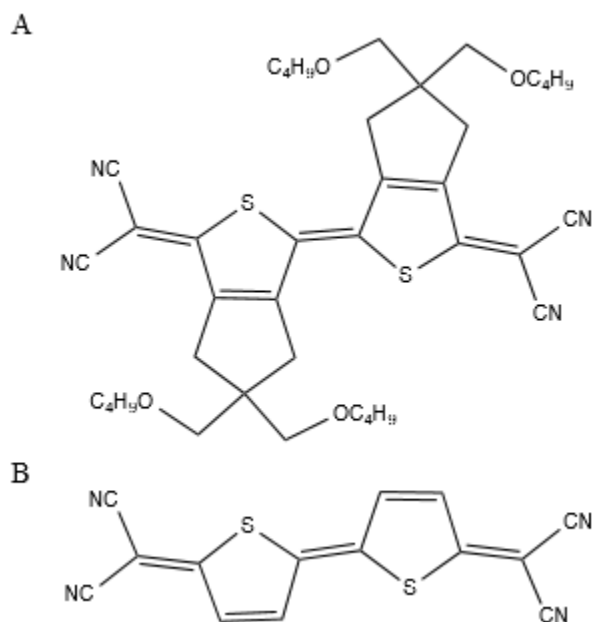


Figure AS1: (A) QOT2 chromophore. (B) Model of QOT2 with the β,β' substituents removed.

A.5.2 Computational Details

A.5.2.1 Thermodynamic Driving Force

Constrained density functional theory (CDFT) is the approach which can diabitize electronic states by imposing the charge and spin constraints on specific regions of molecules.¹ B3LYP functional with empirical dispersion correction of Grimme² (B3LYP-D) and 6-31G* is used to optimize the QOT2/AQ structures. The scaling factor (s_6) of 1.05 for dispersion energy calculation is used as recommended for B3LYP-D. Single point energy is refined by M06-HF-Dfunctional³ with s_6 value of 1.00. M06-HF incorporates full Hartree-Fock (HF) exchange for all interelectronic distances to give improved asymptotic Coulomb interaction, and this functional is known to perform well for charge-transfer reactions.⁴ Detailed charge and spin localization information can be found in Table S1. All CDFT calculations are performed using Q-Chem version 4.0.⁵

Table AS1: Characterization of diabatic states of the QOT2/AQ complex investigated in this study using charge and spin

		QOT2 Half		QOT2 Other Half		AQ	
		Charge	Spin	Charge	Spin	Charge	Spin
Before ET	QOT2 <i>TT</i> /AQ	0	+2 (\uparrow, \uparrow)	0	-2 (\downarrow, \downarrow)	0	0
After 1ET	QOT2 ⁺ <i>TD</i> /AQ ⁻	0	+2 (\uparrow, \uparrow)	+1	-1 (\downarrow)	-1	-1 (\downarrow)
After 2ET	QOT2 ²⁺ <i>DD</i> /AQ ²⁻	+1	+1 (\uparrow)	+1	-1 (\downarrow)	-2	0 (\downarrow, \uparrow)

A.5.2.2 Theoretical Absorption Spectra

Absorption spectra of QOT2 TT, QOT2⁺ TD, and QOT2²⁺ DD (QOT2 2^1A_g , QOT2⁺ 1^2B_g , and QOT2²⁺ 1^1B_u) are predicted to analyze the experimental results. (See Section S8 for symmetry assignment) C_{2h} symmetry is imposed on the QOT2 molecule, and active space consisting of 10 electrons in 8 π orbitals (10e,8o) is selected. Singly and doubly ionized QOT2 TT is described using the active space of (9e,8o) and (8e,8o), respectively, without any changes in the molecular orbitals. All the geometries are optimized using XMS-CASPT2 method⁶ and 6-31G* basis sets with level shift of 0.20. XMS-CASPT2 has been known for better description of energetics than plane CASPT2 near conical intersection.⁷ Also, the XMS-CASPT2 calculation has proven its ability to predict the absorption of neutral QOT2 TT state successfully.⁸ Refined single point energy has been obtained using valence triple-zeta plus polarization basis sets, TZVPP. In addition to level shift, IPEA shift of 0.10 has been applied in single point energy calculations to avoid intruder states.⁹ All XMS-CASPT2 calculations are carried out using MOLPRO version 2012.1.¹⁰

Transition dipole moments (TDM) is necessary to evaluate oscillator strength, but XMS-CASPT2 TDM is not available yet in MOLPRO version 2012.1. CASSCF TDM with relatively small active space gives inconsistent results due to the lack of dynamic correlation.⁸ As an alternative approach, Spin-Flip RAS TDM which has larger amount of dynamic correlation than

CASSCF is implemented by Chien et al. in a development version of Q-Chem 4.0. All TDM value are this work is calculated using Spin-Flip RAS with 6-31G* based on the XMS-CASPT2 geometries.

A.5.3. Experimental Details

A.5.3.1. Chemical Species

AQ is commercially available and used without further purification. QOT2 is prepared by Takahashi et al.¹¹ Acetonitrile (AN) is selected as solvent owing to high solubility of QOT2/AQ mixture. All experiments are performed in AN.

A.5.3.2. Steady-State UV-Vis Absorption and Fluorescence Emission

Steady-state absorption and fluorescence emission property of QOT2 and AQ have been measured in AN with the concentration of 25 μM for both molecules. Mixture of QOT2 and AQ is prepared to have 1:1 molar concentration ratio. The concentration of each chemical is same as the one in their pure form. UV-Vis absorption spectrum were recorded with an Agilent Technologies 8453 spectrophotometer, and fluorescence emission were measured using a Fluomax-2 fluorometer.

A.5.3.3. Time-Resolved Fluorescence Anisotropy

Femto-second upconversion spectroscopy is employed to resolve temporally the polarized fluorescence. The optical arrangement for our upconversion experiments are same that reported in the previous works.^{12,13} The sample solution was exposed to a frequency-doubled light from a modelocked Ti-sapphire laser (Tsunami, Spectra Physics). This setup produces a trained pulse of light with wavelength of 400 nm. The sample was placed in the rotating cuvette to avoid any possible degradation and accumulation effect. The horizontally polarized fluorescence emitted from the sample was upconverted in a nonlinear crystal of β -Ba borate

using a pump beam at about 800 nm that was first passed through a variable delay line. This system acts as an optical gate and enables the fluorescence to be resolved temporally with a time resolution of ~ 200 fs. Spectral resolution was achieved by dispersing the upconverted light in a monochromator and detecting it by using a photo multiplier tube (Hamamatsu R1527P). The excitation average power was kept at a level below 0.5 mW.

A.5.3.4. Transient Absorption Spectroscopy

The output of an amplified laser beam was split to generate pump and probe beam pulses with a beam splitter (85 % and 15 %). The pump beam was produced by an optical parametric amplifier (OPA-800c). The pump beam used in this study was obtained from either the second- or fourth harmonic generation of the signal beam and this was focused on the sample cuvette. The probe beam was delayed with a computer controlled motion controller and then focused on to a 2 mm sapphire plate to generate a white light continuum. The white light was then overlapped with the pump beam in a 1.5 mm quartz cuvette containing the sample and the change in absorbance for the signal was collected by a CCD detector (Ocean Optics). Data acquisition was controlled by software from Ultrafast System Inc. Typical power of probe beam was $< 0.1 \mu\text{J}$, while the pump beam ranged from 0.1 to 0.4 μJ per pulse. The pulse duration was obtained by fitting the solvent response, which was determined as ~ 130 fs. The sample was stirred with a rotating magnetic stirrer.

A.5.3.5. Transmission Profile

For transmission profile, we have investigated the excited state absorption of QOT2 at 880nm (1.41 eV) with a femtosecond pulse trained at 440 nm (2.82 eV). The light with wavelength of 880 nm plays a role of probe beam, produced by tunable MaiTai laser system (SpectraPhysics) giving 130 fs pulses with a repetition rate of 80 MHz. Second harmonic of the

probe beam with wavelength of 440 nm has been produced in BBO crystal and this is a pump laser. The selected wavelength region is reasonable since there is negligible steady-state absorption. A variable neutral density filter is placed to cut down the excitation power. The position of focusing lens is adjusted to place focusing point on the sample. Blank AN solvent gives a reference line. A calibrated photodiode was used to measure the incident power. The transmitted power has been measured with a wide aperture power meter which is free of any thermal lensing effect.

A.5.4. Steady-State UV-Vis Absorption

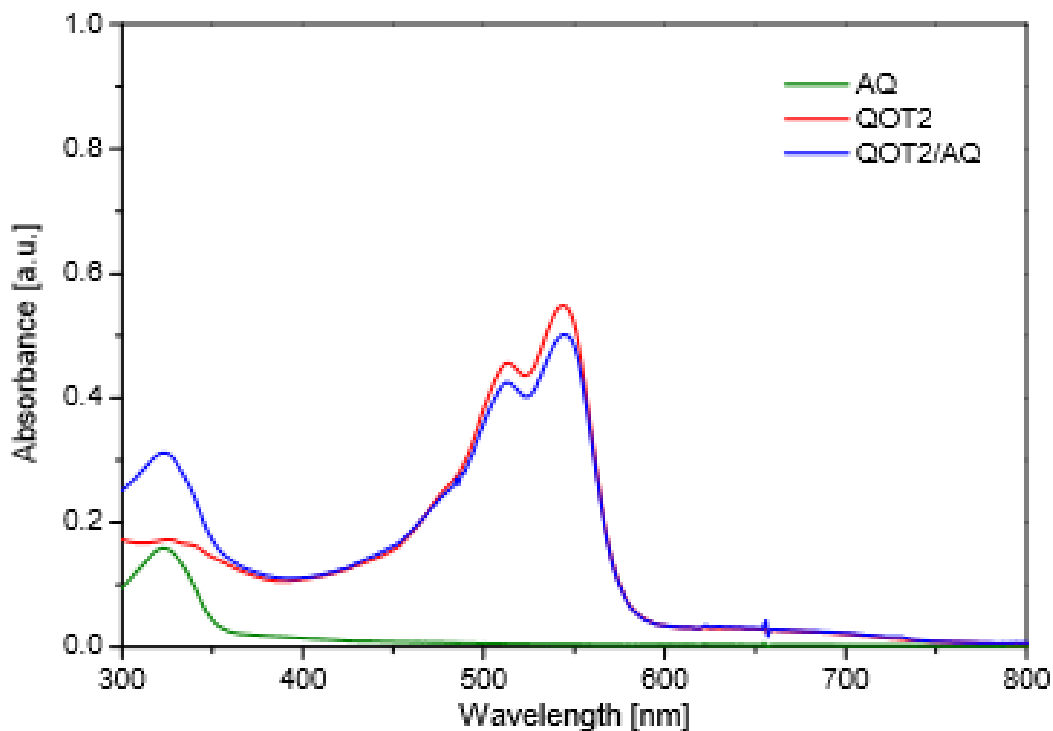


Figure AS2: UV-Vis absorption of QOT2, AQ, and QOT2/AQ in AN.

A.5.5. Steady-State Fluorescence Emission

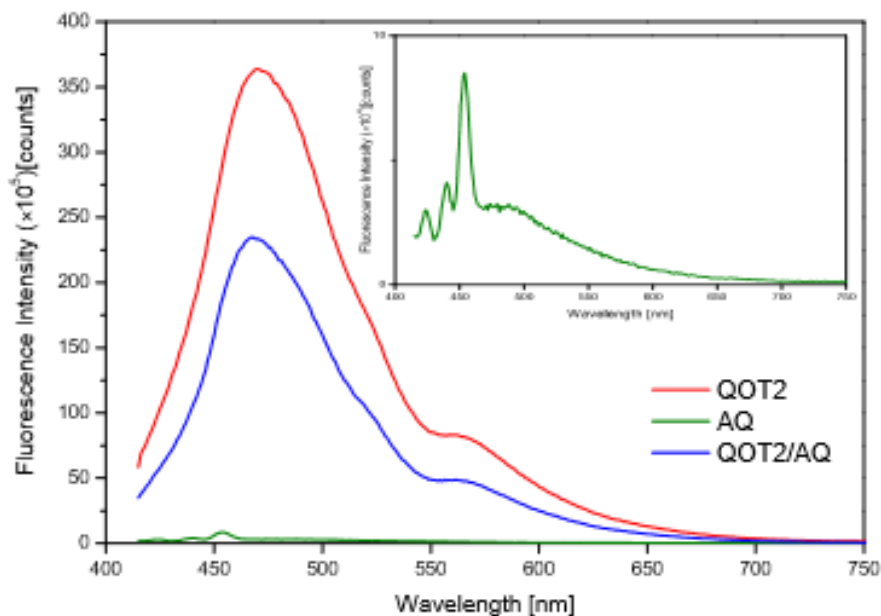


Figure AS3: Fluorescence emission of QOT2, AQ, and QOT2/AQ in AN. The spectrum of AQ is enlarged in the inset.

A.5.6. Four-point Charge Approximation

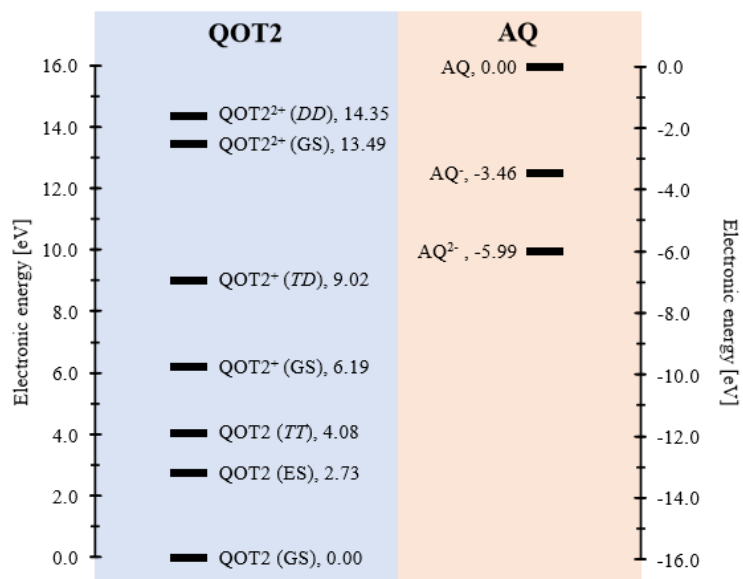


Figure AS4: Relative energy levels of QOT2, AQ, and their relevant ET products

Level of Theory

for GS: ω B97X-D/G3Large/PCM(AN)// ω B97X-D/6-31G*

for QOT2 (TT), QOT2+ (TD) and QOT22+ (DD):

C(ω B97X-D)/G3Large/PCM(AN)//C(ω B97X-D)/6-31G*

C(ω B97X-D): Constrained ω B97X-D

for ES: TD-(ω B97X-D)/G3Large/PCM(AN)// ω B97X-D/6-31G*

DIP for ground state QOT2

$$\text{DIP}_{\text{QOT2 GS}} = E_{\text{QOT2}^{2+}(\text{GS})} - E_{\text{QOT2}(\text{GS})} = 14.35 \text{ eV}$$

$$\text{DIP}_{\text{QOT2 TT}} = E_{\text{QOT2}^{2+}(\text{DD})} - E_{\text{QOT2}(\text{TT})} = 10.27 \text{ eV}$$

DEA for ground state AQ

$$\text{DEA}_{\text{AQ}} = E_{\text{AQ}} - E_{\text{AQ}^{2-}} = -5.99 \text{ eV}$$

Position of Localized Charge

The position of localized charge is determined as the center of mass for the subunit of each molecule.

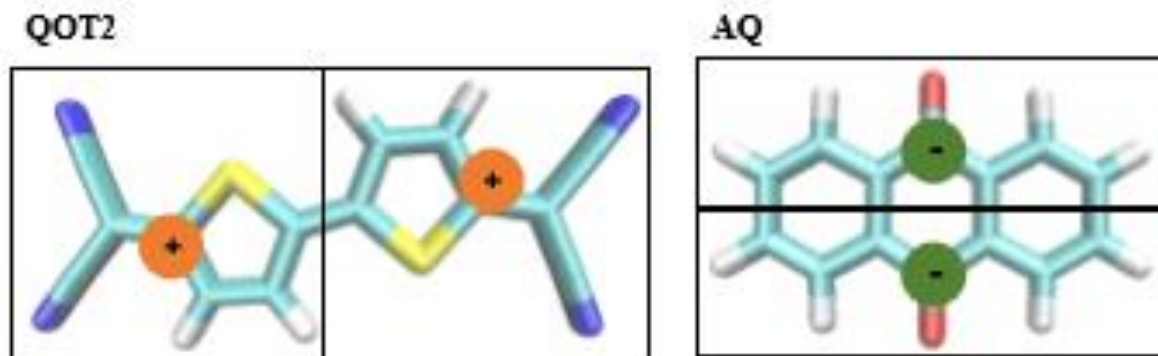


Figure AS5: Position of localized positive (negative) charge on the isolated QOT2 (AQ) molecule

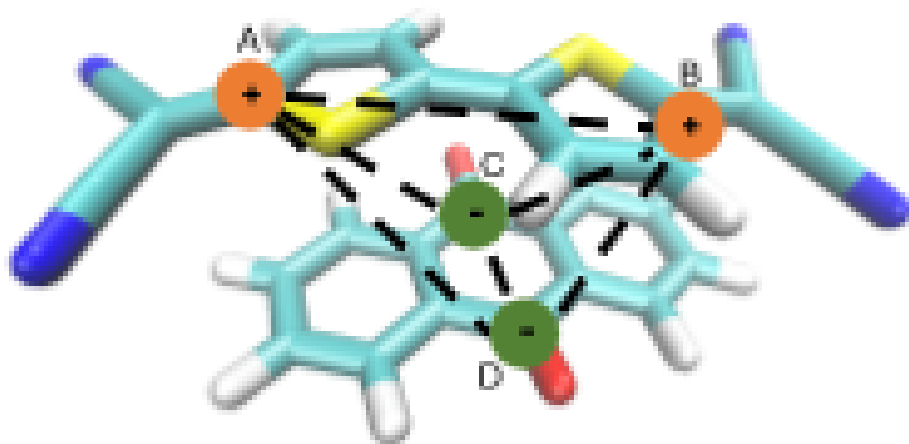


Figure AS6: Position of localized charges on the ground state QOT2/AQ complex

Table AS2: Coulomb interaction between four point charges in QOT2/AQ complex

Index ^a	distance (Å)	Coulomb energy (eV)
A-B	6.70	+2.15
A-C	4.20	-3.43
A-D	4.54	-3.17
B-C	5.76	-2.50
B-D	4.74	-3.04
C-D	2.87	+5.02
Sum		-4.97

a) Index in **Figure S6**

Thermodynamic Driving Force of 2ET

$$\Delta E = \text{DIP}_{\text{QOT2}} + \text{DEA}_{\text{AQ}} + \text{Coulomb Interaction}$$

$$\text{for QOT2 GS: } \Delta E = 14.35 - 5.99 - 4.97 = \mathbf{3.39 \text{ eV}}$$

$$\text{for QOT2 TT: } \Delta E = 10.27 - 5.99 - 4.97 = \mathbf{-0.69 \text{ eV}}$$

A.5.7. CDFT Becke Population Analysis

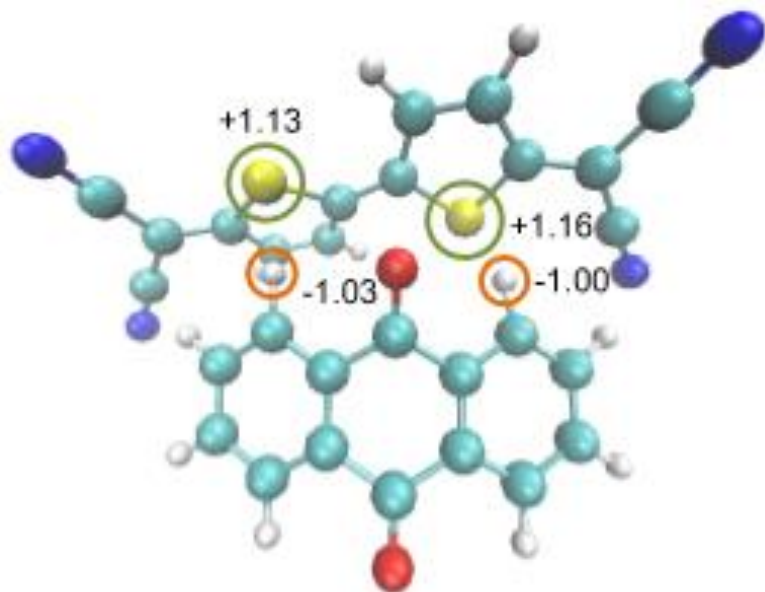


Figure AS7: CDFT Becke population analysis of QOT2/AQ after 2ET

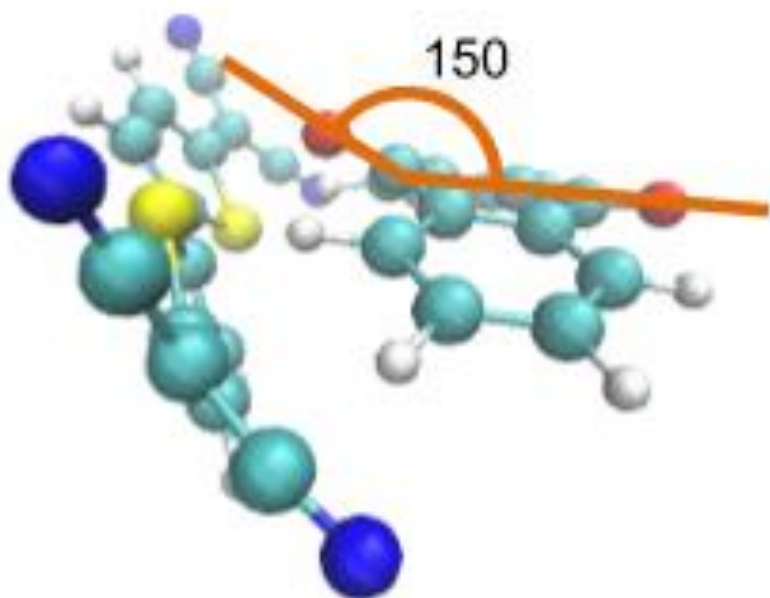


Figure AS8: Distortion of carbonyl group from planarity in AQ as the result of maximizing Coulomb interaction

A.5.8. Natural Orbital Occupancy

Table AS3: Population of QOT2 TT, and ionized QOT2 TT.

	QOT2 TT^a	QOT2 ⁺ TD^b	QOT2 ²⁺ DD^b
Symmetry	2^1A_g	1^2B_g	1^1B_u
8a _u	0.33	0.10	0.15
7b _g	1.16	0.64	0.24
7a _u	0.97	0.89	0.96
6b _g	1.60	1.49	1.11

a) The geometry is optimized using XMS-CASPT2/6-31G* with the active space of (10e,8o). b) The same level of theory used for QOT2 TT is applied with different active spaces, (9e,8o) and (8e,8o) for QOT2+ TD and QOT2²⁺ DD, respectively.

A.5.9. Time-Resolved Fluorescence Anisotropy

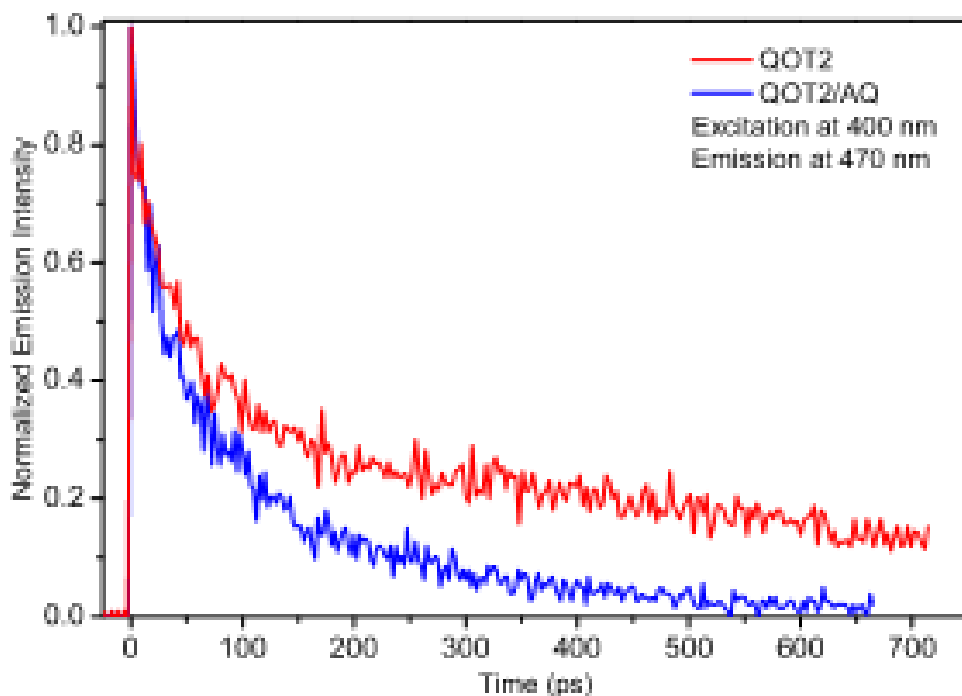


Figure AS9: Time-resolved fluorescence anisotropy measurement of QOT2 and QOT2/AQ

Table AS4: Lifetime excited singlet state of QOT2 and QOT2/AQ using time-resolved fluorescence anisotropy.^a

	τ_1^b	τ_2^b
QOT2	41.5	785.9
QOT2/AQ	27.3	181.2
τ_n ratio ^c	0.66	0.23

a) Normalized fluorescence intensity is fitted to $y = A_1e^{-t/\tau_1} + A_2e^{-t/\tau_2}$

b) τ_1 and τ_2 are the lifetime of short and long component, respectively.

c) τ_n ratio = $\frac{\tau_n \text{ of QOT2/AQ}}{\tau_n \text{ of QOT2}}$ (n = 1 or 2)

A.5.10. Transient Absorption Spectrum of QOT2

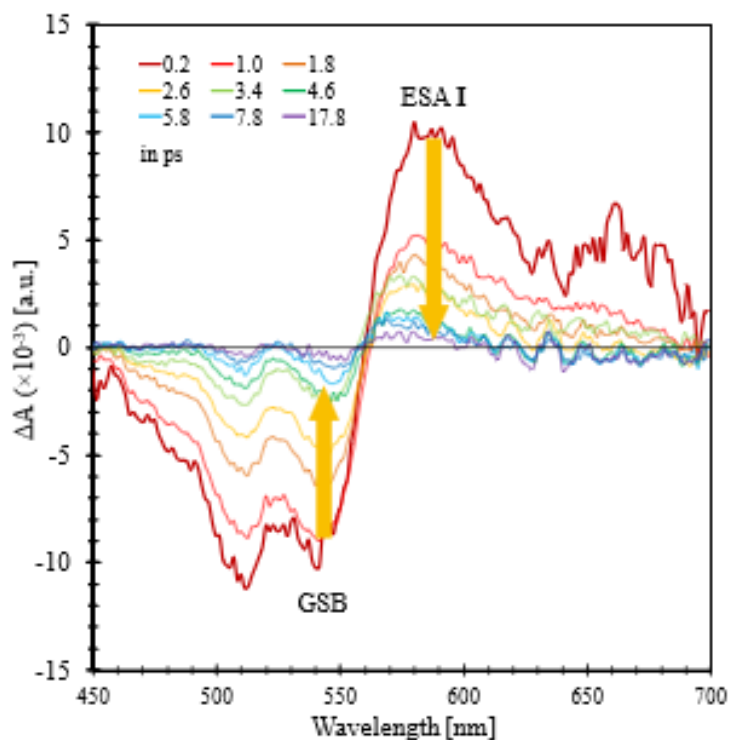


Figure AS10: Transient absorption spectrum of QOT2 at selected decaying time as the function of probe wavelength. The characteristic bands of QOT2 (GSB and ESA I) are marked with yellow arrows

A.5.11. Yield of the QOT2 TT State

Parameter Full power (Pump + Probe) = 44.88 + 1.87 = 46.75 mW

Pump power (440 nm) = 44.88 mW (96 % of full power)

Probe power (880 nm) = 1.87 mW (4 % of full power)

Laser pulse repetition rate (r) = 8×10^7 pulse/s

$$\text{Energy per pump pulse (E}_p\text{)} = \frac{\text{Pump power}}{r} = \frac{44.88 \times 10^{-3}}{8 \times 10^7} = 0.56 \text{ nJ/pulse}$$

Pulse duration (dt) = 130 fs = 1.3×10^{-13} s

Laser beam divergence (full angle) ≤ 1 mrad (Mai-Tai specs) = 10^{-3} rad

Focus of the focusing lens = 12.0 cm

Waist diameter of focal beam (D) = 12.0×10^{-3} cm = 1.20×10^{-2} cm

Focal waist area (A) = $\pi \times \left(\frac{D}{2}\right)^2 = 1.13 \times 10^{-4}$ cm² = 1.20×10^{-2} cm²

Cell length (L) = 1 cm

Excitation volume (V) = A \times L = $1.13 \times 10^{-4} \times 1 = 1.13 \times 10^{-4}$ cm³

$$\text{Energy of a pump photon (e)} = h\nu = \frac{hc}{\lambda} = \frac{6.626 \times 10^{-34} \times 3 \times 10^8}{440 \times 10^{-9}} = 4.52 \times 10^{-19} \text{ J/photon}$$

Constant

Avogadro constant (N_A) = 6.02×10^{23}

Planck constant (h) = 6.626×10^{-34} J·s

Speed of light (c) = 3×10^8 m/s

A.5.11.1. The Number of Singlet Exciton (N_s*)

Optical density of the sample at 440 nm = 0.14 from UV-Vis absorption

Number of absorbed photon per pulse (N_{abs}) = I_{in} - I_{out} = I_{in} \times (1 - $10^{-0.14}$) = I_{in} \times (1 - 0.724) =

0.276 \times I_{in}

$$I_{in} = \frac{Ep}{e} = \frac{0.56 \times 10^{-9}}{4.52 \times 10^{-19}} = 1.24 \times 10^9 \text{ photons}$$

$$N_{abs} = 0.276 \times 1.24 \times 10^9 = 3.42 \times 10^8 \text{ photons}$$

The number of molecules in the excited singlet state will be same as the number of absorbed photons: $N_s^* = N_{abs} = 3.42 \times 10^8$ photons

A.5.11.2. The Number of TT States ($N_{TT,total}$)

Probe power after blank (pure AN) = 1.36 mW

Probe power after QOT2 solution = 0.64 mW

Probe beam attenuation observed under pump of 44.88 mW is $\frac{0.64}{1.36} = 0.471$

No focal mismatch is suggested in this version of calculations.

In order to create this attenuation for the matching part of the probe beam, the concentration of the QOT2 TT states which is responsible for attenuation can be obtained:

$$\frac{I_{out}}{I_{in}} = 0.471 = 10 \times -\epsilon_{TT} \times L \times M_{TT} \quad (\epsilon_{TT}: \text{Molar extinction coefficient of a QOT2 TT state, } M_{TT}:$$

Concentration of a QOT2 TT state)

$$\log(0.471) = -0.327 = -\epsilon_{TT} \times L \times M_{TT}$$

$$M_{TT} = \frac{0.327}{1 \times 1.7 \times 10^4} = 0.192 \times 10^{-4} \text{ M}$$

$\epsilon_{TT} = 1.7 \times 10^4 \text{ M}^{-1} \text{ cm}^{-1}$, the molar extinction coefficient for absorption of QOT2 TT estimated using following equations and calculated numerical values.

$$f = \frac{2}{3} \times \Delta E \times |TDM|^2$$

$$f = 4.39 \times 10^{-9} \times 1.06 \times \epsilon_{TT} \times \Delta v_{0.5}$$

$$\epsilon_{TT} = \frac{\frac{2}{3} \times \Delta E \times |TDM|^2}{4.39 \times 10^{-9} \times 1.06 \times \Delta v_{0.5}}$$

$$\text{Transition} = 2^1 A_g \rightarrow 3^1 B_u$$

Energy difference (ΔE) = 1.347 eV from XMS-CASPT2/TZVPP(IPEA=0.10)//XMS-CASPT2/631G* with (10e,8o)

Transition dipole moments (TDM) = 2.15 from Spin-Flip RAS/6-31G* with (10e,8o) with a heptet reference state

Oscillator strength (f) = 0.153

Line width ($\Delta\nu_{0.5}$) = 1886 cm^{-1} (That of the 570 nm absorption)

This molar concentration corresponds to the TT population density, n_{TT} :

$$n_{\text{TT}} = \frac{N_A}{100} \times M_{\text{TT}} = \frac{6.02 \times 10^{23}}{1000} \times 0.192 \times 10^{-4} = 1.16 \times 10^{16} \text{ triplets/cm}^3$$

Total number of TT states in the excitation volume (V) is:

$$N_{\text{TT, total}} = n_{\text{TT}} \times V = 1.16 \times 10^{16} \times 1.13 \times 10^{-4} = 1.31 \times 10^{12} \text{ molecules}$$

A.5.11.3. Yield of the TT state (α_{TT})

$$\alpha_{\text{TT}} = \frac{\text{The number of TT}}{\text{The number of absorbd } e^-}$$

Lifetime of TT state of QOT2 (τ_{TT}) = 57 μs

Each pulse creates 3.42×10^8 molecules in the singlet state (N_s^*)

The number of TT states created by each pulse ($N_{\text{TT,p}}$) = $\alpha_{\text{TT}} \times N_s^* = \alpha_{\text{TT}} \times 3.42 \times 10^8$ molecules in the TT state in the excitation volume

Now the TT state accumulation at relatively high pulse repetition rate should be taken into account:

$$N_{\text{TT, total}} = N_{\text{TT,p}} \times \tau_{\text{TT}} \times \Gamma$$

$$N_{\text{TT, total}} = (\alpha_{\text{TT}} \times 3.42 \times 10^8) \times (57 \times 10^{-6}) \times (8 \times 10^7)$$

The total number of TT states in the excitation volume should be equal to the number of accumulated TT states.

$$1.31 \times 10^{12} = \alpha_{\text{TT}} \times 3.42 \times 10^8 \times 57 \times 10^{-6} \times 8 \times 10^7$$

$$\alpha_{\text{TT}} = \frac{1.31 \times 10^{12}}{3.42 \times 10^8 \times 57 \times 10^{-6} \times 8 \times 10^7}$$

A.5.12. Yield of Charge Carrier Extraction from the TT state(β_{CE})

$$\begin{aligned}\beta_{TT} &= \frac{\text{The number of harvested } e^-}{\text{The number of TT}} \\ &= \frac{1 \times (\text{the number of 1ET}) + 2 \times (\text{the number of 2ET})}{\text{The number of TT}} \\ &= 1 \times (\text{yield of 1ET at TT}) + 2 \times (\text{yield of 2ET at TT})\end{aligned}$$

Probe power after blank (pure AN solution) = 1.36 mW

Probe power after QOT2/AQ solution = 0.54 mW

Probe beam attenuation by QOT2/AQ under pump of 44.88 mW is $\frac{0.54}{1.33} = 0.397$

Absorption at 880nm

Figure A.3.3 in the main text indicates that absorbance at 880 nm can be given as the sum of QOT2 TT and QOT2²⁺ DD.

$$A_{\text{total}} = A_{\text{QOT2 TT}} + A_{\text{QOT2}^{2+} \text{ DD}} = \epsilon_{\text{TT}} \times L \times M_{\text{TT}} + \epsilon_{\text{DD}} \times L \times M_{\text{DD}}$$

Mass balance for QOT2 without QOT2 degradation

$$M_{\text{QOT2}} = M_{\text{TT}} + M_{\text{TD}} + M_{\text{DD}} = 0.192 \times 10^{-4} \text{ M}$$

$$M_{\text{TT}} = 0.192 \times 10^{-4} - M_{\text{TD}} - M_{\text{DD}}$$

$\epsilon_{\text{DD}} = 3.4 \times 10^4 \text{ M}^{-1} \text{ cm}^{-1}$, the molar extinction coefficient for absorption of QOT2²⁺ DD estimated using following equations and calculated numerical values.

$$f = \frac{2}{3} \times \Delta E \times |TDM|^2$$

$$f = 4.39 \times 10^{-9} \times 1.06 \times \epsilon_{\text{DD}} \times \Delta v_{0.5}$$

$$\epsilon_{\text{DD}} = \frac{\frac{2}{3} \times \Delta E \times |TDM|^2}{4.39 \times 10^{-9} \times 1.06 \times \Delta v_{0.5}}$$

$$\text{Transition} = 1^1\text{B}_u \rightarrow 4^1\text{A}_g$$

Energy difference (ΔE) = 1.353 eV from XMS-CASPT2/TZVPP(IPEA=0.10)//XMS-CASPT2/631G* with (8e,8o)

Transition dipole moments (TDM) = 3.01 from Spin-Flip RAS/6-31G* with (8e,8o) with a heptet reference state

Oscillator strength (f) = 0.300

Line width ($\Delta\nu_{0.5}$) = 1886 cm^{-1} (That of the 570 nm absorption)

$$\frac{I_{out}}{I_{in}} = 0.397 = 10^{-A_{total}} = 10^{-\epsilon_{TT} \times L \times M_{TT} - \epsilon_{DD} \times L \times M_{DD}}$$

As explained in the main text, the available spectroscopies cannot measure the yield of 1ET products directly. Therefore, we have two equations (absorption at 880nm, and mass balance for QOT2) with three unknowns. (M_{TT} , M_{TD} , and M_{DD}) This situation implies that the charge carrier extraction calculation can be expressed with the fixed amount of one-electron transfer.

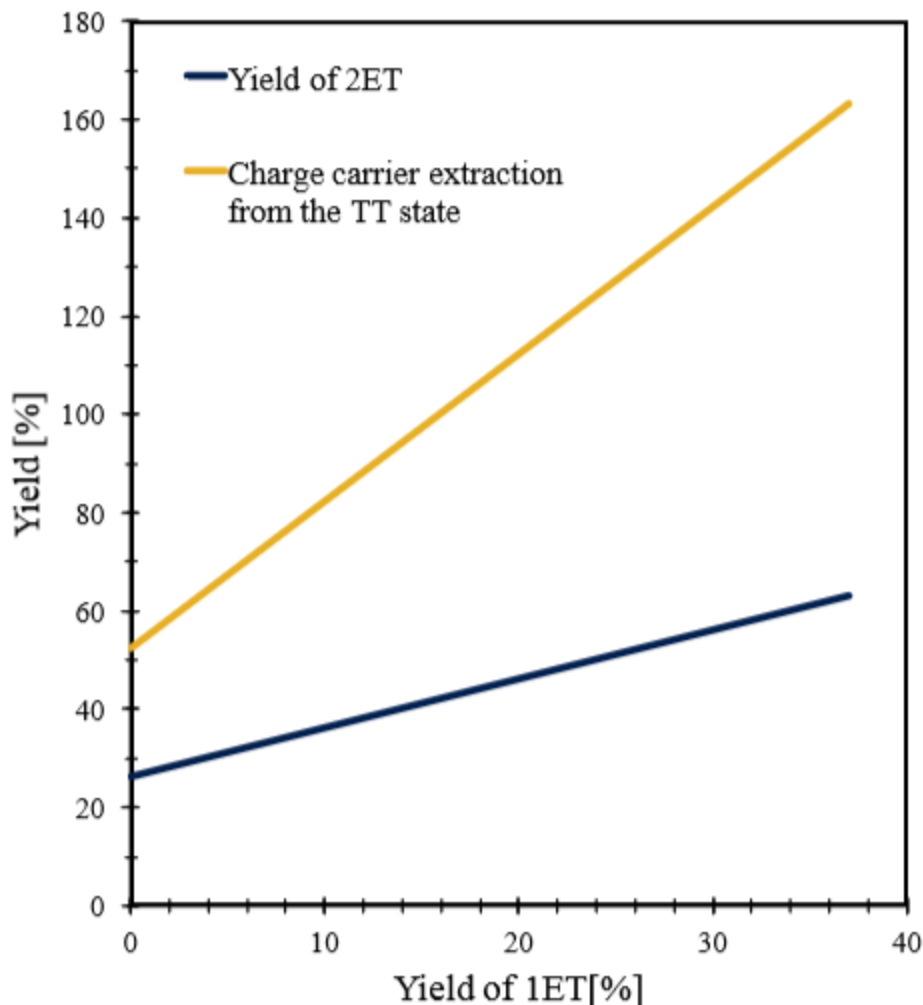


Figure AS11: Yield of two-electron transfer and charge carrier extraction as the function of yield of one-electron transfer.

The 1ET produces the species that are less likely to absorb probe light (**Figure A.3.3**). To explain observed decrease in transmission, 1ET should be accompanied by 2ET which creates better absorbing-probe species, $\text{QOT}2^{2+} 1^1\text{B}_u$ to compensate the loss of $\text{QOT}2 \text{TT}$.

Quantitatively, the oscillator strength of $\text{QOT}2^{2+} 1^1\text{B}_u$ is twice of $\text{QOT}2 1^1\text{A}_g$. Therefore, 1 %p increase in 1ET yield indicates 1 %p increase of 2ET yield. Therefore, 1 %p increase of 1ET results in 3 %p increase in the yield of total charge carrier extraction. (Slope of the yellow line)

This graph indicates that the maximum yield of charge carrier extraction ($\beta_{\text{CE,max}}$) is 163 % where all TT states play a role of charge carrier: 37 % of TT undergo 1ET and the rest TT state

(67 %) via 2ET. With the numerical value of α_{TT} and β_{CE} , we can calculate the internal quantum efficiency (IQE) of the QOT2/AQ system.

$$\begin{aligned}
 IQE &= \frac{\text{the number of harvest } e^-}{\text{the number of absorbed } e^-} \\
 &= \frac{\text{the number of TT}}{\text{the number of absorbed } e^-} \times \frac{\text{the number of harvested } e^-}{\text{the number of TT}} \\
 &= \alpha_{TT} \times \beta_{CE}
 \end{aligned}$$

This relation enables the computation of IQE as the multiplication of two terms, α_{TT} and β_{CE} .

Therefore, the maximum IQE of the QOT2/AQ is therefore approximately 137 % (0.84×1.63).

This analysis implies that we can harvest ~1.4 electrons per photon absorbed

A.4.13. Oscillator Strength of Reduced AQ Anions

For reduced AQs (AQ^- and AQ^{2-}), we have used time-dependent DFT (TDDFT) simulation, PBE0/6-311++G**/PCM. The chemical species responsible for specific ESA and estimated oscillator strength are listed below. XMS-CASPT2 and Spin-Flip RAS results for QOT²⁺ TD and QOT²⁺ DD are also included.

Table AS5: Assignment of ESA II, III, and IV with the position of peak and oscillator strength^a.

Bands	Wavelength [nm]	1ET	2ET
ESA II	~ 488	QOT ²⁺ 1 ² B _g (498 nm, 0.29)	AQ ²⁻ (470 nm, 0.36)
ESA III	~ 528	–	QOT ²⁺ 1 ¹ B _u (529 nm, 0.15)
ESA IV	~ 569	AQ ⁻ (550 nm, 0.19)	–

a) The wavelength of corresponding transition and predicted oscillator strength are given in the parenthesis.

References

- (1) Kaduk, B.; Tsuchimochi, T.; Van Voorhis, T. *J. Chem. Phys.* **2014**, *140*, 18A503.
- (2) Grimme, S. *J. Comput. Chem.* **2006**, *27*, 1787–1799.
- (3) Zhao, Y.; Truhlar, D. G. *J. Phys. Chem. A* **2006**, *110*, 13126–13130.

- (4) Zhao, Y.; Truhlar, D. G. *Acc. Chem. Res.* **2008**, *41*, 157–167.
- (5) Shao, Y. et al. *Mol. Phys.* **2015**, *113*, 184–215.
- (6) Shiozaki, T.; Gyroffly, W.; Celani, P.; Werner, H. J. *J. Chem. Phys.* **2011**, *135*.
- (7) Wang, Z.; Kobayashi, T. *New J. Phys.* **2008**, *10*.
- (8) Chien, A. D.; Molina, A. R.; Abeyasinghe, N.; Varnavski, O. P.; Goodson, T.; Zimmerman, P. M. *J. Phys. Chem. C* **2015**, *119*, 28258–28268.
- (9) Ghigo, G.; Roos, B. O.; Malmqvist, P.-A. *Chem. Phys. Lett.* **2004**, *396*, 142–149.
- (10) Werner, H.-J.; Knowles, P. J.; Knizia, G.; Manby, F. R.; Schutz, M. *Wiley Interdiscip. Rev.: Comput. Mol. Sci.* **2012**, *2*, 242–253.
- (11) Takahashi, T.; Matsuoka, K.-i.; Takimiya, K.; Otsubo, T.; Aso, Y. *J. Am. Chem. Soc.* **2005**, *127*, 8928–8929.
- (12) Varnavski, O.; Leanov, a.; Liu, L.; Takacs, J.; Goodson, T. *Phys. Rev. B* **2000**, *61*, 12732–12738.
- (13) Varnavski, O.; Ispasoiu, R. G.; Balogh, L.; Tomalia, D.; Goodson, T. *J. Chem. Phys.* **2001**, *114*, 1962–1965.

Appendix B. Two-Photon Absorption Enhancement Parallels Intramolecular Charge Transfer Efficiency in Quadrupolar Versus Dipolar Cationic Chromophores

I conducted femtosecond two-photon excitation fluorescence experiments in order to investigate TPA properties for a quadrupolar and dipolar cationic chromophore. This was in collaboration with the Spalletti group.

The work in this chapter was accepted in Journal of Physical Chemistry C (JPC) with the title:

“Two-Photon Absorption Enhancement Parallels Intramolecular Charge Transfer Efficiency in Quadrupolar Versus Dipolar Cationic Chromophores ”

Federica Ricci, Benedetta Carlotti, Bradley Keller, Carmela Bonaccorso, Cosimo G. Fortuna, Theodore Goodson III, Fausto Elisei, and Anna Spalletti

Modifications were made to the manuscript to adapt it to the style of this dissertation. References and supporting information of the manuscript are included in this chapter.

B.1 Abstract

State-of-the-art femtosecond spectroscopies and quantum-chemical methods were used to investigate the excited state dynamics of a $D-\pi-A^+$ (**C1**) and a $D-\pi-A^+-\pi-D$ (**C2**) methyl-pyridinium (acceptor unit, A) derivatives bearing dibutylamino groups as strong electron donors (D) and bithiophenes as highly effective π -rich spacers. The absorption spectra of **C1** and **C2** are broad and are shifted to the red side of the visible spectral range. A significant negative solvatochromism has been observed for the absorption bands of the investigated salts upon increasing the solvent polarity, which have been rationalized in terms of electron density change upon excitation. The absorption spectra of **C2** are red-shifted with respect to those of **C1** whereas the emission bands of the two compounds overlap suggesting a localization of the

excitation on just one branch of the quadrupolar compound, which becomes the fluorescent portion. This is in agreement with our quantum mechanical calculations which predict that the symmetry of **C2** is broken in the relaxed S_1 geometry. The excited state symmetry breaking is observed in all of the investigated solvents regardless of their polarity. Femtosecond transient absorption and fluorescence up-conversion measurements have revealed that the excited state dynamics of **C1** is essentially dominated by solvent relaxation, while in the case of **C2** two distinct excited singlet states have been detected in polar solvents, where an intramolecular charge transfer (ICT) state is efficiently produced. The main photoinduced decay pathway of both the compounds is internal conversion in all the investigated media. High values of Two-Photon Absorption cross sections of 500 and 1400 GM for **C1** and **C2**, respectively, have been obtained by means of femtosecond resolved Two-Photon Excited Fluorescence measurements, thus demonstrating the enhancement in the Nonlinear Optical properties of the quadrupolar compound over its dipolar counterpart, in agreement with the more efficient ICT observed in the case of **C2**.

B.2 Introduction

Organic molecules that can simultaneously absorb two photons to be promoted to their excited states have recently been the subject of much research due to the growing interest in their advanced photonic applications.¹⁻⁵ Two photon absorbing organic compounds may be successfully employed in different fields: in the optoelectronic/photonic field⁶⁻⁹ as low cost materials for nonlinear optics (NLO), and in the medical field¹⁰ as chromophores for imaging, and photodynamic therapy due to the increased penetration depth of the infrared radiation in the tissues, and also due to their ability to form complexes with DNA.¹¹⁻¹³

An intense effort has been devoted to the design of organic materials with large TPA cross sections.¹ Several efficient strategies have been put forward to develop conjugated molecules with improved NLO responses: dipolar type with a donor–bridge–acceptor (D– π –A) motif and quadrupolar type with the D– π –A– π –D structure, the latter having been highlighted for its excellent properties.^{14–16} Indeed, symmetrical quadrupolar compounds have experimentally and theoretically demonstrated enhanced TPA with respect to the dipolar analogues.^{4,17–19} The observed TPA cross sections of dipolar and quadrupolar structures are in accordance with the fact that the donor– π –acceptor molecules with increase in dimensionality possess higher NLO and TPA properties. TPA enhancement for the quadrupolar compounds is attributed to more effective electronic delocalization.^{20–22,10} A deep understanding of the solvatochromic and TPA properties of such quadrupolar chromophores^{23–26} has been often reached by invoking the occurrence of symmetry breaking phenomena.^{18,19,27–33} Several works have unambiguously shown that TPA is strongly influenced by the photoinduced intramolecular charge transfer occurring in these systems containing electron donor and electron acceptor groups.^{4,34} Cationic chromophores (such as methyl pyridinium and methyl quinolinium) have shown to be promising as electron deficient moieties, not only for their significant electron withdrawing ability but also for their water solubility which is very appealing for their possible biological and medical applications.^{35–37} As for the electron donors, dialkyl–amino substituents have shown higher NLO response if employed in molecular structures to replace the well–known and largely used dimethylamino group.^{38,39} In fact, the TPA cross sections are enhanced upon lengthening of the alkyl chain. Moreover, both the ICT and the optical non–linearity have been found to improve in elongated and more conjugated push–pull polyenes with π –linkers of increasing length.^{40–42}

Among the numerous classes of π -conjugated organic materials, oligothiophenes have attracted widespread interest in the last few years due to their high thermal and chemical stability, relative ease of synthesis and good charge transport ability.⁴³ In particular, push-pull oligothiophenes have been largely described in the literature for their applications in organic solar cells,^{44,45} because organic photovoltaic materials are flexible, lightweight, easily processed, and low cost compared to their inorganic counterparts.⁴⁶ However, only scarce examples of oligothiophene derivatives have been reported for two-photon excited applications up to now. In recent works, thiophene based π -conjugating spacers have proven effective in greatly increasing the TPA cross-sections.⁴⁷⁻⁵⁰

In our latest works, cationic push-pull $D-\pi-A^+$ and $D-\pi-A^+-\pi-D$ chromophores bearing a methylpyridinium as electron acceptor and dimethylamino or diphenylamino groups as electron donors have been extensively studied in terms of their excited state dynamics.⁵¹⁻⁵⁴ These compounds have shown a peculiar negative solvatochromic behaviour, rarely observed for dipolar and particularly for quadrupolar systems.¹⁸ A more efficient photoinduced intramolecular charge transfer has been observed in the quadrupolar molecules with respect to their dipolar analogues. Moreover, an excited state symmetry breaking phenomenon has been revealed by a joint experimental and theoretical study for the highly symmetrical quadrupolar structures.^{53,54} These striking results have pushed us to extend the investigation, which employs state-of-the-art femtosecond spectroscopies and quantum-chemical methods, to structurally similar $D-\pi-A^+$ and $D-\pi-A^+-\pi-D$ methyl-pyridinium derivatives bearing dibutylamino groups as strong electron donors and bithiophene as highly effective π -rich spacers (see **Chart B.2.1**).

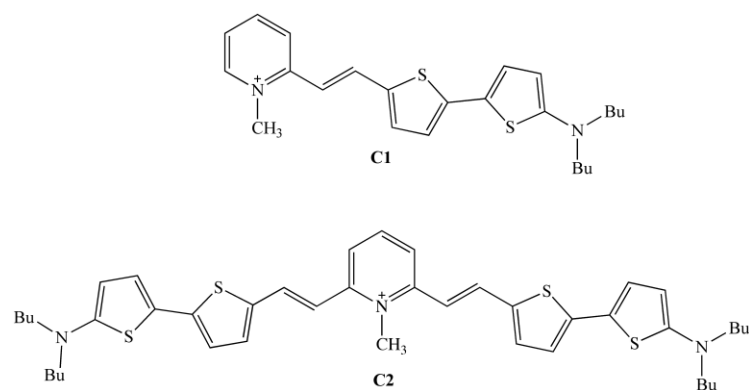


Chart B.2.1. Molecular structures of compounds **C1** and **C2**.

B.3 Experimental

The investigated compounds (shown in **Chart B.2.1**) have been synthesized as iodide salts at the Catania Laboratory following the procedure previously described.^{55,56} Measurements were performed in various solvents: chloroform (CHCl₃), dichloromethane (DCM), 1,2-dichloroethane (DCE), acetone (Ac), acetonitrile (MeCN), 2-propanol (2-PrOH), ethanol (EtOH), methanol (MeOH) and water (W).

A Perkin-Elmer Lambda 800 spectrophotometer was used for the absorption measurements. Experimental error on the measured molar absorption coefficients is 2–3%. The fluorescence spectra were measured by a FluoroMax[®]-4P spectrofluorimeter of HORIBA Scientific operated by FluorEssence[™]. Tetracene ($\phi_F = 0.17$ in aerated cyclohexane)⁵⁷ was used as fluorimetric standard to calculate the fluorescence quantum yield. Estimated error on the fluorescence quantum yield values is approximately 10%. For photochemical measurements, a xenon lamp coupled with an interferential filter ($\lambda_{exc} = 436$ nm) and potassium ferrioxalate in 0.1 N sulphuric acid as actinometer were used. The photoreaction (solute concentration $\sim 10^{-4}$ M) was monitored by HPLC using a Waters apparatus equipped with a Phenomenex Jupiter

C18–300Å (4.6 × 250 mm; 5 μm) column and a UV detector. W/MeCN mixtures with 0.1% trifluoroacetic acid were used as eluent.

Triplet formation quantum yields and lifetimes (ϕ_T and τ_T) were measured by a nanosecond laser flash photolysis setup (Nd:YAG Continuum, Surelite II, second and third harmonics, $\lambda_{exc} = 532$ and 355 nm, pulse width ca. 7 ns and energy ≤ 1 mJ pulse⁻¹). The transient kinetics were obtained by monitoring the change of absorbance over the 300–900 nm range and averaging at least 10 decays at each wavelength. The setup was calibrated by an optically matched solution of benzophenone ($\phi_T = 1$ and $\epsilon_T = 6500$ M⁻¹ cm⁻¹ at the corresponding absorption maximum, $\lambda_{max} = 525$ nm) in MeCN.⁵⁸ Triplet–triplet absorption coefficients (ϵ_T) were determined by energy transfer from benzophenone in MeCN.⁵⁹ The experimental errors were estimated to be about $\pm 10\%$ for τ_T and $\pm 15\%$ for ϵ_T and ϕ_T . The quenching constants of the triplets by molecular oxygen were evaluated by the slope of the linear plots of the triplet lifetime vs. oxygen concentration. All the ns–transient absorption measurements were carried out at room temperature; the solutions were deaerated by bubbling with nitrogen.

The experimental setups for femtosecond transient absorption and fluorescence up–conversion measurements have been widely described elsewhere.^{60–62} The 400 nm excitation pulses of ca. 40 fs were generated by an amplified Ti:Sapphire laser system (Spectra Physics). The transient absorption set up (Helios, Ultrafast Systems) is characterized by temporal resolution of ca. 150 fs and spectral resolution of 1.5 nm. Probe pulses were produced in the 475–750 nm range by passing a small portion of 800 nm light through an optical delay line (with a time window of 3200 ps) and focusing it into a 2 mm thick Sapphire window to generate a white–light continuum. In the up–conversion set–up (Halcyone, Ultrafast Systems) the 400 nm pulses excite the sample and the remaining fundamental laser beam plays the role of the “optical

gate” after passing through a delay line. The fluorescence of the sample is collected and focused onto a BBO crystal together with the delayed fundamental laser beam. The up-converted fluorescence beam is focused into the entrance of a monochromator by a lens, and it is then detected by a photomultiplier connected to a photon counter. The temporal resolution of the up-conversion equipment is about 250 fs, whereas the spectral resolution is 5 nm. The ultrafast spectroscopic data were fitted by Target Analysis assuming several successive steps and resulting in the Species Associated Spectra (SAS)⁶³ using the software Glotaran.⁶⁴ Statistical error on the lifetimes resulting from the global fitting is about 10%.

Quantum-mechanical calculations were carried out on molecular structures where the butyl groups were replaced by methyl ones using Gaussian 09 package.⁶⁵ Density functional theory (DFT) based on the B3LYP method was used to optimize the geometry and to obtain the properties of the substrates in the ground state while the lowest excited singlet states were characterized by time dependent (TD) DFT B3LYP excited-state calculations.⁶⁶ In both cases a 6-31G(d) basis set was employed. DCM solvation effects were included in the calculations by means of the Conductor-like Polarizable Continuum Model (CPCM).⁶⁷ Atomic charges and dipole moments were obtained by use of the quantum theory of atoms in molecules (QTAIM).⁶⁸

In order to measure the Two Photon Absorption (TPA) cross sections, a Two Photon Excited Fluorescence (TPEF) setup was used. The setup employs a mode-locked Spectra-Physics femtosecond Mai Tai laser, which is tunable from 700 to 1000 nm to generate 110-fs pulses. For the present study the Spectra-Physics Mai Tai generated a 775 nm, 110-fs pulse to pump a Spectra-Physics Femtosecond Synchronously Pumped Optical Parametric Oscillator (OPAL), which produced 1300 nm, 150 fs excitation pulses. The 1300 nm beam was directed into a solution in a sample cell (quartz cuvette, 0.4 cm path length) and the resultant

fluorescence was collected in a direction perpendicular to the incident beam. A 1 inch focal length plano-convex lens was used to direct the collected fluorescence into a monochromator. The output from the monochromator was coupled to a PhotoMultiplier Tube (PMT) and the photons were converted into counts by a photon counting unit. The photomultiplier tube is connected to the computer via a photo-counting unit (Hamamatsu) that interfaces the detected signal. A solution of 2-(6-(4-Dimethylaminophenyl)-2,4-neopentylene-1,3,5-hexatrienyl)-3-methylbenzothiazolium Perchlorate (Styryl 9M) in EtOH (10^{-5} M), characterized by a TPA cross section of 580 GM at 1300 nm excitation wavelength and by a fluorescence quantum yield of 0.07,⁶⁹ was used as reference. The experimental uncertainty on the TPA cross sections amounts to ca. $\pm 10\%$.

Two Photon Absorption transition tensors and cross sections of **C1** and **C2** in DCM (PCM solvation model) were computed by use of the B3LYP/6-31G(d) method, Dalton2016.1 package,^{70,71} according to the formulas given by McClain et al.^{72,73} The TPA cross-section is usually expressed in terms of Göppert Mayer (GM) unit, where 1 GM is 10^{-50} cm⁴ s photon⁻¹. The relation between the macroscopic TPA cross section in GM (δ_{GM}) and the immediate computation output in atomic unit (δ_{au}) is given by the following:⁷⁴

$$d_{GM} = \frac{8\rho^2 \alpha a_0^5 \omega_f^2}{cG} d_{au} \quad (1)$$

where α is the fine structure constant, a_0 is the Bohr radius, c is the speed of light in vacuum, Γ is the line-shape function, and ω_f is the excitation energy for the $0 \rightarrow f$ transition. Estimated error on the computed TPA cross sections is approximately $\pm 20\%$.

B.4 Results and Discussion

B.4.1 Absorption and Fluorescence Properties

The absorption and fluorescence spectral properties of both the dipolar and quadrupolar compounds **C1** and **C2** are significantly affected by the solvent polarity (see **Figures B.4.1** and **B.4.2**). In particular, the absorption bands of **C1** and **C2**, placed in the far-red portion of the visible spectral range, are noticeably blue-shifted on going from low polar ($\lambda_{\text{max}}=660$ nm for **C1** and 678 nm for **C2** in DCM) to highly polar solvents ($\lambda_{\text{max}}=556$ nm for **C1** and 566 nm for **C2** in W/EtOH 70/30 mixture). Several solvents have been considered, belonging to three different classes: low polarity chlorinated media, polar protic, and polar non-protic solvents (**Table B.4.1**). A clear correlation of the absorption maximum position with solvent polarity can be seen when solvents of the same class are taken into account and also when alkane chloride and protic solvents are considered together, as reported in the literature for other methyl-pyridinium derivatives.^{51–54,75} The observed negative solvatochromism is in agreement with the substantial decrease of the dipole moment on going from the ground state to the Frank-Condon excited singlet state foreseen in the case of **C1** by the quantum mechanical calculations (see below), whereas in the case of **C2** it is probably related to a bis-dipolar contribution. Even though the molecule is practically nonpolar as a whole (its electric dipole moment is close to zero in the ground state because of the high molecular symmetry), a C_{2v} symmetric V-shaped chromophore such as **C2** can be considered as a charge centered bis-dipole, where two well defined equal and quasi opposite dipoles sharing the positive pole are present.^{76,77} An analogous negatively solvatochromic behavior was observed for structurally similar methyl pyridinium dipolar and quadrupolar compounds bearing strong electron donor groups (such as dimethyl amino and diphenyl amino).^{51–54} However, the presence of the thiophene spacers peculiar to **C1** and **C2** is

responsible for a significant bathochromic shift of their spectra in the far-red portion of the visible, which makes these compounds very appealing for possible applications in organic photovoltaic devices. A strong broadening of the absorption band is observed with increasing the solvent polarity (FWHM changes from 3360 cm⁻¹ and 4260 cm⁻¹ in DCM to 5050 cm⁻¹ and 6570 cm⁻¹ in W for **C1** and **C2**, respectively; see Table S1) together with a significant decrease of the molar absorption coefficient on going from DCM (35000 and 86000 M⁻¹ cm⁻¹ for **C1** and **C2**, respectively) to EtOH (30600 and 60800 M⁻¹ cm⁻¹ for **C1** and **C2**, respectively). These experimental findings (shift, broadening⁷⁸ and intensity decrease of the absorption band in the polar media) may be a hint of the charge transfer character of the absorption transition (further evidence is given by the theoretical investigation, see below). It has to be noted that both **C1** and **C2** exhibit a large Stokes shift, which is significantly enhanced upon increasing the solvent polarity (see **Table B.4.1**). As reported for analogous salts,⁵¹ no evidence of ionic pairs emerged in the considered *media* (no concentration effect has been revealed on the absorption spectra, see **Figures S1** and **S2**) and thus the obtained properties can be ascribed uniquely to the single organic cations, with the only possible exception of CHCl₃ (the least polar among the investigated solvents), which is found to show some anomalies possibly related to a small contribution of ion-pairs.⁷⁹

Unlike what was observed previously in analogous push-pull dipolar cationic systems (for which the emission spectrum maximum position resulted almost unaffected by the change in solvent polarity),^{51,80} in the case of **C1**, a small but clearly visible negative solvatochromism of the fluorescence band has been observed (see **Figure B.4.1**) which is in agreement with an emitting relaxed excited singlet state showing a small dipole moment and a highly polar ground state (see below the results of the quantum mechanical calculations) with a charge transfer

character of the emission transition. A substantial broadening of the fluorescence band has been indeed revealed for **C1** upon increasing the solvent polarity (FWHM from 1470 cm⁻¹ in DCM to 2040 cm⁻¹ in W; see **Table S1**). A similar solvatochromic behaviour has also been observed for the emission spectrum of the quadrupolar derivative **C2**. Indeed, when the normalized absorption and emission spectra of **C1** and **C2** are considered together (**Figure B.4.3**) it can be seen that, whereas the absorption bands of **C2** are red-shifted with respect to those of **C1**, in agreement with a longer conjugated system, the emission bands of the two compounds roughly overlap. This peculiar emissive behaviour of the quadrupolar system has already been observed previously for a structurally similar dimethylamino pyridinium two-branched derivative in highly polar aqueous solution⁵³ but here it is surprisingly observed in all the investigated solvents, characterized by both low and high polarity, as in the case of an analogous diphenylamino quadrupolar system.⁵⁴

The solvent effect has also been investigated on the photophysical properties of both **C1** and **C2**, in particular on the fluorescence efficiency (see **Table B.4.1**). The fluorescence quantum yields are very low for both compounds, scarcely affected (just slightly decreased) by the increase in solvent polarity and lower in the case of the quadrupolar with respect to the dipolar system (ϕ_F of the order of 10⁻³ for **C1** and 10⁻⁴ for **C2**). A scarce solvent effect on the emission intensity is observed here for the bithiophene derivatives **C1** and **C2**; on the contrary, a significant fluorescence quenching upon increasing the solvent polarity was found during previous investigations of analogous styryl containing mono- and two-branched systems.⁵¹⁻⁵⁴ The occurrence of *trans*→*cis* photoisomerization of **C1** and (*trans,trans*)→(*trans,cis*) photoisomerization of **C2** has been monitored in two solvents characterized by different polarity (CHCl₃ and MeCN) and in all cases it has been found to be negligible. Triplet production by

intersystem crossing (ISC) of **C1** and **C2** in DCM was investigated by nanosecond flash-photolysis measurements. A transient signal attributed to the triplet was detected around 760 nm in the case of **C1** under a 532 nm laser excitation, characterized by a lifetime of 8.0 ± 0.8 μs and an oxygen quenching rate constant of $1.8 \times 10^9 \text{ M}^{-1} \text{ s}^{-1}$. Moreover, this triplet state could be successfully produced by sensitization (energy transfer) with benzophenone in MeCN upon irradiation at 355 nm. The obtained triplet absorption coefficient (ϵ_T) was of $18000 \pm 3000 \text{ M}^{-1} \text{ cm}^{-1}$ and the ISC quantum yield for **C1** in DCM (ϕ_T) was found to be of 0.020 ± 0.003 . No signal related to the triplet absorption was detected for **C2**, suggesting a less efficient ISC in this case. These results are in agreement with the femtosecond transient absorption measurements where just a small Rest absorption assignable to the triplet was retrieved by global fitting of the data indicating that, even though not completely negligible, the ISC should play a minor role in the excited state deactivation of the studied systems (see below). Therefore, internal conversion (IC) to the ground state is expected to be the most significant photoinduced decay pathway for both **C1** and **C2** in all the investigated solvents.

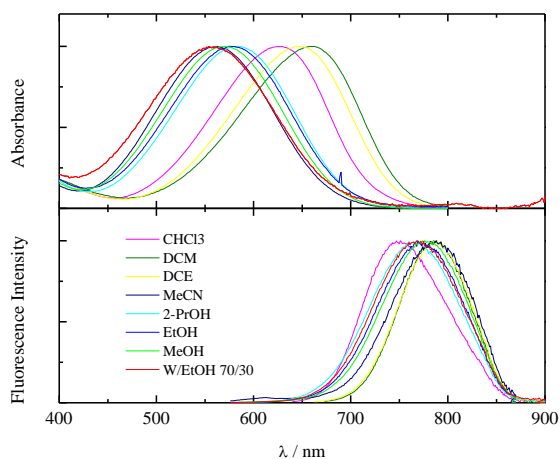


Figure B.4.1. Normalized absorption and emission spectra of **C1** in solvents of different polarity.

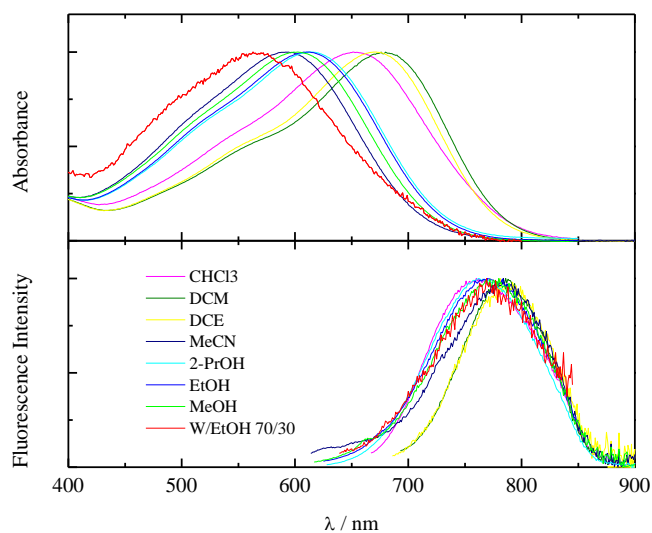


Figure B.4.2. Normalized absorption and emission spectra of **C2** in solvents of different polarity.

Table B.4.1. Spectral properties and fluorescence quantum yields of **C1** and **C2** in several solvents of different polarity $f(\epsilon, n^2) = [(\epsilon - 1)/(2\epsilon + 1)] - [(n^2 - 1)/(2n^2 + 1)]$.

solvent	$f(\epsilon, n^2)$	$\lambda_{max} / \text{nm}$		λ_{em} / nm		$\epsilon / \text{cm}^{-1}$		$\epsilon / \text{M}^{-1} \text{cm}^{-1}$		Φ_f	
		C1	C2	C1	C2	C1	C2	C1	C2	C1	C2
CHCl ₃	0.148	627	654	750	760	2616	2133			0.008	0.002
DCM	0.218	660	678	785	782	2413	1962	35000	86000	0.005	0.0005
DCE	0.223	646	671	788	785	2790	2164			0.008	0.0008
2-PrOH	0.276	584	614	765	763	4051	3180			0.011	0.0022
<i>Ac</i>	<i>0.285</i>	<i>564</i>	<i>596</i>	<i>785</i>	<i>777</i>	<i>4992</i>	<i>3909</i>			<i>0.002</i>	<i>0.0002</i>
EtOH	0.289	578	610	770	770	4314	3406	30600	60800	0.006	0.0006
<i>MeCN</i>	<i>0.305</i>	<i>561</i>	<i>592</i>	<i>785</i>	<i>754</i>	<i>5086</i>	<i>3629</i>			<i>0.002</i>	<i>0.0003</i>
MeOH	0.309	570	602	775	770	4641	3624			0.004	0.0002
W/EtOH 70/30	0.314	556	566	768	770	4965	4681			0.004	0.0003

In italics non protic and polar solvents. Experimental error on the measured molar absorption coefficients is 2–3%. Estimated error on the fluorescence quantum yield values is approximately 10%.

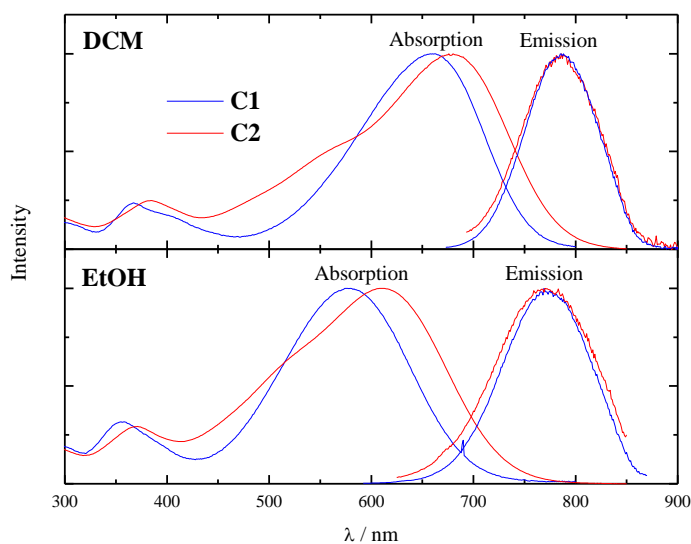


Figure B.4.3. Normalized absorption and emission spectra of **C1** and **C2** in DCM and EtOH.

B.5 Quantum–Mechanical Calculations

A comprehensive computational investigation was carried out about the structural and electronic properties of **C1** and **C2** in DCM by methods rooted into the Density Functional Theory (DFT) and its time dependent (TD–DFT) extension.

The cations of these salts are dipolar or quadrupolar ($A^+ - \pi - D$ or $D - \pi - A^+ - \pi - D$) systems, where the pyridinium unit (A^+) is the strong acceptor and the dibutylamino group (D) the strong donor. Obviously the dipole moment for an ion is undefined since it depends on the choice of the coordinate origin. It is usually convenient to setup a “working definition” based on the mass centre of the system.⁸¹ Thus, the dipole moment of the cation can be defined just like that of conventional polar molecules. The dipole moments shown in **Table B.5.1** were computed for the ground, excited Frank–Condon and relaxed S_1 in DCM.

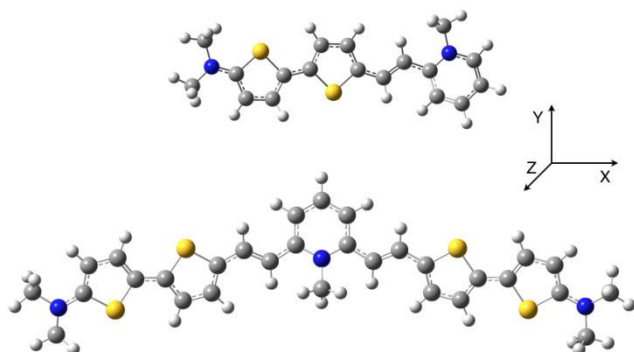
High values ($\mu_{S_0} = 10.2$ D, see **Table B.5.1**) were found for the dipole moment of the most stable ground state conformer of **C1** due to the positive charge largely localized on the

pyridinium group. The absorption transition leads to an electron transfer toward the pyridinium group, which reduces the polar character of the FC excited state ($\mu_{S1,FC} = 2.3$ D). This variation in the dipole moment upon excitation ($\Delta\mu = 7.9$ D) is significant, even more than that predicted for the analogous dimethylamino–styrene–pyridinium ($\Delta\mu = 4.8$ D)⁸² and diphenylamino–styrene–pyridinium ($\Delta\mu = 7.0$ D)⁵⁴ dipolar systems. The dipole moment does not change significantly in the relaxed S₁ state ($\mu_{S1,opt} = 1.7$ D) pointing to a relaxation that does not involve a charge transfer in the excited state. Both the ground state and the relaxed excited singlet state show a quasi–planar geometry in DCM. The theoretical results about the dipole moments furnish an explanation to the negative solvatochromism observed in the absorption and in the emission spectra of **C1**. The fact that the relaxed singlet excited state is characterized by a low dipole moment and by a quasi–planar optimized geometry (probably determined by the presence of the ortho connected thiophene rings in the molecular structure of **C1**)⁸³ may give a possible explanation for the experimentally calculated fluorescence quantum yield almost independent of the solvent polarity. In fact, in previous works on analogous dipolar compounds^{51,80} the strong solvent dependence of the fluorescence efficiency was found to be dependent on the significant Twisted Intramolecular Charge Transfer (TICT) character of the emitting state. Charge displacements in the excited state are indeed usually helped by conformational rearrangements; these might be inhibited by the rigid bithiophene motif in the **C1** molecular structure in comparison to more flexible dimethylamino and diphenylamino styryl containing D– π –A⁺ systems.^{51,80}

In the case of **C2** a small electric dipole moment in the ground state resulted from the calculations ($\mu_{S0} = 0.51$ D, Table 4.5.1); nonzero values are obtained because of the bent structure of compound **C2**, which actually is not a pure quadrupole. A small increase of the electric dipole

moment with no orientation change is foreseen when going from S_0 to the FC S_1 state ($\mu_{S_1,FC} = 2.2$ D). Surprisingly, the dipole moment of the relaxed S_1 state shows a very high value ($\mu_{S_1,opt} = 37.9$ D). The geometry of the ground state calculated in DCM has a C_{2v} symmetry and is almost planar. The symmetry of the system is completely broken in the relaxed S_1 geometry. In this case, one of the arms is co-planar with the pyridinium (dihedral angle around 180 degrees) whereas the other is bent (dihedral angle about 40 degrees). For this reason a very high dipole moment value is calculated for the relaxed S_1 .

Table B.5.1. Dipole moments of the ground state (S_0), the Frank–Condon first excited singlet state ($S_{1,FC}$) and the relaxed first excited singlet state ($S_{1,opt}$) of compounds **C1** and **C2** in DCM obtained by the B3LYP/6–31G(d) model followed by QTAIM: total modulus ($\mu_{Tot.}$) and Cartesian components (μ_x , μ_y and μ_z).



comp.d	State	μ / D			
		μ_x	μ_y	μ_z	$\mu_{Tot.}$
C1	S_0	10.07	1.58	0.28	10.19
	$S_{1,FC}$	1.32	1.90	0.31	2.34
	$S_{1,opt}$	-0.04	1.65	0.24	1.68
	$S_0@S_{1opt}$	9.91	1.63	0.18	10.07
C2	S_0	-0.16	-0.28	-0.41	0.51
	$S_{1,FC}$	-0.51	-2.14	-0.09	2.19
	$S_{1,opt}$	-37.71	-4.17	0.69	37.95
	$S_0@S_{1opt}$	3.86	-0.58	0.13	3.91

The computational predictions of the spectra and the investigation of the singlet excited state nature have been performed for **C1** and **C2** in DCM after S_0 geometry optimization (see the

results collected in **Table S2**). The theoretically predicted absorption spectra are in good agreement with their experimental counterparts.

The electronic properties of **C1** and **C2** were calculated considering both the S_0 and the S_1 optimized geometries in DCM: the plots of the frontier molecular orbitals (MOs) are shown in **Figures B.5.1** and **B.5.2**. In particular, the lowest excited singlet state S_1 is mainly described by the HOMO – LUMO configuration of π, π^* nature in all cases. When considering the ground state optimized geometry, the HOMO \rightarrow LUMO transition implies a charge transfer toward the methyl pyridinium in the case of **C1** and a symmetrical charge displacement from the lateral electron rich dialkylamino groups toward the central electron deficient methyl–pyridinium in the case of **C2** (see **Figure B.5.1**). The solvatochromic effect observed for **C2** is then related to this charge transfer taking place during the absorption transition in each of the two dipolar branches of the quadrupolar structure (see **Figure B.5.1**). When the geometry is optimized for the S_1 state, the molecular orbitals are very similar for **C1**. The emitting species is therefore characterized by a quasi–planar geometry and is described by molecular orbitals distributed on the whole molecular structure. In the case of **C2**, S_1 looks like a symmetry–broken state where a very significant charge displacement occurs from one branch to the other of the molecular structure. Moreover, the findings issuing from the quantum mechanical calculations provide a possible explanation for the emission spectrum of **C2**, which overlaps that of **C1**. In fact, the molecular orbitals involved in the emission transition (LUMO–HOMO) of **C2** are both localized on one branch of the quadrupolar system, which in this case becomes the fluorescent portion of the system, being similar to that involved in the emission of the single–arm **C1** molecule. The charge transfer character of the radiative deactivation (see **Figure B.4.3**) is then increased; this result coupled to the twisted excited state geometry predicted for **C2** gives an explanation for the

reduced quantum efficiency of **C2** as compared with that of **C1**.⁵³ The excited state symmetry breaking, resulting from the calculations (**Figure B.5.2**), is able to explain the experimentally observed overlap of the emission bands of **C1** and **C2** (**Figure B.4.3**) in all the considered solvents, even in those characterized by low polarity. This phenomenon was previously revealed for a dimethylamino pyridinium quadrupolar derivative, structurally similar to **C2**, only in highly polar media.⁵¹ Therefore, a more efficient photoinduced symmetry breaking intramolecular charge transfer occurs in the quadrupolar compound of this work, probably caused by the enhanced electron donor strength of the substituents placed at its lateral ends (dibutylamino groups coupled with electron rich thiophene rings), similarly to what observed for a diphenylamino substituted system.⁵⁴

MO	C1	C2
π_{L+2}^*		
π_{L+1}^*		
π_L^*		
π_H		
π_{H-1}		
π_{H-2}		
π_{H-3}		

Figure B.5.1. Frontier molecular orbitals of **C1** and **C2** at the optimized S_0 geometry (**H** means here HOMO and **L** means LUMO).

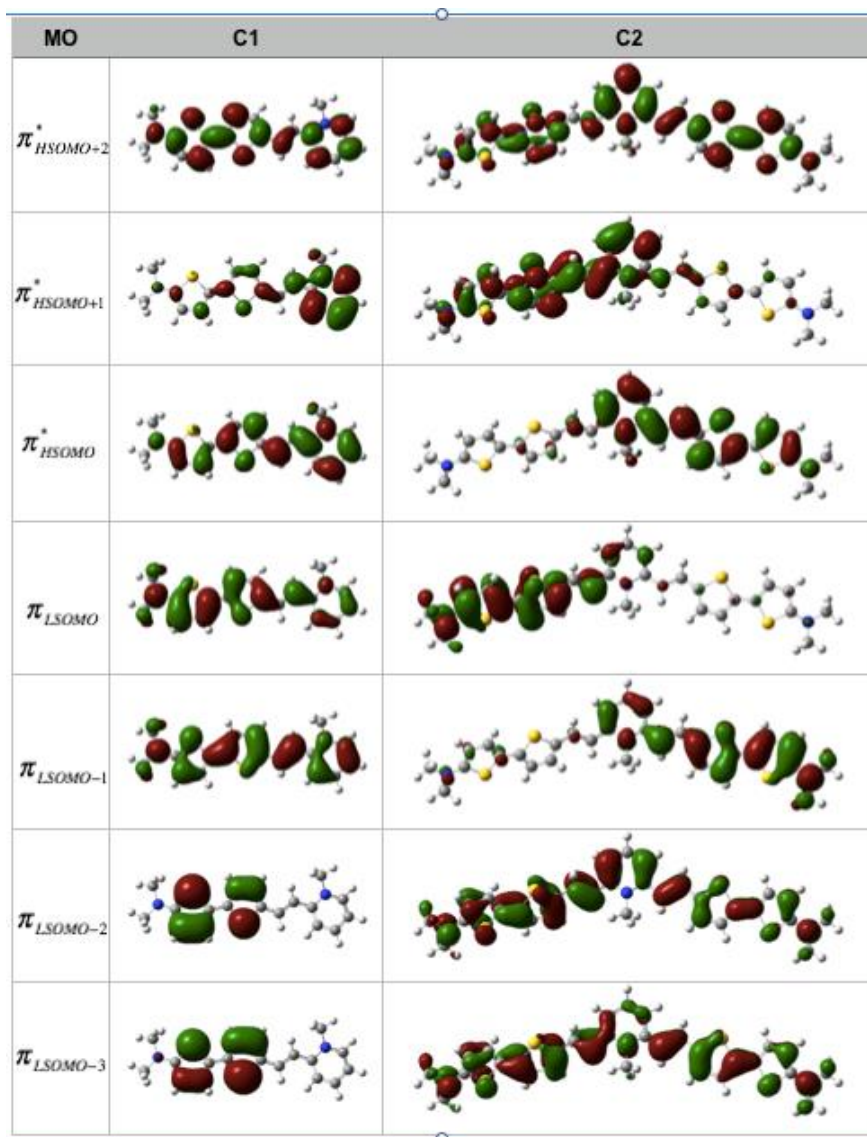


Figure B.5.2. Frontier molecular orbitals of **C1** and **C2** at the optimized S_1 geometry (**LSOMO** is the lowest singly occupied molecular orbital; **HSOMO** is the highest singly occupied molecular orbital).

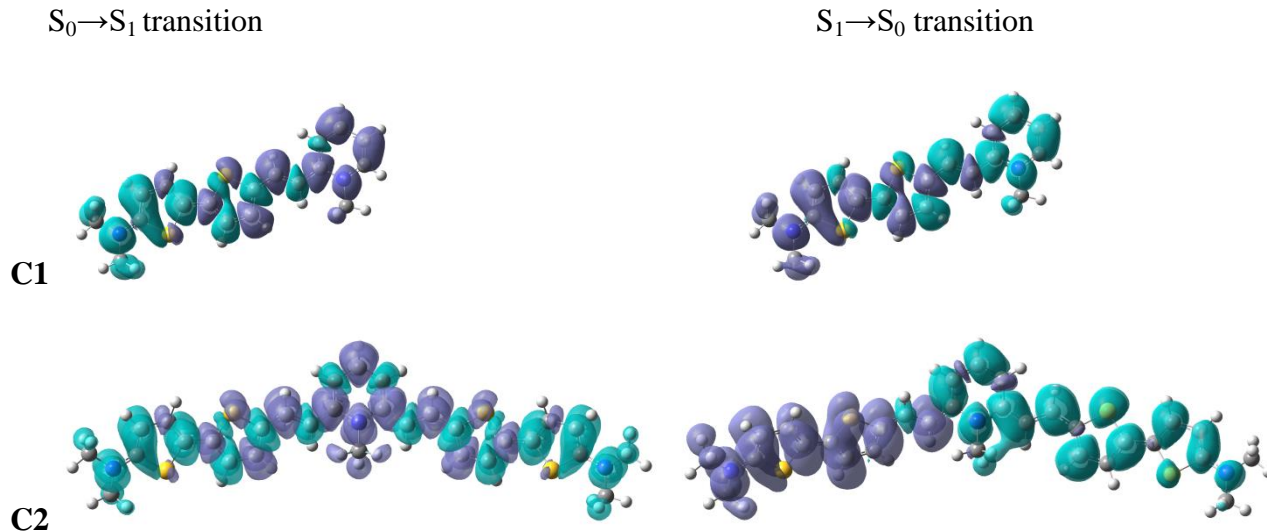


Figure B.5.3. Difference of electron density between states for the $S_0 \rightarrow S_1$ and $S_1 \rightarrow S_0$ transitions of compounds **C1** and **C2** in DCM (in the figures the colours violet and cyan correspond to an increase and a decrease in electron density, respectively).

B.6 Femtosecond Transient Absorption and Fluorescence Up–Conversion

To gain insight into the excited state dynamics of **C1** and **C2**, femtosecond resolved transient absorption measurements were carried out in solvents of different polarity. Figures 7–10 show a contour plot of the experimental data (panel A), the main time–resolved absorption spectra and kinetics recorded at significant wavelengths (panel B), together with the spectral and kinetic properties of the main components obtained by Singular Value Decomposition and Target Analysis (panel C) for **C1** and **C2** in CHCl_3 and MeOH. **Table B.6.1** summarizes the results obtained for the two compounds in four solvents of increasing polarity (CHCl_3 , DCM, EtOH, MeOH), the lifetime (τ) and the Species Associated Spectrum (SAS) of each detected transient.

In the case of compound **C1** (**Figures B.6.1** and **B.6.2**) the time–resolved spectra show the ground state bleaching negative signal (around 650 nm), a stimulated emission band significantly red–shifting in time (around 700–750 nm) and a positive transient absorption signal

centered around 590 nm, which slightly blue shifts and decays during the measurement (an additional small excited state absorption band is observed around 680 nm in polar solvents). The Target Analysis revealed the presence of three/four components with lifetimes of 0.20, 5.3, 115 ps in CHCl₃ and 0.22, 1.0, 5.1 and 41 ps in MeOH together with a last component not decaying in the investigated time window (Rest). The bathochromic shift of the stimulated emission in time and the values of the two/three shorter lifetimes are a signature of the occurrence of solvent relaxation following the excitation of **C1** in CHCl₃ and MeOH, respectively. In fact, solvation is known to show a time-dependence which is at least biexponential concerning both the inertial and diffusive component of the response.⁸⁴ The lifetimes 0.23/5.3 ps in CHCl₃ and 0.22/1.0/5.1 ps in MeOH obtained from the global fitting can be therefore assigned to solvation. The longer living component of 115 ps in CHCl₃ and 41 ps in MeOH can be associated to the relaxed lowest excited singlet state (S₁) and the Rest component to the lowest excited triplet state (T₁). Similar results, in terms of time resolved spectra and revealed transients, have been obtained in DCM and EtOH (see **Figures S3–S4** and **Table B.6.1**). However, a certain dependence of the S₁ lifetime upon solvent polarity (its value decreases by a factor of three on going from CHCl₃ to MeOH) is observed, probably due to its charge transfer character. The small solvent effect observed for **C1** on the lowest excited singlet state lifetime (the fluorescence lifetime) parallels the small effect of solvent polarity observed on the fluorescence quantum yield (see **Table B.6.1**). These experimental results obtained for the emitting state are in agreement with the low dipole moment and planar geometry predicted for this state by the quantum-mechanical calculations. This behavior is different from that revealed for analogous dipolar push-pull dimethylamino/diphenylamino-styrene-pyridinium systems, for which a significant solvent effect has been observed on both the fluorescence efficiency and the lifetime of the highly polar

TICT lowest excited singlet state.^{51,80} Moreover, for these salts previously studied by our group^{51,80} the population of an intramolecular charge transfer state from the locally excited state reached by light absorption was clearly observed during the excited state dynamics studied by ultrafast spectroscopies. This is very different from what revealed in the case of **C1** for which no significant charge rearrangement is found to take place by the ultrafast pump–probe measurements, in agreement with what predicted by the calculations.

In the case of compound **C2** in CHCl_3 (**Figure B.6.2**) the time resolved spectra look very similar to those recorded for **C1** showing a main positive absorption band at 600 nm and a second lower intense band at 725 nm, together with a stimulated emission negative signal between 660 and 750 nm clearly visible at short delays from the excitation. The Target Analysis revealed that after the occurrence of solvation dynamics (reflected by the component of 2.9 ps) only one transient assignable to an excited singlet state is present. This transient is characterized by a lifetime of 24 ps and by a spectrum composed of two absorption bands at 600 and 725 nm, which resembles the spectrum of the S_1 state of **C1** in agreement with the excited state symmetry breaking predicted for the quadrupolar system by the theoretical calculations. **Figure B.6.3** shows the transient spectra recorded for **C2** in MeOH. A narrow band centered around 605 nm, produced right after the laser excitation, decays during the first 2 ps. In the same time scale a broad band at 700 nm is formed and this latter shows a subsequent slower decay within 30 ps. This spectral behavior indicates that a precursor–successor dynamics is operative during the excited state deactivation of **C2** in this solvent: the species absorbing at 605 nm is the precursor of the species absorbing at 700 nm. The global fitting of the ultrafast spectroscopic data of **C2** in MeOH revealed the presence of three exponential components together with a Rest. The first component is characterized by a lifetime of 0.27 ps and a spectrum showing an excited state

absorption at 605 nm, being the most intense recorded signal in the transient absorption spectrum obtained for **C2**. This transient can be assigned to the S_1 state of **C2**. The second component of 3.2 ps is probably related to solvation in MeOH. The third component of 4.2 ps shows an absorption band broader than that of the first transient and centered at 700 nm. It is probably assignable to an intramolecular charge transfer state ($^1\text{ICT}^*$) efficiently produced as a separate species only for the quadrupolar compound in polar solvents. The same components describe the excited state dynamics of **C2** also in EtOH (**Figure S6** and **Table B.6.1**). In DCM the time resolved spectra (see **Figure S5**) are complicated by the presence of a region of negative signal due to the ground state bleaching (being the steady-state absorption of **C2** red-shifted in low polar media). In summary, in the low polar solvents (CHCl_3 and DCM) the production of an intramolecular charge transfer state is not so efficient to be able to generate a separate species and the S_1 SAS is characterized by two bands which are placed in correspondence of the absorption signals of the two distinct singlet states (the locally excited S_1 and the $^1\text{ICT}^*$ state) detected in the more polar EtOH and MeOH media. Significantly shortened excited state lifetimes are observed for **C2** with respect to **C1**, in analogy with its decreased fluorescence quantum yield and in agreement with the symmetry breaking and the stronger ICT character of the quadrupolar compound.^{85,4} Similarly to **C1**, also in the case of **C2** the small Rest component observed in all the investigated solvents is assigned to the lowest excited triplet state.

Fluorescence up-conversion kinetics have been acquired for **C1** and **C2** in EtOH and MeOH (**Figure B.6.4**) by exciting the samples at 400 nm and collecting the up-converted fluorescence at 370 nm which corresponds to the emission of the investigated compounds at 688 nm. This spectral position corresponds to the blue portion of the **C1** and **C2** fluorescence bands (see **Figure B.4.1** and **B.4.2**) but unfortunately it was not possible to acquire the fluorescence

kinetics at lower energies because this is the limit of our experimental set-up. For this reason, the collected decays are dominated by the fast occurrence of solvation dynamics, and the exponential components corresponding to the deactivation of the lowest excited singlet states show a low amplitude. In any case, the best fittings have been obtained by using time constants comparable to those obtained by the transient absorption experiments (see **Table B.6.2**), except for the Rest component which was absent in the up-conversion decays, pointing to the fact that in the up-conversion investigation we are indeed following the S_1 relaxation and deactivation dynamics. Indeed, even though the 400 nm excitation employed for the ultrafast spectroscopic investigation implies that higher excited singlet states are initially populated by light absorption, mainly in the case of **C2** (see Table S2), the S_n-S_1 internal conversion should occur very fast⁸⁶ and therefore should take place together with the inertial solvation in all the investigated solvents. It has to be noted that the results of the fluorescence up-conversion analysis are in full agreement with the assignments of the transient species revealed by Excited State Absorption measurements.

Table B.6.1. Spectral and kinetic properties of the transients of **C1** and **C2** in solvents of different polarity (obtained by femtosecond transient absorption measurements upon excitation at 400 nm).

Solvent	τ / ps [#]	λ / nm [*]	assignment
compound C1			
CHCl ₃	0.20	740(+)	Solvation
	5.3	615(+), 730(-)	Solvation
	115	605(+), 740(-)	S ₁
	Rest	600(+)	T ₁
DCM	0.17	670 (+)	Solvation
	2.5	595(+)	Solvation
	90	590(+), 650(-)	S ₁
	Rest	590(+)	T ₁
EtOH	1.8	605(+), 720(-)	Solvation
	7.0	600(+), 680(-)	Solvation
	29	590(+), 630(-), 685(+)	Solvation
	88	585(+), 625(-), 685(+)	S ₁
	Rest	540(+)	T ₁
MeOH	0.22	740(+)	Solvation
	1.0	600(+), 735(-)	Solvation
	5.1	595(+), 685(+)	Solvation
	41	585(+), 700(+)	S ₁
	Rest	530(+)	T ₁
compound C2			
CHCl ₃	2.9	610(+), >740(-)	Solvation
	24	600(+), 655(-), 725(+)	S ₁
	Rest	565(+), 710(+)	T ₁
DCM	1.4	605(+), 705(-)	Solvation
	2.2	575(+), 675(-), >740(+)	S ₁
	Rest	595(+)	T ₁
EtOH	1.0	605(+), 735(-)	Solvation+S ₁
	3.1	600(+), 705(+)	Solvation
	16	685(+)	S ₁ (ICT)
	Rest	590(+), 670(+)	T ₁
MeOH	0.27	605(+), 740(-)	Solvation+S ₁
	3.2	600(+), 705(+)	Solvation
	4.2	680(+)	S ₁ (ICT)
	Rest	590(+), 670(+)	T ₁

[#]Statistical error on the lifetimes is about 10%. ^{*}Species Associated Spectra (SAS) obtained by Target Analysis.

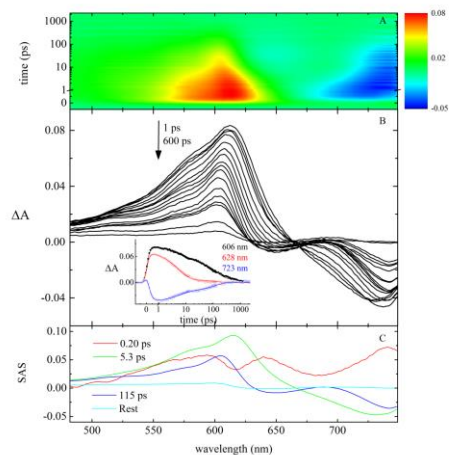


Figure B.6.1. Pump-probe absorption of **C1** in CHCl_3 ($\lambda_{\text{exc}}=400$ nm): A) contour plot of the experimental data, B) time resolved absorption spectra recorded at different delays after the laser pulse. Insets: decay kinetics recorded at meaningful wavelengths together with the corresponding fitting traces and C) Species Associated Spectra (SAS) of the decay components obtained by Target Analysis.

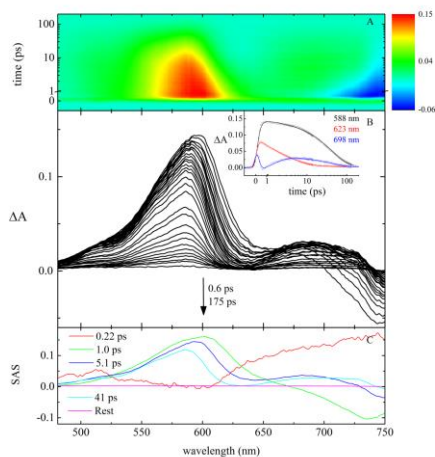


Figure B.6.2. Pump-probe absorption of **C1** in MeOH ($\lambda_{\text{exc}}=400$ nm): A) contour plot of the experimental data, B) time resolved absorption spectra recorded at different delays after the laser pulse. Insets: decay kinetics recorded at meaningful wavelengths together with the corresponding fitting traces and C) Species Associated Spectra (SAS) of the decay components obtained by Target Analysis.

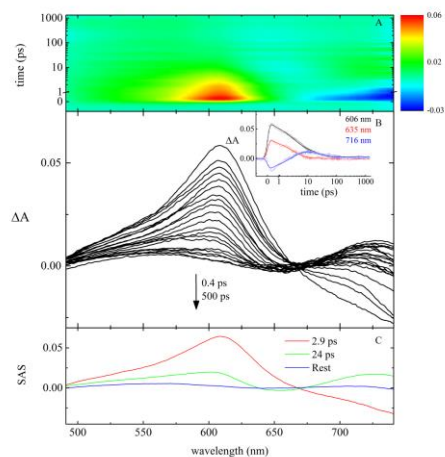


Figure B.6.3. Pump-probe absorption of **C2** in CHCl_3 ($\lambda_{\text{exc}}=400$ nm): A) contour plot of the experimental data, B) time resolved absorption spectra recorded at different delays after the laser pulse. Insets: decay kinetics recorded at meaningful wavelengths together with the corresponding fitting traces and C) Species Associated Spectra (SAS) of the decay components obtained by Target Analysis.

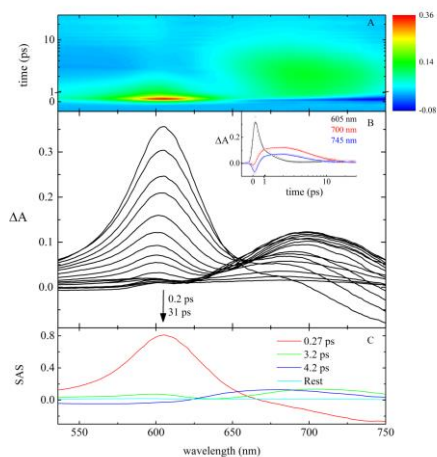


Figure B.6.4. Pump-probe absorption of **C2** in MeOH ($\lambda_{\text{exc}}=400$ nm): A) contour plot of the experimental data, B) time resolved absorption spectra recorded at different delays after the laser pulse. Insets: decay kinetics recorded at meaningful wavelengths together with the corresponding fitting traces and C) Species Associated Spectra (SAS) of the decay components obtained by Target Analysis.

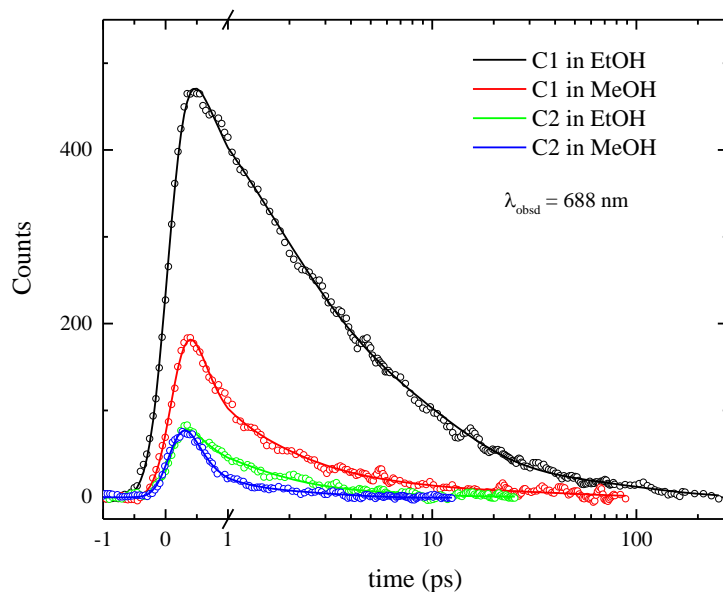


Figure B.6.5. Fluorescence up-conversion kinetics ($\lambda_{\text{exc}}=400$ nm) of **C1** and **C2** in MeOH and EtOH (dots) together with the best fittings (full lines) obtained by use of poly-exponential functions (see Table 4).

Table B.6.2. Decay components of **C1** and **C2** obtained by the decay kinetics of the up-conversion fluorescence recorded at 688 nm ($\lambda_{\text{exc}} = 400$ nm).

Compound	Solvent	τ / ps [#]
C1	EtOH	0.53
		1.5
		9.2
		30
		93
C1	MeOH	0.30
		1.2
		4.8
		45
C2	EtOH	0.75
		3.0
		15
	MeOH	0.30
		4.5

[#]Statistical error on the lifetimes is about 10%.

B.7 Two Photon Excited Fluorescence Measurements

The TPA cross sections were estimated using the TPEF method.⁸⁷ Excitation wavelength of 1300 nm was used because both the compounds show a maximum one photon absorption at 650 nm in DCM and emission wavelength of 800 nm was considered to detect the maximum fluorescence peak.

2-(6-(4-Dimethylaminophenyl)-2,4-neopentylene-1,3,5-hexatrienyl)-3-methylbenzothiazolium Perchlorate (Styryl 9M) dissolved in EtOH was used as the TPA reference to obtain the TPA cross sections.⁶⁹

The intensity of the TPEF signal increases with the square of the intensity: it is important to check this quadratic power dependence, to avoid overestimating the TPA cross section value because of fluorescence contributions from one photon absorption.

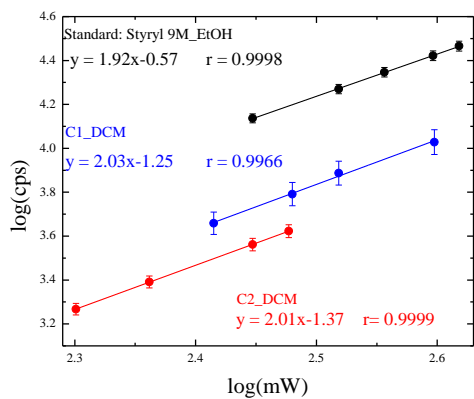


Figure B.7.1. Logarithmic plot of the quadratic dependence (counts vs. power) for: **Styryl 9M** in EtOH (black line), **C1** in DCM (blue line) and **C2** in DCM (red line).

A quadratic dependence was found between the emission counts and the laser pulse power; therefore, a slope of about 2 was found in the plot log (counts) vs. log (power), indicating allowed two-photon excitation (**Figure B.7.1**). The intercepts may be taken directly from the

intensity–power log–log plots provided that the standard and sample slopes are very close to the same value of 2.

The following equation was employed to compute the TPA cross sections (δ) for the two compounds under investigation (samples) with respect to the reference compound Styryl 9M (std):

$$d_{sample} = \frac{10^{b_{sample} - b_{std}} f_{Fstd} d_{std} [c]_{std} n_{std}}{f_{Fsample} [c]_{sample} n_{sample}} \quad (2)$$

where ϕ_F is the fluorescence quantum yield, $[c]$ is the solution concentration, b is the intercept in the quadratic plot and n is the refractive index of the solvent.

Table B.7.1. TPA cross sections determined for **C1** and **C2** in DCM by exciting at 1300 nm together with that of the reference compound (Styryl 9M) in EtOH. The parameters used for the calculations by equation 2 are also reported.

	ϕ_F	$[c] / M$	n	δ / GM
Styryl 9M EtOH^a	0.07	1.81×10^{-6}	1.33	580
C1 DCM	0.005 ^b	1.52×10^{-6}	1.42	500±50
C2 DCM	0.0005 ^b	5.42×10^{-5}	1.42	1400±100

^a from ref. 69; ^b from Table 1.

High values of the TPA cross sections, δ , have been obtained (see **Table B.7.1**): 500 GM (**C1**) and 1400 GM (**C2**). Comparing the results, the quadrupolar **C2** shows a TPA cross section approximately three times higher than the dipolar **C1**. These results indicate that **C2** has better NLO properties compared to **C1**, meaning that dipolar systems seem to give weaker TPA than symmetric dyes of the same complexity. Preliminary TPEF measurements on structurally similar dipolar and quadrupolar dimethylamino–styrene–methylpyridinium derivatives showed lower TPA cross sections for the mono and two branched systems, respectively (unpublished results). These findings suggest that the presence of the bithiophene spacers has a positive impact on the TPA response, with the increased conjugation and molecular dimensionality being crucial in

determining enhanced NLO properties. The obtained results are thus of great interest because the observed cross section for **C2** is of the same order of magnitude (thousands of GM) as the highest reported TPA cross sections for quadrupolar structures,^{1,18} similar or enhanced compared to other thiophene containing NLO organic chromophores^{47–50} and increased with respect to structurally analogous dimethylamino–styrene–methylpyridinium derivatives. In particular, neutral quadrupolar chromophores bearing lateral dibutylamino phenyls as electron donors and ethylene spacers showed TPA cross sections of 640 and 1700 GM in the presence of a central phenyl or dicyano substituted phenyl, as reported in reference 1. Additionally, a cationic quadrupolar dye bearing methylpyridinium as electron deficient portion showed a TPA cross section of 119 GM (see reference 88).

Two Photon Absorption transition tensors and cross sections of **C1** and **C2** in DCM were computed by use of the Dalton package (see **Tables B.7.2** and **S3**). The energy of the excited states obtained by Dalton are slightly underestimated, particularly in the case of **C2**; the difference between the transition energies calculated by Gaussian may be due to the different solvation model used by the two programs. It is evident that the computed probability of biphotonic absorption is strictly linked with the dipolar/quadrupolar nature of the investigated substrates. Indeed, in the case of the dipolar **C1** the S_1 and S_2 states show a δ value of several hundreds of GM whereas in the case of the quadrupolar **C2** the state S_1 is forbidden and S_2 becomes much more intense (ca. 1.9×10^4 GM) because of its high molecular symmetry. The δ values predicted by the calculations are in substantial agreement with those obtained experimentally by exciting at 1300 nm in the case of **C1**. It is possible that the cross section computed for the $S_0 \rightarrow S_2$ transition of the most stable and highly symmetrical conformer of **C2** is quite large and not satisfactorily confirmed by the experiment because of the possible

contribution to the observed real TPA of other low energy and not symmetrical ground state conformations of **C2** exhibiting a reduced TPA cross section for this transition.³¹

Table B.7.2. Wavelengths (λ), cross sections (δ) and polarization ratios (R) computed for the lowest excited singlet states of **C1** and **C2** in DCM (PCM) by B3LYP/6–31G(d) (Dalton2016.1).

comp.nd	State	$\lambda_{\text{OPA}}/\text{nm}$	$\lambda_{\text{TPA}}/\text{nm}$	δ / GM	R
C1	S ₁	678	1356	780	0.67
	S ₂	432	864	970	0.67
	S ₃	391	782	197	0.68
C2	S ₁	761	1522	95.4	1.49
	S ₂	636	1273	18700	0.66
	S ₃	577	1154	597	0.76
	S ₄	551	1103	47.8	1.41

Estimated error on the computed TPA cross sections is approximately $\pm 20\%$.

In the cationic chromophores of the present study (**C1** and **C2**), contrary from what is typically observed in the neutral push–pull systems, the absorption transition shows a strong charge transfer character as clearly evidenced theoretically from the HOMO and LUMO molecular orbitals (**Figure B.5.1**) and experimentally from their strong negative solvatochromism. This charge transfer character of their absorption is in agreement with the high magnitude TPA observed for both **C1** and **C2**. The higher TPA cross section found in **C2** is in agreement with the more significant ICT character of its excited states as previously discussed. In fact, the lower quantum efficiencies (**C1**: 0.005 and **C2**: 0.0005 in DCM) and the shorter decay lifetime (**C1**: 45 ps and **C2**: 4.5 ps in DCM) of **C2** are in agreement with the ultrafast intramolecular charge transfer and localization taking place in the quadrupolar compound.⁸⁹

Experimental evidence has shown that an increase in intramolecular charge transfer results in an enhanced TPA cross section.⁹⁰ The TPA process is an instantaneous process and it is mainly influenced by the Franck–Condon (FC) excited state. Even though it is not easy to monitor the FC state, it is possible to trace back its characteristics by following the nature of the ICT relaxed state. Thus, the obtained results suggest that there is a higher amount of charge

transfer in the FC configuration for **C2** with respect to **C1**, which might contribute to the enhanced TPA cross section.

Furthermore, the presence of intramolecular charge transfer character is supported by the Density Functional Theory (DFT) and time dependent DFT (TD-DFT) theoretical calculations that predicted a high dipole moment in the ground state for **C1**, which is decreased in the excited state. In the case of **C2**, the theoretical investigation revealed a symmetry breaking in the optimized geometry and in the molecular orbitals describing the relaxed excited S_1 state. The quantum-mechanical calculations showed that in the quadrupolar compound the dipole moment calculated in the ground state is very low because of the molecular symmetry, but the one calculated for the relaxed S_1 is found to be very high pointing to significant excited state ICT character. In the case of **C2** the symmetry of the system is completely broken in the relaxed S_1 geometry and this gives a possible explanation for the high dipole moment calculated for the relaxed S_1 .

However, the details of the excited state formation in symmetrical donor-acceptor systems are not clearly understood. A considerable fundamental interest arises from the fact that such systems possess a charge-transfer character of the excited state, which may be accompanied by a stabilization of the excitation at one branch and breaking of the molecular symmetry.⁹¹

The obtained results are very interesting and demonstrate the enhancement in the NLO properties of the quadrupolar compound (two branched system) compared to its dipolar counterpart (mono branched system), in agreement with the more efficient ICT and the charge localization clearly observed in the electronic structure predicted by the calculations in the case of **C2**. This suggests that multi-branched systems can be used to increase the TPA cross section

in order to promote charge transfer characteristic, as stated in previous works on similar organic compounds.⁵³

B.8 Conclusions

A comprehensive experimental and quantum-mechanical study has allowed us to obtain information about the solvent effect on the spectral and photophysical properties of two cationic pyridinium derivatives: a dipolar, one-branched (**C1**: D- π -A⁺) system and a quadrupolar, two-branched (**C2**: D- π -A⁺- π -D) compound, bearing a dibutylamino as electron donor group (D), a methyl-pyridinium as electron acceptor portion (A) and an ethylene linked with electron rich thiophene rings as π -spacers. The absorption spectra of **C1** and **C2** are broad and shifted to the red side of the visible spectral range with this peculiarity which is due to the presence of the bithiophene bridges largely increasing molecular conjugation and dimensionality. A significant negative solvatochromism has been observed for the absorption bands of the investigated salts together with a lower magnitude blue shift of the emission spectra upon increasing the solvent polarity, which have been rationalized by considering the results of the theoretical investigation. In fact, the dipole moment for **C1** is predicted to be high in the ground state and to be significantly decreased in the Frank-Condon excited state reached by light absorption, whereas no significant change in the dipole moment is obtained during the relaxation of S₁. These theoretical results are in agreement with the solvent effect on the absorption and emission transitions, which both show a significant charge transfer character, whereas no significant charge rearrangement is predicted to occur during the excited state dynamics. This behaviour of **C1** is very different from that exhibited by analogous structures bearing a styryl π -spacer and thus characterized by increased flexibility, for which a highly polar TICT relaxed excited state was predicted by the theoretical investigation. Femtosecond transient absorption and

fluorescence up-conversion measurements have indeed revealed that the excited state dynamics of **C1** are essentially dominated by simple solvent relaxation phenomena of the S_1 state, whose lifetime shows a little dependence upon the solvent polarity. Also the low fluorescence quantum yields of **C1** (ca. 10^{-3}) are scarcely affected by the solvent and the main photoinduced decay pathway is internal conversion in all the investigated media.

The absorption spectra of **C2** are red-shifted with respect to those of **C1** whereas the emission bands of the two compounds overlap in both low polarity and high polarity solvents suggesting a localization of the excitation on just one branch of the quadrupolar compound, which becomes the fluorescent portion. In fact, in the case of **C2** the quantum-mechanical calculations have shown that the symmetry of the system is broken in the relaxed S_1 geometry and that a very significant charge displacement in the LUMO-HOMO molecular orbitals occurs from one branch to the other of the quadrupolar system. The excited state symmetry breaking, the first time revealed for an analogous dimethylamino derivative only in highly polar media,⁴⁸ is here observed in all the investigated solvents regardless of their polarity as previously observed in a diphenylamino-analogue.⁴⁹ The ultrafast spectroscopic investigation has pointed out that in the case of the quadrupolar compound, two distinct excited singlet states are detected in polar solvents, where an intramolecular charge transfer (ICT) state is efficiently produced as a separate species. These findings are in line with the decreased fluorescence efficiency of the quadrupolar system with respect to the dipolar analogue (ϕ_F ca. 10^{-4}) and with the strong TICT character foreseen for the relaxed excited S_1 state of **C2** by the theoretical calculations.

High values of Two-Photon Absorption cross sections have been obtained by means of femtosecond excited Two-Photon Excited Fluorescence measurements: 500 and 1400 GM for **C1** and **C2**, respectively. These results are very interesting and demonstrate the strong

enhancement in the Nonlinear Optical properties of the quadrupolar compound over its dipolar counterpart. The present investigation revealed that an ultrafast localization on one of the branches to give an ICT state takes place after photoexcitation in **C2**; a higher charge transfer character in the FC configuration for **C2** with respect to **C1** could thus be speculated, which might contribute to the increased TPA cross section of the quadrupolar system. TPA cross section was enhanced by the presence of the bithiophene π -bridges motif, compared to that exhibited by structurally similar styryl containing compounds. Thus, the highly two-photon absorbing **C2** is a promising candidate for potential applications in the medical and optoelectronic fields. Moreover, since the absorption spectra of **C1** and **C2** are broad and on the red side of the visible spectral range, these compounds may be promising for a possible use as photosensitizers in organic photovoltaic solar cells.

B.9 Supporting Information. The Supporting Information file contains additional data concerning: the concentration effect on the absorption spectra, the femtosecond transient absorption measurements and the quantum chemical calculations.

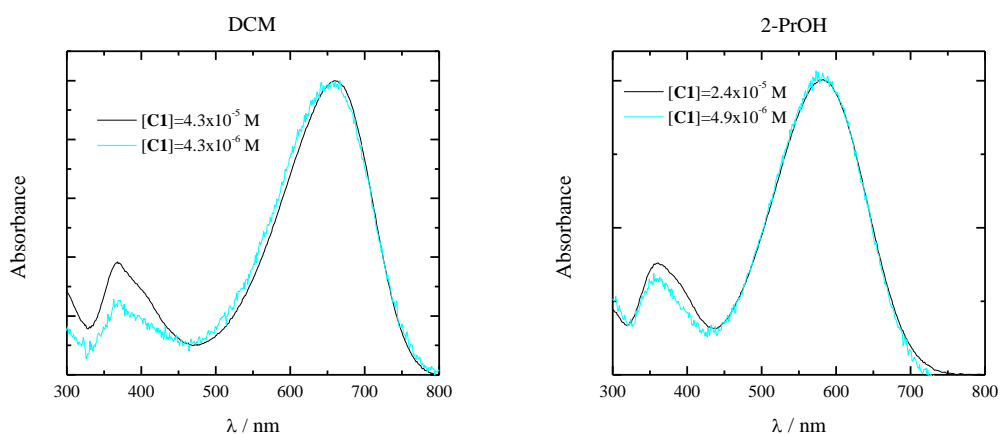


Figure BS1. Normalized absorption spectra of concentrated and diluted solution of **C1** in DCM and 2-PrOH.

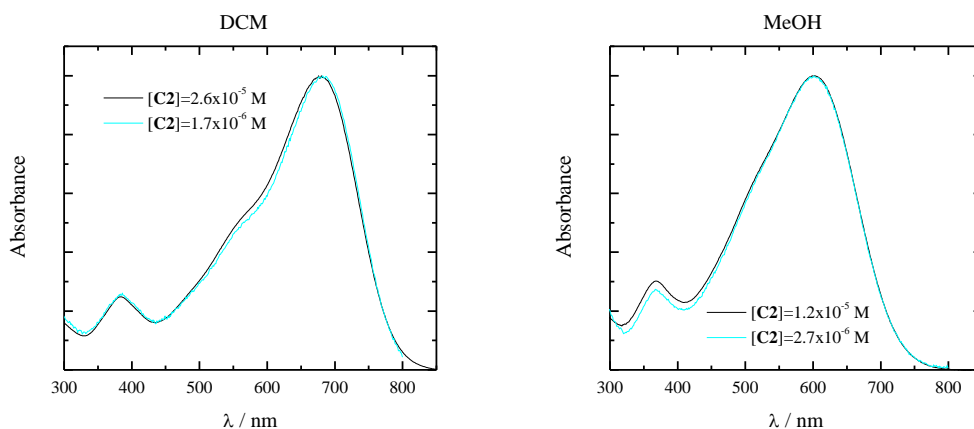


Figure BS2. Normalized absorption spectra of concentrated and diluted solution of **C2** in DCM and MeOH.

Table BS1. Full Width at Half Maximum (FWHM) of the absorption and emission bands of **C1** and **C2** in different solvents.

Solvent	FWHM _{abs} / cm ⁻¹		FWHM _{em} / cm ⁻¹	
	C1	C2	C1	C2
CHCl ₃	3570	5110	1630	1920
DCM	3360	4360	1470	1570
DCE	3450	4490	1510	1690
2-PrOH	4280	5580	2080	2890
<i>Ac</i>	4450	5560	1860	2690
EtOH	4440	5600	2000	2450
<i>MeCN</i>	4510	5710	1840	1850
MeOH	4490	5650	1960	2780
W/EtOH 70/30	5050	6570	2040	2450

Table BS2. Transition energy, nature and oscillator strength of the lowest excited singlet states of **C1** in DCM calculated by TD-DFT B3LYP/6-31G(d), together with the experimental absorption and emission maxima (λ_{exp}) in the same solvent.

comp.d	transition	nature	%	$\lambda_{\text{calc}} / \text{nm}$	f	$\lambda_{\text{exp}} / \text{nm}$
C1	$S_0 \rightarrow T_1$	$\pi_{\text{H}} \rightarrow \pi_{\text{L}}^*$	96	1098	0.000	
	$S_0 \rightarrow S_1$	$\pi_{\text{H}} \rightarrow \pi_{\text{L}}^*$	100	618	1.509	663
	$S_0 \rightarrow T_2$	$\pi_{\text{H-1}} \rightarrow \pi_{\text{L}}^*$	48	532	0.000	
	$S_0 \rightarrow S_2$	$\pi_{\text{H}} \rightarrow \pi_{\text{L+1}}^*$	97	437	0.074	
	$S_0 \rightarrow S_3$	$\pi_{\text{H-1}} \rightarrow \pi_{\text{L}}^*$	73	387	0.233	
	$S_0 \rightarrow S_4$	$\pi_{\text{H}} \rightarrow \pi_{\text{L+2}}^*$	69	338	0.009	
	$S_0 \rightarrow S_5$	$\pi_{\text{H-2}} \rightarrow \pi_{\text{L}}^*$	91	322	0.013	
	$S_0 \rightarrow S_6$	$\pi_{\text{H-3}} \rightarrow \pi_{\text{L}}^*$	95	309	0.026	
C2	$S_0 \rightarrow T_1$	$\pi_{\text{H}} \rightarrow \pi_{\text{L}}^*$	79	1031	0.000	
	$S_0 \rightarrow T_2$	$\pi_{\text{H}} \rightarrow \pi_{\text{L+1}}^*$	50	969	0.000	
	$S_0 \rightarrow S_1$	$\pi_{\text{H}} \rightarrow \pi_{\text{L}}^*$	99	724 ^a	2.094	677
	$S_0 \rightarrow S_2$	$\pi_{\text{H-1}} \rightarrow \pi_{\text{L}}^*$	82	625	0.010	
	$S_0 \rightarrow S_3$	$\pi_{\text{H-1}} \rightarrow \pi_{\text{L+1}}^*$	98	544	0.729	
	$S_0 \rightarrow S_4$	$\pi_{\text{H}} \rightarrow \pi_{\text{L+1}}^*$	82	541	0.138	
	$S_0 \rightarrow S_5$	$\pi_{\text{H-2}} \rightarrow \pi_{\text{L}}^*$	80	409	0.316	
	$S_0 \rightarrow S_6$	$\pi_{\text{H}} \rightarrow \pi_{\text{L+2}}^*$	82	381	0.081	

^a The absorption maximum of the calculated spectrum is ca. 700 nm

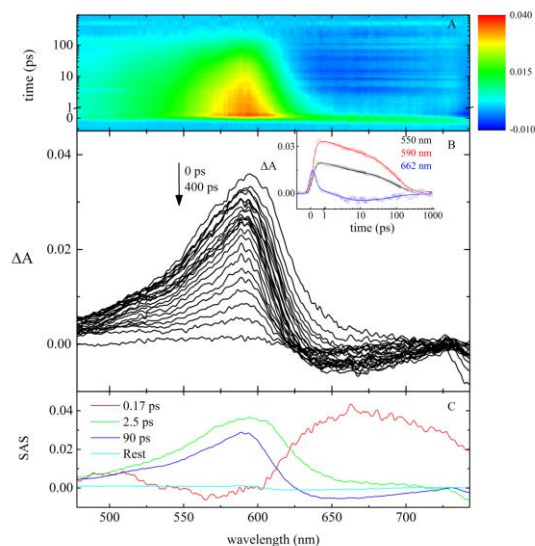


Figure BS3. Pump-probe absorption of **C1** in DCM ($\lambda_{\text{exc}}=400$ nm): A) contour plot of the experimental data, B) time resolved absorption spectra recorded at different delays after the laser pulse. Insets: decay kinetics recorded at meaningful wavelengths together with the corresponding fitting traces and C) Species Associated Spectra (SAS) of the decay components obtained by Target Analysis.

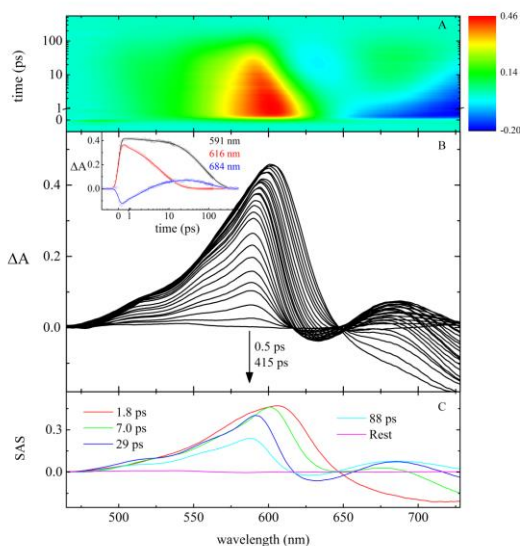


Figure BS4. Pump-probe absorption of **C1** in EtOH ($\lambda_{\text{exc}}=400$ nm): A) contour plot of the experimental data, B) time resolved absorption spectra recorded at different delays after the laser pulse. Insets: decay kinetics recorded at meaningful wavelengths together with the corresponding fitting traces and C) Species Associated Spectra (SAS) of the decay components obtained by Target Analysis.

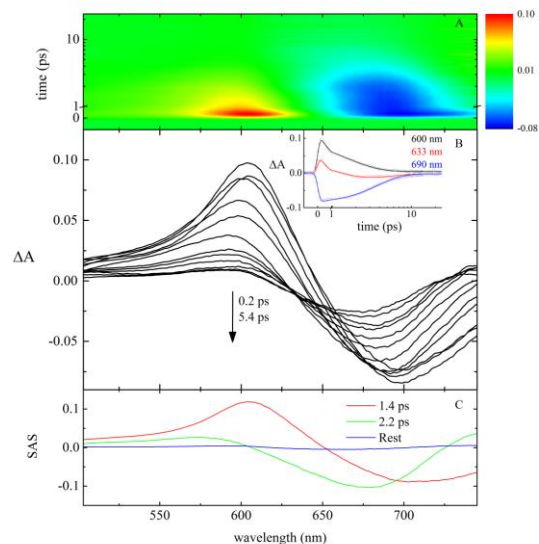


Figure BS5. Pump-probe absorption of **C2** in DCM ($\lambda_{exc}=400$ nm): A) contour plot of the experimental data, B) time resolved absorption spectra recorded at different delays after the laser pulse. Insets: decay kinetics recorded at meaningful wavelengths together with the corresponding fitting traces and C) Species Associated Spectra (SAS) of the decay components obtained by Target Analysis.

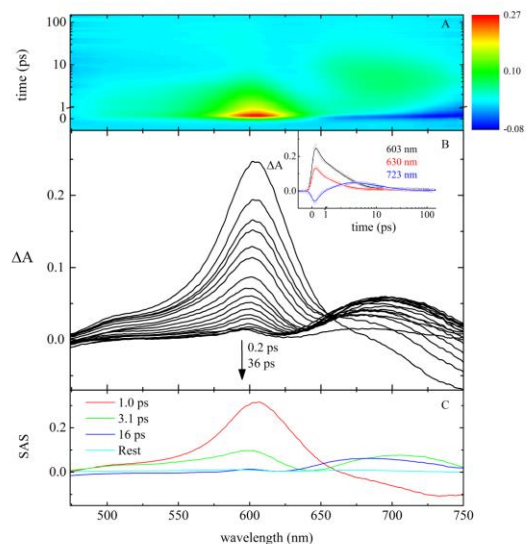


Figure BS6. Pump-probe absorption of **C2** in EtOH ($\lambda_{exc}=400$ nm): A) contour plot of the experimental data, B) time resolved absorption spectra recorded at different delays after the laser pulse. Insets: decay kinetics recorded at meaningful wavelengths together with the corresponding fitting traces and C) Species Associated Spectra (SAS) of the decay components obtained by Target Analysis.

Table BS3. Two photon transition tensor (a.u.; 1 a.u.= 1.896788×10^{-50} cm⁴ s photon⁻¹) of **C1** and **C2** in DCM (PCM) computed by B3LYP/6-31G* (Dalton2016.1).

Comp.nd	State	Energy (eV)	S _{XX}	S _{YY}	S _{ZZ}	S _{XY}	S _{XZ}	S _{YZ}
C1	S ₁	1.83	1182.7	70.9	0.1	-305.6	-25.7	6.4
	S ₂	2.84	-821.5	-82.1	-0.5	264.8	14.3	-4.9
	S ₃	3.17	357.3	5.8	-0.4	-59.8	5.7	-2.1
	S ₄	3.54	26489.4	1940.7	12.1	-7179.0	-584.0	158.3
C2	S ₁	1.63	38.7	0.3	0.4	-418.0	92.7	-0.6
	S ₂	1.95	-5794.8	-50.2	-2.5	-2.3	-3.1	16.2
	S ₃	2.15	-959.6	70.2	2.7	-7.1	6.9	-21.0
	S ₄	2.25	83.7	0.0	0.4	-201.9	45.7	-0.6

AUTHOR INFORMATION

Corresponding Author

benedetta.carlotti@gmail.com

Author Contributions

The manuscript was written through equal contributions of all authors. All authors have given approval to the final version of the manuscript.

ACKNOWLEDGMENT

The authors acknowledge support from the Italian “Ministero per l’Università e la Ricerca Scientifica e Tecnologica”, MIUR (Rome, Italy) under the FIRB “Futuro in Ricerca” 2013, no. RBFR13PSB6; ACS International Research Experience for Undergraduates (IREU) Program 2014 and “Programmi di mobilità e Scambi Culturali di Studenti nell’ambito di accordi

quadro” 2016. Dr. Mirco Natali and Prof. Maria Teresa Indelli are kindly acknowledged for their help with the nanosecond flash photolysis measurements.

References

- (1) Pawlicki, M.; Collins, H. A.; Denning, R. G.; Anderson, H. L. Two-Photon Absorption and the Design of Two-Photon Dyes. *Angew. Chem. Int. Ed.* **2009**, *48*, 3244–3266.
- (2) Terenziani, F.; Katan, C.; Badaeva, E.; Tretiak, S.; Blanchard-Desce, M. Enhanced Two-Photon Absorption of Organic Chromophores: Theoretical and Experimental Assessments. *Adv. Mater.* **2008**, *20*, 4641–4678.
- (3) Gallavardin, T.; Maurin, M.; Marotte, S.; Simon, T.; Gabudean, A.; Bretonniere, Y.; Lindgren, M.; Lerouge, F.; Baldeck, P. L.; Stephan, O. et al. Photodynamic Therapy and Two-Photon Bio-Imaging Applications of Hydrophobic Chromophores Through Amphiphilic Polymer Delivery. *Photochem. Photobiol. Sci.* **2011**, *10*, 1216–1225.
- (4) Ramakrishna G.; Goodson III, T. Excited-State Deactivation of Branched Two-Photon Absorbing Chromophores: A Femtosecond Transient Absorption Investigation. *J. Phys. Chem. A* **2007**, *111*, 993–1000.
- (5) Varnavski, O.; Yan, X.; Mongin, O.; Blanchard-Desce, M.; Goodson, III, T. Strongly Interacting Organic Conjugated Dendrimers with Enhanced Two-Photon Absorption. *J. Phys. Chem. C* **2007**, *111*, 149–162.
- (6) Adegoke, O. O.; Ince, M.; Mishra, A.; Green, A.; Varnavski, O.; Martínez-Díaz, M.; Bäuerle, P.; Torres, T.; Goodson, III, T. Synthesis and Ultrafast Time Resolved Spectroscopy of Peripherally Functionalized Zinc Phthalocyanine Bearing Oligothiophylene-ethynylene Subunits. *J. Phys. Chem. C*, **2013**, *117*, 20912–20918.
- (7) Harpham, M. R.; Suzer, O.; Ma, C.; Bauerle, P.; Goodson III, T. Thiophene Dendrimers as Entangled Photon Sensor Materials. *J. Am. Chem. Soc.* **2009**, *131*, 973–979.
- (8) Lahankar, S. A.; West, R.; Varnavski, O.; Xie, X.; Goodson III, T.; Sukhomlinova, L.; Twieg, R. Electronic Interactions in a Branched Chromophore Investigated by Nonlinear Optical and Time-Resolved Spectroscopy. *J. Chem. Phys.* **2004**, *120*, 337–344.
- (9) Ranasinghe, M. I.; Hager, M. W.; Gorman, C. B.; Goodson III, T. Time-Resolved Fluorescence Investigation of Energy Transfer in Compact Phenylacetylene Dendrimers. *J. Phys. Chem. B* **2004**, *108*, 8543–8549.
- (10) Goodson III, T. Time-Resolved Spectroscopy of Organic Dendrimers and Branched Chromophores. *Annu. Rev. Phys. Chem.* **2005**, *56*, 581–603.
- (11) Mazzoli, A.; Carlotti, B.; Fortuna, C. G.; Spalletti, A. Photobehaviour and DNA Interaction of Styrylquinolinium Salts Bearing Thiophene Substituents. *Photochem. Photobiol. Sci.*, **2011**, *10*, 973–979.
- (12) Mazzoli, A.; Carlotti, B.; Consiglio, G.; Fortuna, C. G.; Miolo, G.; Spalletti, A. Photobehaviour of Methyl-Pyridinium and Quinolinium Iodide Derivatives, Free and

- Complexed with DNA. A Case of Bisintercalation. *Photochem. Photobiol. Sci.* **2014**, *13*, 939–950.
- (13) Doan, P. H.; Pitter, D. R. G.; Kocher, A.; Wilson, J. N.; Goodson III, T. Two-Photon Spectroscopy as a New Sensitive Method for Determining the DNA Binding Mode of Fluorescent Nuclear Dyes. *J. Am. Chem. Soc.* **2015**, *137*, 9198–9201.
- (14) Huang, T.; Wang, Y.; Kang, Z.; Yao, J.; Lu, R.; Zhang, H. Investigation on Photophysical Properties of D- π -A- π -D-Type Fluorenone-Based Linear Conjugated Oligomers by Using Femtosecond Transient Absorption Spectroscopy. *Photochem. Photobiol.* **2014**, *90*, 29–34.
- (15) Lavanya Devi, C.; Yesudas, K.; Makarov, N. S.; Jayathirtha Rao, V.; Bhanuprakash, K.; Perry, J. W. Combined Experimental and Theoretical Study of One- and Two-Photon Absorption Properties of D- π -A- π -D Type Bis(Carbazolylfluorenylethynyl) Arene Derivatives: Influence of Aromatic Acceptor Bridge. *Dyes and Pigments* **2015**, *113*, 682–691.
- (16) Breukers, R. D.; Janssens, S.; Raymond, S. G.; Bhuiyan, M. D. H.; Kay, A. J. Synthesis and Characterization of Strongly Two Photon Absorbing and Photoswitchable Azo Molecules. *Dyes and Pigments* **2015**, *112*, 17–23.
- (17) Wang, X.; Wang, D.; Zhou, G.; Yu, W.; Zhou, Y.; Fang, Q.; Jiang, M. Symmetric and Asymmetric Charge Transfer Process of Two-Photon Absorbing Chromophores: Bis-Donor Substituted Stilbenes, and Substituted Styrylquinolinium and Styrylpyridinium Derivatives. *J. Mater. Chem.* **2001**, *11*, 1600–1605.
- (18) Terenziani, F.; Painelli, A.; Katan, C.; Charlot, M.; Blanchard-Desce, M. Charge Instability in Quadrupolar Chromophores: Symmetry Breaking and Solvatochromism. *J. Am. Chem. Soc.* **2006**, *128*, 15742–15755.
- (19) Katan, C.; Terenziani, F.; Mongin, O.; Werts, M. H. V.; Porres, L.; Pons, T.; Mertz, J.; Tretiak, S.; Blanchard-Desce, M. Effects of (Multi)branching of Dipolar Chromophores on Photophysical Properties and Two-Photon Absorption. *J. Phys. Chem. A* **2005**, *109*, 3024–3037.
- (20) Ramakrishna, G.; Bhaskar, A.; Goodson, III T. Ultrafast Excited State Relaxation Dynamics of Branched Donor- π -Acceptor Chromophore: Evidence of a Charge-Delocalized State. *J. Phys. Chem. B* **2006**, *110*, 20872–20878.
- (21) Bhaskar, A.; Ramakrishna, G.; Lu, Z.; Twieg, R.; Hales, J. M.; Hagan, D. J.; Stryland, E.; Goodson III, T. Investigation of Two-Photon Absorption Properties in Branched Alkene and Alkyne Chromophores. *J. Am. Chem. Soc.* **2006**, *128*, 11840–11849.
- (22) Wang, Y.; He, G. S.; Prasad, P. N.; Goodson III, T. Ultrafast Dynamics in Multibranching Structures with Enhanced Two-Photon Absorption. *J. Am. Chem. Soc.* **2005**, *127*, 10128–10129.
- (23) Correa, D. S.; Oliveira, S. L.; Misoguti, L.; Zilio, S. C.; Aroca, R. F.; Constantino, C. J. L.; Mendonca, C. R. Investigation of the Two-Photon Absorption Cross-Section in Perylene Tetracarboxylic Derivatives: Nonlinear Spectra and Molecular Structure. *J. Phys. Chem. A* **2006**, *110*, 6433–6438.

- (24) Rogers, J. E.; Slagle, J. E.; McLean, D. G.; Sutherland, R. L.; Brant, M. C.; Heinrichs, J.; Jakubiak, R.; Kannan, R.; Tan, L.; Fleitz, P. A. Insight into the Nonlinear Absorbance of Two Related Series of Two-Photon Absorbing Chromophores. *J. Phys. Chem. A* **2007**, *111*, 1899–1906.
- (25) Padilha, L. A.; Webster, S.; Przhonska, O. V.; Hu, H.; Peceli, D.; Ensley, T. R.; Bondar, M. V.; Gerasov, A. O.; Kovtun, Y. P.; Shandura, M. P. et al. Efficient Two-Photon Absorbing Acceptor- π -Acceptor Polymethine Dyes. *J. Phys. Chem. A* **2010**, *114*, 6493–6501.
- (26) Yan, L.; Chen, X.; He, Q.; Wang, Y.; Wang, X.; Guo, Q.; Bai, F.; Xia, A. Localized Emitting State and Energy Transfer Properties of Quadrupolar Chromophores and (Multi)Branched Derivatives. *J. Phys. Chem. A* **2012**, *116*, 8693–8705.
- (27) Terenziani, F.; Sissa, C.; Painelli, A. Symmetry Breaking in Octupolar Chromophores: Solvatochromism and Electroabsorption. *J. Phys. Chem. B* **2008**, *112*, 5079–5087.
- (28) Terenziani, F.; Przhonska, O. V.; Webster, S.; Padilha, L. A.; Slominsky, Y. L.; Davydenko, I. G.; Gerasov, A. O.; Kovtun, Y. P.; Shandura, M. P.; Kachkovski, A. D. et al. Essential-State Model for Polymethine Dyes: Symmetry Breaking and Optical Spectra. *J. Phys. Chem. Lett.* **2010**, *1*, 1800–1804.
- (29) Hu, H.; Przhonska, O. V.; Terenziani, F.; Painelli, A.; Fishman, D.; Ensley, T. R.; Reichert, M.; Webster, S.; Bricks, J. L.; Kachkovski, A. D.; Hagan, D. J. et al. Two-Photon Absorption Spectra of a Near Infrared 2-Azaazulene Polymethine Dye: Solvation and Ground-State Symmetry Breaking. *Phys. Chem. Chem. Phys.* **2013**, *15*, 7666–7678.
- (30) Gutierrez-Arzaluz, L.; Guarin, C. A.; Rodriguez-Cordoba, W.; Peon, J. Dynamics of the Formation of a Charge Transfer State in 1,2-Bis(9-anthryl)acetylene in Polar Solvents: Symmetry Reduction with the Participation of an Intramolecular Torsional Coordinate. *J. Phys. Chem. B* **2013**, *117*, 12175–12183.
- (31) Rebane, A.; Drobizhev, M.; Makarov, N. S.; Wicks, G.; Wnuk, P.; Stepanenko, Y.; Haley, J. E.; Krein, D. M.; Fore, J. L.; Burke et al. Symmetry Breaking in Platinum Acetylide Chromophores Studied by Femtosecond Two-Photon Absorption Spectroscopy. *J. Phys. Chem. A* **2014**, *118*, 3749–3759.
- (32) Trinh, C.; Kirkikovali, K.; Das, S.; Ener, M. E.; Gray, H. B.; Djurovich, P.; Bradforth, S. E.; Thompson, M. E. Symmetry Breaking Charge Transfer of Visible Light Absorbing Systems: Zinc Dipyrins. *J. Phys. Chem. C* **2014**, *118*, 21834–21845.
- (33) Kim, W.; Sung, J.; Grzybowski, M.; Gryko, D. T.; Kim, D. Modulation of Symmetry-Breaking Intramolecular Charge Transfer Dynamics Assisted by Pendant Side Chains in π -Linkers in Quadrupolar Diketopyrrolopyrrole Derivatives. *J. Phys. Chem. Lett.* **2016**, *7*, 3060–3066.
- (34) Wang, X.; Wang, C.; Yu, W.; Zhou, Y.; Fang, Q.; Jiang, M. Two-Photon Absorption of Styryl-Quinolinium, -Pyridinium, and -Barbituric Acid Derivatives, and Intramolecular Charge Transfer. *Can. J. Chem.* **2001**, *79*, 174–182.
- (35) Zhu, Y.; Xiao, L.; Zhao, M.; Zhou, J.; Zhang, Q.; Wang, H.; Li, S.; Zhou, H.; Wu, J.; Tian, Y. A Series of Imidazole Derivatives: Synthesis, Two-Photon Absorption, and

Application for Bioimaging. *BioMed Research International* **2015**, Article ID 965386, 1–8.

- (36) Zheng, Y. C.; Zheng, M. L.; Chen, S.; Zhao, Z. S.; Duan, X. M. Biscarbazolymethane–Based Cyanine: A Two–Photon Excited Fluorescent Probe for DNA and Selective Cell Imaging. *J. Mater. Chem. B* **2014**, *2*, 2301–2310.
- (37) Miao, F.; Zhang, W.; Sun, Y.; Zhang, R.; Liu, Y.; Guo, F.; Song, G.; Tian, M.; Yu, X. Novel Fluorescent Probes for Highly Selective Two–Photon Imaging of Mitochondria in Living Cells. *Biosensors and Bioelectronics* **2014**, *55*, 423–429.
- (38) Hrobarik, P.; Hrobarikova, V.; Semak, V.; Kasak, P.; Rakovsky, E.; Polyzos, I.; Fakis, M.; Persephonis, P. Quadrupolar Benzobisthiazole–Cored Arylamines as Highly Efficient Two–Photon Absorbing Fluorophores. *Org. Lett.* **2014**, *16*, 6358–6361.
- (39) Hao, F.; Zhu, D.; Ma, J.; Chai, L. Synthesis and Nonlinear Optical Properties in the Near–IR Range of Stilbazolium Dyes. *Spectrochimica Acta A: Mol. Biomol. Spectr.* **2014**, *123*, 46–53.
- (40) Blanchard–Desce, M.; Wortmann, R.; Lebus, S.; Lehn, J. M.; Kramer P. Intramolecular Charge Transfer in Elongated Donor–Acceptor Conjugated Polyenes. *Chem. Phys. Letts.* **1995**, *243*, 526–532.
- (41) Blanchard–Desce, M.; Alain, V.; Midrier, L.; Wortmann, R.; Lebus, S.; Glania, C.; Kramer, P.; Fort, A.; Muller, J.; Barzoukas, M. Intramolecular Charge Transfer and Enhanced Quadratic Optical Non–Linearities in Push Pull Polyenes. *J. Photochem. Photobiol. A: Chem.* **1997**, *105*, 115–121.
- (42) Alain, V.; Redoglia, S.; Blanchard–Desce, M.; Lebus, S.; Lukaszuk, K.; Wortmann, R.; Gubler, U.; Bosshard, C.; Gunter, P. Elongated Push–Pull Diphenylpolyenes for Nonlinear Optics: Molecular Engineering of Quadratic and Cubic Optical Nonlinearities Via Tuning of Intramolecular Charge Transfer. *Chem. Phys.* **1999**, *245*, 51–71.
- (43) Barbarella, G.; Melucci, M.; Sotgiu, G. The Versatile Thiophene: An Overview of Recent Research on Thiophene–Based Materials. *Adv. Mater.* **2005**, *17*, 1581–1593.
- (44) Zhang, F.; Wu, D.; Xu, Y.; Feng, X. Thiophene–Based Conjugated Oligomers for Organic Solar Cells. *J. Mater. Chem.* **2011**, *21*, 17590–17600.
- (45) Mallet, C.; Savitha, G.; Allain, M.; Kozmik, V.; Svoboda, J.; Frere, P.; Roncali, J. Synthesis and Electronic Properties of D–A–D Triads Based on 3–Alkoxy–4–cyanothiophene and Benzothienothiophene Blocks. *J. Org. Chem.* **2012**, *77*, 2041–2046.
- (46) Keller, B.; McLean, A.; Kim, B.; Chung, K.; Kim, J.; Goodson III, T. Ultrafast Spectroscopic Study of Donor–Acceptor Benzodithiophene Light Harvesting Organic Conjugated Polymers. *J. Phys Chem. C* **2016**, *120*, 9088–9096.
- (47) Genin, E.; Hugues, V.; Clermont, G.; Herbivo, C.; Castro, M. C. R.; Comel, A.; Raposo, M. M. M.; Blanchard–Desce, M. Fluorescence and Two–Photon Absorption of Push–Pull Aryl(Bi)Thiophenes: Structure–Property Relationships. *Photochem. Photobiol. Sci.* **2012**, *11*, 1756–1766.

- (48) Chen, D.; Zhong, C.; Dong, X.; Liu, Z.; Qin, J. A New Building Block, Bis(Thiophene Vinyl)–Pyrimidine, for Constructing Excellent Two–Photon Absorption Materials: Synthesis, Crystal Structure and Properties. *J. Mater. Chem.* **2012**, *22*, 4343–4348.
- (49) Zhou, H.; Zhou, F.; Tang, S.; Wu, P.; Chen, Y.; Tu, Y.; Wu, J.; Tian, Y. Two–Photon Absorption Dyes with Thiophene as π Electron Bridge: Synthesis, Photophysical Properties and Optical Data Storage. *Dyes and Pigments* **2011**, *92*, 633–641.
- (50) Chow, C. Two–Photon Induced Emissive Thiophene Donor–Acceptor Systems as Molecular Probes for *In Vitro* Bio–Imaging: Synthesis, Crystal Structure, and Spectroscopic Properties. *RSC Advances* **2013**, *3*, 18835–18843.
- (51) Carlotti, B.; Elisei, F.; Fortuna, C. G.; Mazzucato, U.; Spalletti, A. Intramolecular Charge Transfer of Push–Pull Pyridinium Salts in the Singlet Manifold. *J. Phys. Chem. A* **2014**, *118*, 3580–3592.
- (52) Carlotti, B.; Cesaretti, A.; Fortuna, C. G.; Spalletti, A.; Elisei, F. Experimental Evidence of Dual Emission in a Negatively Solvatochromic Push–Pull Pyridinium Derivative. *Phys. Chem. Chem. Phys.* **2015**, *17*, 1877–1882.
- (53) Carlotti, B.; Benassi, E.; Spalletti, A.; Fortuna, C. G.; Elisei, F. Photoinduced Symmetry–Breaking Intramolecular Charge Transfer in a Quadrupolar Pyridinium Derivative. *Phys. Chem. Chem. Phys.* **2014**, *16*, 13984–13994.
- (54) Carlotti, B.; Benassi, E.; Fortuna, C. G.; Barone, V.; Spalletti, A.; Elisei, F. Efficient Excited–State Symmetry Breaking in a Cationic Quadrupolar System Bearing Diphenylamino Donors. *ChemPhysChem* **2016**, *17*, 136–146.
- (55) Fortuna, C. G.; Bonaccorso, C.; Qamar, F.; Anu, A.; Ledoux, I.; Musumarra, G. Synthesis and NLO Properties of New *Trans*2–(Thiophen–2–Y1) Vinyl Heteroaromatic Iodides. *Org. Biomol. Chem.* **2011**, *9*, 1608–1613.
- (56) Fortuna, C. G.; Barresi, V.; Bonaccorso, C.; Consiglio, G.; Failla, S.; Trovato–Salinaro, A.; Musumarra, G. Design, Synthesis and *In Vitro* Antitumour Activity of New Heteroaryl Ethylenes. *European Journal of Medicinal Chemistry* **2012**, *47*, 221–227.
- (57) Birks, J. B. *Photophysics of Aromatic Molecules*, Wiley–Interscience, London, **1970**, p.123.
- (58) Romani, A.; Elisei, F.; Masetti, F.; Favaro, G. pH–Induced Effects on the Photophysics of Dipyrindyl Ketones. *J. Chem. Soc., Faraday Trans.* **1992**, *88*, 2147–2154.
- (59) Carmichael, I.; Hug, G. L. Triplet–Triplet Absorption Spectra of Organic Molecules in Condensed Phases. *J. Phys. Chem. Ref. Data* **1986**, *15*, 1–204.
- (60) Barbafina, A.; Latterini, L.; Carlotti, B.; Elisei, F. Characterization of Excited States of Quinones and Identification of Their Deactivation Pathways. *J. Phys. Chem. A* **2010**, *114*, 5980–5984.
- (61) Del Giacco, T.; Carlotti, B.; De Solis, S.; Barbafina, A.; Elisei, F. Photophysics of Aromatic Thiourea Derivatives and Their Complexes with Anions. Fast and Ultrafast Spectroscopic Investigations. *Phys. Chem. Chem. Phys.* **2010**, *12*, 8062–8071.

- (62) Cesaretti, A.; Carlotti, B.; Gentili, P. L.; Clementi, C.; Germani, R.; Elisei, F. Spectroscopic Investigation of the pH Controlled Inclusion of Doxycycline and Oxytetracycline Antibiotics in Cationic Micelles and Their Magnesium Driven Release. *J. Phys. Chem. B* **2014**, *118*, 8601–8613.
- (63) van Stokkum, I. H. M.; Larsen, D. S.; van Grondelle, R. Global and Target Analysis of Time-Resolved Spectra. *Biochim. Biophys. Acta* **2004**, *1657*, 82–104.
- (64) Snellenburg, J. J.; Laptенок, S.; Seger, R.; Mullen, K. M.; van Stokkum, I. H. M. Glotaran: A Java-Based Graphical User Interface for the R Package TIMP. *J. Stat. Soft.* **2012**, *49*, 1–23.
- (65) Frisch, M. J.; Trucks, G. W.; Schlegel, H. B.; Scuseria, G. E.; Robb, M. A.; Cheeseman, J. R.; Scalmani, G.; Barone, V.; Mennucci, B.; Petersson, G. A. et al. Gaussian 09, Revision B.01, Gaussian, Inc., Wallingford CT, **2010**.
- (66) Becke, A. D. Density-Functional Thermochemistry. III. The Role of Exact Exchange. *J. Chem. Phys.* **1993**, *98*, 5648–5652.
- (67) Barone, V.; Cossi, M. Quantum Calculation of Molecular Energies and Energy Gradients in Solution by a Conductor Solvent Model. *J. Phys. Chem. A* **1998**, *102*, 1995–2001.
- (68) Keith, T.A. AIMAll (Version 16.08.17), TK Gristmill Software, Overland Park KS, USA, **2016** (aim.tkgristmill.com).
- (69) Makarov, N. S.; Drobizhev, M.; Rebane, A. Two-Photon Absorption Standards in the 550–1600 nm Excitation Wavelength Range. *Optics Express* **2008**, *16*, 4029–4047.
- (70) Aidas, K.; Angeli, C.; Bak, K. L.; Bakken, V.; Bast, R.; Boman, L.; Christiansen, O.; Cimiraglia, R.; Coriani, S.; Dahle, P. et al. The Dalton Quantum Chemistry Program System. *Comput. Mol. Sci.* **2014**, 269–284.
- (71) Dalton, a Molecular Electronic Structure Program, Release Dalton2016.1, **2016**, see <http://daltonprogram.org>.
- (72) Monson, P.R.; McClain, W.M. Polarization Dependence of the Two-Photon Absorption of Tumbling Molecules with Application to Liquid 1-Chloronaphthalene and Benzene. *J. Chem. Phys.* **1970**, *53*, 29–37.
- (73) McClain, W.M. Excited State Symmetry Assignment Through Polarized Two-Photon Absorption Studies of Fluids. *J. Chem. Phys.*, **1971**, *55*, 2789–2796.
- (74) Murugan, N. A.; Kongsted, J.; Rinkevicius, Z.; Aidas, K.; Mikkelsen, K. V.; Ågren, H. Hybrid Density Functional Theory/Molecular Mechanics Calculations of Two-Photon Absorption of Dimethylamino Nitro Stilbene in Solution. *Phys. Chem. Chem. Phys.* **2011**, *13*, 12506–12516.
- (75) Zhang, C. L.; Wang, D. Y. Nonlinear Dependence of Solvent Polarity Effects on Twisted Intramolecular Charge-Transfer States and Linear Relation for Electronic Spectra in a Stilbazolium-Like Dye. *J. Photochem. Photobiol. A: Chem.* **2002**, *147*, 93–101.

- (76) Pascal, S.; Haeefe, A.; Monnereau, C.; Charaf-Eddin, A.; Jacquemin, D.; Le Guennic, B.; Andraud, C.; Maury, O. Expanding the Polymethine Paradigm: Evidence for the Contribution of a Bis-Dipolar Electronic Structure. *J. Phys. Chem. A* **2014**, *118*, 4038–4047.
- (77) Ghoneim, N.; Suppan, P. Solvatochromic Shifts of Non-Dipolar Molecules in Polar Solvents. *Spectrochim. Acta*, **1995** *51A*, 1043–1050.
- (78) Grabowski, Z. R.; Rotkiewicz, K.; Rettig, W. Structural Changes Accompanying Intramolecular Electron Transfer: Focus on Twisted Intramolecular Charge-Transfer States and Structures. *Chem. Rev.* **2003**, *103*, 3899–4032.
- (79) Görner, H. Charge Transfer Fluorescence of trans-Styrylpyridinium Iodides. *J. Photochem. Photobiol. A: Chem.* **2011**, *218*, 199–203.
- (80) Carlotti, B.; Benassi, E.; Barone, V.; Consiglio, G.; Elisei, F.; Mazzoli, A.; Spalletti, A. Effect of the π Bridge and Acceptor on Intramolecular Charge Transfer in Push-Pull Cationic Chromophores: An Ultrafast Spectroscopic and TD-DFT Computational Study. *ChemPhysChem* **2015**, *16*, 1440–1450.
- (81) Daudel, R.; Lefebvre, R.; Moser, C. Quantum Chemistry. Methods and Applications, Interscience Publishers Inc., New York, **1959**, Cap. IX.
- (82) E. Benassi, B. Carlotti, M. Segado, A. Cesaretti, A. Spalletti, F. Elisei and V. Barone, “Presence of Two Emissive Minima in the Lowest Excited State of a Push-Pull Cationic Dye Unequivocally Proved by Femtosecond Up-Conversion Spectroscopy and Vibronic Quantum-Mechanical Computations”, *J. Phys. Chem. B*, 2015, **119** (19), 6035–6040.
- (83) Bartocci, G.; Spalletti, A.; Becker, R. S.; Elisei, F.; Floridi, S.; Mazzucato, U. Excited-State Behavior of Some *All-Trans- α,ω -Dithienylpolyenes*. *J. Am. Chem. Soc.* **1999**, *121*, 1065–1075.
- (84) Horng, M. L.; Gardecki, J. A.; Papazyan, A.; Maroncelli, M. Subpicosecond Measurements of Polar Solvation Dynamics: Coumarin 153 Revisited. *J. Phys. Chem.* **1995**, *99*, 17311–17337.
- (85) Bhaskar, A.; Ramakrishna, G.; Lu, Z.; Twieg, R.; Hales, J. M.; Hagan, D. J.; Van Stryland, E.; Goodson III, T. Investigation of Two-Photon Absorption Properties in Branched Alkene and Alkyne Chromophores. *J. Am. Chem. Soc.* **2006**, *128*, 11840–11849.
- (86) Wang, H.; Zhang, H.; Rettig, W.; Tolmachev, A. I.; Glasbeek, M. Femtosecond Dynamics of the S_2 And S_1 Fluorescence of Ionic Styryl Dyes in Polar Solvents. *Phys. Chem. Chem. Phys.* **2004**, *6*, 3437–3446.
- (87) Xu, C.; Webb, W. W. Measurement of Two-Photon Excitation Cross Sections of Molecular Fluorophores with Data From 690 to 1050 nm. *J. Opt. Soc. Am. B.* **1996**, *13*, 481–491.
- (88) Abbotto, A.; Beverina, L.; Bozio, R.; Facchetti, A.; Ferrante, C.; Pagani, G. A.; Pedron, D.; Signorini, R. Novel heteroaromatic-based multi-branched dyes with enhanced two-photon absorption activity. *Chem. Commun.* **2003**, 2144–2145.

- (89) Strehmel, B.; Sarker, A. M.; Detert, H. The Influence of σ and π Acceptors on Two-Photon Absorption and Solvatochromism of Dipolar and Quadrupolar Unsaturated Organic Compounds. *ChemPhysChem* **2003**, *4*, 249–259.
- (90) Adegoke, O. O.; Jung, I. H.; Orr, M.; Yu, L.; Goodson III, T. Effect of Acceptor Strength on Optical and Electronic Properties in Conjugated Polymers for Solar Applications. *J. Am. Chem. Soc.* **2015**, *137*, 5759–5769.
- (91) Varnavski, O.; Goodson III, T. Ultrafast Exciton Dynamics in a Branched Molecule Investigated by Time-Resolved Fluorescence, Transient Absorption, and Three-Pulse Photon Echo Peak Shift Measurements. *J. Phys. Chem. B* **2004**, *108*, 10484–10492.

Appendix C. Two Photon Absorption Study of Low-Bandgap, Fully Conjugated Perylene Diimide Thienoacene Perylene Diimide Ladder-Type Molecules

I conducted femtosecond fluorescence upconversion experiments in order to investigate fluorescence decay dynamics of ladder-type molecules. This was in collaboration with the Yu group.

The work in this chapter was accepted in Chemistry Materials (Chem. Mater.) with the title:

“Two Photon Absorption Study of Low-Bandgap, Fully Conjugated Perylene Diimide Thienoacene Perylene Diimide Ladder-Type Molecules”

Zhengxu Cai, Ricardo J Vázquez, Donglin Zhao, Lianwei Li, Wai-yip Lo, Na Zhang, Qinghe Wu, Bradley Keller, Audrey Eshun, Neranga Abeyasinghe, Halley Banaszak-Holl, Theodore Goodson, III, and Luping Yu

Modifications were made to the manuscript to adapt it to the style of this dissertation.

References and supporting information of the manuscript are included in this chapter.

C.1 Abstract

A new series of donor-acceptor ladder-type molecules were synthesized via Scholl reaction. These molecules contain up to 25-fused rings but still show good air stability and good solubility. We found that the ring-fusing reaction is sensitive to the nature of the side-chain in donor units. The molecular conformations were investigated by 2D NMR and DFT calculations. The photo-physical properties were investigated and an intense intramolecular charge-transfer was observed. All of the molecules exhibited two-photon absorption (TPA) activity and their

TPA cross-section shows a linear relationship with increasing conjugation length of the thienoacene-PDI derivatives.

C.2 Introduction

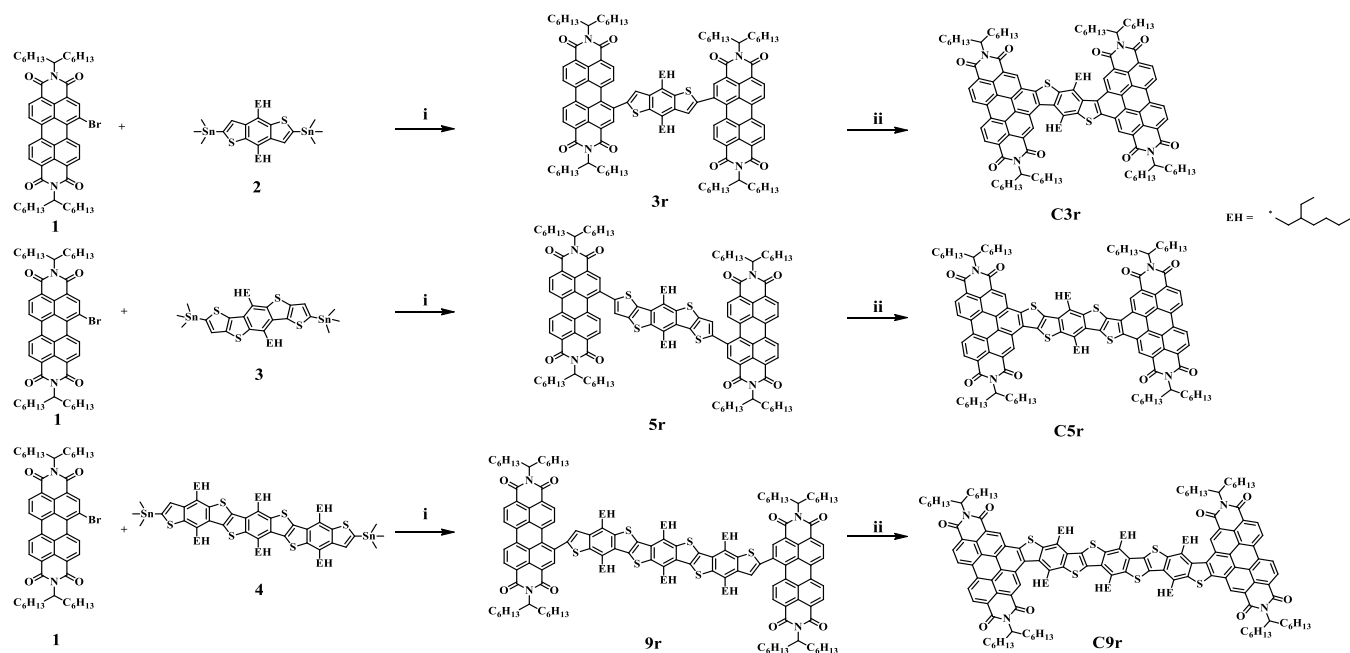
The nature of excited states in organic molecules is what determines their numerous optical properties such as energy transfer, electron transfer, light emission, photovoltaic effect, two-photon absorption (TPA), singlet fission, and so on.¹⁻⁶ However, rational design of organic materials to achieve an excited state with tailored optical properties is still a significant challenge.^{7,8} The control in the degree of electron delocalization on π -orbitals is an effective approach to the modification of physical and optical properties of organic conjugated molecules.^{9,10} In the past few decades, ladder-type materials have been continuously investigated for their potential applications in organic electronics.¹¹⁻¹³ Different types of structures have been developed, ranging from all hydrocarbon polyacenes to systems containing heterocyclic aromatic rings.^{14,15} In the past years, different polyacenes have been reported, but their stability, solubility, and processability are major issues that prevent them from extensive exploration for applications.^{16,17} Recently, we reported a novel method to synthesize conjugated heteroacenes with excellent solubility in organic solvents due to the side chain modification. These molecules were investigated via nonlinear optical techniques and were shown to exhibit a sizable TPA cross-section.¹⁸⁻²⁰ However, these materials are rather electron-rich and can be slowly oxidized due to high HOMO energy level caused by fused thienyl units. The TPA cross-section was only moderate because of their rather uniform structures that lack functionality necessary for enhanced optical nonlinearity.²¹ In order to address these issues, we designed new molecules that incorporated an electron withdrawing unit to the heteroacene cores. Recent studies also suggest that the intra- and intermolecular interactions of the donor and acceptor moieties can modulate

the excited state properties.²²⁻²⁵ The D–A ladder-type structures lock the π systems into a planar conformation that minimizes the bond twisting observed in linear conjugated structures, which can offer an effective way to improve properties.²⁶⁻³² In this paper, we report the synthesis, characterization, electrochemical, and photophysical properties of these new ladder-type oligomers. The compounds consisted of thienoacene derivatives (D_n) as the donor and perylene diimide (PDI) as the acceptor. The PDI motif was introduced in order to further extend the conjugation, stabilize the molecular structures due to its strong electron withdrawing property, and modulate the optical and electronic properties. 2D NMR measurements and density functional theory (DFT) calculation were used to investigate molecular structure and conformation and the relationship between the structure and optical/electrical properties.

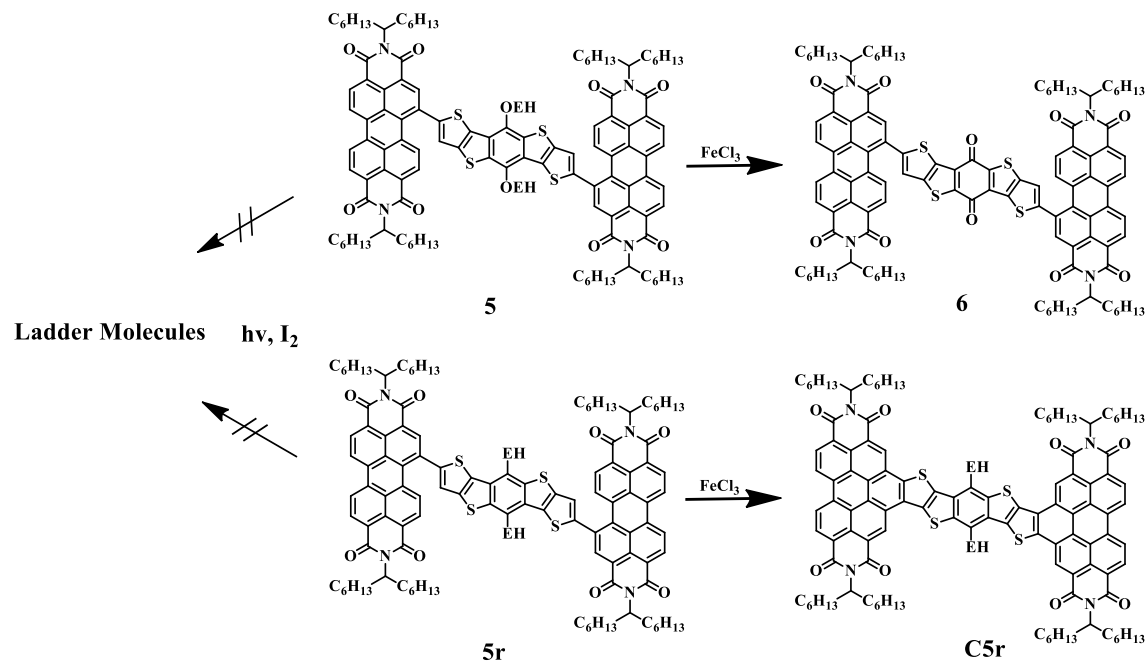
C.3 Results and discussion

C.3.1 Synthesis and characterization of the ladder-type molecules

A strategy was developed to synthesize the compounds (**Scheme C.3.1**). First, the Stille coupling reaction was used to connect the heteroacenes derivative with the PDI units. Photochemical reaction was attempted to form the cyclized product and failed. It was found that Scholl reaction using ferric chloride can efficiently cyclize the heteroacenes derivatives with the PDI units. The desired annulated compounds were obtained in high yields (>90%), if the side chain was an alkyl group (**Scheme C.3.2**). Quinonoidal structure was formed with the same ring fusing method for the compounds with alkoxy substituent (**Scheme C.3.2**).³³ It was noted that the electron rich substituent favors oxidative cyclodehydrogenation.³⁴⁻³⁵ Thus, the successful cyclodehydrogenation of these fused-ring compounds with electron deficient PDI to the desired product is an attractive outcome.



Scheme C.3.1. Synthetic route of fused ring molecules. (i) Pd₂(dba)₃, P(o-MePh)₃; (ii) FeCl₃.



Scheme C.3.2. Synthetic strategies of conjugated molecules.

NMR spectroscopic techniques were used to elucidate the molecular conformations of the resulting compounds. Both 1D and 2D NMR experiments were carried out for the non-fused

systems for the sake of comparison and elucidation of the fully conjugated materials. It was found that the non-fused ring compounds (3r, 5r and 9r in **Scheme C.3.1**) shows similar chemical shifts in the aryl region (**Figure C.3.1**). The proton signal in benzodithiophene unit (e in **Figure C.3.1**) and aryl gulf-facing protons (b) disappeared for the fused ring compounds, while the other four gulf-facing protons (a and c) in PDI were down-shifted to ~10 ppm.²⁶⁻²⁸ All aryl protons in C3r and C9r experience a diatropic shift to low field after cyclization. The chemical shifts of proton peaks d in C5r showed only a minor change compared with the uncyclized version. NOESY spectra of C3r and C5r were obtained to explain these differences (C9r showed strong tendency to form aggregation and a very weak 2D NMR signal). We found that the NOESY spectra of C3r showed the Nuclear Overhauser Effect (NOE) between the CH₂ in 2-ethylhexyl group (proton f) and proton a in the PDI core (**Figure S4**), indicating that two proton nuclei are spatially close. A strong steric hindrance between the alkyl chains in benzodithiophene (BDT) and the PDI cores causes twisted conformation for the C3r molecule and the PDI moiety. The lateral hydrogen (proton d) in PDI thus shifted to low field, as observed in other twisted structures.^{26,28,35} The C5r molecule showed only the cross peaks in that region in NOESY spectrum (**Figure S4**), indicating the lack of sterically hindered interaction in the molecule. As shown by density functional theory calculation, the molecule is highly planar, so the and lateral hydrogen (proton d) and in PDI exhibited minimum change after cyclization, with a dihedral angle of only 2.0° (**Table C.3.1**).

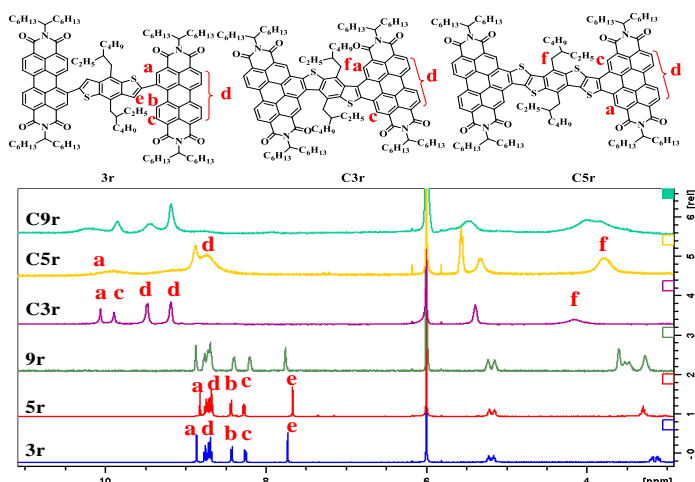


Figure C.3.1. NMR spectra of fused and non-fused compounds.

Density functional theory (DFT) calculations offer further confirmation that the fused ring compounds C3r and C9r are twisted because the strong steric hindrance between the alkyl chain in heteroacenes and PDI core. These results are in consistency with the NMR result discussed above. A pictorial presentation of molecular structures and the LUMO and HOMO are shown in Figure S5 and S6, respectively. The resulting energy levels are summarized in **Table C.3.1**. It was found that the HOMO orbitals are mainly localized on thienoacene parts, while the LUMO orbitals are localized on the PDI units (**Figure S6**). Both the HOMO and LUMO orbital, to some degree, extend to the whole molecules in the fused ring system due to ring-fusing effect.

	HOMO ^a (eV)	LUMO ^a (eV)	Bandgap ^b (opt ^b /cv ^a /cal ^c)	Dihedral ^d	QY. (%)	τ_1 (ps)	τ_2 (ps)	TPA (GM)	
								440-460 nm	700-720 nm
C3r	-5.90	-3.84	2.03/2.06/2.48	23.9°	13.5	18.5	n/a ^e	0.02	1.2
C5r	-5.69	-3.82	1.86/1.87/2.22	2.0°	5.0	3.3	121.8	0.08	29.8
C9r	-5.51	-3.78	1.77/1.73/2.02	28.6°	0.2	0.9	9.5	6.04	124.6

^a Energy levels were calculated based on the respective onset oxidation and reduction potentials of the ladder molecules with the following equations: LUMO = $-(E_{\text{onset red}} - E_{\text{onset Fc}} + 4.8)$ eV, HOMO = $-(E_{\text{onset ox}} - E_{\text{onset Fc}} + 4.8)$ eV, Ferrocene (Fc) was used as inner reference which the HOMO energy level was considered as -4.8 eV; ^b Based on the absorption spectra data; ^c Based on DFT calculations ^dDihedral angles between the PDI plane and adjacent thienoacene parts based on DFT calculations; ^e

C3r shows mono-exponential decay behavior with an energy rising time of 120 fs.

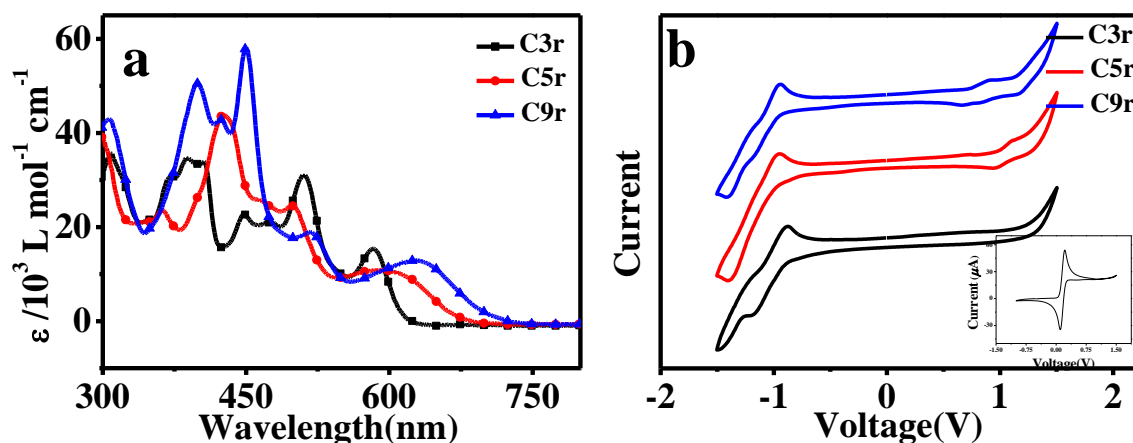


Figure C.3.1.2. (a) Absorption spectra of ladder molecules; (b) CV of ladder molecules in CHCl₃.

C.3.2 Optical and electrical properties of the ladder type molecules

The absorption spectra of all molecules were shown in **Figure C.3.1.2a**. As expected, the molar extinction coefficient increased as the conjugation of the BDT derivative units increased in the region of 300-450 nm (**Figure S8a**). The peaks around 525 nm attributed to the PDI unit gradually became weaker as the conjugation length increased. The absorption peak at 600-650 nm range was attributed to the charge transfer state between thienoacenes and PDI units. The spectra of the fused ring series in this region exhibit higher intensity than the non-fused system, suggesting a stronger intramolecular charge transfer in fused ring compounds (**Figure. S7c**).^{35, 36} Both the HOMO and LUMO energy levels were determined by cyclic voltammetry (vs. Fc/Fc+) (**Figure. C.3.1.2b**), and the HOMO energy levels show an increase and LUMO a slightly increase as the donor length increase because the large conjugation enhances the electron donating abilities, resulting in narrowed bandgaps. All these trends are in agreement with those obtained from theoretical calculation and optical measurements.

The emission spectra of three ladder molecules were shown in **Figure C.3.2a**, in which some of the emission peaks observed in thienoacenes and PDI were retained (**Figure S8b**). A marked difference is that both the C3r and C9r showed emission peaks between 450 nm to 550 nm, while C5r showed no emission in that region. These emissions observed from the thienoacene and PDI unit can be attributed to the twisted structures of the C3r and C9r and C3r and C5r molecules retain the localized emission peaks observed in PDI. The main emission peaks are red-shifted when the length of the thienoacene cores is extended. The emission peaks at 600-700 nm are new and not observed in the emission spectra of thienoacenes alone nor in the emission spectra of the PDI monomer (**Figure S8b**). Thus, the fluorescence decay dynamics at 600 nm can be attributed to the electronically coupled PDI and thienoacene charge transfer state.

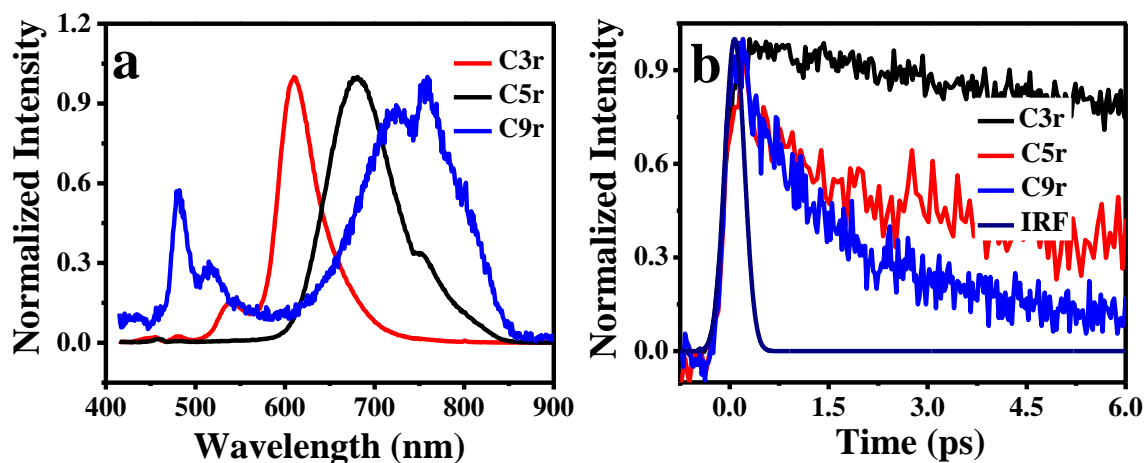


Figure C.3.2. (a) Emission spectra of ladder molecules; (b) Fluorescence decay dynamic of ladder molecules at ~ 600 nm emission.

In order to investigate this effect of extending the conjugation length of the thienoacene core on the fluorescence decay dynamics, studies in time-resolved fluorescence up-conversion was carried out.³⁷⁻³⁹ The dynamics of the C3r exhibited a rise time (**Figure S9**) of 120 fs before a slower relaxation of the fluorescence at 18.5 ps, suggesting energy transfer from the BDT core to the charge transfer state.⁴⁰ Interestingly, the C3r molecule demonstrates the longest-lived mono-

exponential emission (t_1) while the lifetimes are gradually decreased (**Table C.3.1**) with increasing of the conjugation length. The C5r shows a very long lifetime, t_2 (**Table C.3.1**). This can be attributed to the increased conjugation length and planar structure in the C5r system, which will make the excited state more delocalized, thus increasing the t_2 lifetime.⁴¹ From C3r to C9r, the conjugation length is increased, allowing an expanding excitation. From C3r to C9r, the conjugation length is increased, allowing the excitation delocalization to occur throughout the molecular system. This opens up many possible non-radiative relaxation channels causing the quantum yield to gradually drop as the conjugation length is increased. The charge transfer from the thienoacene core to the PDI core may quench the fluorescence of the molecule as the electron donating abilities increase.⁴² The trend in the lifetimes is consistent with the observed trend in the quantum yield values for the three fused ring systems with the quantum yield of the C3r being 13.5% and that of C9r approaching <0.2% (**Table C.3.1**).

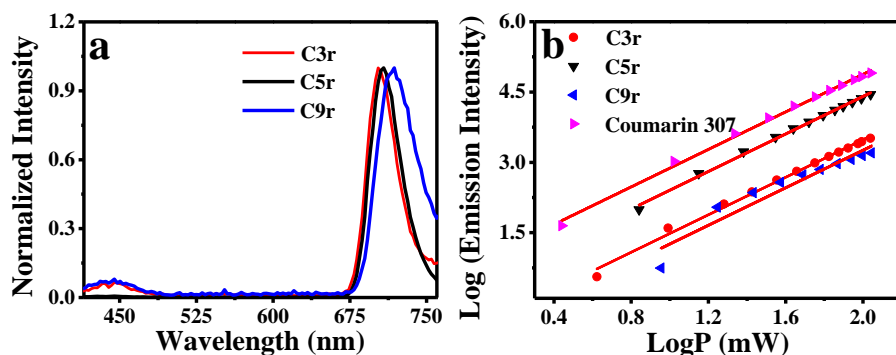


Figure C.3.3. (a) Two photon emission spectra of ladder molecules; (b) Power dependence of the two-photon-excited emission of ladder molecules at ~ 720 nm.

Efficient charge delocalization and charge transfer due to increase in conjugation have been previously documented and can be investigated using the TPA technique.⁴³ Specifically, a proportional relationship between the TPA cross-section and increasing the conjugation length (π -orbitals) of the thienoacenes core has been reported.¹⁸ However, the TPA properties will

significantly be changed in these molecules with electron deficient PDI units fused. The minor 440-460 nm two-photon emission band is attributed to the respective emissive relaxation process from the thienoacenes core while the 700-720 nm two photon emission is attributed to the thienoacene-PDI charge transfer state. As expected, the compounds showed an enhancement in the TPA cross-section proportional to the length of the thienoacene-PDI cores (**Table C.3.1**). It has been also documented that a TPA cross-section enhancement can be achieved by the incorporation of an electron withdrawing groups such as a trivalent boron group.⁴⁴⁻⁴⁵ The data suggest that both the extension in the conjugation length of the thienoacene and the addition of an electron withdrawing group can enhance the TPA cross-section. However, it is clear that enhancing the delocalization in the thienoacene units exhibited more profound effect in the TPA cross-section than merely adding the acceptor unit. The TPA cross-section is strongly associated with the charge transfer character of the material.¹⁸ A large internal polarization of a molecule suggest a better optical nonlinearity, thus larger TPA effect.

C.4 Conclusions

A series of A-D-A conjugated molecules based on heteroacenes were designed, synthesized, and characterized. To avoid dealkylation/oxidation reaction, the Scholl reaction using ferric chloride as oxidant was used to the synthesis of annulated compounds. Optical and electrochemical characterization of these ladder-type molecules indicated intramolecular charge transfer states between the donor and the acceptor units, which was corroborated with the ultra-fast optical measurements. All of the materials exhibited good TPA activity. The results indicate that the ladder type A-D-A structures can enhance the TPA cross-section of the heteroacene derivatives. These molecules are of interest for further exploration in electrical and optical

properties, such as their applications in photovoltaic devices due to their internal charge transfer properties.

C.5 Experimental Section

C.5.1 Materials and Characterization Techniques

All of the chemicals were purchased from Aldrich. All reagents purchased commercially were used without further purification except for toluene and tetrahydrofuran (THF), which were dried over sodium/benzophenone. ¹H NMR and ¹³C NMR spectra were recorded on a Bruker DRX-400 spectrometer and Bruker DRX-500 spectrometer with tetramethylsilane as an internal reference. High Resolution MALDI-TOF spectra were recorded on Bruker Solarix 9.4T. Compound 2-4 (Scheme S1) were synthesized according to the procedures developed in our lab¹⁸⁻²⁰.

Synthesis of Compound 3r: To a round-bottom flask equipped with a condenser was added 1 (530 mg, 0.64 mmol), 2 (215 mg, 0.29 mmol), Pd₂(dba)₃ (26 mg, 0.03 mmol) and P(o-MePh)₃ (43 mg, 0.12 mmol). The system was evacuated and refilled with N₂ three times, then charged with toluene (50 ml). The reaction mixture was refluxed under N₂ for 16 hours. After cooling to room temperature, the reaction mixture was concentrated under reduced pressure. The residue was purified by column chromatography with hexane and CH₂Cl₂ (1:1, v/v) as the eluent.

Compound 3r was obtained as a red solid (422 mg, 75.8% yield). ¹H NMR (CD₂Cl₂ 353K ppm): δ 8.86 (s, 2H), 8.77-8.67 (m, 8H), 8.42 (d, J = 10, 2H), 8.25 (d, J = 10, 2H), 7.72 (s, 2H), 5.24-5.15 (m, 4H), 3.22-3.09 (m 4H), 2.30-2.22 (m, 8H), 2.01-1.92 (m, 10H), 1.40-1.28 (m, 80H), 0.92-0.86 (m, 30H), 0.77 (t, J = 7.5, 6H). ¹³C NMR (CDCl₃, ppm): δ 164.7, 164.3, 163.7, 163.5, 144.4, 139.5, 139.01, 139.4, 137.9, 137.8, 136.9, 136.1, 135.0, 134.2, 131.8, 131.5, 131.1, 130.8, 130.1, 130.0, 129.2, 129.1, 128.1, 127.5, 124.1, 123.7, 123.4, 123.0, 122.7, 122.2, 122.0,

54.9, 54.7, 40.3, 38.4, 32.4, 31.8, 31.8, 29.3, 29.2, 28.8, 27.0, 26.9, 23.0, 22.6, 22.6, 14.1, 14.1, 14.0, 11.1. High Resolution MALDI-TOF: calcd for [C₁₂₆H₁₅₈N₄O₈S₂]-, 1919.15266, found, 1919.15098. Elemental analysis: calcd. for C₁₂₆H₁₅₈N₄O₈S₂: C, 78.79; H, 8.29, N, 2.92, S, 3.34; found: C, 78.66; H, 8.38, N, 2.97, S, 3.14.

Synthesis of Compound 5r: To a round-bottom flask equipped with a condenser was added 1 (462 mg, 0.55 mmol), 3 (215 mg, 0.25 mmol), Pd₂(dba)₃ (26 mg, 0.03 mmol) and P(o-MePh)₃ (43 mg, 0.12 mmol). The system was evacuated and refilled with N₂ three times, then charged with toluene (40 ml). The reaction mixture was refluxed under N₂ for 16 hours. After cooling to room temperature, the reaction mixture was concentrated under reduced pressure. The residue was purified by column chromatography with hexane and CH₂Cl₂ (1:1, v/v) as the eluent.

Compound 5r was obtained as a red solid (403 mg, 78.4% yield). ¹H NMR (CD₂Cl₂ 353K ppm): δ 8.82 (s, 2H), 8.76-8.66 (m, 8H), 8.43 (d, J = 8.5, 2H), 8.27 (d, J = 8.5, 2H), 7.67 (s, 2H), 5.22 (m, 2H), 5.15 (m, 2H), 3.30 (m, 4H), 2.31-2.22 (m, 10H), 1.97-1.90 (m, 8H), 1.50-1.20 (m, 80H), 0.92-0.87 (m, 30H), 0.76 (t, J = 11, 6H). ¹³C NMR (CDCl₃, ppm): δ 164.7, 164.5, 163.6, 163.3, 147.0, 141.8, 139.0, 137.1, 136.3, 135.1, 135.0, 134.1, 133.8, 133.1, 131.8, 131.5, 130.8, 130.1, 129.9, 129.1, 129.0, 128.7, 127.5, 124.1, 123.7, 123.4, 122.9, 122.7, 122.3, 119.9, 54.9, 54.7, 39.1, 39.0, 32.8, 32.4, 31.8, 31.8, 29.7, 29.2, 28.7, 27.0, 23.0, 22.6, 22.6, 14.1, 14.0, 13.9, 11.2. High Resolution MALDI-TOF: calcd for [C₁₃₀H₁₅₈N₄O₈S₄]-, 2031.09680, found, 2031.09616. Elemental analysis: calcd. for C₁₃₀H₁₅₈N₄O₈S₄: C, 76.81, H, 7.83, N, 2.76, S, 6.31; found: C, 77.00; H, 7.90, N, 2.80, S, 6.13.

Synthesis of Compound 9r: To a round-bottom flask equipped with a condenser was added 1 (240 mg, 0.29 mmol), 4 (198 mg, 0.13 mmol), Pd₂(dba)₃ (12 mg, 0.01 mmol) and P(o-MePh)₃ (14 mg, 0.04 mmol). The system was evacuated and refilled with N₂ three times, then charged

with toluene (40 ml). The reaction mixture was refluxed under N₂ for 16 hours. After cooling to room temperature, the reaction mixture was concentrated under reduced pressure. The residue was purified by column chromatography with hexane and CH₂Cl₂ (1:1, v/v) as the eluent.

Compound 9r was obtained as a solid (323 mg, 91.7% yield). ¹H NMR (CDCl₃ ppm): δ 8.87 (s, 2H), 8.72 (m, 8H), 8.39 (s, 2H), 8.20 (d, J = 7.5, 2H), 7.76 (s, 2H), 5.23 (s, 2H), 5.15 (s, 2H), 3.60-3.27 (m, 12H), 2.47 (s, 2H), 2.38 (s, 2H), 2.30 (s, 4H), 2.24 (s, 4H), 2.13 (s, 2H), 1.98 (s, 4H), 1.90 (s, 4H), 1.73-1.33 (m, 108H), 1.08-0.89 (m, 64H). ¹³C NMR (CDCl₃, ppm): δ 164.7, 163.7, 144.0, 142.1, 141.5, 140.1, 137.6, 136.8, 136.1, 135.0, 134.0, 133.8, 132.3, 131.8, 130.6, 130.3, 129.9, 129.1, 128.8, 128.5, 128.1, 127.3, 123.7, 123.4, 122.9, 122.0, 54.9, 54.7, 40.1, 39.8, 39.4, 38.8, 37.9, 31.8, 29.2, 27.0, 23.2, 22.6, 22.6, 14.1, 14.1, 11.2, 11.0. High Resolution MALDI-TOF: calcd for [C₁₇₄H₂₂₆N₄O₈S₆]⁺, 2091.57195, found, 2091.57202. Elemental analysis: calcd. for C₁₇₄H₂₂₆N₄O₈S₆: C, 77.57; H, 8.46, N, 2.08, S, 7.14; found: C, 77.72; H, 8.51, N, 2.09, S, 6.95.

Synthesis of Compound C3r: A solution of FeCl₃ (676 mg, 4.17 mmol) in 2 ml nitromethane was added dropwise to a stirred solution of compound 3r (400 mg, 0.21 mmol) in 10 ml CH₂Cl₂. The reaction was stirred with argon. After stirring for 10 h at room temperature, 1 ml methanol was added to the solution. The solvent was evaporated under reduced pressure, and the crude product was filtered with silica gel with a large amount of CHCl₃ to yield the solid product (367 mg, 92%). ¹H NMR (C₂D₂Cl₄, ppm, 353 K): δ 10.01 (s, 2H), 9.84 (s, 2H), 9.42 (s, 4H), 9.13 (s, 4H), 5.50 (s, 4H), 4.11 (s, 4H), 2.38 (s, 8H), 2.01 (br, 10H), 1.45-1.14 (m, 78H), 0.93-0.72 (m, 38H). ¹³C NMR (CDCl₃, ppm): δ 165.4, 164.1, 141.6, 140.1, 134.9, 133.7, 133.3, 131.9, 131.4, 129.4, 128.7, 127.7, 126.6, 125.7, 124.6, 124.4, 123.5, 122.9, 122.3, 122.0, 55.1, 39.6, 39.1, 32.6, 32.2, 31.8, 29.7, 29.3, 27.1, 22.6, 14.1, 10.8. High Resolution MALDI-TOF: calcd for

[C₁₂₆H₁₅₄N₄O₈S₂]⁺, 1915.12026, found, 1915.12064. Elemental analysis: calcd. for C₁₂₆H₁₅₄N₄O₈S₂: C, 78.95; H, 8.10, N, 2.92, S, 3.35; found: C, 78.65; H, 8.11, N, 2.95, S, 3.51. Elemental analysis: calcd. for C₁₃₀H₁₅₄N₄O₈S₄: C, 76.96, H, 7.65, N, 2.76, S, 6.32; found: C, 77.12; H, 7.73, N, 2.80, S, 6.46.

Synthesis of Compound C5r: A solution of FeCl₃ (319 mg, 1.97 mmol) in 2 ml nitromethane was added dropwise to a stirred solution of compound 5r (200 mg, 0.10 mmol) in 8 ml CH₂Cl₂. The reaction was stirred with argon. After stirring for 10 h at room temperature, 1 ml methanol was added to the solution. The solvent was evaporated under reduced pressure, and the crude product was filtered with silica gel with a large amount of CHCl₃ to yield the solid product (180 mg, 90%). ¹H NMR (C₂D₂C₁₄ ppm, 353 K): δ 9.88 (s, 2H), 8.82-8.70 (br, 10H), 5.51 (s 2H), 5.32 (s 2H), 3.76 (s, 4H), 2.61-2.21 (m, 18H), 1.55-1.42 (m, 82H), 1.09-0.86 (m, 34H). ¹³C NMR (CDCl₃, ppm): δ 164.6, 163.6, 142.6, 141.6, 134.2, 134.0, 131.7, 129.7, 129.1, 128.8, 128.7, 128.5, 128.0, 126.7, 125.8, 124.8, 124.4, 123.7, 123.2, 122.7, 122.2, 121.1, 55.7, 33.4, 32.4, 32.3, 32.2, 31.9, 30.3, 30.1, 29.7, 29.3, 29.1, 27.7, 27.2, 23.1, 23.0, 22.6, 14.4, 14.1. High Resolution MALDI-TOF: calcd for [C₁₃₀H₁₅₄N₄O₈S₄]⁺, 2027.06440, found, 2027.06477. Elemental analysis: calcd. for C₁₃₀H₁₅₄N₄O₈S₄: C, 76.96, H, 7.65, N, 2.76, S, 6.32; found: C, 77.12; H, 7.73, N, 2.80, S, 6.46.

Synthesis of Compound C9r: A solution of FeCl₃ (240 mg, 1.48 mmol) in 2 ml nitromethane was added dropwise to a stirred solution of compound 9r (200 mg, 0.07 mmol) in 8 ml CH₂Cl₂. The reaction was stirred with argon. After stirring for 10 h at room temperature, 1 ml methanol was added to the solution. The solvent was evaporated under reduced pressure, and the crude product was filtered with silica gel with a large amount of CHCl₃ to yield the solid product (187 mg, 94%). ¹H NMR (C₂D₄C₁₄, 353K, ppm): δ 10.22 (br, 2H), 9.83 (s, 2H), 9.42 (s, 4H), 9.16 (s,

4H), 5.46 (s, 4H), 3.99 (br, 12H), 2.10 (br, 12H), 1.84 (br, 10H), 1.48-0.92 (m, 172H). ¹³C NMR (CDCl₃, ppm): δ 165.5, 164.4, 131.9, 131.5, 129.2, 128.0, 127.6, 126.7, 124.6, 123.5, 122.5, 121.9, 55.0, 39.6, 39.4, 32.6, 32.2, 32.0, 31.9, 29.7, 29.3, 27.4, 27.1, 22.8, 22.7, 14.2, 14.1. High Resolution MALDI-TOF: calcd for [C₁₇₄H₂₂₂N₄O₈S₆]⁺, 2687.54684, found, 2687.54150. Elemental analysis: calcd. for C₁₇₄H₂₂₂N₄O₈S₆: C, 77.69, H, 8.32, N, 2.08, S, 7.15; found: C, 76.67, H, 8.42, N, 2.05, S, 6.97.

ASSOCIATED CONTENT

Supporting Information. Structural information for the compounds, TGA and DSC measurements, NOESY and COSY NMR spectra, DFT calculation results, experimental details for the photo-physical studies. This material is available free of charge via the Internet at <http://pubs.acs.org>.

ACKNOWLEDGMENT

This work was mainly supported by NSF (DMR-1503852) and partially by NSF (DMR-1263006). This work also benefited from NSF MRSEC at the University of Chicago.

AUTHOR INFORMATION

Corresponding Author

lupingyu@uchicago.edu

tgoodson@umich.edu

AUTHOR CONTRIBUTIONS

Z. Cai and R. Vázquez contributed equally to this work

References

(1) Demchenko, A. P.; Tang, K.-C.; Chou, P.-T. Excited-state proton coupled charge transfer modulated by molecular structure and media polarization. *Chem. Soc. Rev.* 2013, 42, 1379-1408.

- (2) Ito, A.; Shimizu, A.; Kishida, N.; Kawanaka, Y.; Kosumi, D.; Hashimoto, H.; Teki, Y. Excited-state dynamics of pentacene derivatives with stable radical substituents. *Angew. Chem. Int. Ed.* 2014, 53, 6715-6719.
- (3) Goushi, K.; Yoshida, K.; Sato, K.; Adachi, C. Organic light-emitting diodes employing efficient reverse intersystem crossing for triplet-to-singlet state conversion. *Nat. Photon.* 2012, 6, 253-258.
- (4) Zhao, D.; Wu, Q.; Cai, Z.; Zheng, T.; Chen, W.; Lu, J.; Yu, L. Electron acceptors based on α -substituted perylene diimide (PDI) for organic solar cells. *Chem. Mater.* 2016, 28, 1139-1146.
- (5) Harpham, M. R.; Süzer, Ö.; Ma, C.-Q.; Bäuerle, P.; Goodson, T. Thiophene dendrimers as entangled photon sensor materials. *J. Am. Chem. Soc.* 2009, 131, 973-979.
- (6) Sanders, S. N.; Kumarasamy, E.; Pun, A. B.; Steigerwald, M. L.; Sfeir, M. Y.; Campos, L. M. Intramolecular singlet fission in oligoacene heterodimers. *Angew. Chem. Int. Ed.* 2016, 55, 3373-3377.
- (7) Rosenberg, M.; Dahlstrand, C.; Kilså, K.; Ottosson, H. Excited state aromaticity and antiaromaticity: opportunities for photophysical and photochemical rationalizations. *Chem. Rev.* 2014, 114, 5379-5425.
- (8) Würthner, F.; Saha-Möller, C. R.; Fimmel, B.; Ogi, S.; Leowanawat, P.; Schmidt, D. Perylene bisimide dye assemblies as archetype functional supramolecular materials. *Chem. Rev.* 2016, 116, 962-1052.
- (9) Kang, H.; Kim, G.; Kim, J.; Kwon, S.; Kim, H.; Lee, K. Bulk-heterojunction organic solar cells: five core technologies for their commercialization. *Adv. Mater.* 2016, 28, 7821-7861.
- (10) Wu, J.-S.; Cheng, S.-W.; Cheng, Y.-J.; Hsu, C.-S. Donor-acceptor conjugated polymers based on multifused ladder-type arenes for organic solar cells. *Chem. Soc. Rev.* 2015, 44, 1113-1154.
- (11) Liu, J.; Narita, A.; Osella, S.; Zhang, W.; Schollmeyer, D.; Beljonne, D.; Feng, X.; Müllen, K. Unexpected Scholl reaction of 6,7,13,14-tetraarylbenzo[k]tetraphene: selective formation of five-membered rings in polycyclic aromatic hydrocarbons. *J. Am. Chem. Soc.* 2016, 138, 2602-2608.
- (12) Ip, H.-W.; Ng, C.-F.; Chow, H.-F.; Kuck, D. Three-fold Scholl-type cycloheptatriene ring formation around a tribenzotriquinacene core: toward warped graphenes. *J. Am. Chem. Soc.* 2016, 138, 13778-13781.
- (13) Cai, Z.; Zhang, H.; Geng, H.; Liu, Z.; Yang, S.; Luo, H.; Jiang, L.; Peng, Q.; Zhang, G.; Chen, J.; Yi, Y.; Hu, W.; Zhang, D. Thiophene-fused heteroacenes: simple synthesis, unusual structure, and semiconductors with less anisotropic behavior. *Chem. Eur. J.* 2013, 19, 14573-14580.
- (14) Bunz, U. H. F. The larger linear N-heteroacenes. *Acc. Chem. Res.* 2015, 48, 1676-1686.
- (15) Stępień, M.; Gońka, E.; Żyła, M.; Sprutta, N. Heterocyclic nanographenes and other polycyclic heteroaromatic compounds: synthetic routes, properties, and applications. *Chem. Rev.* 2016, 117, 3479-3716.

- (16) Narita, A.; Wang, X.-Y.; Feng, X.; Müllen, K. New advances in nanographene chemistry. *Chem. Soc. Rev.* 2015, 44, 6616-6643.
- (17) Hammer, B. A. G.; Müllen, K. Dimensional evolution of polyphenylenes: expanding in all directions. *Chem. Rev.* 2016, 116, 2103-2140.
- (18) Zheng, T.; Cai, Z.; Ho-Wu, R.; Yau, S. H.; Shaparov, V.; Goodson, T.; Yu, L. Synthesis of ladder-type thienoacenes and their electronic and optical properties. *J. Am. Chem. Soc.* 2016, 138, 868-875.
- (19) Cai, Z.; Lo, W.-Y.; Zheng, T.; Li, L.; Zhang, N.; Hu, Y.; Yu, L. Exceptional single-molecule transport properties of ladder-type heteroacene molecular wires. *J. Am. Chem. Soc.* 2016, 138, 10630-10635.
- (20) Zheng, T.; Lu, L.; Jackson, N. E.; Lou, S. J.; Chen, L. X.; Yu, L. Roles of quinoidal character and regioregularity in determining the optoelectronic and photovoltaic properties of conjugated copolymers. *Macromolecules* 2014, 47, 6252-6259.
- (21) Usta, H.; Risko, C.; Wang, Z.; Huang, H.; Deliomeroglu, M. K.; Zhukhovitskiy, A.; Facchetti, A.; Marks, T. J. Design, synthesis, and characterization of ladder-type molecules and polymers. air-stable, solution-processable n-channel and ambipolar semiconductors for thin-film transistors via experiment and theory. *J. Am. Chem. Soc.* 2009, 131, 5586-5608.
- (22) Cai, Z.; Guo, Y.; Yang, S.; Peng, Q.; Luo, H.; Liu, Z.; Zhang, G.; Liu, Y.; Zhang, D. New donor-acceptor-donor molecules with Pechmann dye as the core moiety for solution-processed good-performance organic field-effect transistors. *Chem. Mater.* 2013, 25, 471-478.
- (23) Cai, Z.; Luo, H.; Chen, X.; Zhang, G.; Liu, Z.; Zhang, D. Extended conjugated donor-acceptor molecules with E-(1,2-difluorovinyl) and diketopyrrolopyrrole (DPP) moieties toward high-performance ambipolar organic semiconductors. *Chem. Asian J.* 2014, 9, 1068-1075.
- (24) Cai, Z.; Luo, H.; Qi, P.; Wang, J.; Zhang, G.; Liu, Z.; Zhang, D. Alternating conjugated electron donor-acceptor polymers entailing Pechmann dye framework as the electron acceptor moieties for high performance organic semiconductors with tunable characteristics. *Macromolecules* 2014, 47, 2899-2906.
- (25) Sekita, M.; Ballesteros, B.; Diederich, F.; Guldi, D. M.; Bottari, G.; Torres, T. Intense ground-state charge-transfer interactions in low-bandgap, panchromatic phthalocyanine-tetracyanobuta-1,3-diene conjugates. *Angew. Chem. Int. Ed.* 2016, 55, 5560-5564.
- (26) Zhong, Y.; Kumar, B.; Oh, S.; Trinh, M. T.; Wu, Y.; Elbert, K.; Li, P.; Zhu, X.; Xiao, S.; Ng, F.; Steigerwald, M. L.; Nuckolls, C. Helical ribbons for molecular electronics. *J. Am. Chem. Soc.* 2014, 136, 8122-8130.
- (27) Chiu, C.-Y.; Kim, B.; Gorodetsky, A. A.; Sattler, W.; Wei, S.; Sattler, A.; Steigerwald, M.; Nuckolls, C. Shape-shifting in contorted dibenzotetrathienocoronenes. *Chem. Sci.* 2011, 2, 1480-1486.
- (28) Nagarajan, K.; Mallia, A. R.; Muraleedharan, K.; Hari-haran, M. Enhanced intersystem crossing in core-twisted aromatics. *Chem. Sci.* 2017, 8, 1776-1782.
- (29) Yuan, Z.; Lee, S.-L.; Chen, L. Li, C.; Mali, K. S.; De Feyter, S.; Müllen, K. Processable rylene diimide dyes up to 4 nm in length: synthesis and STM visualization. *Chem. Eur. J.* 2013, 19, 11842-11846.

- (30) Yuan, Z.; Xiao, Y.; Yang, Y.; Xiong, T. Soluble ladder conjugated polymer composed of perylenediimides and thieno[3,2-b]thiophene (LCPT): a highly efficient synthesis via photocyclization with the sunlight. *Macromolecules* 2011, 44, 1788-1791.
- (31) Kass, K.-J.; Forster, M.; Scherf, U. Incorporating an alternating donor-acceptor structure into a ladder polymer backbone. *Angew.Chem. Int. Ed.* 2016, 55,7816-7820.
- (32) Lee, J.; Kalin, A. J.; Yuan, T.; Al-Hashimi, M.; Fang, L. Fully conjugated ladder polymers. *Chem. Sci.*, 2017, 8, 2503-2521. (33) Both the fused and non-fused structures were observed in the ring fusing process, the major product is non-fused ring product, details see supporting information.
- (34) Hilton, C. L.; Crowfoot, J. M.; Rempala, P.; King, B. T. 18,18'-Dihexyl[9,9']biphenanthro[9,10-b]triphenylene: construction and consequences of a profoundly hindered aryl-aryl single bond. *J. Am. Chem. Soc.* 2008, 130, 13392-13399.
- (35) Zhong, H.; Wu, C.-H.; Li, C.-Z.; Carpenter, J.; Chueh, C.-C.; Chen, J.-Y.; Ade, H.; Jen, A. K.-Y. Rigidifying non-planar perylene diimides by ring fusion toward geometry-tunable acceptors for high-performance fullerene-free solar cells. *Adv. Mater.* 2016, 28, 951-958.
- (36) Yu, Y. W.; Li, Y. J.; Qin, Z. H.; Jiang, R. S.; Liu, H. B.; Li, Y. L. Designed synthesis and supramolecular architectures of furan-substituted perylene diimide. *J. Colloid Interface Sci.* 2013, 399, 13-18.
- (37) Badaeva, E.; Harpham, M. R.; Guda, R.; Süzer, Ö.; Ma, C.-Q.; Bäuerle, P.; Goodson, T.; Tretiak, S. Excited-state structure of oligothiophene dendrimers: computational and experimental study. *J. Phys. Chem. B* 2010, 114, 15808-15817.
- (38) Furgal, J. C.; Jung, J. H.; Goodson, T.; Laine, R. M. Analyzing structure-photophysical property relationships for isolated T8, T10, and T12 stilbenevinylsilsequioxanes. *J. Am. Chem. Soc.* 2013, 135, 12259-12269.
- (39) Guo, M.; Yan, X.; Goodson, T. Electron mobility in a novel hyper-branched phthalocyanine dendrimer. *Adv. Mater.* 2008, 20, 4167-4171.
- (40) Yuan, M.; Durban, M. M.; Kazarinoff, P. D.; Zeigler, D. F.; Rice, A. H.; Segawa, Y.; Luscombe, C. K. Synthesis and characterization of fused-thiophene containing naphthalene diimide n-type copolymers for organic thin film transistor and all-polymer solar cell applications. *J. Polym. Sci., Part A: Polym. Chem.* 2013, 51, 4061-4069.
- (41) Ramakrishna, G.; Bhaskar, A.; Goodson, T. Ultrafast excited state relaxation dynamics of branched donor- π -acceptor chromophore: evidence of a charge-delocalized state. *J. Phys. Chem. B* 2006, 110, 20872-20878.
- (42) Irie, M.; Sakemura, K.; Okinaka, M.; Uchida, K. Photochromism of dithienylethenes with electron-donating substituents. *J. Org. Chem.* 1995, 60, 8305-8309.
- (43) Bhaskar, A.; Ramakrishna, G.; Lu, Z.; Twieg, R.; Hales, J. M.; Hagan, D. J.; Van Stryland, E.; Goodson, T. Investigation of two-photon absorption properties in branched alkene and alkyne chromophores. *J. Am. Chem. Soc.* 2006, 128, 11840-11849.
- (44) Alam, M. M.; Chattopadhyaya, M.; Chakrabarti, S.; Ruud, K. Chemical control of channel interference in two-photon absorption processes. *Acc. Chem. Res.* 2014, 47, 1604-1612.

(45) Guo, L.; Wong, M. S. Multiphoton excited fluorescent materials for frequency upconversion emission and fluorescent probes. *Adv. Mater.* 2014, 26, 5400-5428.

C.6 Supporting Information

C.6.1 Materials and Characterization Techniques

1.

Their DFT calculation were performed at the level of B3LYP /6-31G** by using Gaussian 09 in vacuum model. To facilitate the calculation, the heptylhexyl chains in PDI were replaced with a methyl group, while the ethylhexyl groups in heteroacenes were replaced by isobutyl to avoid missing the steric hindrance effect. Isovalue for printing the frontier molecular orbitals was 0.02. Thermogravimetric analysis (TGA) (SDT Q600 TGA/DSC) measurements were performed under a nitrogen atmosphere at a heating rate of 10 °C/min.

Cyclic voltammetry was used to study the electrochemical properties of these compounds. They were measured as 10^{-3} M solutions in anhydrous CHCl_3 containing 0.1 M Bu_4NPF_6 as the electrolyte with Pt as the working electrode, Ag/Ag^+ as the reference electrode, and a Pt wire as the contrast electrode at a scan rate of 50 mV/s. For calibration, the redox potential of ferrocene/ ferrocenium (Fc/Fc^+) was measured under the same conditions and it was located at 0.15 V vs Ag/Ag^+ . It was assumed that the redox potential of Fc/Fc^+ has an absolute energy level of -4.80 eV relative to vacuum. Energy levels were calculated based on the respective onset oxidation and reduction potentials of A-D-A molecules and their fused-ring compounds with the following equations: $\text{LUMO} = - (E_{\text{onset red}} - E_{\text{onset Fc}} + 4.8) \text{ eV}$, $\text{HOMO} = - (E_{\text{onset ox}} - E_{\text{onset Fc}} + 4.8) \text{ eV}$.

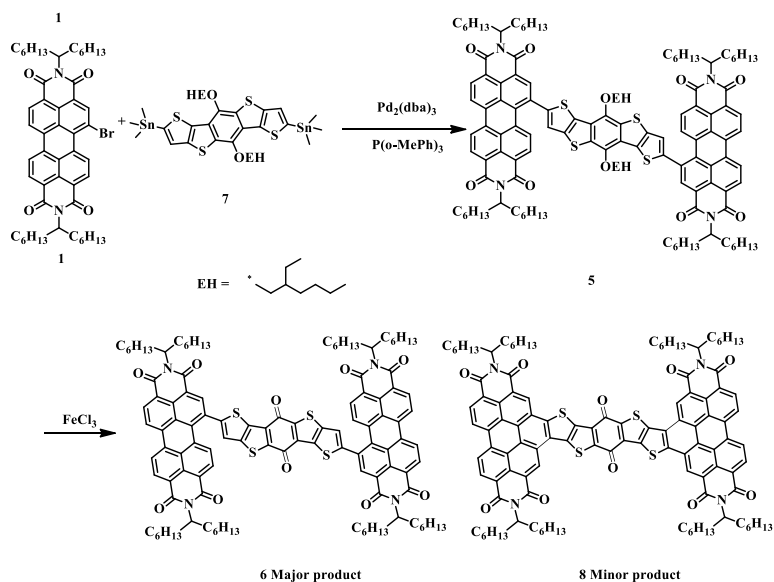
Steady-state absorbance spectra were measured using an Agilent 8432 UV–visible absorption spectrophotometer in chloroform solutions. The emission spectrum measurements were performed with a Fluoromax-2 spectrophotometer. Absorption spectra measurements were

taken before and after each measurement to ensure that there was no appreciable photo-degradation during the fluorescence lifetime measurements or two-photon absorption. The fluorescence quantum yields of the samples were calculated using a known procedure,¹⁻² and Zinc Phthalocyanine in toluene ($\phi = 0.074$) were used as the standard.³

The time-resolved fluorescence experiments were performed using a ultrafast fluorescence Up-Conversion setup that had previously been described.⁴ Mode-locked Ti-sapphire femtosecond laser (Spectra Physics Tsunami) was used to generate 80 fs pulses at 800 nm wavelength with a repetition rate of 82 MHz. This mode-locked laser was pumped by a 532 nm continuous light output from another laser (Spectra Physics Millennia), which has a gain medium of neodymium-doped yttrium vanadate (Nd:YVO₄). An excitation pulse of 400 nm was generated by a second harmonic β -barium borate crystal, and the residual 800 nm beam was made to pass through a computer-controlled motorized optical delay line. The polarization of the excitation beam was controlled by a berek compensator. The power of the excitation beam varied between 17 and 20 mW. The fluorescence emitted by the sample was up-converted by a nonlinear crystal of β -barium borate by using the residual 800 nm beam, which had been delayed by the optical delay line with a gate step of 6.25 fs. This procedure enabled the fluorescence to be measured temporally. The monochromator is used to select the wavelength of the up-converted beam of interest, and the selected beam is detected by a photomultiplier tube (R152P, Hamamatsu, Hamamatsu City, Japan). The photomultiplier tube converts the detected beam into photon counts, which can be read from a computer. Coumarin 30 and Cresyl violet dyes were used for calibrating the laser. The instrument response function (IRF) has been determined from the Raman signal of water to have a width of 110 fs.⁵ Lifetimes of fluorescence decay were

obtained by fitting the fluorescence decay profile with multi-exponential decay functions convoluted with IRF in MATLAB and Origin 8.

Two-photon spectroscopy was performed using a mode-locked Ti : Sapphire laser which is tunable from 700 to 900 nm delivering 110 fs output pulses at a repetition rate of 80 MHz which pumps an OPAL optical parametric oscillator (OPO) lithium borate (LBO) crystal which allows for 1.3 and 1.5 μm output excitations with output power of 200 mW. Emission scans were performed at 800 nm excitation while scanning 415-760 nm emission, but the exact emission detection wavelength during the power dependence scan was selected by the emission wavelength that produced the highest number of counts at ~ 450 nm and ~ 715 nm. Coumarin 307 was used as the standard. Input power from the laser was varied using a variable neutral density filter. Two-photon power-dependent fluorescence intensity was utilized to determine the two-photon absorption cross section through the two-photon emission fluorescence (TPEF) method.⁶



Scheme CS1. Synthetic routes of quinoidal structure.

Synthesis of Compound **5**: To a round-bottom flask equipped with a condenser was added **1** (177 mg, 0.21 mmol), **7** (75 mg, 0.09 mmol), $\text{Pd}_2(\text{dba})_3$ (13 mg, 0.02 mmol) and $\text{P}(o\text{-MePh})_3$ (16 mg,

0.05 mmol). The system was evacuated and refilled with N₂ three times, then charged with toluene (40 ml). The reaction mixture was refluxed under N₂ for 16 hours. After cooling to room temperature, the reaction mixture was concentrated under reduced pressure. The residue was purified by column chromatography with hexane and CH₂Cl₂ (1:1, v/v) as the eluent. Compound **5** was obtained as a red solid (152 mg, 86.9% yield). ¹H NMR (CDCl₃ ppm): δ 8.83-8.66 (m, 10H), 8.40 (d, *J* = 8 Hz, 2H), 8.27 (br, 2H), 7.56 (s, 2H), 5.25-5.17 (br, 4H), 4.30 (s, 4H), 2.28-2.22 (br, 8H), 1.89-1.86 (br, 10H), 1.35-1.22 (m, 80H), 0.89-0.83 (m, 30H), 0.77 (t, *J* = 7 Hz, 6H). ¹³C NMR (CDCl₃, ppm): δ 164.8, 164.3, 163.7, 163.2, 147.9, 144.1, 138.4, 134.2, 133.5, 133.4, 131.3, 129.8, 129.2, 129.1, 128.1, 127.5, 125.8, 123.8, 122.9, 119.7, 129.0, 128.7, 127.5, 124.1, 123.7, 123.4, 122.9, 122.7, 122.3, 119.9, 76.1, 54.9, 54.7, 40.6, 32.4, 31.8, 31.8, 30.2, 29.2, 29.0, 26.9, 23.5, 23.0, 22.6, 14.1, 14.1, 14.0, 11.2. MALDI-TOF: calcd for [C₁₃₀H₁₅₈N₄O₁₀S₄], 2063.1, found, 2063.7.

Synthesis of Compound **6** and **8**: A solution of FeCl₃ (75 mg, 0.46 mmol) in 2 ml nitromethane was added dropwise to a stirred solution of compound **5** (98 mg, 0.05 mmol) in 8 ml CH₂Cl₂. The reaction was stirred with N₂. After stirring for 10 h at room temperature, 1 ml methanol was added to the solution. The solvent was evaporated under reduced pressure, and the residue was purified by column chromatography with hexane and CH₂Cl₂ (1:3, v/v) as the eluent to obtain **6** (58 mg, 67%), then further with CH₂Cl₂ and MeOH (20:1, v/v) to obtain **8** (6 mg, 7%).

Compound **6**: ¹H NMR (CDCl₃ ppm): δ 8.70-8.69 (m, 10H), 8.27 (d, *J* = 8.5 Hz, 4H), 7.66 (s, 2H), 5.24-5.15 (br, 4H), 2.29-2.22 (br, 8H), 1.89-1.85 (br, 8H), 1.36-1.24 (m, 64H), 0.86 (m, 24H). ¹³C NMR (CDCl₃, ppm): δ 173.7, 164.6, 164.3, 163.5, 163.2, 154.1, 145.1, 144.5, 138.3, 135.8, 135.0, 134.0, 133.9, 133.5, 132.0, 131.7, 131.4, 130.9, 130.0, 129.3, 129.1, 128.0, 127.3, 124.2, 123.9, 123.7, 123.4, 123.2, 54.9, 54.8, 31.8, 31.7, 29.2, 29.2, 26.9, 22.6, 14.1, 14.1.

MALDI-TOF: calcd for [C₁₁₄H₁₂₄N₄O₁₀S₄], 1836.8, found, 1837.1. Compound **8**: MALDI-TOF: calcd for [C₁₁₄H₁₂₀N₄O₁₀S₄], 1832.8, found, 1833.0. ¹H NMR was also measured in CD₂Cl₄ in 353 K, very weak signal was shown in aromatic region due to the poor solubility.

1. TGA analysis

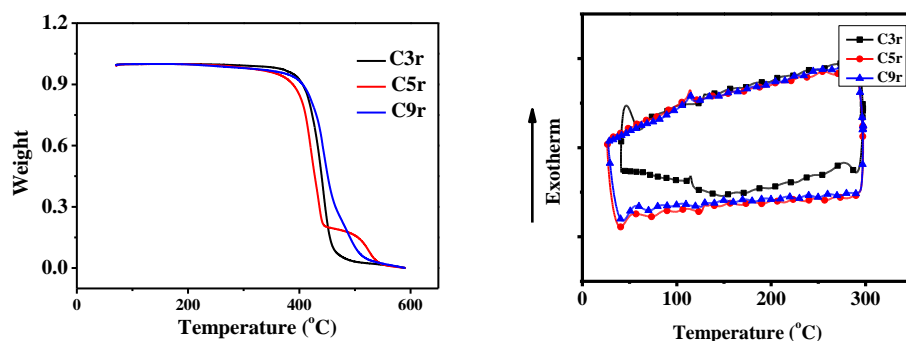


Figure CS1. TGA curves (*left*) of all compounds: heating rate: 10 °C /min. from 70 °C to 550 °C under nitrogen atmosphere. Thermogravimetric analysis (TGA) reveals that both non-fused ring and fused ring molecules are thermally stable up to 400 °C. DSC measurements (*right*) were also performed on a DSC 2920 instrument. Samples (~5 mg) were annealed by heating to 300 °C at 20 °C/min, cooled to 0 °C at 20 °C/min, and then analyzed while being heated to 300 °C at 20 °C/min. No obvious melting peak was shown in the temperature window.

2. NMR spectra.

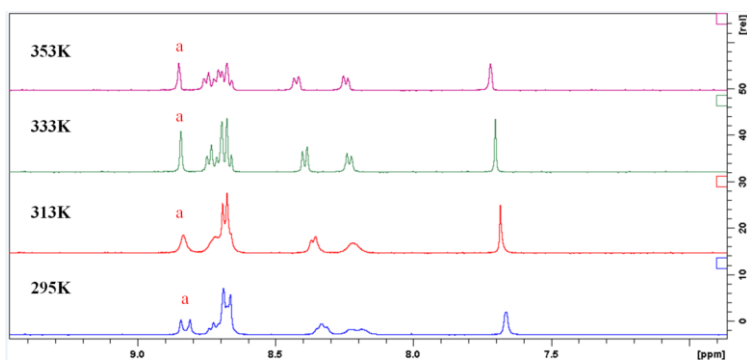


Figure CS2. Variable temperature ¹H NMR spectra of 3r showing the split of proton *a* result from hindered rotation of the asymmetry ethylhexyl groups

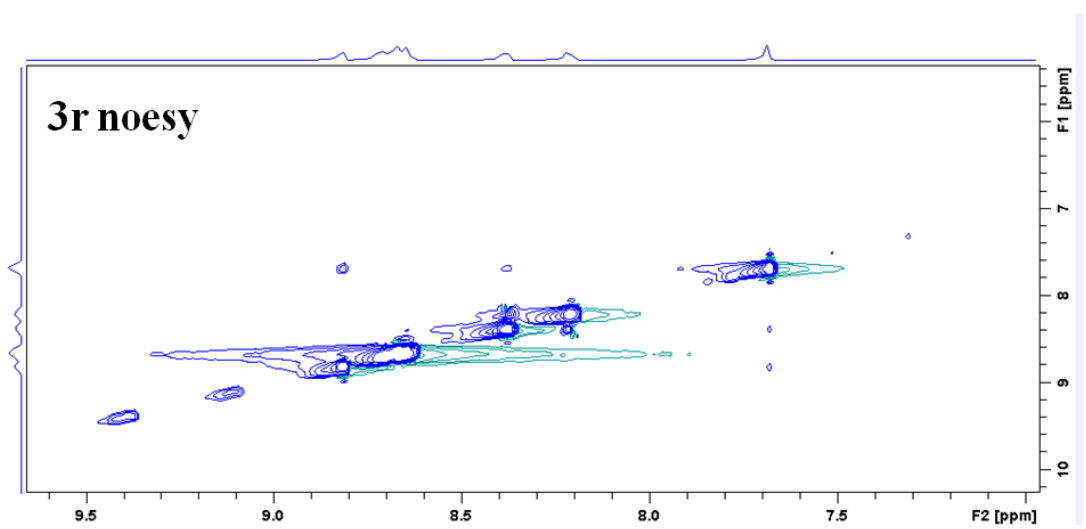
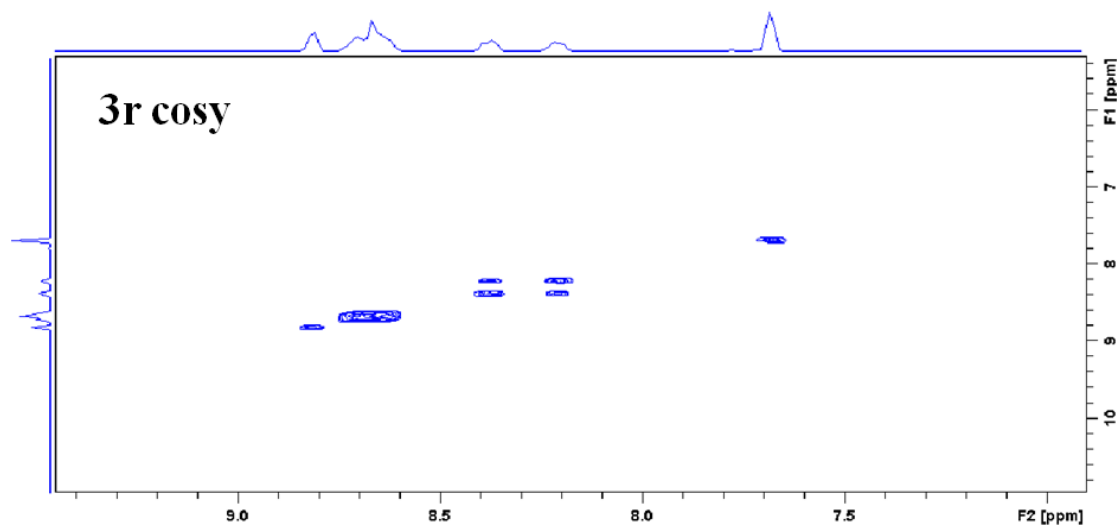
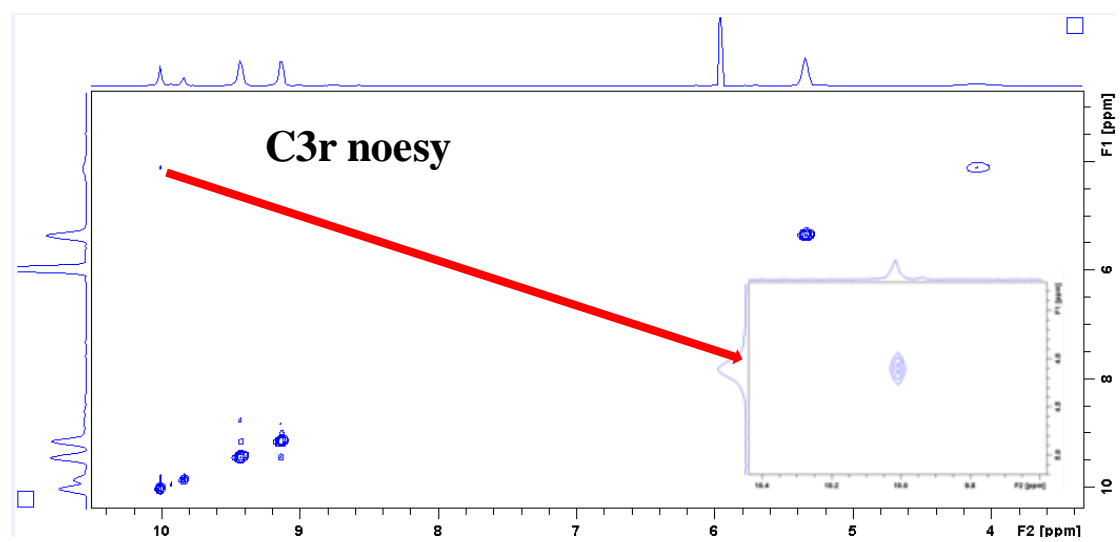


Figure CS3. COSY (up) and NOESY (down) spectra of 3r in 353 K in C₂D₂Cl₄



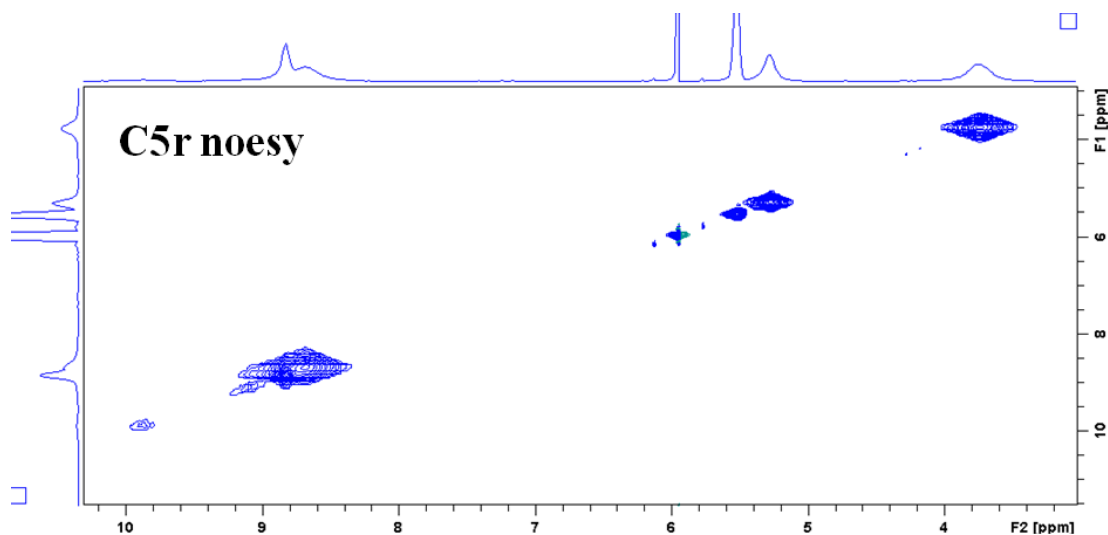


Figure CS4. NOESY spectra of C3r (up) and C5r (down) in 353 K in $C_2D_2Cl_4$

3. DFT calculation

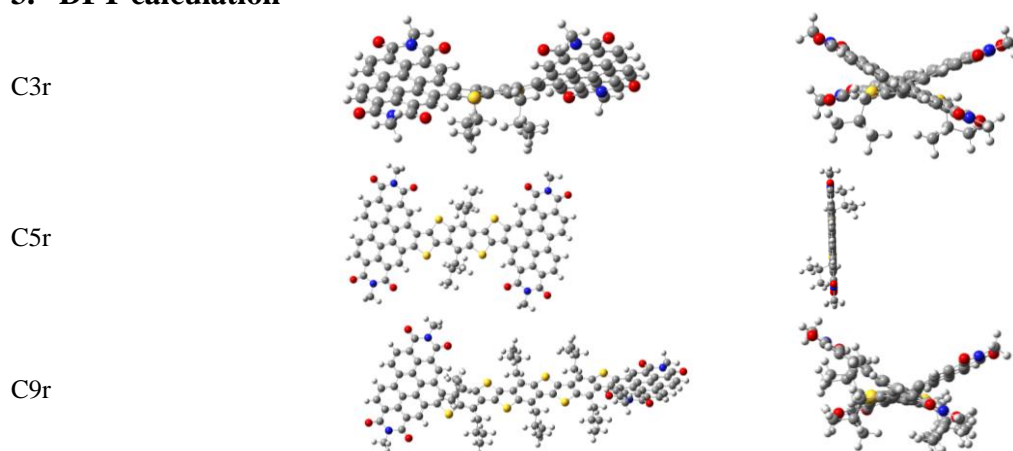
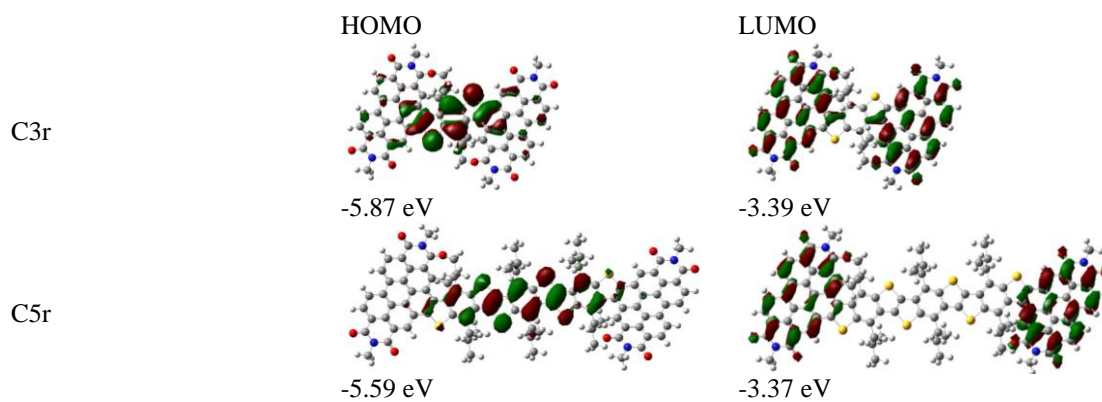


Figure CS5. Optimized geometry of ladder type molecules. To facilitate the calculation, the heptylhexyl chains in PDI were replaced with a methyl group, while the ethylhexyl groups in heteroacenes were replaced by isobutyl to avoid missing the steric hindrance effect.



C9r

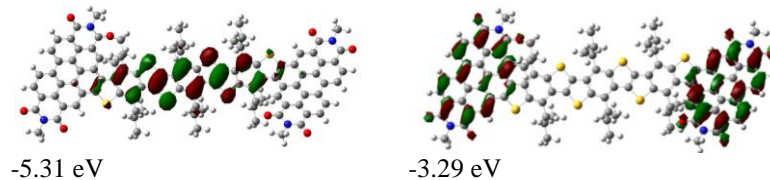


Figure CS6. HOMO and LUMO molecular orbital distribution and the energy levels of ladder type molecules. Isovalue was 0.02 for printing both HOMO and LUMO orbitals.

5. Optical and electrical properties.

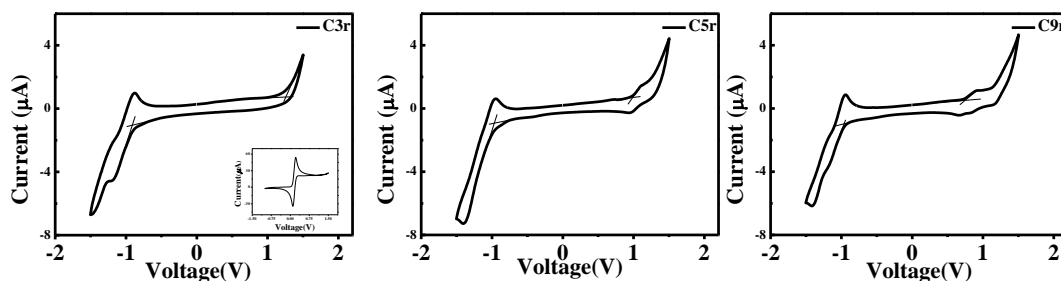


Figure S7. CV of ladder type molecules in CHCl_3 .

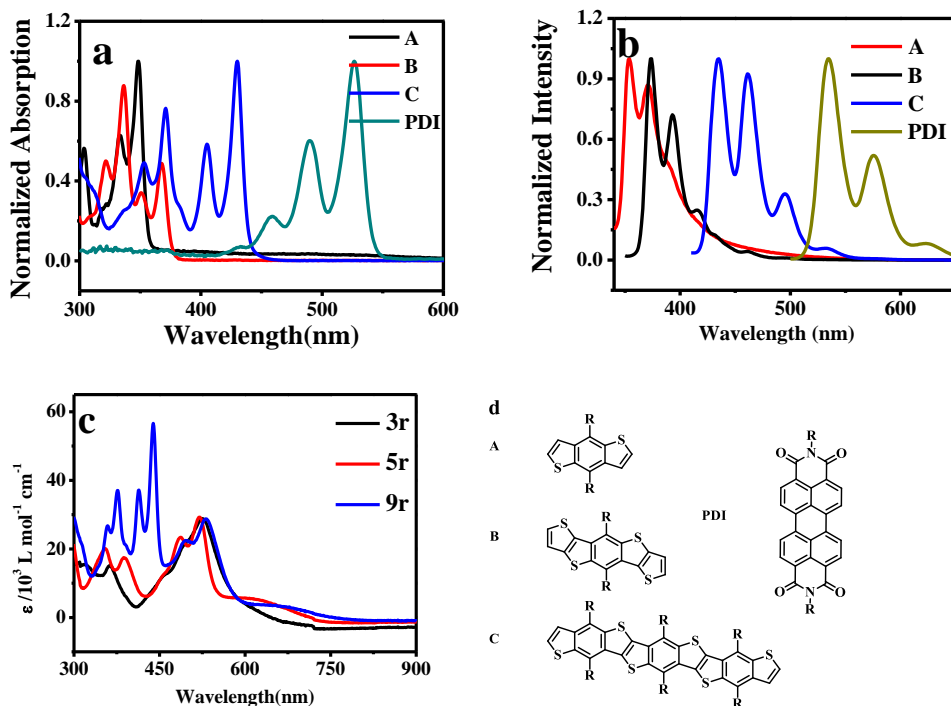


Figure CS8. (a) Absorption spectra of thienoacenes and PDI unit; (b) Fluorescence spectra of thienoacenes and PDI unit; (c) Absorption spectra of non-fused ring compounds; (d) Molecular structures of thienoacenes and PDI unit.

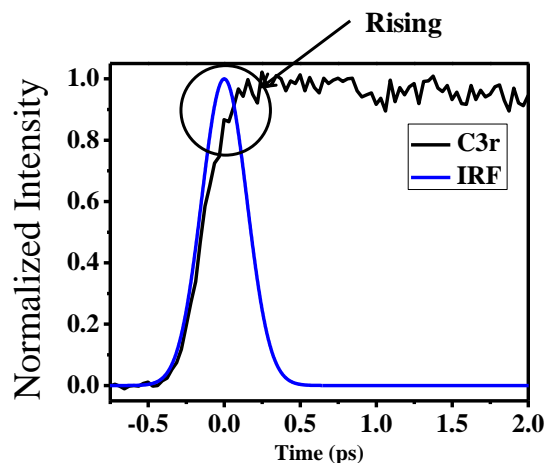


Figure CS9. Energy rising component of the C3r at 600 emission wavelength.

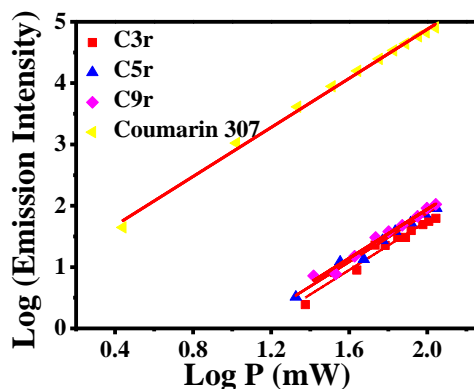


Figure CS10. Power dependence of the two-photon-excited emission of all molecules at ~ 440 - 460 nm.

References

- (1) Furgal, J. C., Jung, J. H., Goodson III, T. and Laine, R.M. *Analyzing Structure–Photophysical Property Relationships for Isolated T8, T10, and T12 Stilbenevinylsilsesquioxanes*. *Journal of the American Chemical Society*. **2013**, *135*, 12259-12269.
- (2) Maciejewski, A. and Steer, R. P. *Spectral and photophysical properties of 9, 10-diphenylanthracene in perfluoro-*n*-hexane: the influence of solute–solvent interactions*. *Journal of photochemistry*. **1986**, *35*, 59-69.
- (3) Adegoke, O. O., Ince, M., Mishra, A., Green, A., Varnavski, O., Martínez-Díaz, M. V., Bäuerle, P., Torres, T. and Goodson III, T. *Synthesis and Ultrafast Time Resolved Spectroscopy of Peripherally Functionalized Zinc Phthalocyanine Bearing Oligothiénylene-ethynylene Subunits*. *The Journal of Physical Chemistry C*. **2013**, *117*, 20912-20918.
- (4) Varnavski, O., Samuel, I. D. W., Pålsson, L. O., Beavington, R., Burn, P. L. and Goodson III, T. *Investigations of excitation energy transfer and intramolecular interactions in a nitrogen corded distyrylbenzene dendrimer system*. *The Journal of chemical physics*. **2002**, *116*, 8893-8903.

- (5) Flynn, D. C., Ramakrishna, G., Yang, H. B., Northrop, B. H., Stang, P. J. and Goodson III, T. *Ultrafast optical excitations in supramolecular metallacycles with charge transfer properties. Journal of the American Chemical Society.* **2010**, *132*, 1348-1358.
- (6) Chi, C. Y., Chen, M. C., Liaw, D. J., Wu, H. Y., Huang, Y. C. and Tai, Y. *A bifunctional copolymer additive to utilize photoenergy transfer and to improve hole mobility for organic ternary bulk-heterojunction solar cell. ACS applied materials & interfaces.* 2014, *6*, 12119-12125.